

UNIVERSITY OF PRETORIA

DEPARTMENT OF CIVIL ENGINEERING

USING SMALL-STRAIN
STIFFNESS TO PREDICT THE
SETTLEMENT OF SHALLOW
FOUNDATIONS ON SAND

May 2014

**USING SMALL-STRAIN STIFFNESS TO PREDICT THE
SETTLEMENT OF SHALLOW FOUNDATIONS ON
SAND**

ANDRE ARCHER

**A project dissertation submitted in partial fulfilment of the requirements for the degree of
MASTER OF ENGINEERING (GEOTECHNICAL ENGINEERING)**

**In the
FACULTY OF ENGINEERING
UNIVERSITY OF PRETORIA**

May 2014

The financial assistance of the National Research Foundation (NRF) towards this research is hereby acknowledged.
Opinions expressed and conclusions arrived at, are those of the author and are not necessarily to be attributed to the NRF.

DISSERTATION SUMMARY

USING SMALL-STRAIN STIFFNESS TO PREDICT THE SETTLEMENT OF SHALLOW FOUNDATIONS ON SAND

A ARCHER

Supervisor: Professor G. Heymann
Department: Civil Engineering
University: University of Pretoria
Degree: Master of Engineering (Geotechnical engineering)

Settlement prediction of shallow foundations is an essential part for the design of a structure. Accuracy is important, and to increase the accuracy, reliable input parameters are required. However, reliable input parameters do not necessarily render accurate results since the parameters used in design are only as good as the prediction method. Foundation design on sands consists of two aspects: bearing capacity and settlement, with settlement being the governing factor in almost all cases. Settlement prediction is not always an easy task. The main reason being that engineers are unable to measure stiffness accurately as well as how to use the stiffness value measured in certain settlement methods. An important soil stiffness value is the initial small-strain shear modulus (G_0) which can be obtained relatively easy with in-situ test methods and the values obtained are generally reliable. With in-situ testing becoming increasingly popular, settlement prediction methods utilising the initial small-strain shear stiffness are also becoming more common.

The main objective of this project is to determine whether the load-settlement behaviour of a shallow foundation can be estimated accurately using only the small-strain shear modulus of the granular soil below the foundation. Centrifuge tests were conducted on an equivalent 5m circular shallow foundation at three different density sands to establish if the stress-settlement behaviour can be predicted and to what level of accuracy. The different density sands were loose, medium dense and dense sands. Bender- and extender elements were used to determine the small-strain stiffness data which were used for the analysis.

The main conclusion drawn from the study is divided into two parts; Full-range load-settlement behaviour and Practical-range load-settlement behaviour. The full-range results relate to full stress-settlement curve with the practical-scale results up to settlements of 0.1D. The method proposed for

the load-settlement prediction is a non-linear stepwise method. The proposed method requires utilising a stiffness degradation curve and it was found that curves presented by Oztoprak & Bolton (2013) and Bolton & Whittle (1999) produced the best results. For the full-range load-settlement results, accurate predictions were found between the predicted and measured load-settlement curves for low density sand. However accuracy decreases with increase in density. For settlements up to 0.1D the load-settlement behaviour was predicted with reasonably good accuracy.

The study showed that the settlement of a shallow foundation can be predicted with reasonable accuracy up to 0.1D settlement using only the small-strain shear stiffness value of the soil below the foundation and that there is merit in the proposed method for future use.

DECLARATION

I, the undersigned hereby declare that:

I understand what plagiarism is and I am aware of the University's policy in this regard;

The work contained in this thesis is my own original work;

I did not refer to work of current or previous students, lecture notes, handbooks or any other study material without proper referencing;

Where other people's work has been used this has been properly acknowledged and referenced;

I have not allowed anyone to copy any part of my thesis;

I have not previously in its entirety or in part submitted this thesis at any university for a degree.

Andre Archer

26124808

10 August 2014

ACKNOWLEDGEMENTS

This dissertation would not have been possible without the assistance and guidance from several individuals or organisations and I wish to express my appreciation to the following:

- a) Firstly, my sincere appreciation to my supervisor Prof. Gerhard Heymann for his continuous support and immense knowledge, but most of all for his enthusiasm and motivation during times of hardship. I cannot imagine a better supervisor and mentor for a project like this and without him this dissertation would not be possible.
- b) My fiancée at the time, Leandi Bain, for her immense support, love, encouragement and late night snacks that provided me with the necessary motivation and focus to complete this project. I thank you sincerely, the love of my life.
- c) My Lord and Saviour for strength, wisdom and the opportunity.
- d) My mother, Christine Rothmann, for her financial assistance, emotional support and love.
- e) The head of the Civil Engineering Department of the University of Pretoria, Prof. Elsabe Kearsley, for her financial support, believe and keeping me on my toes to finish the project.
- f) Prof. SW Jacobsz, for his assistance in the centrifuge lab, practical guidance and motivation.
- g) Dr. Eduard Vorster from Aurecon, for his motivation, support and understanding for doing a Master's degree.
- h) The following persons from the University of Pretoria Civil laboratory for their immense practical advice, the fact that were always ready to assist and motivation:
 - Mr. Johan Scholtz
 - Mr. Jurie van Staden
 - Mr. Jaco Botha
 - Mr. Derick Mostert
 - Mr. Rikus Kock
- i) My family and friends for their continual support, guidance and motivation.
- j) Mr. Madder Steyn for his assistance with the design of the bender- and extender element housing.

TABLE OF CONTENTS

	PAGE
1 INTRODUCTION	1-1
1.1 Objectives of the study	1-2
1.2 Scope of the study	1-2
1.3 Methodology	1-2
1.4 Organisation of the report	1-3
2 LITERATURE STUDY	2-1
2.1 Introduction	2-1
2.2 Shallow foundation design	2-1
2.2.1 Shallow foundation settlement	2-3
2.2.2 Bearing capacity of shallow foundations	2-23
2.3 Small-strain stiffness of soil	2-28
2.3.1 Modulus reduction curves	2-30
2.3.2 Measurements of G_0	2-35
2.3.3 Settlement calculation using G_0 from CSW tests	2-39
2.4 Geotechnical centrifuge testing	2-40
2.4.1 Scaling laws and principles	2-42
2.4.2 Shallow foundation modelling considerations	2-43
2.5 Piezoelectric transducers	2-44
2.5.1 Bender and Extender elements description and behaviour	2-45
2.5.2 Measurement of seismic wave velocity using piezo transducers	2-47
2.5.3 Signal interpretation	2-49
2.5.4 Technical considerations	2-53
2.6 Summary	2-57
3 EXPERIMENTAL WORK	3-1
3.1 Sand classification	3-1
3.1.1 Density	3-1
3.1.2 Particle size distribution	3-3
3.1.3 Specific gravity	3-5
3.1.4 Triaxial test results	3-5
3.1.5 High Load Oedometer test results	3-19
3.1.6 Oedometer with Bender and Extender elements test results	3-27
3.1.7 Scanning electron microscope photos	3-39
3.1.8 Summary	3-41
3.2 Centrifuge Model Design	3-41
3.2.1 Centrifuge	3-42
3.2.2 Model container	3-43
3.2.3 Model foundation	3-44
3.2.4 Bender and extender Elements	3-46
3.2.5 Load-Displacement measurement system	3-53
3.2.6 Sand settlement LVDT's	3-60
3.3 Data acquisition system	3-62
3.4 Complete experimental setup	3-62
4 DISCUSSION	4-1
4.1 Soil density	4-1
4.2 Small-strain stiffness data	4-2
4.2.1 Bender- and Extender data analysis	4-3
4.2.2 20%RD Small-strain stiffness results	4-6

4.2.3	50%RD Small-strain stiffness results	4-11
4.2.4	80%RD Small-strain stiffness results	4-15
4.2.5	Effect of increasing density and stress	4-19
4.3	Load-settlement results	4-21
4.4	Foundation settlement prediction	4-23
4.4.1	Full-range results	4-25
4.4.2	Practical-range Results	4-30
5	CONCLUSIONS AND RECOMMENDATIONS	5-1
5.1	Conclusions	5-1
5.2	Recommendations	5-3
6	REFERENCES	6-1
	APPENDIX A – MODEL FOUNDATION SCALING CALCULATION	A-1

LIST OF TABLES

	PAGE
Table 2.1: Foundation rigidity factors (obtained from Mayne & Poulos, 1999)	2-9
Table 2.2: Summary of different settlement methods for granular materials	2-11
Table 2.3: Modulus reduction curves based on strength parameters	2-31
Table 2.4: Laboratory and in-situ test methods for small-strain stiffness determination (after Clayton, 2011)	2-37
Table 2.5: Geotechnical centrifuge modelling scaling laws (Wood, 2004)	2-42
Table 2.6: Technical considerations for bender/extender elements	2-54
Table 3.1. Minimum and maximum density test results.	3-2
Table 3.2. Density values based on relative densities results.	3-3
Table 3.3: Initial conditions for triaxial tests	3-6
Table 3.4: Triaxial permeability results	3-8
Table 3.5: Coefficient of permeability (Reproduced from Craig, 2004)	3-9
Table 3.6: Relative density prior to shear stage	3-9
Table 3.7: Strength parameters from triaxial tests	3-11
Table 3.8: Typical friction angle values from Look (2014)	3-11
Table 3.9: Critical state ratio, M , values from triaxial tests	3-19
Table 3.10: Initial conditions for high load oedometer tests	3-20
Table 3.11: Preconsolidation pressure values	3-23
Table 3.12: Critical state parameters from high load oedometer test results	3-25
Table 3.13: Initial conditions from oedometer tests	3-27
Table 3.14: Compressibility characteristics from oedometer results	3-30
Table 3.15: Small-strain results for standard oedometer tests	3-33
Table 3.16: Regression parameters C_g and n_g for G_0 calculation	3-37
Table 3.17: Regression parameters C_g and n_g for M_0 calculation	3-38
Table 3.18: Summary of Cullinan sand properties	3-41
Table 3.19: University of Pretoria geotechnical centrifuge specifications (Jacobsz et al. 2014)	3-43
Table 3.20: Model foundation rigidity	3-45
Table 3.21: Performance guidelines for bender- and extender elements (Piezo Systems, Inc., 2011)	3-46
Table 3.22: Specifications for SHE3.1 mechanical ball screw jack	3-53

Table 3.23: U93 load cell specifications	3-55
Table 3.24: General specifications for the HBM WA50 displacement transducer	3-57
Table 3.25: General specifications for the AS/15 S series LVDT	3-61
Table 3.26: Calibration factors for LVDT 1-4	3-62
Table 4.1: Sand settlement LVDT results	4-2
Table 4.2: Densities obtained during model tests	4-2
Table 4.3: Small-strain stiffness results for 20%RD Test 1	4-8
Table 4.4: Small-strain stiffness results for 20%RD Test 2	4-9
Table 4.5: 20%RD Tests regression line values	4-11
Table 4.6: Small-strain stiffness results for 50%RD Test 1	4-12
Table 4.7: Small-strain stiffness results for 50%RD Test 2	4-13
Table 4.8: 50%RD Tests regression line values	4-15
Table 4.9: Small-strain stiffness results for 80%RD Test 1	4-16
Table 4.10: Small-strain stiffness results for 80%RD Test 2	4-17
Table 4.11: 80%RD Tests regression line values	4-19
Table 4.12: Proposed method stiffness degradation curve variables - Full range results	4-28
Table 4.13: Proposed method stiffness degradation curve variables - Practical range results	4-33

LIST OF FIGURES

	PAGE
Figure 2.1: Typical shallow foundation types	2-2
Figure 2.2: Stresses due to a point load – Boussinesq theory (redrawn from Craig, 2004)	2-6
Figure 2.3: Vertical stresses below the centre of a circular area	2-7
Figure 2.4: Circular foundation pressure bulbs (after Holtz, 1991)	2-8
Figure 2.5: Shear stress pressure bulbs for circular foundations (after Smith, 2006)	2-8
Figure 2.6: Contact stress under rigid and flexible foundation on granular material (after Barnes, 2000)	2-9
Figure 2.7: Probabilistic design chart (after Das & Sivakugan, 2007)	2-22
Figure 2.8: Bearing pressures vs. settlement (modified from Barnes, 2000)	2-24
Figure 2.9: Bearing capacity modes of failure (adapted from Craig, 2004)	2-25
Figure 2.10: Modes of failure for sands compared with relative density (after Das, 2011)	2-25
Figure 2.11: Footing width effect on failure for foundations (modified from Zhou, 2006)	2-27
Figure 2.12: Stiffness modulus terms (after Yongqing, 2011)	2-29
Figure 2.13: Typical modulus reduction curve (after Mair, 1993)	2-30
Figure 2.14: Strain levels for different test methods (modified from Jastrzębska & Lupieżowicz, 2011)	2-36
Figure 2.15: Schematic of different types of centrifuges (after Fu, 2004)	2-40
Figure 2.16: Stress variation between model and prototype (after Taylor, 1995)	2-42
Figure 2.17: Composition of piezoelectric transducers (after Fu, 2004)	2-44
Figure 2.18: Piezoelectric elements polarization configurations	2-46
Figure 2.19: Bender and extender elements wiring configurations	2-46
Figure 2.20: Bender- and extender element working principle	2-48
Figure 2.21: Typical schematic of bender/extender setup	2-49
Figure 2.22: Schematic of typical received signal with visual picking technique	2-50
Figure 3.1. Particle size distribution of Cullinan sand.	3-4
Figure 3.2: Consolidation curve for 20% RD 200eff test showing c_v t_{90} determination	3-8
Figure 3.3: Stress path results for 20% RD test	3-10
Figure 3.4: Stress path results for 50% RD test	3-10
Figure 3.5: Stress path results for 80% RD test	3-11
Figure 3.6: Stiffness behaviour of 20% RD Cullinan sand	3-13

Figure 3.7: Stiffness behaviour of 50% RD Cullinan sand	3-13
Figure 3.8: Stiffness behaviour of 80% RD Cullinan sand	3-14
Figure 3.9: Combined stiffness behaviour of Cullinan sand	3-14
Figure 3.10: Critical state space plot (adapted from (Barnes 2000))	3-15
Figure 3.11: Critical state lines from triaxial tests (redrawn from Atkinson (1993))	3-16
Figure 3.12: Triaxial critical state plot - 20% RD test	3-17
Figure 3.13: Triaxial critical state plot - 50% RD test	3-17
Figure 3.14: Triaxial critical state plot - 80% RD test	3-18
Figure 3.15: High load oedometer test setup	3-20
Figure 3.16: e vs. σ'_v curve for 20% RD high load oedometer test	3-21
Figure 3.17: e vs. σ'_v curve for 50% RD high load oedometer test	3-21
Figure 3.18: e vs. σ'_v curve for 80% RD high load oedometer test	3-22
Figure 3.19: Empirical construction to determine σ'_p for 50% RD test	3-22
Figure 3.20: Critical state plot from consolidation data	3-24
Figure 3.21: v vs. $\ln p'$ for 50% RD high load oedometer test	3-24
Figure 3.22: Isotropic compression of Chattahoochee River sand (redrawn form Atkinson & Bransby, 1978)	3-25
Figure 3.23: Combined high load oedometer results	3-26
Figure 3.24: e vs. $\log \sigma'_v$ for 20% RD oedometer test	3-28
Figure 3.25: e vs. $\log \sigma'_v$ for 50% RD oedometer test	3-29
Figure 3.26: e vs. $\log \sigma'_v$ for 80% RD oedometer test	3-29
Figure 3.27: Example of bender element results from oedometer test	3-31
Figure 3.28: Example of extender element results from oedometer test	3-31
Figure 3.29: G_0 vs. Vertical strain from standard oedometer results	3-32
Figure 3.30: M_0 vs. Vertical strain from standard oedometer results	3-34
Figure 3.31: G_0 vs. Vertical effective stress from standard oedometer results	3-34
Figure 3.32: M_0 vs. Vertical effective stress from standard oedometer results	3-35
Figure 3.33: Regression data plot for G_0 empirical equation	3-37
Figure 3.34: Regression data plot for M_0 empirical equation	3-37
Figure 3.35: Measure vs. Predicted G_0	3-38
Figure 3.36: Measure vs. Predicted M_0	3-39

Figure 3.37: SEM image of Cullinan sand	3-40
Figure 3.38: SEM image of surface of sand particle	3-40
Figure 3.39: University of Pretoria geotechnical centrifuge	3-42
Figure 3.40: Centrifuge model container	3-43
Figure 3.41: Model foundation	3-45
Figure 3.42: Dimensions of bender and extender elements	3-47
Figure 3.43: Picture of a typical bender element used	3-47
Figure 3.44: Design drawing of bender- and extender element housing	3-48
Figure 3.45: Completed housing with element inside	3-48
Figure 3.46: Stripped wire used for bender- and extender elements	3-49
Figure 3.47: Schematic of the bender- and extender element isolation	3-50
Figure 3.48: Mechanical noise problem schematic	3-50
Figure 3.49: Charge amplifier circuit design	3-52
Figure 3.50: Picture of the completed charge amplifier box	3-53
Figure 3.51: Schematic of SHE3.1 mechanical ball screw jack (Pfaff-silberblau, 2010)	3-54
Figure 3.52: Calibration curve for the U93 load cell	3-55
Figure 3.53: Load cell calibration confirmation	3-56
Figure 3.54: Close up of load cell	3-56
Figure 3.55: Calibration curve for the displacement LVDT	3-57
Figure 3.56: Calibration confirmation of the displacement LVDT	3-58
Figure 3.57: Close up of displacement transducer attached to jack	3-58
Figure 3.58: Load-displacement system assessment setup	3-59
Figure 3.59: Load-displacement system assessment curve	3-60
Figure 3.60: Close-up of AS/15 S series LVDT	3-61
Figure 3.61: Calibration curve for LVDT 1	3-61
Figure 3.62: Initial placement of the sand in the model container	3-64
Figure 3.63: A bender- and extender element pair placed in the soil	3-65
Figure 3.64: Model after foundation and elements have been placed in the soil	3-65
Figure 3.65: Schematic of model setup showing the inside of the model	3-65
Figure 3.66: Complete experimental model setup	3-66

Figure 4.1: 20%RD Test 1 sand settlement result	4-2
Figure 4.2: Typical bender element result before stacking	4-4
Figure 4.3: Typical results of bender element before and after stacking	4-4
Figure 4.4: Received stacked signal for middle extender 40g 80%RD Test 2	4-5
Figure 4.5: Received stacked signal for middle bender 40g 80%RD Test 2	4-6
Figure 4.6: V_s and V_p for the 20%RD Tests	4-10
Figure 4.7: G_0 and M_0 for the 20%RD Tests	4-10
Figure 4.8: V_s and V_p for the 50%RD Tests	4-14
Figure 4.9: G_0 and M_0 for the 50%RD Tests	4-14
Figure 4.10: V_s and V_p for the 80%RD Tests	4-18
Figure 4.11: G_0 and M_0 for the 80%RD Tests	4-18
Figure 4.12: Wave velocities vs. density 20%RD Test 1	4-20
Figure 4.13: Overburden stress vs. wave velocities 20%RD Test 1	4-20
Figure 4.14: Force vs. relative settlement for prototype foundation	4-22
Figure 4.15: Stress vs. relative settlement for prototype foundation	4-22
Figure 4.16: Stress vs. relative settlement for tolerable settlement of 25mm	4-23
Figure 4.17: Predicted vs. measured results - 20%RD Tests – Full range	4-26
Figure 4.18: Predicted vs. measured results - 50%RD Tests – Full range	4-27
Figure 4.19: Predicted vs. measured results - 80%RD Tests – Full range	4-27
Figure 4.20: Proposed method stiffness degradation curves - Full range results	4-29
Figure 4.21: Predicted vs. measured results - 20%RD Tests – Practical range	4-31
Figure 4.22: Predicted vs. measured results - 50%RD Tests – Practical range	4-31
Figure 4.23: Predicted vs. measured results - 80%RD Tests – Practical range	4-32
Figure 4.24: Proposed method stiffness degradation curves - Practical range results	4-33

1 INTRODUCTION

Engineers are continually seeking design methods which will predict structural behaviour more accurately. In most cases more accurate results require reliable input parameters which can be a costly exercise to achieve. On the other hand, reliable input parameters do not necessarily render accurate results if an inaccurate prediction method is used.

When considering the design of a structure, one of the main aspects and in some instances a governing factor, is the design of the foundation. When considering foundation design, two aspects are considered, (1) the bearing capacity, and (2) the settlement, with settlement being the governing factor in most cases (particularly quartz to silica sands). Settlement prediction is not always an easy task for practicing engineers due to two main reasons. The first being the fact that there are so many methods to choose from together with the problem that the assumptions made with some methods do not conform to the design problem at hand. The second, which goes hand in hand with the first reason, is the inability of engineers to quantify the stiffness of the soil required for most settlement prediction methods (Das & Sivakugan 2007).

When considering soil stiffness, the initial small-strain shear modulus (G_0) value can be obtained with more certainty than stiffness values at intermediate and higher strains. One of the main reasons for the increase in use of small-strain stiffness is the fact that the value can be obtained relatively easy with in-situ and laboratory test methods and the values obtained are reliable (Campanella, 1994; Woods, 1978).

In-situ testing is becoming increasingly popular, due to the fact that measurements are obtained quickly compared to laboratory testing, and taking the time factor into account it is often more cost effective. In other words, is it worth paying and doing laboratory tests, where the results might not be reliable, when in-situ testing can be done which will render more reliable results in a shorter time frame? Since small-strain stiffness is an important parameter for settlement prediction, it would be worthwhile investigating settlement prediction methods incorporating G_0 . A major objective of this research project was to find a settlement prediction method that only uses G_0 , hence no laboratory testing would be required. Since values for G_0 can be obtained from in-situ tests rapidly, settlement prediction can be done quickly, and possibly more cost effective, if a suitable method is available. The author therefore set out to try and establish if there is a settlement prediction method that can be proposed to practicing engineers, incorporating only the G_0 value.

1.1 OBJECTIVES OF THE STUDY

The main objective of this study was to experimentally determine if the load-settlement behaviour of a shallow foundation can be estimated using only the small-strain shear modulus value of the soil below the foundation. Centrifuge testing was done to obtain the measured load-settlement behaviour.

The study also includes other objectives, relating to the experimental work:

- To characterise the sand to be used in the centrifuge model for this projects, but for future projects as well.
- To develop instrumentation to be used in the centrifuge which can measure the small-strain shear stiffness of the sand.

1.2 SCOPE OF THE STUDY

The scope of this study is limited to the following aspects:

- The research project was laboratory based with physical modelling of a shallow foundation done by means of geotechnical centrifuge testing.
- Only a shallow circular foundation, 5m diameter was assessed. No square, strip or rectangular foundations were tested.
- The geomaterial used was a dry silica sand which was characterised with various laboratory tests.
- Only three relative densities were used for the experiment: 20%, 50% and 80%.
- No strain measurements were taken below the foundation, only the load-settlement behaviour was measured together with the small-strain stiffness of the soil below the foundation.
- Small-strain stiffness values were obtained with the use of bender- and extender elements.
- The proposed method is for a young uncemented sand.
- Stiffness degradation curves used for the proposed method were only based on stiffness characteristics and not strength characteristics.

1.3 METHODOLOGY

The methodology followed to achieve the set objectives are as follows:

- A literature review of settlement prediction methods, general shallow foundation design, small-strain stiffness, geotechnical centrifuge testing and piezoelectric elements were conducted. The information obtained provided insight into the problem and was used to develop the experimental part of the project.
- An experimental test setup was developed to measure the load-settlement behaviour together with the small-strain stiffness of the soil. The experimental work was broken up into two sections:
 1. Firstly, characterising the sand to be used during the test;
 2. Secondly, conducting geotechnical centrifuge tests on different density sands.
- The centrifuge data was analysed to obtain load-settlement and small-strain stiffness with depth for the three different relative densities tested.
- A settlement prediction method was adopted and based on the results obtained from the centrifuge tests; the load-settlement behaviour of the experimental foundation was estimated.
- Finally, the predicted and measured results were compared to assess the proposed method from which conclusions were drawn.

1.4 ORGANISATION OF THE REPORT

The arrangement of the report is as follows:

- **Chapter 1** serves as introduction to the report, providing a brief overview of the topic and conveying the importance and reasons for the research. The introduction outlines the objectives, scope and methodology of the report and experimental work.
- **Chapter 2** is a review of the applicable and current literature. It reviews settlement prediction methods, general shallow foundation design, small-strain stiffness, geotechnical centrifuge testing and piezoelectric elements.
- **Chapter 3** describes the experimental work conducted. Firstly the sand characteristics are discussed in detail, where after the centrifuge model design and setup is conveyed.
- **Chapter 4** presents the results obtained from the centrifuge tests, which is divided into two sections, the small-strain stiffness data and the load-settlement data. Lastly the proposed method is presented and the results between the measured and predicted values are discussed.

- **Chapter 5** presents the main conclusions and recommendations of this dissertation.
- **Chapter 6** provides the list of references used in the report.
- **Appendix A** contains a summary of the model foundation scaling calculation.

2 LITERATURE STUDY

2.1 INTRODUCTION

In this chapter relevant information regarding shallow foundations and small-strain stiffness of soils will be discussed as well as information on geotechnical centrifuge testing and piezoceramic elements. The aim of this chapter is to gain insight into all the different aspects of the subject matter relevant to the research conducted and to guide the reader into understanding the problem the researcher wanted to address. As stated previously, the focus of the report is on shallow foundations only and for this reason only information relevant to shallow foundations will be conveyed in this chapter. A hypothesis will be given which will be used, together with the information presented in this chapter, for the design of the experimental work.

2.2 SHALLOW FOUNDATION DESIGN

The foundation of a structure is that part that transmits the loads from the structure onto the underlying soil. Depending on the soil conditions, safety requirements, serviceability and economic factors, there are two main foundation types typically considered namely shallow- or deep foundations. If the underlying soil near the surface is sufficiently strong to withstand the structural loads, then it is possible to use shallow foundations, alternatively deep foundations should be considered.

Smith (2006) defined shallow foundations as: “*A foundation whose depth below the surface, z , is equal to or less than its least dimension, B* ” (i.e. $z/B \leq 1$). Holtz (1991) provided an additional definition of a shallow foundation stating that a shallow foundation need not be near the ground surface, but is “shallow” in relation to the superimposing structure. This means that the foundation might be in excess of 10m below the ground surface, but still be a shallow foundation. Das (2009) states that individual footings supporting column loads such as square or rectangular as well as strip footings supporting walls fall under the description of shallow foundations. Circular footings are not mentioned, but these also fall under individual footings and are also a shallow foundation type. Another shallow foundation type is known as raft foundations. These foundations are known to cover large areas (Smith, 2006) and are also known as combined footings (Peck et al. 1953), since they support walls as well as column loads. Their design is different from the individual types, for example they are not prone to bearing capacity failure (which will be discussed subsequently), and it will therefore not be included in this report. Typical shallow foundation types are shown in Figure 2.1.

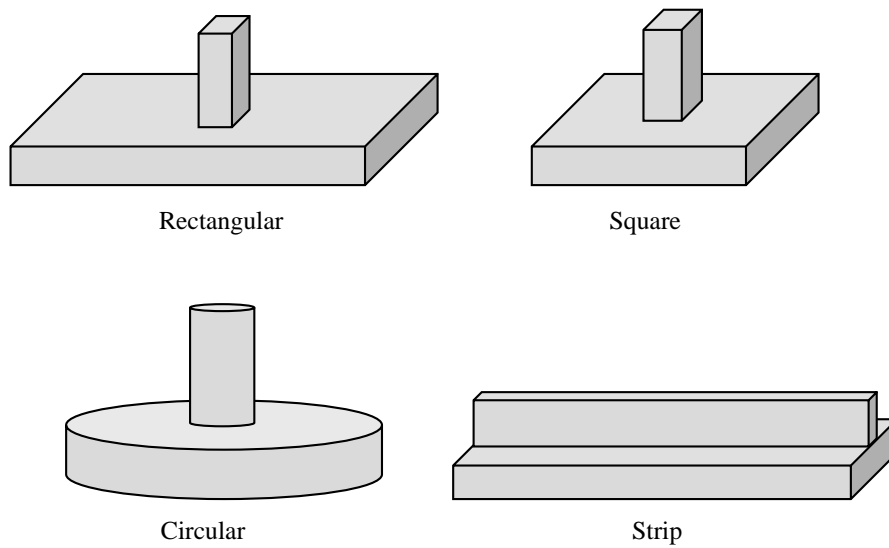


Figure 2.1: Typical shallow foundation types

Foundations are typically designed to meet serviceability as well as strength criteria (Chen & McCarron, 1991). Serviceability criteria relates to the settlement of the foundation and is seen as a long term consideration under normal loads, whereas the strength criteria relates to short term problems concerning the occasional excessive large load and relates to the bearing capacity (Chen & McCarron, 1991). Strength and serviceability criteria are treated as separate design responsibilities, but both of these aspects should be adhered to, and for that reason they are related. In most cases the required bearing capacity can be easily achieved and therefore the performance of most shallow foundations is controlled by the settlement (Chen & McCarron, 1991).

Shallow foundations can be constructed on weak or strong soil types, but in weak soil, some mitigating measures may be required in order to reduce the excessive settlement that may occur. Whether the soil underneath the foundation is strong or weak, the type of foundation to be constructed will depend on the soil parameters. The soil may be in different layers, with each layer having different characteristics as well as different soil types for example clay or sand.

If a foundation is to be constructed on sand, Peck et al. (1953) states that the foundation selection depends on the relative density as well as the depth of the water table. The relative density of coarse-grained soils (i.e. sand) is commonly defined as the degree of compaction of the soil (Das 2008). Hence, if a soil is in its most compacted state, i.e. the maximum density, the relative density is high and for a very loose soil, i.e. minimum density, the relative density

value is low. The relative density can be expressed as a value from 0 to 1 or as a percentage value of 0% to 100%, with the 0-values denoting a minimum relative density and 1 and 100% respectively a maximum relative density. Peck et al. (1953) also notes that the relative density regulates the bearing capacity and is also an important factor for settlement prediction in sandy materials. If a shallow foundation should fail, the failure mode is influenced by the relative density as well as the embedment, load and drainage conditions (Chai, 2000). It is however stated in the literature (e.g. Craig (2004) and Das (2009)) that the failure mode is related to the bearing capacity of the soil and not the settlement. Therefore, depending on the relative density of a soil and the resulting bearing capacity, a specific failure type will occur and these failure types will be discussed in the ensuing sections.

Considering the aforementioned, there are various aspects that need to be considered in order to design a shallow foundation, and with all these aspects there are uncertainties that will arise during the design process. The Canadian Geotechnical Society (2006) provides four categories of uncertainties for which allowances must be made during design namely:

1. *Uncertainties in estimating the load effects*
2. *Uncertainties associated with inherent variability of the ground*
3. *Uncertainties in evaluation of geotechnical material properties*
4. *Uncertainties associated with the degree to which the analysis represents the actual behaviour/response of the foundation, structure, and the ground that supports the structure.*

These uncertainties are usually accounted for by means of safety factors, which might significantly increase project cost, due to a high uncertainty leading to a high factor of safety and over design. Since cost is a major concern on many projects, engineers are always optimizing designs from a cost perspective without compromising the quality or reliability of the design. Since foundations are an integral part of a structure it is therefore necessary to strive for improvements in the design to reduce uncertainty and cost without compromising on quality and reliability.

2.2.1 SHALLOW FOUNDATION SETTLEMENT

As mentioned previously and stated by Das & Sivakugan (2007), settlement criteria is more often the governing factor in the design of shallow foundation, especially on sandy soils and foundations with a footing width larger than 1.5 m. The settlement can either be the total (uniform) settlement or differential settlement and a foundation should be designed to keep these within allowable limits. Usually the allowable limits is client or project specific, but as a general rule the maximum allowable settlement for any footing on granular soil is limited to

25 mm (Terzaghi et al. 1996). Settlement of shallow foundations depend on various factors given by Canadian Geotechnical Society (2006) as the magnitude of the applied load, foundation geometry and size, ground conditions, ground stiffness and the strength of the underlying soil. All the aforementioned factors may lead to uncertainty and, as stated by Yongqing (2011), accurate estimation of foundation settlement remains a big challenge in foundation design. Numerous methods for estimating foundation settlement have been proposed and in 1986 Douglas reported the existence of more than forty methods for the estimation of foundation settlement on granular soils (Das & Sivakugan 2007). Since then some methods have proved to be more reliable than others with some new methods that have been proposed. Various methods will be discussed in brief later in the chapter.

Enkhtur et al. (2013) categorised settlement calculation methods into three approaches: (1) empirical methods where the settlement is predicted in correlation with in-situ test parameters, (2) theoretical methods based on elastic deformation and strain influence factors, and (3) methods based on load-settlement curves. Finite element methods (FEM) are also used extensively and in some instances have become common practice. Although FEM have proved to be reliable, in depth knowledge of settlement prediction from conventional methods are necessary in order to understand if the FEM produces correct results. Holtz (1991) provides 8 steps for foundation settlement analysis, which in brief are as follows:

1. Establish the soil profile as well as the level of the water table and compute the effective stress profile with depth;
2. Estimate the foundation loading including the rate of loading and magnitude;
3. Estimate the stress distribution with depth;
4. Estimate the preconsolidation pressure,
5. Calculate the consolidation settlements;
6. Estimate the time rate of consolidation;
7. Estimate the secondary compression rate;
8. If necessary, calculate the distortion (initial) settlements. For granular, cohesionless materials use empirical methods.

For cohesionless soils, the distortion as well as primary consolidation settlements occur more or less together due to the high permeabilities associated with these soils (Smith, 2006; Venkatramaiah, 2006). Therefore, for this project, only steps 1, 2, 3 and 8. Considering step 3, it is necessary to estimate the stress distribution, it is implied that a function of the settlement is the additional stresses imposed on the soil due to the foundation load. The stresses can be estimated with reasonable accuracy if the boundary conditions in the analytical model approximate the in-situ conditions (Holtz, 1991). It is therefore desirable and

necessary to evaluate the relationship of stress increase with load application before any of the settlement calculations are discussed.

In most cases Boussinesq theory introduced in 1885 for the estimation of vertical stresses within in a semi-infinite, homogeneous, isotropic mass is used. This method does not require specific material constants to calculate the vertical stress distribution (Holtz, 1991). Westergaard in 1938 also introduced a method to determine the vertical stresses in soil due to a point load, but this method is for a solid elastic medium with thin reinforced layers. Das (2009) states that Westergaard's assumption may be illustrated as a clay layer with thin layers of sand which is not relevant for this project. Boussinesq's theory is therefore more applicable and will be discussed further.

According to Boussinesq and with reference to Figure 2.2, the stress at any point, point A in the figure, due to a point load at the surface can be calculated as follows:

$$\sigma_z = \frac{3Q}{2\pi z^2} \left\{ \frac{1}{1+(r/z)^2} \right\}^{5/2} \quad 2.1$$

$$\sigma_r = \frac{Q}{2\pi} \left\{ \frac{3r^2z}{(r^2+z^2)^{5/2}} - \frac{1-2\nu}{r^2+z^2+z(r^2+z^2)^{1/2}} \right\} \quad 2.2$$

$$\sigma_\theta = -\frac{Q}{2\pi} (1-2\nu) \left\{ \frac{z}{(r^2+z^2)^{3/2}} - \frac{1}{r^2+z^2+z(r^2+z^2)^{1/2}} \right\} \quad 2.3$$

$$\tau_{rz} = \frac{3Q}{2\pi} \left\{ \frac{rz^2}{(r^2+z^2)^{5/2}} \right\} \quad 2.4$$

where: ν = Poisson's ratio

σ = normal stress in the direction as shown

τ = shear stress in the direction as shown

Q = point load

In practice Equation 2.1 is written in terms of an influence factor, I_p , with:

$$I_p = \frac{3}{2\pi} \left\{ \frac{1}{1+(r/z)^2} \right\}^{5/2} \quad 2.5$$

Thus,

$$\sigma_z = \frac{Q}{z^2} I_p$$

2.6

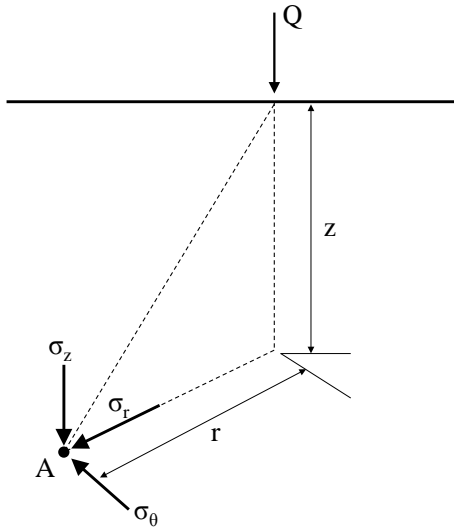


Figure 2.2: Stresses due to a point load – Boussinesq theory (redrawn from Craig, 2004)

Any loaded area on the surface may be reduced to a system of point loads and Boussinesq's solution for each of these point loads may be integrated to determine the stresses underneath any area (Powrie 1997). Since the scope of this project is confined to circular foundations, only Boussinesq's equations for circular areas will be discussed.

In line with Boussinesq's theory, the vertical stresses below the centre of a circular area (illustrated in Figure 2.3) can be calculated using Equations 2.7 and 2.8:

$$\sigma_z = q \left[1 - \left\{ \frac{1}{1 + (R/z)^2} \right\}^{3/2} \right] = q I_c \quad 2.7$$

$$\sigma_r = \sigma_\theta = \frac{q}{2} \left[(1 + 2\nu) - \frac{2(1 + \nu)}{\{1 + (R/z)^2\}^{1/2}} + \frac{1}{\{1 + (R/z)^2\}^{3/2}} \right] \quad 2.8$$

Where: R = radius

q = uniform pressure

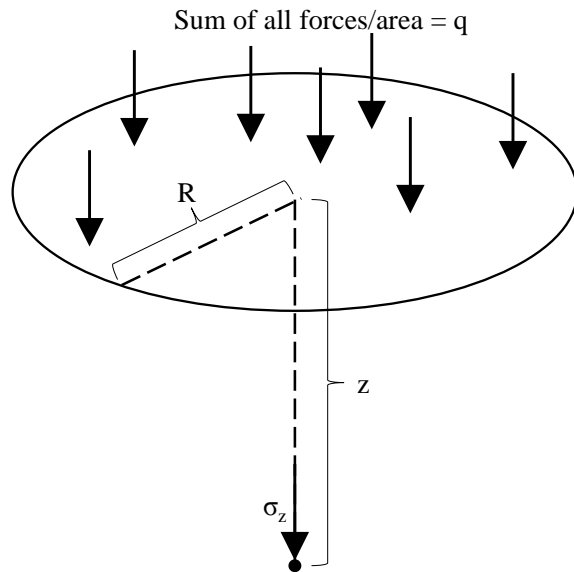


Figure 2.3: Vertical stresses below the centre of a circular area

A useful way of presenting the stress distribution is to consider contours of equal vertical stress which can be presented graphically. These contours are often called isobars (Holtz, 1991) or referred to as bulbs of pressure (Smith 2006). A representation of the pressure bulbs for a circular footing, calculated using Boussinesq's method, are shown in Figure 2.4. From these bulbs the depth of influence of a loaded foundation can be seen and for in practice pressures below a circular foundation down to depth of about $1.5B - 2B$ are important, as pressures below these depths are of little consequence. Perloff (1975) states that importance of the pressure bulbs cannot be overrated, especially for settlement purposes. It is worth mentioning that Smith (2006) presents pressure bulbs for shear stresses for circular foundations. This is important since it is essential to check that shear strength is not exceeded (Smith 2006). The shear stress pressure bulbs related to circular foundation are presented in Figure 2.5. Comparing Figure 2.4 with Figure 2.5 it should be noticed that the influence depth of the shear stresses are shallower than for the vertical stresses.

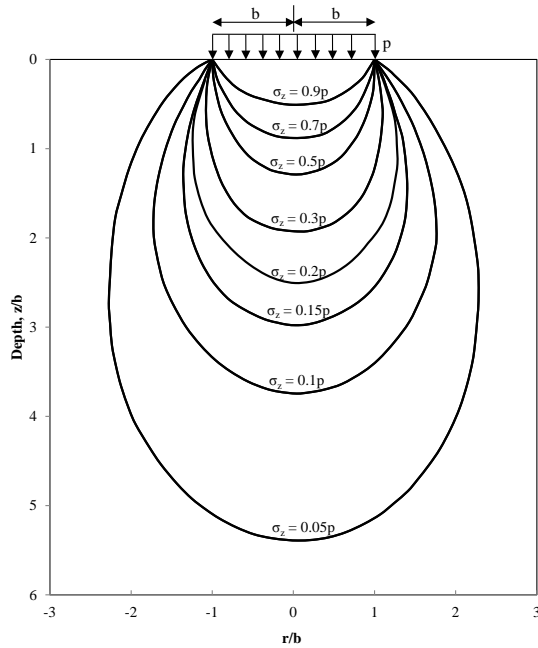


Figure 2.4: Circular foundation pressure bulbs (after Holtz, 1991)

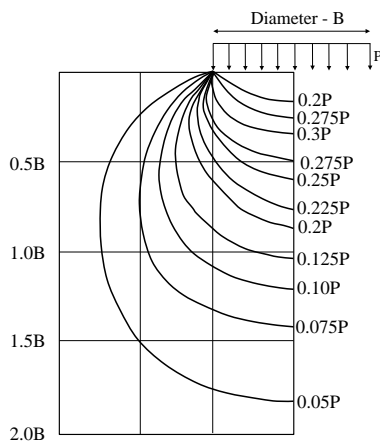


Figure 2.5: Shear stress pressure bulbs for circular foundations (after Smith, 2006)

From the aforementioned the assumption is that the stress distribution, and hence the contact pressure below the foundation is uniform. This is not true since the contact pressure is a function of the foundation rigidity (Smith 2006). This is an important aspect for structural design purposes (Holtz, 1991), but as will be discussed later, it is also important from a settlement perspective due to certain assumptions made for certain methods. Also, it is assumed that the vertical displacements underneath a rigid foundation are uniform across the foundation (Craig 2004). Figure 2.6 presents the different contact stresses underneath rigid and flexible foundations for foundations on granular material. The main difference is that for

the rigid case there is failure at the edges, hence the zero stress on the edge. In contrast, for a flexible foundation the contact stress is approximately constant.

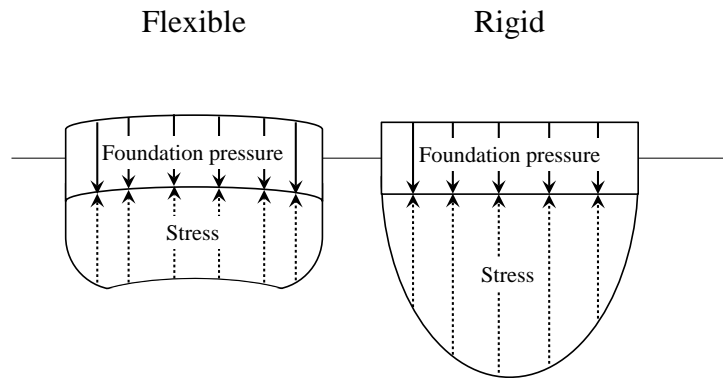


Figure 2.6: Contact stress under rigid and flexible foundation on granular material (after Barnes, 2000)

To determine the rigidity of the foundation, Brown (1969) presented Equation 2.9 to calculate the foundation rigidity factor (K_F). Using this equation it can be established whether a foundation is rigid or flexible depending on the value obtained. Table 2.1 presents values obtained from Mayne & Poulos (1999) which can be used to establish the rigidity of the foundation.

$$K_F = \frac{E_r \cdot (1 - \nu_r^2) \cdot t^3}{E_s \cdot a^3} \quad 2.9$$

where: a = foundation radius

E_r = elastic modulus of foundation material

E_s = representative elastic soil modulus located beneath the foundation base

t = foundation thickness

ν_r = Poisson's ratio of foundation material

Table 2.1: Foundation rigidity factors (obtained from Mayne & Poulos, 1999)

Rigidity factor value	Foundation rigidity
$K_F > 10$	Perfectly rigid
$10 > K_F > 0.01$	Intermediate flexibility
$K_F < 0.01$	Perfectly flexible

In step 8 given by Holtz (1991) it is stated that if it is necessary, the distortion settlements should be calculated. Also stated in step 8 is that for sands, empirical methods should be used which is correlated with in-situ test methods (indicated previously). It was decided for this project to only focus on theoretical methods using elastic theory. Methods correlated with penetration tests (typically standard penetration tests and cone penetration tests) are omitted as these methods are usually for specific conditions and soils types. Methods based solely on elastic theory are more useful for this research project since it can be looked at from a principle perspective which is not subject to a specific test method.

During a survey, the researcher found an abundance of settlement methods for granular soils. Considering a report by Lutenecker & DeGroot (1995) on settlement methods for granular soils, they found in excess of 50 different methods, with only 9 of the methods based purely on elastic theory. This shows that more methods rely on indirect correlations, which are in most cases site specific, showing the merit of only considering methods based on elastic theory. A summary of the elastic theory based methods to predict load-settlement curves found during the survey is presented Table 2.2. The table is not an exhaustive list of all available methods based on elasticity theory, but serves as a representative sample of these methods. The list illustrates the differences in approach taken by the various authors.

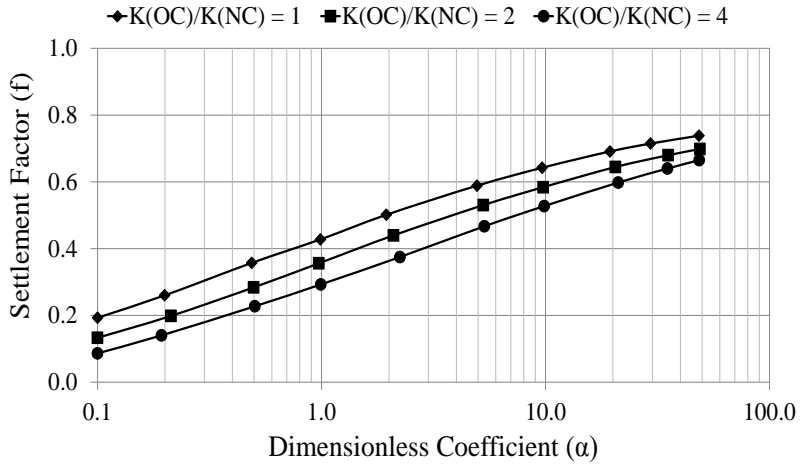
Considering all the settlement methods presented, it is clear that there is a similarity between all the methods which is that they all are in the form of the general elastic solution. All the assumptions, explanations and relevant remarks related to each method are presented in the table. What should also be noticed is that all of the recent methods incorporate the initial small-strain stiffness value (either the shear- or Young's modulus) demonstrating the realisation of the relevance and importance of the initial small-strain stiffness value for foundation settlement calculation. Some methods use influence factors, with different influence factors used depending on the influence on the settlement mechanism based on the researcher's observations and judgement. It should therefore be pointed out that the use of these methods should be considered together with the relevant assumption and remarks taken into account.

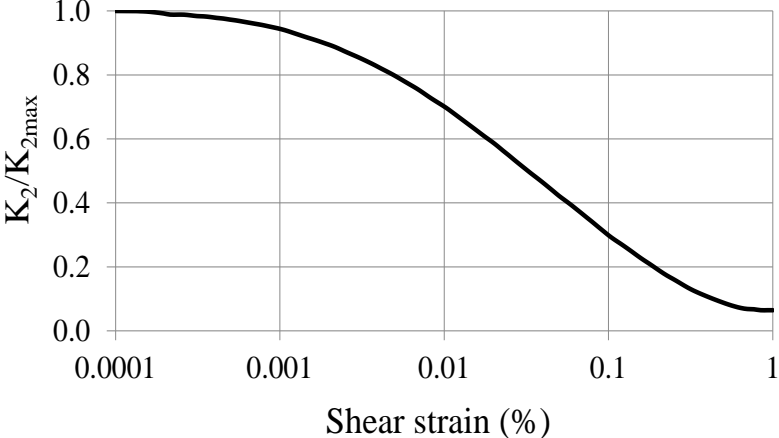
Table 2.2: Summary of different settlement methods for granular materials

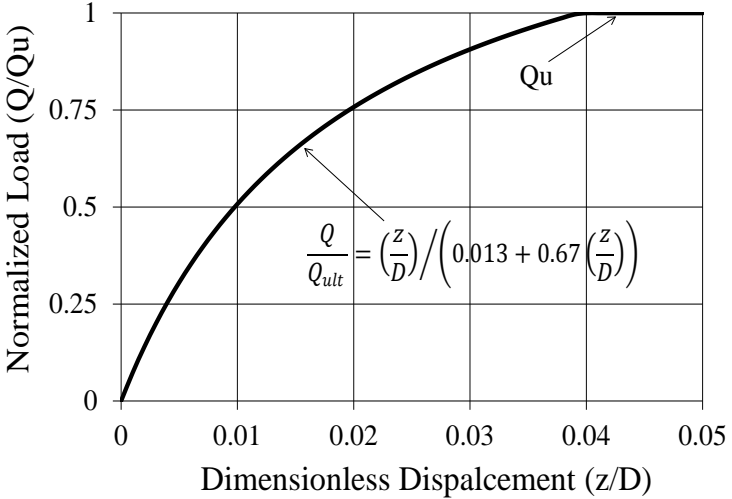
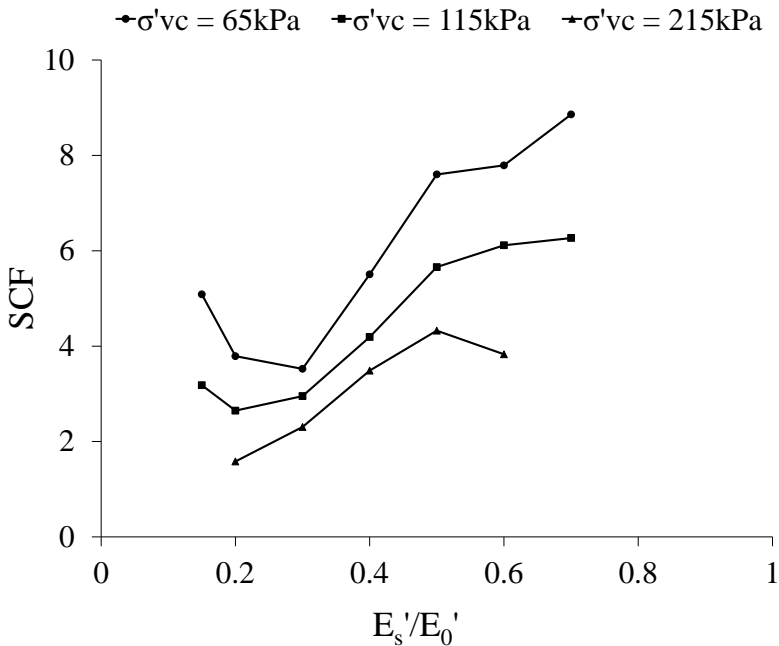
Method	Settlement Expression	Definitions	Explanation	Assumptions	Remarks	Reference
General Elastic Solution	$s = \left(\frac{qB}{E}\right)I$	s = settlement q = applied foundation stress B = foundation width (or diameter) E = Young's modulus I = Influence factor	I = Included to account for the size, shape, embedment of foundation and thickness of compression zones	<ul style="list-style-type: none"> Uniformly loaded plate on surface Isotropic soil conditions Homogeneous soil profile Semi-infinite elastic half-space Soil stiffness related to mean stress level 	<ul style="list-style-type: none"> Solution from Boussinesq and general elasticity theory 	(Lutenegger & DeGroot 1995)
Tschebotari-off (1953, 1971)	For $\alpha = 30^\circ$: $s = \frac{0.867qbC_s}{E}$	s = settlement q = applied stress b = footing width C _s = layer thickness correction factor E = Young's modulus H = Pyramid height		<ul style="list-style-type: none"> For footings resting on sand and other cohesionless soils Assumes surface load is carried within the soil mass by a truncated pyramid of soil Surface settlement is equal to the entire compression of the pyramid Applies to square footings 	<ul style="list-style-type: none"> C_s (a function of H/b) is to account for values of H < ∞ Figure 4.13 in Lutenegger & DeGroot (1995) provides values for C_s 	(Lutenegger & DeGroot 1995) (Tschebotari-off 1971) (Tschebotari-off 1953)

Method	Settlement Expression	Definitions	Explanation	Assumptions	Remarks	Reference
Oweiss (1979)	$s = qB \sum_{i=1}^n \left(\frac{\Psi_i}{E_i} \right)$	<p>s = settlement (ft)</p> <p>q = applied footing stress (ksf)</p> <p>B = footing width (ft)</p> <p>I = individual layer</p> <p>n = total number of layers</p> <p>Ψ_i = settlement factor of layer i</p> <p>E_i = elastic modulus of layer i</p> <p>E_{max} = maximum soil elastic modulus (ksf)</p> <p>λ_i = strain parameter</p> <p>z = layer thickness</p>	$\Psi_i = F_i - F_{i-1}$ $E_i = \left(\frac{E}{E_{max}} \right)_i \times (E_{max})_i$ $\lambda_i = \frac{\Psi_i q B}{z E_{max}} (\%)$	<p style="text-align: center;">Settlement Factor F</p>	<ul style="list-style-type: none"> Maximum soil modulus (E_{max}) corresponds to a strain level of 0.001%. Strain parameter is used to adjust E_{max} to an “operational” soil modulus. Compressible zone beneath foundation = $D+2B$, where D = embedment depth. Values are limited to the graphs maximum and minimum values. 	(Lutenegger & DeGroot 1995)
Das (2011)	$s' = \left(\frac{(q\alpha B')(1 - \nu^2)}{E} \right) I_s I_f$	<p>s = settlement</p> <p>q = net applied pressure on the foundation</p> <p>H = finite thickness of compressible layer</p> <p>$B' = B/2$</p> <p>Ism = modified Steinbrenner influence factor</p>	$I_s = F_1 + \frac{1 - 2\nu}{1 - \nu} F_2$ $F_1 = \frac{1}{\pi} (A_0 + A_1)$ $F_2 = \frac{n'}{2\pi} \tan^{-1} A_2$ $A_0 = m' \ln \frac{(1 + \sqrt{m'^2 + 1}) \sqrt{m'^2 + n'^2}}{m' (1 + \sqrt{m'^2 + n'^2 + 1})}$ $A_1 = \ln \frac{(m' + \sqrt{m'^2 + 1}) \sqrt{1 + n'^2}}{m' + \sqrt{m'^2 + n'^2 + 1}}$	<ul style="list-style-type: none"> For perfectly flexible foundation Young’s modulus is the average value up to B Rigid foundation settlement = 0.93 x Flexible foundation settlement 	<ul style="list-style-type: none"> If the Young’s modulus varies with depth, a weighted average value should be used down to a maximum depth of 5B. 	(Das 2011)

Method	Settlement Expression	Definitions	Explanation	Assumptions	Remarks	Reference
		<p>ν = Poisson's ratio</p> <p>E = average modulus of elasticity of the soil under the foundation</p> <p>I_s = shape factor</p> <p>I_f = depth factor</p> <p>α = factor that depends on the location on the foundation where settlement is being calculated</p>	$A_2 = \frac{m'}{n' \sqrt{m'^2 + n'^2 + 1}}$ <p>$\alpha = 4$ – centre of foundation $\alpha = 1$ – corner of foundation</p> $m' = \frac{L}{B}$ $n' = \frac{H}{B/2} \text{ - Centre}$ $n' = \frac{H}{B} \text{ - Corner}$			
Bowles (1987)	$s = \left(\frac{qB}{E_{s(ave)}} \right) I \times \text{Fox Factor}$	<p>s = settlement</p> <p>q = applied footing stress</p> <p>B = footing width</p> <p>z = compressible zone</p> <p>E_s = Soil Young's modulus in compressible zone</p> <p>E_{hard} = Soil Young's modulus in hard layer ($\pm 10E_s$)</p> <p>μ = Poisson's ratio</p> <p>I = Steinbrenner influence factor</p>	<p><u>Method</u></p> <p>Estimate the applied footing stress (q). Convert to equivalent square footing if circular. Determine point where settlement is to be calculated and divide base so point is at the common corner of contributing rectangles. Thickness of compressible zone: $z = 5B$, or $z =$ depth the "hard" layer if $< 5B$ Compute H/B' ratio: For $H = z = 5B$ Centre – $H/B' = 10$ ($B' = 0.5B$) Corner – $H/B' = 5$ ($B' = 1B$) Use Steinbrenner's equation with an appropriate μ to calculate I. Estimate Fox (1948) embedment correction factor. Obtain weighted average $E_{s(ave)}$ in compressible zone. Use general elastic solution together with the Fox embedment factor (depth factor) to calculate the settlement.</p>	<ul style="list-style-type: none"> For footings on sand. Value of $H = 5B$ taken to be slightly conservative. <p>Fox embedment factor:</p>	<ul style="list-style-type: none"> A detailed re-evaluation of the general elastic solution. Average E_s is used since E increases with depth. 	(Lutenegger & DeGroot 1995) (Bowles 1987)
Papadopoulos (1992)	$s = \left(\frac{qB}{E_s} \right) f$	<p>s = settlement</p> <p>q = foundation stress</p> <p>B = width of rectangular footing</p> <p>E_s = constrained modulus of the footing for the appropriate stress range</p>	$\alpha = \frac{q}{\gamma' B}$ $E_s = E_{50} + \lambda \sigma'$	<ul style="list-style-type: none"> E_s is related to effective stress for stresses $\sigma' \leq 600\text{kPa}$ by a linear expression. The dimensionless settlement factor "f" depends on the soil stress history, foundation geometry, foundation loading and the relation between the constrained modulus and the effective stress. 	<ul style="list-style-type: none"> It may be difficult to evaluate "lambda" from undisturbed samples, as an alternative and average E_s can be used with $\lambda = 0$. In 90% of cases comparing measured and estimated settlement using this method, a 	(Lutenegger & DeGroot 1995) (Papadopoulos 1992)

Method	Settlement Expression	Definitions	Explanation	Assumptions	Remarks	Reference
		<p>f = dimensionless settlement factor</p> <p>α = dimensionless coefficient</p> <p>γ' = effective soil unit weight</p> <p>λ = rate of E_s increase with stress</p> <p>E_{50} = constrained modulus for zero effective stress</p>			<p>difference of $\pm 50\%$ was reported.</p> <ul style="list-style-type: none"> Stiffness values are dependent on laboratory test. 	
<p>Canadian Foundation Manual (1992)</p> <p>Canadian Foundation Manual (2006)</p>	$s = \sum E_z \times h_z$	<p>s = Settlement</p> <p>E_z = Layer strain</p> <p>q_z = Applied stress at midpoint of layer</p> <p>E_s = Apparent modulus of elasticity</p> <p>h_z = Thickness of individual layers</p> <p>q_0 = Applied foundation stress</p> <p>B = Footing width</p> <p>L = Footing length</p> <p>z = Depth to midpoint of each layer</p>	$E_z = \frac{q_z}{E_s}$ $q_z = \frac{q_0 BL}{(B+z)(L+z)}$	<ul style="list-style-type: none"> Stress distribution calculated according to the 2:1 method 	<ul style="list-style-type: none"> For a more refined analysis use: $s = \left(\frac{q_0 B}{E_s}\right) i_c$ i_c = Influence factor from (Canadian Geotechnical Society 2006) 	<p>(Lutenegger & DeGroot 1995)</p> <p>(Canadian Geotechnical Society 1992)</p> <p>(Canadian Geotechnical Society 2006)</p>

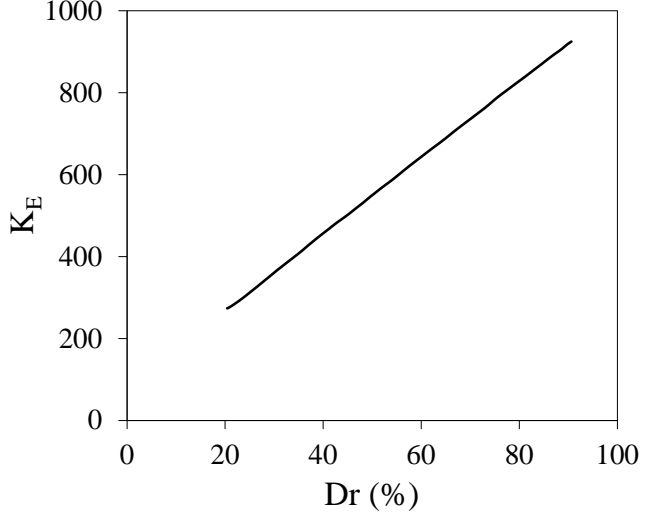
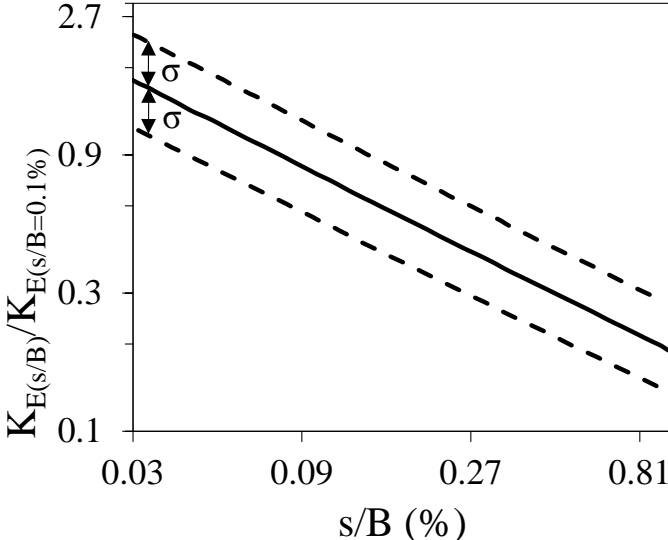
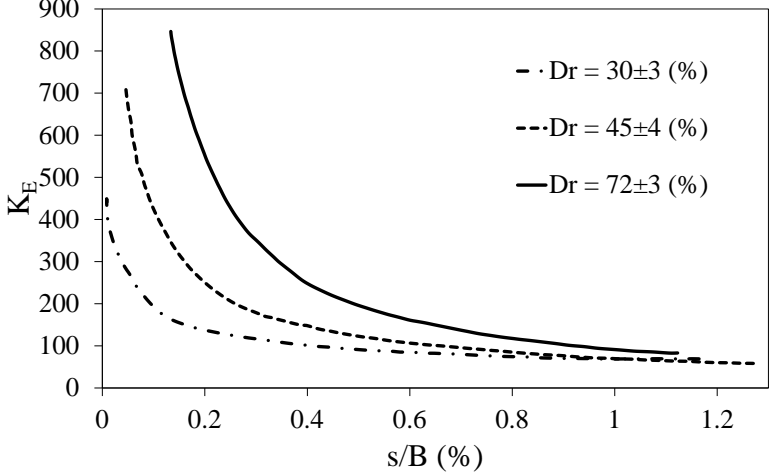
Method	Settlement Expression	Definitions	Explanation	Assumptions	Remarks	Reference
Wahls & Gupta (1994)	$s = \sum_{i=1}^n (\Delta E_z \times \Delta Z)_i$	s = settlement ΔE_z = vertical strain in an element at depth Z ΔZ = sublayer thickness q = applied foundation stress I_s = strain influence factor E_{z0} = modulus coefficient σ'_m = mean stress I_z, I_m = stress influence factor M = L/B N = Z/B L = length of footing Z = depth below footing K_2 = coefficient that is a function of the relative density K_{2max} = K_2 at shear strain equal to 0.0001% = 0.6 D_r + 16 D_r = relative density (%) μ = Poisson's ratio	$\Delta E_z = \frac{qI_s}{E_{z0}(\sigma'_m)^{0.5}}$ $I_s = 4(I_z - I_m)/3$ $I_z = \frac{2}{\pi} \left[\tan^{-1} \left(\frac{M}{2N(M^2 + 4N^2 + 1)^{0.5}} \right) + \frac{2MN}{(M^2 + 4N^2 + 1)^{0.5}} \left(\frac{1}{(M^2 + 4N^2)} + \frac{1}{(4N^2 + 1)} \right) \right]$ $I_m = \frac{4}{3\pi} \left[\tan^{-1} \left(\frac{M}{2N(M^2 + 4N^2 + 1)^{0.5}} \right) \right]$ $\sigma'_m = (\sigma'_m)_0 + 0.5\Delta\sigma'_m = (\sigma'_m)_0 + 0.5q(1 + \mu)I_m$ $(\sigma'_m)_0 = (\sigma'_{v0})(1 + 2K_0)/3$ $E_{z0} = 43.8(1 + \mu)K_2(\sigma_{atm})^{0.5}$	<ul style="list-style-type: none"> Method based on elastic stress-strain theory. Maximum zone of influence: <ul style="list-style-type: none"> 2B for L/B ≤ 3 4B for L/B > 3 Use layer thickness if layer does not extend to maximum influence zone For initial loading, K_2 is set equal to K_{2max}. For subsequent loading increments, reduce K_2 (with modulus reduction curve) to account for the reaction of the soil modulus with strain level. Modulus reduction curve: 	<ul style="list-style-type: none"> Recommended to use 5 sub layers of equal thickness in compressible zone. Predicted settlements were within 6mm of measured settlements for 75% of 120 cases considered. 	(Lutenegger & DeGroot 1995) (Wahls & Gupta 1994)

Method	Settlement Expression	Definitions	Explanation	Assumptions	Remarks	Reference
Load-settlement behaviour – Universal approach	$\frac{Q}{Q_{ult}} = \left(\frac{z}{D}\right) / \left(0.013 + 0.67 \left(\frac{z}{D}\right)\right)$	<p>Q = current load Q_{ult} = ultimate load z = displacement D = embedment depth of foundation</p>		<ul style="list-style-type: none"> Failure of foundation in granular soil occurs at a corresponding displacement of 0.005D. Method developed based on uplift loads. Q_{ult} based on standard ultimate bearing capacity formula by Terzaghi. 	<ul style="list-style-type: none"> Direct connection between deformation and load capacity for both deep and shallow foundations 	(Lutenegger & DeGroot 1995)
Bovolenta (2011)	$\frac{s}{B} = \frac{q}{E'} (1 - \nu^2) I_s$	<p>s = settlement B = foundation width (diameter) q = applied pressure E' = elastic soil modulus in the field ν = Poisson's ratio I_s = influence factor - combined influence factors from Mayne & Poulos (1999) E'₀ = initial stiffness σ'_{ve} = vertical effective consolidation stress F(e) = void ration function e = void ratio p_a = reference pressure = 98.1 kPa</p> <p>Subscript <i>l</i> and <i>f</i> denote secant and initial stiffness values in the lab and field respectively.</p>	$E'_0 = 1510 F(e) \sigma'_{ve}{}^{0.53} p_a{}^{0.47}$ $F(e) = \frac{(2.17 - e)^2}{(1 + e)}$ $SCF = \frac{s/B}{\epsilon_a} \text{ for a given } \frac{E'_{sf}}{E'_{of}} = \frac{E'_{sl}}{E'_{ol}}$ $MCF = \frac{E'_{sf}/E'_{of}}{E'_{sl}/E'_{ol}} \text{ for a given } \epsilon_a = \frac{s}{B}$	<ul style="list-style-type: none"> An alternative to routine design could be to assume field stiffness values equal to 0.3E'₀ – 0.6E'₀. Factors to be used (i.e. MCF, SCF and E'₀) based on tests conducted on Ticino sand. <p>Correction factor curves:</p> 	<ul style="list-style-type: none"> Draw a load – settlement curve by using the settlement equation together with the correction factors. Use figures or equations (if data is known) for correction factors together with settlement equation. After 1% relative settlement (s/B) measured and estimated load-settlement curves diverge. 	(Bovolenta 2011)

Method	Settlement Expression	Definitions	Explanation	Assumptions	Remarks	Reference
				<p style="text-align: center;"> $\blacktriangle \sigma'_{vc} = 65\text{kPa}$ $\blacksquare \sigma'_{vc} = 115\text{kPa}$ $\blacktriangleright \sigma'_{vc} = 215\text{kPa}$ </p>		
Hadad & Ahidashti (2013)	$S = \frac{\varepsilon_{\%}}{100} \cdot 2B = \left(\frac{313.75q}{E_{max}} \right)^2 \cdot \frac{B}{50}$	<p>E_{max} = maximum stiffness</p> <p>ν = Poisson's ratio</p> <p>B = diameter of footing</p> <p>S = settlement</p> <p>q = applied pressure at foundation level</p> <p>$\varepsilon_{\%}$ = axial strain (%)</p> <p>$\gamma_{\%}$ = shear strain (%)</p> <p>G = current shear modulus</p> <p>G_{max} = maximum shear modulus</p>	$E_{max} = 2(1 - \nu)G_{max}$ $\gamma_{\%} = (1 + \nu)\varepsilon_{\%}$	<ul style="list-style-type: none"> • Influence zone equal to $2B$ • Poisson's ratio equal to 0.3 • Strain at centre of layer: <ul style="list-style-type: none"> ○ $\varepsilon = \frac{\sigma_z}{E} - \nu \left(\frac{\sigma_x}{E} + \frac{\sigma_y}{E} \right)$ ○ $\sigma_x = \sigma_y = k_0 \cdot \sigma_z = 0.5 \cdot \sigma_z$ ○ $k_0 = 0.5$ for soil deposits that have not been significantly preloaded • Stiffness degradation curve: <ul style="list-style-type: none"> ○ $\frac{G}{G_{max}} = \frac{0.0725}{\sqrt{\gamma_{\%}}}$ • Boussinesq formula used to calculate vertical stress at depth for settlement equation derivation 	<ul style="list-style-type: none"> • Power law function for small-strain stiffness modification based on laboratory data from various scientific papers and reports. • SASW or CSW tests can be conducted in field to obtain the small-strain stiffness with depth. • Ratio of predicted to measured loads for 25mm displacement is 0.98 for 9 case studies. 	(Hadad & Ahidashti 2013)

Method	Settlement Expression	Definitions	Explanation	Assumptions	Remarks	Reference
Yongqing (2011)	<p>Approximate closed-form solution:</p> $s = \frac{q \cdot B \cdot I}{E_0 \left(1 - f^* \left(\frac{q}{q_{ult}}\right)^{g^*}\right)}$ <p>Modulus degradation method:</p> $= C_c C_D \frac{s}{E_{0ave} \left(1 - \left(\frac{q}{(q_{ult})_v}\right)^{g^*}\right)}$	<p>C_D = depth correction factor</p> <p>C_c = creep factor</p> <p>s = settlement</p> <p>I_z = vertical strain distribution factor</p> <p>Δz = individual layer thickness</p> <p>I = displacement influence factor</p> <p>$I_f, I_h, I_{L/B}$ = correction factors</p> <p>g^*, f^* = fitting parameters describing the normalized average modulus degradation of soil-foundation system</p> <p>q_{ult} = ultimate bearing capacity</p> <p>q = footing load</p> <p>E_0 = small-strain stiffness</p> <p>E_{0ave} = average small-strain stiffness</p> <p>G_0 = small-strain shear modulus</p> <p>ν = Poisson's ratio</p>	$C_D = 1 - 0.5 \left(\frac{\sigma_{vo}}{\Delta q}\right)$ $C_c = 1 + 0.2 \log \left(\frac{t(\text{year})}{0.1}\right)$ $E_0 = 2G_0(1 + \nu)$ $I_{zpeak} = 0.5 + 0.1 \sqrt{\frac{\Delta q}{\sigma'_{vp}}}$	<ul style="list-style-type: none"> Developed for cohesionless soils. For practical applications f^* is assumed to be 1. For the estimation of E_0 from G_0, a Poisson's ratio of 0.2 can be assumed. q_{ult} in the modulus degradation method is calculated using the equation proposed by Vesic (hence the subscript "v"). Both the "modified Schmetsmann method" as well as the "modulus degradation method" follows the normal procedure set out by Schertmann. In both methods the strain influence factor diagram is plotted and the values obtained from the diagram are used for the settlement calculations. 	<ul style="list-style-type: none"> These methods are primarily based on CPT data which is used to determine and calibrate certain parameters (in some instances plate load tests were used for parameter calibration). Although these equations require CPT data for analysis purposes making it semi-empirical solutions, the outline of the equations will assist with the analysis in this report. 	(Yongqing 2011)
Elkahim (2005)	<p>Proposed closed-form method:</p> $s = \frac{q \cdot B \cdot I}{2 \cdot G_{max} \cdot (1 + \nu) \cdot r_f}$ <p>Procedure:</p> <ol style="list-style-type: none"> Calculate ultimate bearing capacity. Compute K_i. Evaluate x_L. 	<p>s = settlement</p> <p>q = applied stress</p> <p>K_i = initial "global" soil footing stiffness</p> <p>G_{max} = maximum small-strain shear modulus</p> <p>ν = Poisson's ratio</p> <p>B = footing width</p> <p>I_h = displacement influence factor</p> <p>I_F = foundation</p>	$K_i = \frac{2 \cdot G_{max} \cdot (1 + \nu)}{B \cdot I_h \cdot I_F \cdot I_E}$ $x_L = \frac{G_{max}}{G_{min}}$ $G_{max} = \rho \cdot V_s^2 \quad G_{min} = \frac{\tau_{max}}{\gamma_f}$	<ul style="list-style-type: none"> Failure is defined by the ultimate bearing capacity, based on conventional solutions (i.e. Terzaghi). Poisson's ratio: <ul style="list-style-type: none"> 0.5 for undrained conditions 0.2 for drained conditions <p>Modulus reduction factor:</p>	<ul style="list-style-type: none"> This settlement calculation starts with the small-strain stiffness value (G_{max}) and is then adjusted up to failure. Failure is defined by the ultimate bearing capacity, the initial slope is calculated by K_i and the rest of the stress-displacement curve is calculated 	(Elkahim 2005)

Method	Settlement Expression	Definitions	Explanation	Assumptions	Remarks	Reference																					
	4. Calculate r_f based on x_L and conditions set out in the table in the explanation column. 5. Evaluate the stress-displacement response from the closed-form solution.	flexibility influence factor I_E = embedment influence factor r_f = modulus reduction factor x_L = normalised limiting stain value V_s = shear wave velocity ρ = soil density τ_{max} = shear strength γ_f = shear strain at failure		<table border="1"> <thead> <tr> <th>Footing shape</th> <th>Drainage</th> <th>Reduction factor, r_f</th> </tr> </thead> <tbody> <tr> <td rowspan="4">Circular</td> <td>Undrained</td> <td>$r_f = 1 - 0.99 \left(\frac{q}{q_{ult}} \right)^{\left(\frac{14.29}{x_L^{1.05}} - 0.034 \right)}$</td> </tr> <tr> <td>Drained, $\phi' = 30^\circ$</td> <td>$r_f = 1 - 0.99 \left(\frac{q}{q_{ult}} \right)^{\left(\frac{9.09}{x_L} - 0.03 \right)}$</td> </tr> <tr> <td>Drained, $\phi' = 35^\circ$</td> <td>$r_f = 1 - 0.99 \left(\frac{q}{q_{ult}} \right)^{\left(\frac{1.96}{x_L} - 0.17 \right)}$</td> </tr> <tr> <td>Drained, $\phi' = 40^\circ$</td> <td>$r_f = 1 - \left(\frac{q}{q_{ult}} \right)^{\left(\frac{2.00}{x_L^{0.91}} \right)}$</td> </tr> <tr> <td rowspan="4">Strip</td> <td>Undrained</td> <td>$r_f = 1 - 0.99 \left(\frac{q}{q_{ult}} \right)^{\left(\frac{37.04}{x_L^{1.16}} - 0.041 \right)}$</td> </tr> <tr> <td>Drained, $\phi' = 30^\circ$</td> <td>$r_f = 1 - \left(0.99 - \frac{2.12}{x_L} \right) \cdot \left(\frac{q}{q_{ult}} \right)^{\left(\frac{4.35}{x_L^{0.7}} - 0.06 \right)}$</td> </tr> <tr> <td>Drained, $\phi' = 35^\circ$</td> <td>$r_f = 1 - \left(0.99 - \frac{1.89}{x_L} \right) \cdot \left(\frac{q}{q_{ult}} \right)^{\left(\frac{3.45}{x_L^{0.7}} - 0.06 \right)}$</td> </tr> <tr> <td>Drained, $\phi' = 40^\circ$</td> <td>$r_f = 1 - \left(0.99 - \frac{1.66}{x_L} \right) \cdot \left(\frac{q}{q_{ult}} \right)^{\left(\frac{2.50}{x_L^{0.7}} - 0.05 \right)}$</td> </tr> </tbody> </table>	Footing shape	Drainage	Reduction factor, r_f	Circular	Undrained	$r_f = 1 - 0.99 \left(\frac{q}{q_{ult}} \right)^{\left(\frac{14.29}{x_L^{1.05}} - 0.034 \right)}$	Drained, $\phi' = 30^\circ$	$r_f = 1 - 0.99 \left(\frac{q}{q_{ult}} \right)^{\left(\frac{9.09}{x_L} - 0.03 \right)}$	Drained, $\phi' = 35^\circ$	$r_f = 1 - 0.99 \left(\frac{q}{q_{ult}} \right)^{\left(\frac{1.96}{x_L} - 0.17 \right)}$	Drained, $\phi' = 40^\circ$	$r_f = 1 - \left(\frac{q}{q_{ult}} \right)^{\left(\frac{2.00}{x_L^{0.91}} \right)}$	Strip	Undrained	$r_f = 1 - 0.99 \left(\frac{q}{q_{ult}} \right)^{\left(\frac{37.04}{x_L^{1.16}} - 0.041 \right)}$	Drained, $\phi' = 30^\circ$	$r_f = 1 - \left(0.99 - \frac{2.12}{x_L} \right) \cdot \left(\frac{q}{q_{ult}} \right)^{\left(\frac{4.35}{x_L^{0.7}} - 0.06 \right)}$	Drained, $\phi' = 35^\circ$	$r_f = 1 - \left(0.99 - \frac{1.89}{x_L} \right) \cdot \left(\frac{q}{q_{ult}} \right)^{\left(\frac{3.45}{x_L^{0.7}} - 0.06 \right)}$	Drained, $\phi' = 40^\circ$	$r_f = 1 - \left(0.99 - \frac{1.66}{x_L} \right) \cdot \left(\frac{q}{q_{ult}} \right)^{\left(\frac{2.50}{x_L^{0.7}} - 0.05 \right)}$	with the modulus reduction factor. • For this method q_{ult} should be calculated which requires laboratory test to be conducted to obtain the necessary parameters. • Two simplified equations are also presented, but they are based on the proposed closed form solution.	
Footing shape	Drainage	Reduction factor, r_f																									
Circular	Undrained	$r_f = 1 - 0.99 \left(\frac{q}{q_{ult}} \right)^{\left(\frac{14.29}{x_L^{1.05}} - 0.034 \right)}$																									
	Drained, $\phi' = 30^\circ$	$r_f = 1 - 0.99 \left(\frac{q}{q_{ult}} \right)^{\left(\frac{9.09}{x_L} - 0.03 \right)}$																									
	Drained, $\phi' = 35^\circ$	$r_f = 1 - 0.99 \left(\frac{q}{q_{ult}} \right)^{\left(\frac{1.96}{x_L} - 0.17 \right)}$																									
	Drained, $\phi' = 40^\circ$	$r_f = 1 - \left(\frac{q}{q_{ult}} \right)^{\left(\frac{2.00}{x_L^{0.91}} \right)}$																									
Strip	Undrained	$r_f = 1 - 0.99 \left(\frac{q}{q_{ult}} \right)^{\left(\frac{37.04}{x_L^{1.16}} - 0.041 \right)}$																									
	Drained, $\phi' = 30^\circ$	$r_f = 1 - \left(0.99 - \frac{2.12}{x_L} \right) \cdot \left(\frac{q}{q_{ult}} \right)^{\left(\frac{4.35}{x_L^{0.7}} - 0.06 \right)}$																									
	Drained, $\phi' = 35^\circ$	$r_f = 1 - \left(0.99 - \frac{1.89}{x_L} \right) \cdot \left(\frac{q}{q_{ult}} \right)^{\left(\frac{3.45}{x_L^{0.7}} - 0.06 \right)}$																									
	Drained, $\phi' = 40^\circ$	$r_f = 1 - \left(0.99 - \frac{1.66}{x_L} \right) \cdot \left(\frac{q}{q_{ult}} \right)^{\left(\frac{2.50}{x_L^{0.7}} - 0.05 \right)}$																									
Mayne & Poulos (1999)	$s = \frac{q \cdot B' \cdot I_G \cdot I_F \cdot I_E \cdot (1 - \nu^2)}{E_0}$	s = settlement q = foundation load ν = Poisson's ratio I_G = displacement influence factor I_E = settlement coefficient factor (to take depth of embedment into account) I_F = rigidity coefficient factor B' = equivalent diameter of rectangular footing E_f = modulus of elasticity of the footing material t = footing thickness k = increase in soil stiffness per unit	$B' = \sqrt{\frac{4BL}{\pi}}$ $I_E = 1 - \frac{1}{3.5e^{(1.22\nu-0.4)} \left[\left(\frac{B'}{D_f} \right) + 1.6 \right]}$ $I_F = \frac{\pi}{4} + \frac{1}{4.6 + 10 \left(\frac{E_f}{E_0 + \frac{B'}{2}k} \right) \left(\frac{2t}{B'} \right)^3}$ <p> ...Hs/B' = 5.0 - Hs/B' = 2.0 - Hs/B' = 1.0 - Hs/B' = 0.5 - Hs/B' = 0.2 </p>	<ul style="list-style-type: none"> Calculates the elastic settlement below the centre of the foundation. Influence factors derived from elasticity continuum theory. One of the main assumptions is that the soil stiffness increases linearly with depth. For homogeneous to nonhomogeneous ground. 	<ul style="list-style-type: none"> This method was developed as a spreadsheet integration technique method and derives the influence factors for use in the settlement calculation. The specific solution addresses circular- and raft foundations. 	(Mayne & Poulos 1999), (Das & Sivakugan 2007)																					

Method	Settlement Expression	Definitions	Explanation	Assumptions	Remarks	Reference
		depth E_0 = stiffness at footing level				
Berardi & Lancelotta (1991)	$s = \frac{q'_n B}{E'} I_s$ <p>Suggested procedure:</p> <ol style="list-style-type: none"> Determine the average relative density (D_r) With the known D_r, estimate K_E for 0.1% ($K_{E(0.1\%)}$) relative settlement (s/B) can be determined from which E' can be calculated for $s/B = 0.1\%$. The footing settlement can then be calculated. If the calculated and assumed s/B values are not the same, then revise K_E with the calculated s/B value and calculate the new settlement. The procedure is repeated until the calculated and assumed values coincide. Alternatively, to account for non-linearity correct the K_E value and the new settlement can be determined. 	q_n = net increase of effective pressure I_s = influence factor which accounts for the shape and rigidity of the foundation, Poisson's ratio (ν), and the ratio of the depth of the compressible stratum to the foundation width (B) E = modulus of elasticity (relationship suggested by Janbu (1963)) σ'_{v0} = effective vertical pressure at depth equal to $0.5B$ (kg/cm^2) p_a = reference pressure (atmospheric) K_E = non-dimensional modulus number	$E' = K_E p_a \left(\frac{\sigma'_{v0} + 0.5 \Delta \sigma'_v}{p_a} \right)^{0.5}$ <p>Initial K_E estimation curve:</p>  	<ul style="list-style-type: none"> K_E is a function of the relative settlement (S/B). Poisson's ratio (ν) equal to 0.15 assumed for the influence factor determination. <p>K_E adjustment curves for difference D_r values:</p> 	<ul style="list-style-type: none"> Although this a semi-empirical method based on SPT N-values to calculate the relative density from which K_E is obtained, it should be included since it incorporates the non-linearity of the stiffness modulus. The rationale behind the method is important. 	(Berardi & Lancelotta 1991), (Das & Sivakugan 2007)

Method	Settlement Expression	Definitions	Explanation	Assumptions	Remarks	Reference
Mayne & Poulos (2001)	$s = \frac{q \cdot d \cdot I_G \cdot I_F \cdot I_E \cdot (1 - \nu^2)}{E_0 \left[1 - f \left(\frac{q}{q_{ult}} \right)^g \right]}$	<p>s = settlement</p> <p>q = applied surface stress</p> <p>q_{ult} = ultimate bearing stress</p> <p>ν = Poisson's ratio</p> <p>I_G = displacement influence factor</p> <p>I_E = settlement coefficient factor (to take depth of embedment into account)</p> <p>I_F = rigidity coefficient factor</p> <p>d = equivalent footing diameter</p> <p>E_0 = initial elastic modulus</p>	$E_0 = 2G_0(1 + \nu)$ $f = 1$ $g = 0.3$	<ul style="list-style-type: none"> Fitting parameter values "f" and "g" are for "well behaved" soils. The term $\frac{q}{q_{ult}}$ is reciprocal of the factor of safety (FS). Based on a modified hyperbola function for modulus reduction: $\frac{E}{E_0} = 1 - f \left(\frac{q}{q_{ult}} \right)^g = 1 - f(FS)^{-g}$ 	<ul style="list-style-type: none"> The method is a crude means of combining the initial stiffness with bearing capacity from limit plasticity theory. 	<p>(Mayne 1995),</p> <p>(Mayne & Poulos 2001)</p>

Given the fact that there are so many different methods available, it is not surprising that there are discrepancies between the methods. This is illustrated by a probabilistic approach presented by Das & Sivakugan (2007). A chart comparing different analysis methods is presented and it indicates the probability that the actual settlement will exceed a predicted value. Figure 2.7 is a depiction of the comparison chart presented by Das & Sivakugan (2007), which not only shows the conservativeness of the difference methods, but also the difference in results between the methods.

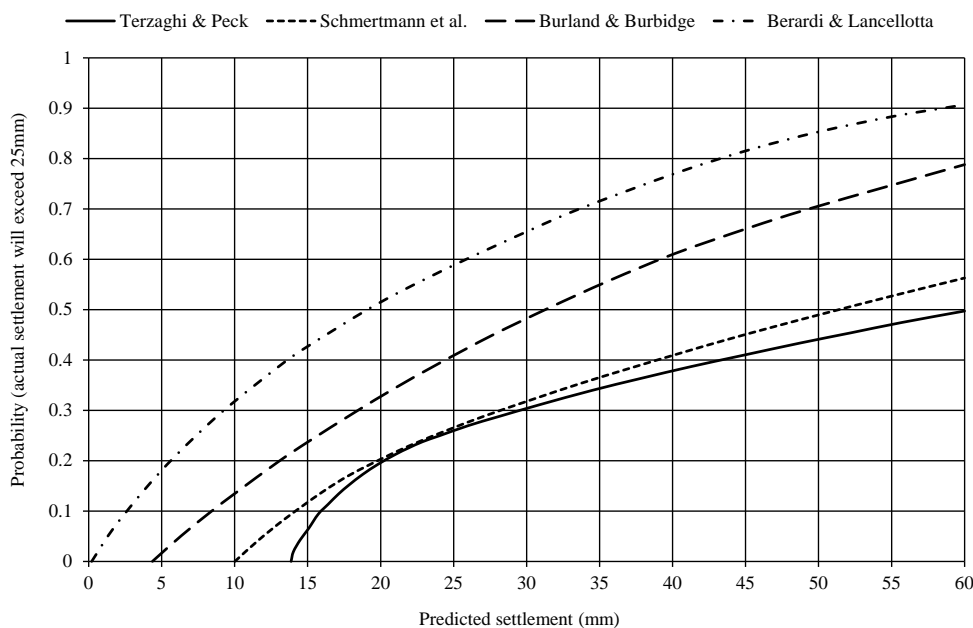


Figure 2.7: Probabilistic design chart (after Das & Sivakugan, 2007)

Das & Sivakugan (2007) deduced that the uncertainty in the different settlement methods is due to the inability of engineers to quantify the soil stiffness correctly. This is also stated in Craig (2004) who states that due to uncertainty in obtaining elastic parameters, some vertical displacement methods are more reliable than other. However, Holtz (1991) argued that the nature of the elastic theory methods depends more on soil non-linearity than on the stress calculations. Mayne & Poulos (2001) states that numerical schemes may be the most realistic way of addressing soil non-linearity, but this may sometimes be a tedious and time consuming task. They suggest that a more convenient preliminary solution might be to use a method where the soil modulus is degraded with strain levels where the soil initial small-strain modulus is used which is a more fundamental parameter and can be obtained with more certainty. This conceptual method is one of the current research topics in Europe (Mayne & Poulos 2001). The abovementioned information demonstrates that further work is required to improve settlement prediction, with the focus on soil non-linearity and the initial small-strain

soil modulus. Powrie (1997) suggested that a more versatile method might be not to assume an average stiffness value for the soil underneath a foundation, but to use difference stiffness values by dividing the soil into discrete layers and assigning a stiffness value for each layer.

2.2.2 BEARING CAPACITY OF SHALLOW FOUNDATIONS

As stated previously, shallow foundations usually have adequate bearing resistance, but this remains an important part of the design process. It is however important to view the bearing capacity in relation with the settlement of a foundation. Bearing capacity is defined as the pressure applied on soil to cause shear failure. Barnes (2000) provides the definition of failure as the mobilisation of the full shear strength of the soil, accompanied by large and excessive settlements. This means that there is an ultimate value for the bearing capacity (q_{ult}), which corresponds to settlement values that will exceed tolerable limits. This is best illustrated by Figure 2.8 which shows a typical bearing pressure distribution with settlement, and can be seen as a load-settlement curve. What should be noted are the ultimate bearing capacity value (q_{ult}) that tends towards a maximum, as well as the allowable bearing capacity value (q_{all}), where the term “allowable” refers to the bearing pressure value which corresponds to an allowable settlement value. The ratio between the q_{ult} and q_{all} values is the factor of safety ($FS = q_{ult}/q_{all}$). For foundation design the common acceptable factor of safety used is 3. It is clear that the ultimate value would rarely be mobilised due to the safety factor, but the ultimate value is necessary to calculate the allowable value. An alternative way of considering this is that since the allowable value is smaller than the ultimate value and still on a fairly linear part of the curve, from a practical perspective, it might be worthwhile to consider methods to only determine the initial section of the curve.

As the load applied to a foundation is gradually increased, it causes an increase in settlement until it reaches a maximum value (i.e. the ultimate bearing capacity value) and when the ultimate value is reached, failure will occur. The nature of the failure will depend on the foundation type, size and soil strength and compressibility as well as foundation embedment (Das 2009). This implies that there are difference modes of failure associated with bearing capacity failure depending on different circumstances. Three different modes of failure are presented in literature (Craig, 2004; Das, 2009; Das, 2011) and are given as:

- General shear failure
- Local shear failure
- Punching shear failure

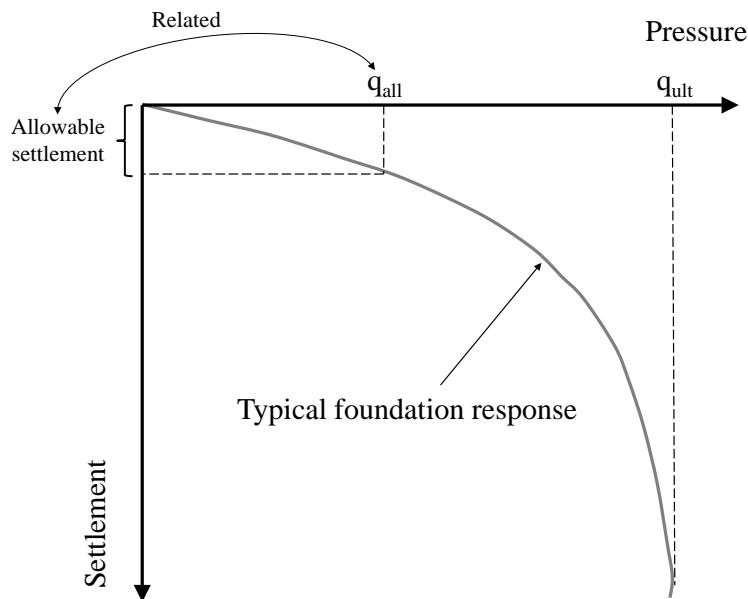


Figure 2.8: Bearing pressures vs. settlement (modified from Barnes, 2000)

Each of these failures corresponds to a specific type of bearing pressure-settlement curve. The failures are best presented graphically as shown in Figure 2.9. What should be noted from these schematic drawings is that the general shear failure requires a large bearing pressure for relatively little settlement where punching shear failure will produce large settlements for relatively low bearing pressure values. Comparing the three failure modes with respect to soil deformation, general shear failure would cause the soil to heave around the foundation with failure on the failure planes. For local shear failure, compression is more significant than for the general case together with a partial failure plane. During punching shear, soil compression is the dominant mechanism and no heaving takes place (Craig 2004).

As stated previously, different factors influence the failure mode, but with reference to sands, the relative density plays an important role in the failure mode. Vesic (1973) proved this and produced a graphical representation comparing the foundation embedment with relative density values for different failure modes (Figure 2.10). It is clear from this graph, is that when conducting foundation experiments/research on sands, it would be worthwhile choosing different relative density values corresponding to different failure types. For relatively shallow foundations (i.e. foundation depth/width < 1.5) relative density values of 20%, 50% and 80% would result in punching, local and general shear failures, respectively. Barnes (2000) states that general, local and punching shear failure corresponds to dense, medium dense and loose soil, respectively. It can thus be inferred that the relative density values of 20%, 50% and 80% would correspond to dense, medium dense and loose soil types.

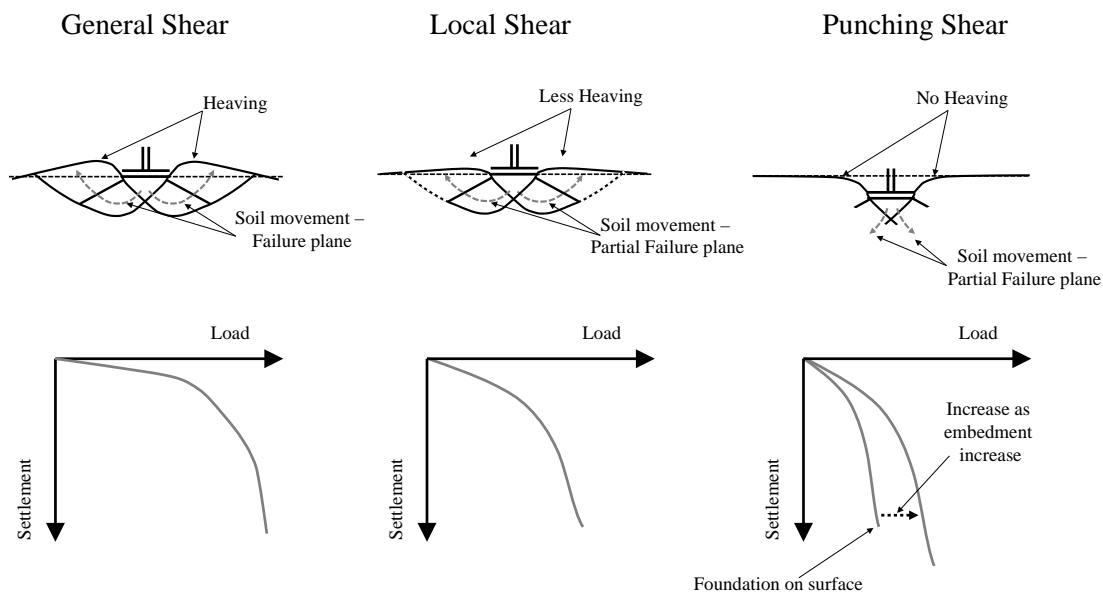


Figure 2.9: Bearing capacity modes of failure (adapted from Craig, 2004)

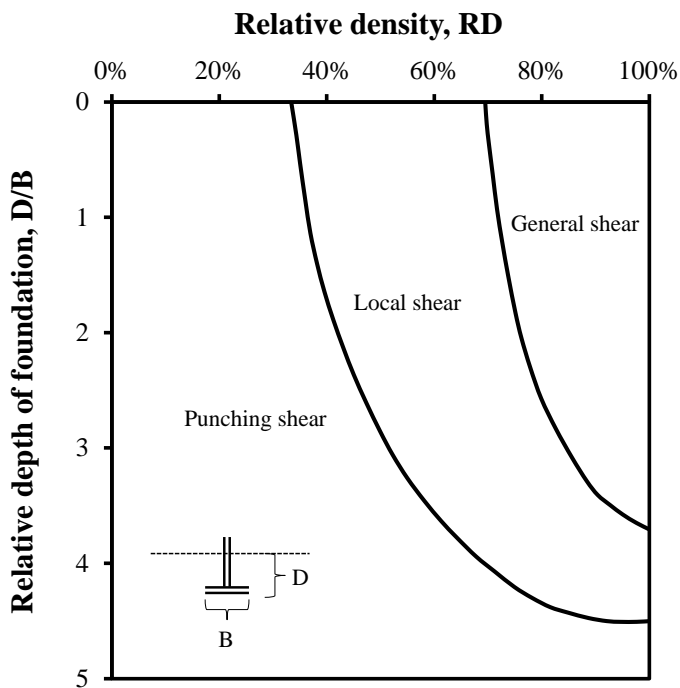


Figure 2.10: Modes of failure for sands compared with relative density (after Das, 2011)

To calculate the ultimate bearing capacity value, the general equation presented by Terzaghi is commonly used by engineers. Equation 2.10 presents that formula for the ultimate bearing capacity for a strip footing with various factors. In essence these factors are related to the

foundation width, depth and the soil strength parameters cohesion (c') and angle of friction (φ') as well as shape factors to take into account circular, square or rectangular foundations. It should be noted that in this report the term “cohesion” refers to the effective cohesion intercept in a two-dimensional stress state.

$$q_{ult} = c' N_c s_c + \gamma D N_q s_q + \frac{1}{2} \gamma B N_\gamma s_\gamma \quad 2.10$$

where: D = embedment depth

B = foundation width or diameter

γ = soil unit weight

c' = effective cohesion intercept

N_c, N_q, N_γ = bearing capacity factors depending on φ'

$$N_q = e^{(\pi \tan \varphi')} \tan^2 \left(45^\circ + \frac{\varphi'}{2} \right)$$

$$N_\gamma = 1.8(N_q - 1) \tan \varphi' \quad (\text{Hansen})$$

$$N_\gamma = (N_q - 1) \tan(1.4\varphi') \quad (\text{Meyerhof})$$

$$N_\gamma = 2.0(N_q - 1) \tan \varphi' \quad (\text{EC7})$$

$$N_c = (N_q - 1) \cot \varphi'$$

s_c, s_q, s_γ = shape factors – simplified values which are sufficiently accurate are:

$$s_c = s_q = 1.2 \text{ for square and circular foundations}$$

$$s_\gamma = 0.8 \text{ – square foundations, } 0.6 \text{ – circular foundations}$$

Other factors such as inclination factors (to compensate for inclined loads) and depth factors can be included in Equation 2.10.

With respect to the “ N_γ ” value, it has been observed that this value is prone to scale effects. It has been found that the value for N_γ decreases as the foundation size increases (Kusakabe, 1995). To compensate for this, it was concluded by Kusakabe (1995), that the method by Kutter et al. (1988) is the most effective. With specific reference to sands, the aforementioned method does not assume a zero value for the cohesion, but rather uses a straight-line fit to determine c' and φ' from stress path data obtained from triaxial results which will result in a cohesion value. The method should however be applied to stress ranges

which are of interest to the problem at hand which was approximated as the range between 0 and $0.6q_{ult}$. The values obtained for c' and ϕ' are then used with Equation 2.10.

Effect of footing width

The footing width has an impact on the bearing capacity. The foundation width also affects the settlement in the sense that for a certain width, the failure mode will either be general, local or punching failure. This is an important concept to understand (Zhou 2006) and it is best described graphically. Figure 2.11 presents the effect of footing width on allowable stress and settlement potential and it should be mentioned that the concept behind this graph is the focus and not the application.

Firstly, the transition between shear failure and settlement potential zones should be noticed with the transition line calculated purely from ultimate bearing capacity theory together with the factor of safety. The different settlement lines indicate that if the criterion for allowable settlement is lowered (i.e. decreasing allowable settlement from 3S-to-2S-to-S), the allowable stress is similarly reduced. This is in conjunction with the effect the foundation width has on the settlement and bearing capacity. As Zhou (2006) explains, as the foundation width increases, the stress increase in the soil will decrease but the effect of the applied stress will extend deeper into the soil stratum and the foundation settlement will be a function of the foundation width. Therefore, a foundation can be designed accordingly by choosing a suitable foundation width that will correspond to design specifications (i.e. if bearing capacity is an issue, a greater foundation width should be used, and vice versa).

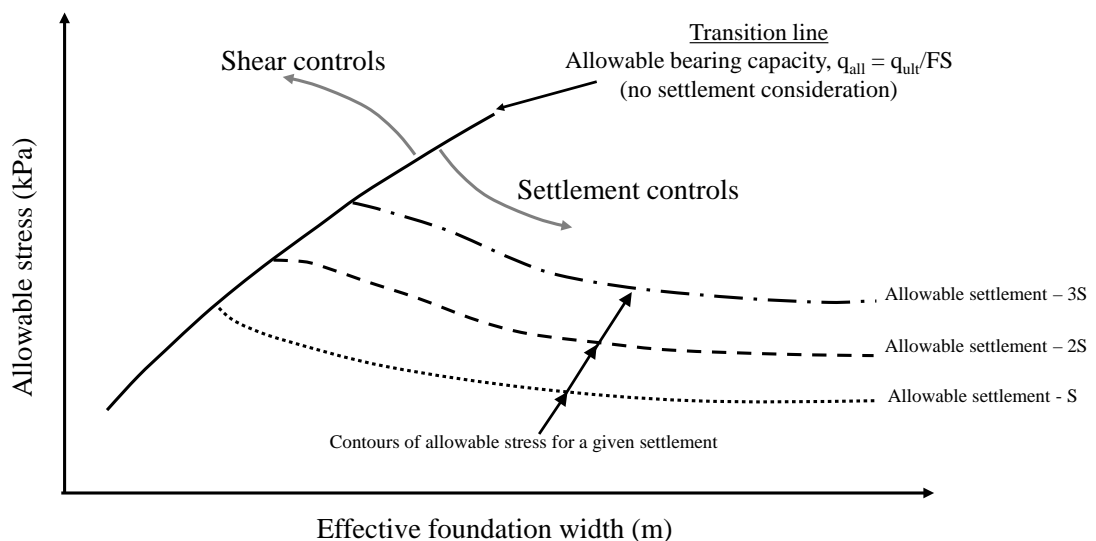


Figure 2.11: Footing width effect on failure for foundations (modified from Zhou, 2006)

2.3 SMALL-STRAIN STIFFNESS OF SOIL

As stated in Section 2.2.1, the uncertainty with foundation settlement prediction is due to the inability of engineers to accurately quantify the soil stiffness and this is echoed by Yongqing (2011). This is exacerbated by the fact the stiffness degrades as strain levels increase. In recent times the better understanding of the non-linear behaviour of the stiffness, also known as the modulus degradation, has provided engineers with an efficient approach to produce more reliable stiffness values for design (Yongqing 2011). The soil elastic stiffness is expressed in different forms including: shear modulus (G), constrained modulus (M), bulk modulus (K) and Young's modulus (E) (Elhakim 2005). Equations 2.11 to 2.14 show relationships for the calculation of the different stiffness moduli and it can be seen that they are all interrelated by Poisson's ratio (ν).

$$E=2G(1+\nu) \quad 2.11$$

$$M=\frac{2G(1-\nu)}{(1-2\nu)} \quad 2.12$$

$$K=\frac{2G(1+\nu)}{3(1-2\nu)} \quad 2.13$$

$$G=\frac{E}{2(1+\nu)} \quad 2.14$$

For the purpose of foundation design the values of shear- and Young's modulus are of main concern. As can be seen from Equations 2.11 to 2.14 the shear modulus is important since this value can be used to determine the other three mentioned stiffness moduli. The shear modulus will therefore be the focus of this report. Stiffness moduli can be expressed in different terms namely the secant modulus or the tangent modulus. The secant stiffness is defined as the ratio of the change in stress to the change in strain measured from the same origin value with the tangent stiffness measured between two consecutive data points. Considering a typical triaxial stress-strain curve, presented in Figure 2.12, the different secant and tangent moduli for the shear modulus (equivalent Young's modulus in brackets) can be presented graphically. When the secant and tangent stiffness values are calculated at very small strains, these values converge to a stiffness value commonly referred to as the small-strain stiffness as presented in Figure 2.12. This small-strain stiffness value is denoted in

literature as either G_0 or G_{\max} . For this report the term G_0 will be used as reference to the small strain stiffness.

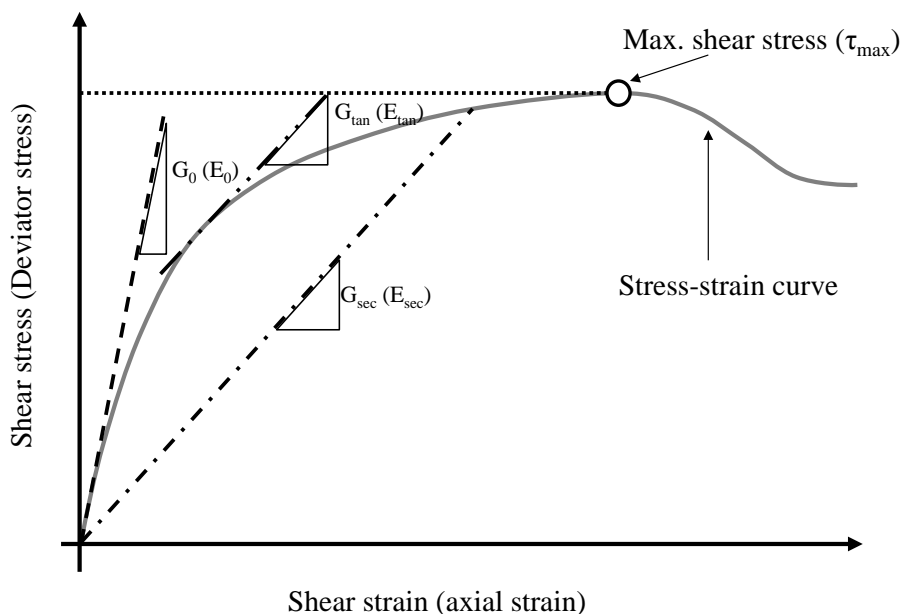


Figure 2.12: Stiffness modulus terms (after Yongqing, 2011)

The small-strain stiffness is, for all practical purposes, considered to be constant for small strain values up to a strain level of about 0.001% (Clayton 2011) and at strain levels below this value it can be said that the soil behaves elastically. From 0.001% strain non-linear behaviour of the soil is observed as strain levels increase and as Clayton (2011) states, both the stiffness at very small strains as well as the stiffness degradation data are essential for ground movement prediction. This is again an indication of the importance of the small-strain stiffness (G_0) value as indicated by Asslan (2008) where it is stated that G_0 is an important parameter for various geotechnical designs. Asslan (2008) also indicates that the important role of small-strain stiffness in geotechnical design and analysis is widely accepted. High stiffness values are associated with very small-strain values which are not always related to specific geotechnical problems. It is therefore important to reduce the small-strain stiffness value to a value relating to the specific design problem. Figure 2.13 shows a typical modulus reduction curve that indicates the typical strain ranges for different design problems. What should also be noticed on Figure 2.13 is the indication of the difference strain levels ranging from small- to large strains. The modulus reduction curve is typically plotted as G/G_0 vs. shear strain. The term G/G_0 is a common method of normalising the reduction in shear modulus with increasing strain (Vardanega & Bolton 2013).

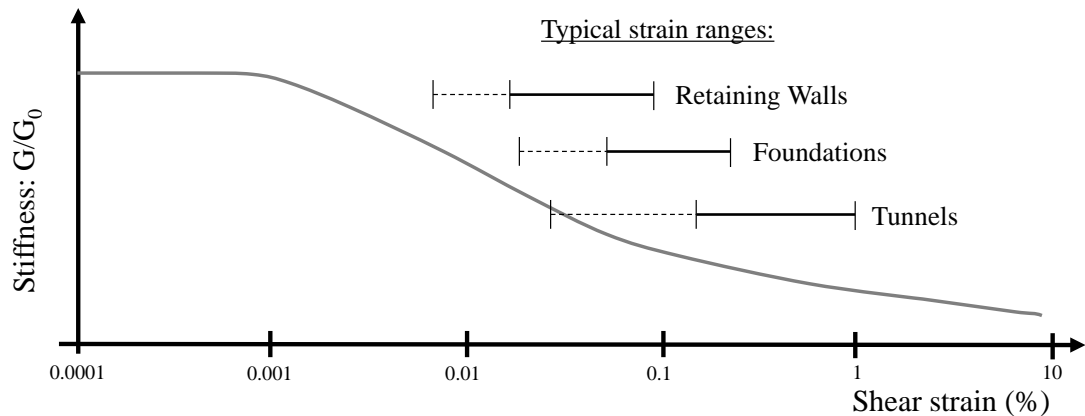


Figure 2.13: Typical modulus reduction curve (after Mair, 1993)

2.3.1 MODULUS REDUCTION CURVES

As seen from the previous section, the modulus reduction curve is an important element for design purposes and various authors have presented equations to represent the modulus reduction curve based on various parameters. Elkahim (2005) indicates that suitable modulus reduction curves should satisfy three requirements:

1. It should have a minimum number of constants for defining the non-linear relationship without compromising on accuracy;
2. The material constants should have physical meaning; and
3. The material constants should be easily derived.

From the literature, modulus reduction curves can be divided into two categories: (1) Curves based on strength parameters, and (2) curves based only on stiffness parameters, with both categories including the current shear strain as an input value. Table 2.3 presents modulus reduction curve equations from various sources which are based on strength parameters. The table indicates the number of variables required to use each method.

Table 2.3: Modulus reduction curves based on strength parameters

Equation	Reference	Number of variables
$\frac{E_t}{E_0} = \frac{1}{1 + \alpha \cdot R \cdot y^{R-1}}$ <p>where: $y = \frac{\varepsilon/\varepsilon_r}{1 + \varepsilon/\varepsilon_r}$</p> <p>$\varepsilon_r = \frac{q_{max}}{E_0}$ = reference strain</p> <p>ε = axial strain at current stress level</p> <p>α, R = soil parameters based on the soil stress strain behaviour</p> <p>E_t = tangent Young's modulus</p> <p>E_0 = maximum Young's modulus</p> <p>q_{max} = maximum bearing capacity</p>	Ramberg & Osgood (1943)	4
$\frac{G}{G_0} = \frac{1}{1 + \gamma_h}$ $\gamma_h = \frac{\gamma}{\gamma_r} \left[1 + a \cdot e^{-b(\gamma/\gamma_r)} \right]$ <p>where: G = shear modulus</p> <p>γ = current strain</p> <p>γ_h = hyperbolic strain</p> <p>$\gamma_r = \frac{\tau_{max}}{G_0}$ = reference strain</p> <p>a, b = soil parameters</p> <p>τ_{max} = maximum shear stress</p>	Hardin & Drnevich (1972)	4
$\frac{G_{sec}}{G_0} = \frac{\tau_1}{\tau_1 + \gamma \cdot G_0} \cdot \tau_1 \cdot \frac{\frac{\tau_1}{G_0^2}}{\left(\frac{\tau_1}{G_0} + \gamma_{max}\right)^2} \cdot \frac{1}{\gamma_{max}^m} \cdot \frac{\gamma^m}{m+1}$ <p>where: τ_1, m = positive and real number of the modified hyperbolic equations</p> <p>G_{sec} = secant shear modulus</p> <p>G_0 = small-strain shear modulus</p>	Prevost & Keane (1990)	2

Equation	Reference	Number of variables
<p>γ = shear strain</p> <p>γ_{\max} = maximum shear strain</p> <p>τ_{\max} = maximum shear stress</p> <p>Hyperbolic model parameters:</p> <p>$m \geq 4y_{\max} - 1$</p> $\tau_1 = \frac{y_1 \cdot G_0}{\gamma_{\max}}$ $y_1 = \frac{y_{\max} - \frac{1}{2} + \sqrt{\frac{1}{4} - \frac{\gamma_{\max}}{m+1}}}{\frac{m}{m+1} - y_{\max}}$ $y_{\max} = \frac{\tau_{\max}}{G_0 - \gamma_{\max}}$		
$\frac{G_{\text{sec}}}{G_0} = 1 - f \left(\frac{\tau}{\tau_{\max}} \right)^g$ <p>where: G_{sec} = secant shear modulus at a specific stress level = $\frac{\tau}{\epsilon_{\text{shear}}}$</p> <p>$\tau$ = current shear stress level</p> <p>τ_{\max} = max shear stress</p> <p>f, g = model fitting parameters – reasonable values for sand is $f = 1$ and $g = 0.3$</p> <p>The term $\frac{\tau}{\tau_{\max}}$ can be considered as the reciprocal of the factor of safety (FS) and be written as $\frac{Q}{Q_{\text{ult}}}$ (where Q = current bearing capacity value and Q_{ult} = ultimate bearing capacity value).</p>	Fahey & Carter (1993); Mayne (1995)	4
$\frac{G_{\text{sec}}}{G_0} = 1 - \alpha \cdot \frac{x - x_{\text{th}}}{x} \cdot [\ln(1 + x - x_{\text{th}})]^R$ <p>where: G_{sec}, G_0 = secant and small-strain shear moduli, respectively</p> <p>x = normalized shear strain = $\frac{\epsilon_{\text{shear}}}{\epsilon_{\text{shear}(r)}}$</p> <p>$\epsilon_{\text{shear}(r)}$ = reference shear strain = $\frac{\tau_{\max} - \tau_0}{G_0}$</p>	Puzrin and Burland (1996, 1998)	5

Equation	Reference	Number of variables
$\tau_{\max} = \text{max shear stress}$ $\tau_0 = \text{initial shear stress}$ $R = \left(\frac{1-x_{th}}{x_L-x_{th}} \right) \cdot \frac{(1+x_L-x_{th}) \ln(1+x_L-x_{th})}{x_L-1}$ $\alpha = \frac{x_L-1}{(x_L-x_{th}) [\ln(1+x_L-x_{th})]^R}$ $x_L = \text{normalised limiting strain} = \frac{\epsilon_{\text{shear}(f)}}{\epsilon_{\text{shear}(r)}}$ $\epsilon_{\text{shear}(f)} = \text{shear strain at failure}$ $x_{th} = \text{normalized threshold shear strain} = \frac{\epsilon_{\text{shear}(th)}}{\epsilon_{\text{shear}(r)}}$ $\epsilon_{\text{shear}(th)} = \text{elastic threshold strain} = 0.001\%$		
$\frac{E_t}{E_0} = \left(1 - \left(\frac{\Delta q}{\Delta q_{\max}} \right)^m \right)^n$ <p>where: E_t = tangent Young's modulus at any stress level</p> <p>E_0 = initial Young's modulus</p> <p>Δq = increase in deviator stress = $\Delta\sigma_1 - \Delta\sigma_3$</p> <p>$\Delta q_{\max}$ = maximum value of Δq in compression</p> <p>m, n = material constants</p>	Shibuya et al. (1997)	3

Two issues with the modulus reduction curves presented in Table 2.3 are (1) the fact that either laboratory- or field tests are required to use the curves (to determine the maximum bearing capacity or maximum shear stress), and (2) the number of variables required are in some cases not practical for design engineers. Some of the methods do however require only two variables, but they are dependent on some form of strength testing, reducing the simplicity of the method. Considering point 3 made by Elhakim (2005), laboratory testing required for some of the methods creates a difficulty due to the difficulty to obtain high quality samples (especially in sands).

The second category of curves is based only on stiffness parameters, together with current strain levels. This implies that only the small-strain stiffness of the soil must be known, and consequently no strength tests are required. For the purpose of this project three modulus reduction curves will be considered due to their simplicity.

The first method is a modified hyperbolic relationship presented by Oztoprak & Bolton (2013). The relationship was obtained from a laboratory test database of sands which included 454 tests. The best fit relationship obtained from the large database is presented in Equation 2.15. Although the relationship requires three variables, the elastic threshold strain value is usually fixed rendering a relationship with only two variables.

$$\frac{G}{G_0} = \frac{1}{\left[1 + \left(\frac{\gamma - \gamma_e}{\gamma_r}\right)^a\right]} \quad 2.15$$

where: γ = shear strain (%)

γ_e (%) = elastic threshold strain (end of linear plateau)

γ_r (%) = reference shear strain where $G/G_0 = 0.5$

a = curvature parameter

noting for $\gamma < \gamma_e$, $G/G_0 = 1.0$

The second relationship was first presented by Gunn (1993) used of surface settlement prediction due to tunnelling. The relationship is based on an undrained non-linear 'elastic' response which is a power law function. Equation 2.16 shows the expression presented by Gunn (1993).

$$E_{u_{sec}} = a\varepsilon^{n-1} \quad 2.16$$

where: $E_{u_{sec}}$ = secant undrained Young's modulus

ε = axial strain

a, n = soil fitting parameters

Bolton & Whittle (1999) later reproduced the relationship in the form of the shear strain and stiffness parameters given by Equation 2.17. Although the relationship is used for undrained cases, the curve shape is of importance together with the fact that there are only two variables in the relationship.

$$\frac{G}{G_0} = \alpha\gamma^{\beta-1} \quad 2.17$$

where: G = secant shear modulus

G_0 = secant small-strain shear modulus

γ = shear strain

α, β = curve fitting parameters

The third method is the relationship for fine-grained soils given by Massarsch (2004) which is a variation of the fixed relationships presented by Rollins et al. (1998). Equations 2.18 and 2.19 show the relationships presented by Massarsch (2004) and Rollins et al. (1998), respectively. As with the previous method, this relationship also requires two variables. It should be mentioned that the material coefficients used by Massarsch (2004) are a function of the plasticity index, but as for the relationship from Bolton & Whittle (1999), the values for α and β can be determined by observing the behaviour of a specific soil.

$$\frac{G}{G_0} = \frac{1}{[1 + \alpha\gamma(1 + 10^{-\beta\gamma})]} \quad 2.18$$

$$\frac{G}{G_0} = \frac{1}{[1 + 16\gamma(1.2 + 10^{-20\gamma})]} \quad 2.19$$

where: γ = shear strain

α, β = curve fitting coefficients

The three methods presented above require only small-strain stiffness and might therefore be more appealing to engineers in practice due to the simplicity of the methods. In addition only two variables are required to quantify the shape of the stiffness degradation curve. If the variables can be determined from 'real' data and fixed for certain soil conditions, the relationships may be used in settlement prediction methods. Heymann (2007) states that the rate at which stiffness reduces is relatively independent of soil type. This indicates that if the small-strain modulus value is known, a modulus reduction function can be used to predict the stiffness at higher strain levels using only the shear strain value (Heymann, 2007). The simplicity of this method is appealing; however it will require calibration against real test data.

2.3.2 MEASUREMENTS OF G_0

In general soil stiffness can be assessed by laboratory tests as well as by in-situ tests. Test methods, whether laboratory or in-situ, should correspond to a strain level associated with a specific engineering problem (Szczepański 2008). Different test methods can only calculate stiffness values at certain strain levels, and therefore not all methods are applicable for small-

strain shear stiffness determination. Figure 2.14 shows a typical modulus reduction curve indicating the different test methods (laboratory and in-situ) corresponding to various strain levels. In the previous section it was indicated that this section will focus on methods to predict foundation settlement that only require the small-strain shear stiffness value and as such, the focus in Figure 2.14 and for the remainder of the report will be on the tests applicable to the small-strain shear stiffness (i.e. strain levels $< 0.001\%$). It is clear that whether laboratory or in-situ tests, the determination of the small-strain shear stiffness involves dynamic or geophysical methods. Menzies (2000) states that geophysical techniques combined with stiffness reduction to account for strain level are a far more superior method for stiffness estimation than many techniques used today.

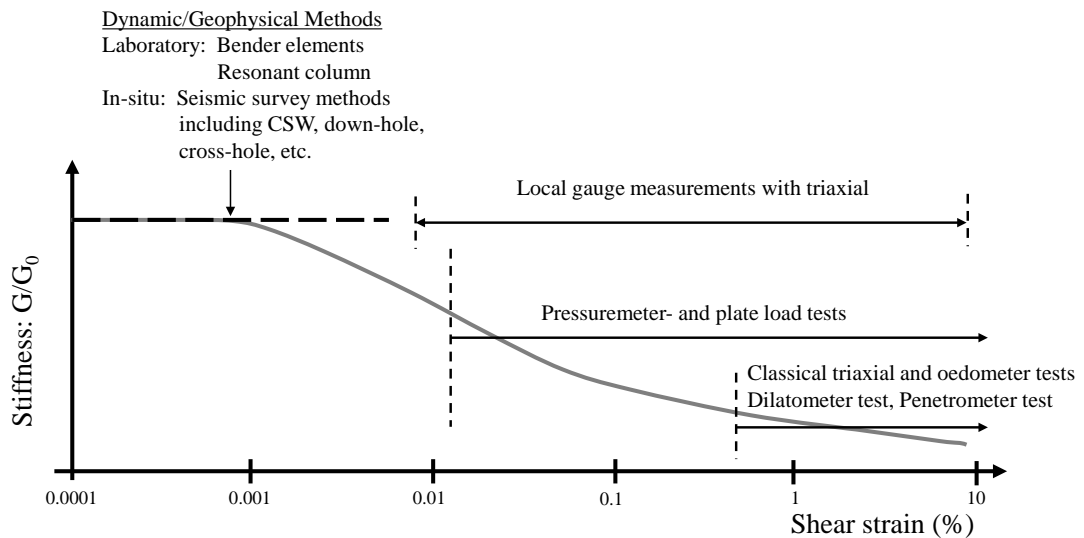


Figure 2.14: Strain levels for different test methods (modified from Jastrzębska & Lupieżowiec, 2011)

Geophysical or dynamic tests involve the determination of the wave velocity which can then be used together with the bulk density (ρ_{bulk}) to calculate the small-strain stiffness. Shear wave velocity (V_s) measurement is common in geotechnical tests and if measured, the small-strain shear stiffness can be calculated using Equation 2.20. In the same manner, if the compression wave velocity (V_p) is measured, the small-strain constrained modulus (M_0) can be calculated using Equation 2.21. Although V_p measurements are not that common in geotechnical tests, it was used during this research project. Equation 2.22 shows that if the shear and compression wave velocities are measured, the Poisson's ratio (ν) of the soil can be calculated.

$$G_0 = \rho_{\text{bulk}} \times V_s^2 \quad 2.20$$

$$M_0 = \rho_{\text{bulk}} \times V_p^2 \quad 2.21$$

$$v = \frac{\frac{1}{2} \left(\frac{V_p}{V_s} \right)^2 - 1}{\left(\frac{V_p}{V_s} \right)^2 - 1} \quad 2.22$$

Table 2.4 shows the various test methods from which stiffness parameters can be derived. Since the test methods are not the main focus of this project, no detail will be given on any of the test methods with the exception of bender elements which will be discussed in an ensuing section. The two most widely used methods for in-situ and laboratory measurements are CSW testing and bender elements testing, respectively (Szczepański 2008).

Table 2.4: Laboratory and in-situ test methods for small-strain stiffness determination (after Clayton, 2011)

Laboratory methods	In-situ methods
Bender element testing	Continuous surface wave (CSW) testing
Resonant column testing	Down-hole geophysics
Advanced triaxial testing	Cross-hole geophysics

Considering the difference between laboratory and in-situ test methods, in most cases results obtained through in-situ test methods are superior to the laboratory counterparts (Elhakim & Mayne 2003). Reasons for this is the fact that laboratory samples are subjected to sampling disturbance as well as unrepresentative sampling (Menzies 2000), laboratory tests produce lower stiffness values than in-situ tests (Benz et al. 2009) and impractical long testing times which can delay design processes (Clayton 2011). Sampling methods involving freezing techniques to procure laboratory samples, specifically for sands, has provided results similar to in-situ tests, but these sampling techniques are very costly. Advantages of in-situ tests include the fact that large volumes of soil can be tested and that the test is conducted at the current stress condition. With respect to surface wave tests, these tests have the further advantage of being non-invasive and non-destructive, can be done relatively cheaply and values can be obtained on site in some instances (Menzies 2000). One thing that laboratory and in-situ test measurements of shear wave velocities have in common is the problem with background noise (Clayton 2011). Fundamentally, small-strain stiffness values are affected by three factors namely (Clayton 2011):

- The void ratio;
- Interparticle contact stiffness which depends on the effective stress; and
- Deformation and flexing of individual particles

Yongqing (2011) gives three additional factors affecting the small-strain stiffness, which is:

- Mean effective stress (σ'_m);
- Stress history, i.e. the over consolidation ratio (OCR); and
- Silt content

The aforementioned factors also indicate the advantage of in-situ tests over laboratory tests. These factors can easily be influenced or altered when sampling and tests are done incorrectly. Although in-situ tests are more preferable, laboratory tests still play an important role since certain parameters require laboratory testing and in some instances it is the only testing that can be done. Notwithstanding the method used, care should be taken to ensure proper, reliable and accurate measurements taking into account any shortcomings of a particular method.

If laboratory- or in-situ testing cannot be done, an empirical correlation can be used. Seed & Idriss (1970) developed a simple expression for sand to determine the small-strain shear stiffness (G_0), independent of any laboratory- or in-situ tests, only requiring an indication of the density. The equations by Seed & Idriss (1970) were reworked to present equations for loose, medium dense and dense sand which is expressed in Equations 2.23, 2.24 and 2.25 respectively.

$$G_0 = 8000\sqrt{p_0'} \quad (\text{Loose sand}) \quad 2.23$$

$$G_0 = 10000\sqrt{p_0'} \quad (\text{Medium dense sand}) \quad 2.24$$

$$G_0 = 12000\sqrt{p_0'} \quad (\text{Dense sand}) \quad 2.25$$

Where p_0' = mean effective stress.

Equation 2.26 may be used to calculate the mean effective stress in terms of to the vertical effective stress (σ'_v). Equation 2.26 requires the calculation of K_0 , known as the coefficient of earth pressure at rest which for normally consolidated soil can be estimated with Jaky's equation given by Equation 2.27 which is related to the angle of friction (ϕ'). This methodology is the same methodology used by Fu et al. (2004).

$$p_0' = \frac{1}{3} \sigma_v'(1+2K_0) \quad 2.26$$

$$K_0 = 1 - \sin \phi' \quad 2.27$$

2.3.3 SETTLEMENT CALCULATION USING G_0 FROM CSW TESTS

Table 2.2 summarised methods to predict load-settlement curves. In addition Table 2.2 showed methods by which the stiffness degradation curve can be estimated for soils. Moxhay et al. (2008) combined these two concepts by using a non-linear stepwise methodology.

This method involves reducing the soil stiffness, starting from the small-strain stiffness value, as the foundation is loaded. The data required for the calculation as given by Moxhay et al. (2008) is:

- The measured small-strain stiffness value (G_0) versus depth;
- Foundation geometry and shape; and
- Applied load

The calculation procedure is then as follows summarised from Moxhay et al. (2008):

1. Subdivide material below foundation into layers based on the CSW results, which should be at least to depth equalling twice the foundation width.
2. Assign E_0 as initial Young's modulus for each layer calculated from G_0 .
3. Using Boussinesq's theory, calculate the vertical stress increment at centre of each layer.
4. An initial strain value can be calculated for each layer by dividing the vertical stress by E_0 .
5. Decide on the number of load steps to reach the maximum applied load (based on the discretion of the design engineer).
6. For each load step, the strain can be calculated which can be used together with a stiffness reduction curve to calculate a new Young's modulus (E_i) at each strain value (ϵ_i).
7. Step 6 is repeated for each load step.
8. The total settlement is the sum of the product of the height (H) of each layer and the vertical strain calculated for each load step:

$$\text{Total settlement} = \Sigma(H_i \cdot \epsilon_i)$$

The advantage of this method is that for each load increments, the history (i.e. the stiffness degradation) is taken into account. In addition the settlement is calculated for each load step,

and the complete load-settlement curve is therefore determined. Disadvantages of this particular method is firstly, Poisson's ratio is not included in the calculation of the strain values (i.e. steps 4 and 6) and secondly a standard stiffness reduction curve is used which may not conform to specific site conditions. Also, there is no mention by Moxhay et al. (2008) whether the strains calculated is the axial strains or that is should be converted to shear strains.

2.4 GEOTECHNICAL CENTRIFUGE TESTING

Geotechnical centrifuge modelling has become a widely-used modelling tool in the field of geotechnical engineering which complements numerical analysis as well as field testing and monitoring (Ng et al. 2001). Centrifuge modelling has also become a routine geotechnical modelling tool used world-wide for the reason that it provides the engineering industry with a cost-effective modelling tool providing validation and verification (Fu et al. 2004). Two types of centrifuges exist, a beam centrifuge where the model is swung on a basket and a drum centrifuge where the model is placed in a rotating channel and in both types the model is situated a radius (r) away from the centre of the centrifuge (Fu 2004). Figure 2.15 shows schematics of the two types of centrifuges.

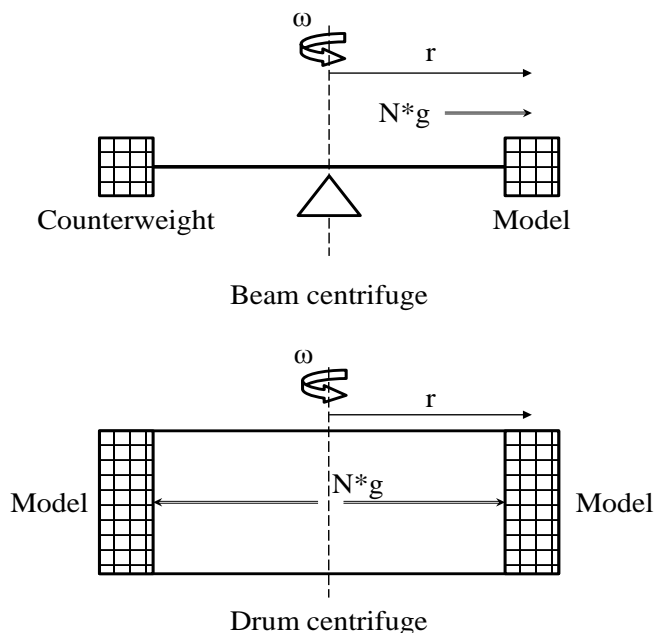


Figure 2.15: Schematic of different types of centrifuges (after Fu, 2004)

The working principle is that as a model is subjected to centripetal force while spinning, and artificial gravity is induced, the self-weight of the model will increase. This will induce gravity stress conditions in the soil sample that corresponds to the prototype, i.e. the full scale version (Fu 2004). Since the stress conditions in the models resemble the prototype, it is then assumed that the overall behaviour of the model, i.e. displacements and failure mechanisms, etc. will be identical to the prototype (Fu 2004). Wood (2004) explains that the reason the self-weight increase is due to the constant centripetal acceleration ($r\omega^2$) which can be normalised with earth's gravity (g). The model is therefore subjected to a larger body force of $N \cdot g$, i.e. "N" times the earth's gravity (Ng et al. 2001). The value of N is known as a scaling factor indicating that if the model is spun in the centrifuge to a certain g-level, the size of the model will be a factor $1/N$ reduction of the prototype. Equation 2.28 shows the relationship of the scale factor with the earth's gravity and the centrifuge centripetal acceleration ($r\omega^2$):

$$N = \frac{r\omega^2}{g} \quad 2.28$$

where: r = centrifuge radius

ω = angular velocity

Fu (2004) states that the key aspects involved with centrifuge testing are:

- Model/payload capacity, i.e. the maximum mass/weight
- Centrifuge arm radius
- Level of acceleration
- Model/payload size, i.e. the physical dimensions

These are properties of the specific centrifuge to be used. The initial "unknowns" are based on the model design and these are affected by two key issues involved with centrifuge testing namely scaling laws and scaling errors (Fu 2004). Scaling laws are used to scale the prototype to a model suitable for testing where the scaling involves different geotechnical aspects. Scaling errors are identified as the difficulty of representing adequate detail from the prototype and a non-uniform acceleration field developed in the centrifuge. It is however seldom possible to have adequate prototype detail and some approximations should be made (Fu 2004). The non-uniform acceleration field will induce a variation of the stress with depth between the prototype and model which is presented graphically in Figure 2.16. It should be noted that the non-linearity for the model is exaggerated for clarity. From the figure it can be seen that at $2/3$ model depth the prototype and model stresses are the same. The difference between stress profiles is however quite small and will produce a maximum error of less than

3%, indicating that the effect will not significantly influence the modelling behaviour (Taylor, 1995).

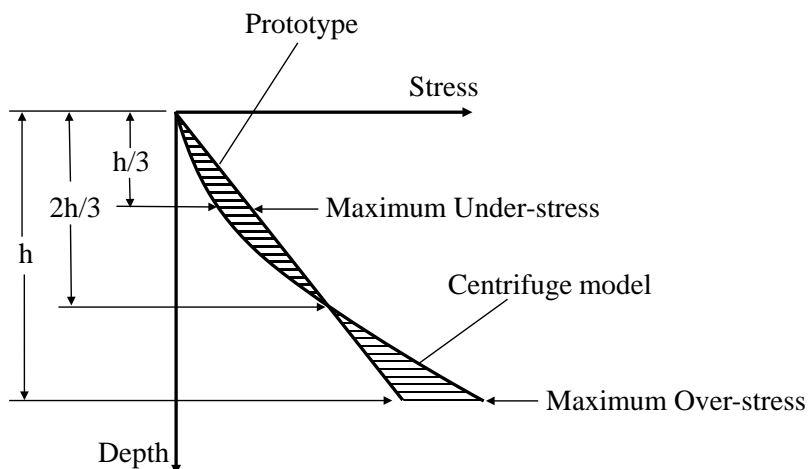


Figure 2.16: Stress variation between model and prototype (after Taylor, 1995)

2.4.1 SCALING LAWS AND PRINCIPLES

Basic scaling laws are derived from the need to ensure that there is stress correspondence between the model and prototype. Scaling laws have been extensively discussed by Taylor (1995) which provided derivations for most of the scaling laws, as well as Garnier et al. (2007). A summary of the most common scaling laws used is provided by Wood (2004) which is presented in Table 2.5. The use of these scaling laws should be adhered to in order to ensure satisfactory correspondence between the model and prototype. The scale factor in Table 2.5 is the factor that should be applied to the prototype quantity of which the result will be the quantity to be used for an equivalent model.

Table 2.5: Geotechnical centrifuge modelling scaling laws (Wood, 2004)

Quantity (Prototype)	Scale factor (Model)
Length	$1/N$
Mass density	1
Acceleration	N
Stiffness	1
Stress	1
Force	$1/N^2$
Force/unit length	$1/N$
Strain	1
Displacement	$1/N$
Pore fluid viscosity	1

Quantity (Prototype)	Scale factor (Model)
Pore fluid density	1
Permeability	1
Hydraulic gradient	1
Time (creep)	1
Time (diffusion)	$1/N^2$
Time (dynamic)	$1/N$
Velocity	1
Frequency	N
Shear wave velocity	1

2.4.2 SHALLOW FOUNDATION MODELLING CONSIDERATIONS

When conducting centrifuge tests, certain modelling considerations should be taken into account in order to ensure that the desired behaviour is modelled as accurately as possible. Different test types involve different considerations depending on the aspects of the test involved. Kusakabe (1995) provides some modelling considerations that should be kept in mind when designing a centrifuge experiment involving shallow foundation on cohesionless soils. The modelling considerations presented by Kusakabe (1995) are the following:

- **Footing roughness** – In most practical foundation problems, the base of the foundation is assumed to be rough. When conducting centrifuge tests it is common practice to ensure that the rough condition of the base is replicated on the model foundation. Efforts to achieve this rough condition include gluing sand particles or sand paper to the base. If a rough base is not properly achieved, inaccurate results may be obtained due to the behaviour being influenced.
- **Loading system** – Two types of loading systems is used: displacement controlled and force controlled. The freedom of rotation of the model foundation is also important.
- **Loading rate** – For dry sand the loading rate is not a crucial aspect for consideration. The loading rate effect becomes important when testing on saturated sand due to pore pressure build up. It should be kept in mind that a too fast loading rate might produce inaccurate load-settlement response.
- **Reproducibility** – When conducting multiple tests errors can stem from inconsistent test setups. Inconsistencies include model preparation, loading rate, freedom of rotation, load application point on the foundation, differences in centrifuge acceleration, base roughness and change in boundary conditions. Care should be taken to ensure test results are as repeatable as possible.

- **Grain-size effect** – Grain-size effect becomes prominent when the foundation width to mean grain-size ratio (B/D_{50}) is less than about 50-100. Garnier et al. (2007) states that to reduce the grain-size effect bearing capacity a $B/D_{50} > 35$ should be achieved. If particle scaling is done to satisfy rupture formation and permeability, the resistance to crushing of small particles may influence the results.
- **Boundary conditions** – Since models are built in containers (i.e. model boxes) boundaries are imposed that is not necessarily the same as in the prototype. Scaling should be done in such a manner to reduce the effect. Three major boundary effects are of concern: the effect on the (1) stress field, the (2) strain field, and on (3) seismic waves.

2.5 PIEZOELECTRIC TRANSDUCERS

Piezoelectric transducers have been successfully used for over 25 years as a method of measuring velocities of wave through specimens (Deniz 2008). An advantage of these piezoelectric transducers is that non-destructive tests can be carried out using these elements. The piezoelectric transducers can be specially designed to transmit shear and compression waves through soil by means of vibrating signals (Deniz 2008). The piezoelectric transducers exhibit mechanical deformation due to an applied voltage or an electrical output due to a mechanical distortion (Amat 2007).

These piezoelectric transducers consist of two conductive outer electrodes, two ceramic plates and conductive metal shim in the centre and are made piezoelectric by means of polarization (Brandenberg et al. 2006). Figure 2.17 shows a schematic of the composition of the piezoelectric transducers.

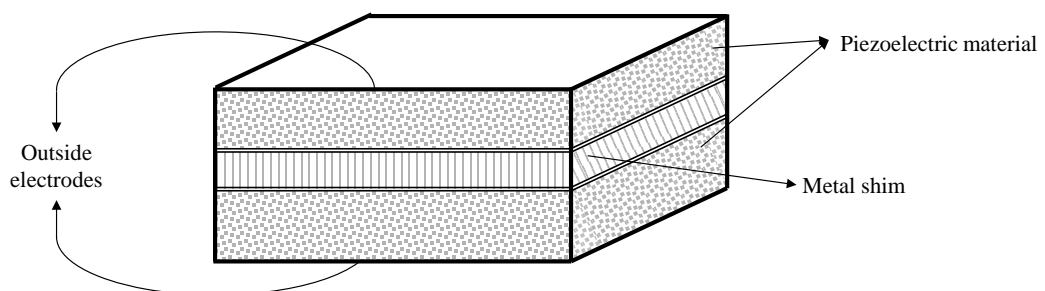


Figure 2.17: Composition of piezoelectric transducers (after Fu, 2004)

Once these piezoelectric transducers are wired they can behave in different ways depending on the wiring configuration. The elements can be made to bend, twist or elongate (Piezo

Systems, Inc. 2011) and when the elements bend they are referred to as bender elements and when they elongate they are referred to as extender elements, which will produce shear- and compression waves respectively. Bender- and extender elements are therefore two-layer piezoelectric transducers and are two of the main piezoelectric transducers used in geotechnical centrifuge testing and due to its perceived simplicity it has become ever more popular in laboratory and centrifuge tests (Clayton 2011). These elements will be discussed in this section of the report, as they are to be used as part of the experiments for this project.

2.5.1 BENDER AND EXTENDER ELEMENTS DESCRIPTION AND BEHAVIOUR

As mentioned previously, bender and extender elements convert electrical energy into mechanical energy and vice versa and the behaviour (bending, extending or twist) depends on the wiring of the piezoelectric transducer. It should be noticed that if an electrical voltage is applied to the element, it will vibrate which will cause deformation of the soil and will transmit a wave through the soil (i.e. the element is referred to as a transmitter). The opposite infers that if the elements are vibrated, due to deformation, the mechanical vibration will convert into electrical energy which can be transmitted to a readout unit meaning the element behaved as a receiver.

The behaviour of these elements depends on the wiring configuration with two types of wiring configurations indicated in literature (Lee & Santamarina, 2005; Leong et al., 2009; Asslan, 2008) namely series and parallel configuration. When the supply voltage is applied across all the piezo layers at once, the voltage applied to each layer is the total voltage divided by the number of layers (in the case of bender and extender elements two) and this configuration is referred to as a series connection. Therefore, for the series connection two wires are required and the wires are connected to the outer electrodes only. For the parallel configuration, the supply voltage is applied to each layer independently meaning three wires are required where wires are connected to the each outside electrode as well as a wire connected to the centre metal shim. The reason for these different configurations is due to the polarization of the piezoelectric elements with different connections inducing different polarization directions. Two types of polarization are available namely x-poled and y-poled with the x-poled referring to the case where the direction of polarization in each element points in opposite directions and for the y-poled case the polarizations point in the same direction. Figure 2.18 shows a schematic of the polarization configurations for the piezoelectric elements. For the bender elements, the reason for the bending is due to differential elongation or contraction of the two piezoelectric elements depending on the polarization (Deniz 2008). The extension of the extender elements works in the same manner, with the only difference being that the two piezoelectric elements elongate or

contract at the same time. The polarity is established during the manufacturing process and due to the direction of the polarization certain wiring configurations apply to different polarizations depending on the element type (Deniz 2008). To behave as a bender element transmitting and (or) receiving signals, x-poled and y-poled piezoelectric transducers should be connected in series and parallel, respectively. For extender elements transmitting and (or) receiving signals, x-poled and y-poled piezoelectric transducers should be connected in parallel and series, respectively (Leong et al. 2009).

Figure 2.19 presents the different wiring configurations for the bender- and extender elements. The different polarizations are also indicated in the figure together with the direction of deformation.

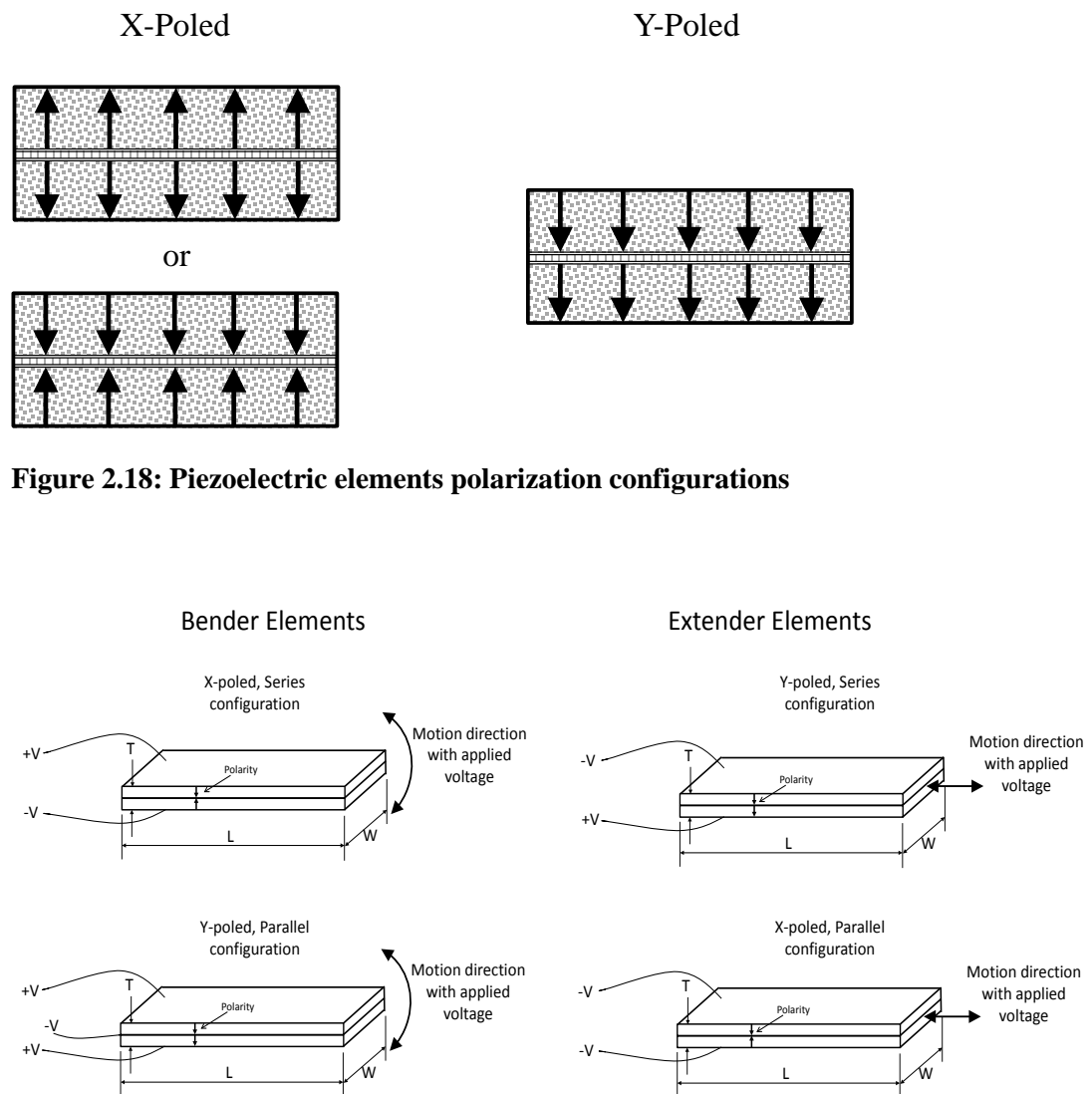


Figure 2.18: Piezoelectric elements polarization configurations

Figure 2.19: Bender and extender elements wiring configurations

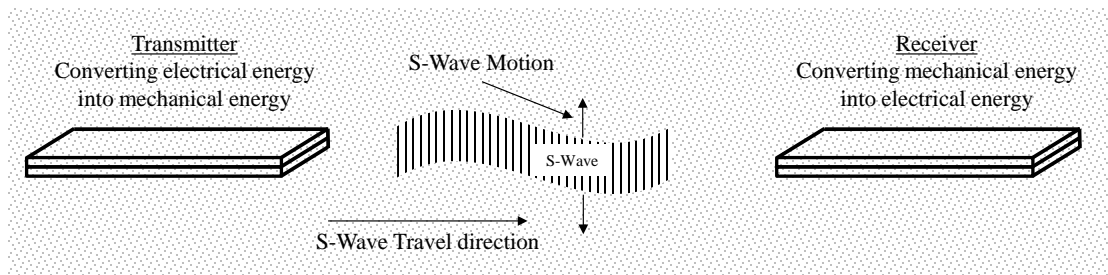
As mentioned, the benders or extenders can be used as transmitters or receivers, but some configurations work better as receivers and other better as transmitters. In some instances the transmitting elements are referred to as “piezo motors” and the receiver elements as “piezo generators”. In the bender element case, for the same voltage application a parallel connected y-pole bender will render twice the deformation than that of a series connected x-poled bender. Leong et al. (2009) reports that in terms of deflection per unit applied voltage, the parallel configuration deformation is greater by a factor of two compared to the series connection. Hence, parallel connected y-pole benders are more favourable as transmitters where series connected x-poled benders work better as receivers since they will produce a higher output voltage for the same deformation (Leong et al. 2009). The opposite is the case for extender elements where the most suited configuration for transmitter is x-poled parallel connection and for a receiver a y-poled series connection (Leong et al. 2009).

2.5.2 MEASUREMENT OF SEISMIC WAVE VELOCITY USING PIEZO TRANSDUCERS

As mentioned, shear- and compression waves can be generated by bender- and extender elements respectively, due to the behaviour characteristics. The shear- and compression waves can be used together with Equations 2.20 and 2.21 to determine the small-strain shear- and compression moduli as discussed in Section 2.3.2. When bender- and extender elements are placed in soil and a differential voltage is applied, small deformations due to vibrations generate waves that propagate through the soil. Since the mechanical vibrations can be converted to a voltage output, as discussed in the previous section, the arrival of the wave can be determined. Therefore, when conducting test with bender- extender elements, a pair is usually used with one configured as a transmitter and the other as a receiver.

The bending effect of the bender elements will produce shear waves (s-waves) and the extending effect of the extender elements will render compression waves (p-waves). Figure 2.20 shows a schematic of the working principle of the bender- and extender elements in the soil.

Bender Element



Extender Element

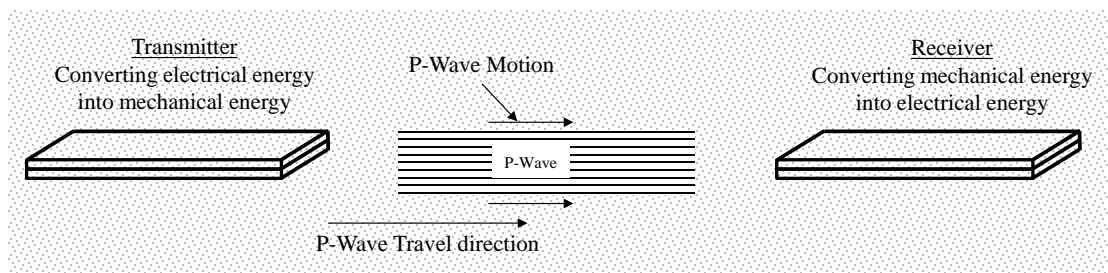


Figure 2.20: Bender- and extender element working principle

Based on the working principle, when a voltage applied to the transmitting elements and the output voltage is read from the same readout unit, the travel time of the wave can be determined. The voltage applied to the transmitting elements is referred to as the trigger with the output voltage referred to as the received signal. This is the same whether a bender- or extender element is used. Different trigger signals may be applied with the help of a function generator to produce a differential voltage and a data acquisition system that can read both signals simultaneously. Figure 2.21 shows a typical schematic of a bender/extender setup indicating the trigger and the received signal together with the travel time. The components as well as the different trigger signals used during the setup will be discussed in subsequent sections. The distance that the transmitter and receiver is placed from each other, known as the tip-to-tip distance, together with the travel time can be used to calculate the s-wave velocity (V_s) and p-wave velocity (V_p) using Equation 2.29.

$$V_s = V_p = \frac{L_{tt}}{\Delta t} \quad 2.29$$

where: L_{tt} = tip-to-tip distance

Δt = travel time

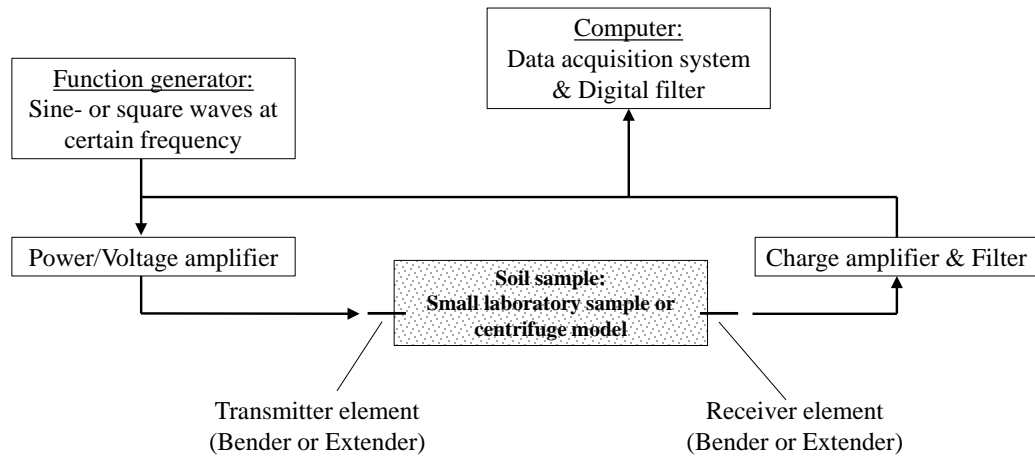


Figure 2.21: Typical schematic of bender/extender setup

2.5.3 SIGNAL INTERPRETATION

Signal interpretation of bender and extender elements means identifying the travel time and in some instances identifying the travel time can be controversial (Lee & Santamarina 2005). An international parallel test on the measure of G_0 using bender elements indicated that there are currently three different approaches to identify the arrival time (Yamashita et al. 2009). Since the shear- and compression wave velocities are dependent on the travel time, it is important to find a method that is best suited depending on the test limitations. Chan (2010) concluded that the reliability of s-wave velocity measurements can be considerably improved if the same arrival time identification method is used throughout a test series. It is therefore important to discuss the different methods in order to identify the method best suited.

The methods identified by Yamashita et al. (2009) as well as Chan (2010) are as follows:

1. Visual picking - First arrival or Peak-to-peak
2. Cross correlation
3. Frequency domain or Cross spectrum analysis

Visual picking

This is the most commonly used method and its popularity is due to the fact the method is straightforward (Chan 2010). The method involves visually identifying the time at the first major deflection (or break) of the received signal. The first major break can be identified when there is a significant departure from zero amplitude and this break can be positive or negative depending on the polarization and arrangement of the bender or extender element (Chan 2010). This method is also referred to as a time domain technique since the arrival time is identified with a time base axis. A disadvantage of this method is the impact of near-

field effects which are believed to be due to the influence of p-waves arriving before the actual s-wave (Yamashita et al. 2009). Other effects include electrical and background noise having the same frequency characteristics as the received signal, as well as wave reflections and in some instances the received signal does not display a distinct or sharp deflection.

Another method that falls within the visual picking category is the first major peak-to-peak method. The method is based on the assumption that the received signal and the input signal bears a high resemblance (Chan 2010). The time difference between the first major peak of the input signal and that of the received signal is taken as the travel time. The difficulty with using this method is the fact that the received signal is usually distorted, due to the sample geometry or the energy-absorbing nature of the soil, and identifying the first major peak can prove troublesome since the resemblance is affected (Chan 2010).

Both these aforementioned techniques are affected by the quality of the received signal which in return is dependent on installation, application and the input signal (Lee & Santamarina 2005). If the electrical noise or background noise can be reduced, visual picking is perhaps the easiest to apply. Figure 2.22 shows schematic of a typical received signal indicating the first major break as well as the major first peak for the visual picking technique.

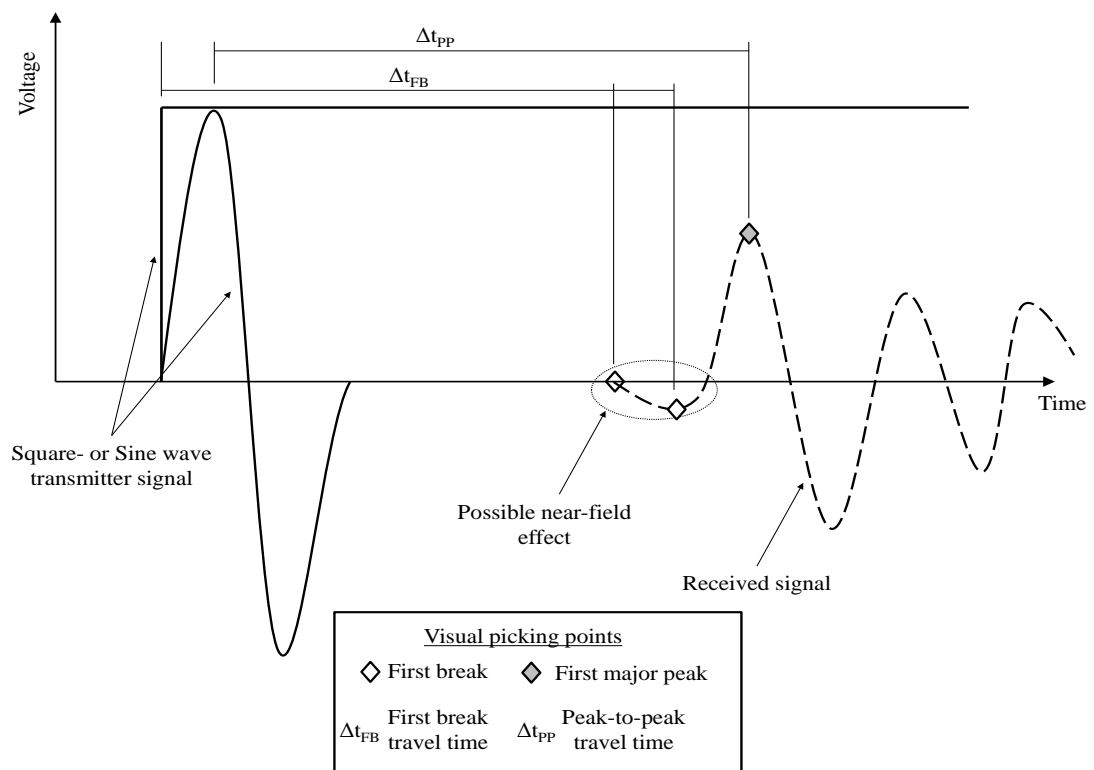


Figure 2.22: Schematic of typical received signal with visual picking technique

Cross correlation

This method involves calculating the cross correlation between the transmitted (T) and the received (R) signal. The assumption on which the method is based is that the input wave retains its shape when propagating through the soil, i.e. the frequency of the transmitted wave gets passed onto the receiver (Yamashita et al. 2009). Since the frequency is passed on and hence the shape of the wave, cross correlation is used to measure the level of interrelationship between the input and received signal (Chan 2010). Some researchers (Chan, 2010; Rio, 2006) have provided equations to calculate a cross correlation coefficient, $CC(t_s)$, which takes the form presented in Equation 2.30.

$$CC(t_s) = \lim_{T_r \rightarrow \infty} \frac{1}{T_r} \int_{T_r}^{T_r + t_s} T(t) R(t) dt \quad 2.30$$

where: T_r = time record

t_s = time shift between two signals

In essence, Equation 2.30 describes a method of shifting the received signal until it best matches the transmitted signal, therefore the time shift producing the maximum cross correlation value will be the travel time. This method can be performed in the time domain as well as the frequency domain using a Fast Fourier Transform (FFT) to convert the time domain signals to the frequency domain (Chan 2010).

A problem with this method is that in some instances the frequencies of the transmitted and received signals does not match, which makes interpretation difficult and an experienced interpreter is required (Yamashita et al. 2009). Rio (2006) indicated that the cross correlation method is the most complex signal processing method for travel time determination. From the aforementioned it can be seen that for this method to be used the input signal should be of the same wave type as that of the received signal, which in most cases resemble sine waves.

Frequency domain analysis (cross spectrum)

This method produces the relationships of amplitude and phase angle with frequency by calculating the cross spectrum of the transmitting and receiving signals (Yamashita et al. 2009). The method involves firstly calculating the FFT of the transmitted and received signals from which the amplitude and phase angle can be determined and is presented by Viggiani & Atkinson (1995). The amplitude and phase angle, as given by Viggiani & Atkinson (1995), is the product of the amplitudes and the phase differences of the components

(complex conjugates), respectively of the two signals at a specific frequency. The unwrapped phase algorithm (i.e. phase angles are not fixed between values which is most cases are between -180° and 180°) is used which is presented by Lee & Santamarina (2005) and given in Equation 2.31. The unwrapped phase algorithm is calculated using the frequency response of the transmitted and received signals (i.e. the FFT results) given by Equation 2.32.

$$\Phi(f) = \tan^{-1} \left(\frac{I_m (H_{soil})}{R_e (H_{soil})} \right) \quad 2.31$$

where: $\Phi(f)$ = phase angle at a specific frequency, f

I_m = imaginary number from FFT analysis

R_e = real number from FFT analysis

H_{soil} = frequency response at a specific frequency, f

$$H_{soil}(f) = \frac{\text{FFT}[\text{Signal 1}]}{\text{FFT}[\text{Signal 2}]} \quad 2.32$$

The unwrapped phase angles can be plotted against the corresponding frequencies, which is referred to as the absolute cross power spectrum, and the travel time is taken as the inclination/slope of the graph (Yamashita et al. 2009).

The reason the slope of the travel time is based on the fact that the phase velocity ($V(f)$) can be determined for each frequency (f) using Equation 2.33 with the wavelength (λ_w) presented by Equation 2.34 (Leong et al. 2005). Combining Equations 2.33 and 2.34 will give the travel time, given by Equation 2.35, which is the gradient of the absolute cross power spectrum plot divided by 2π or 360° depending on the unit of the phase angle (Leong et al. 2005).

$$V(f) = \lambda_w f = \frac{L_{tt}}{\Delta t} \quad 2.33$$

$$\lambda_w = \frac{2\pi L_{tt}}{\Phi(f)} \quad 2.34$$

$$\Delta t = \frac{\Phi(f)}{2\pi f} \quad 2.35$$

2.5.4 TECHNICAL CONSIDERATIONS

Clayton (2011) indicated that the use of bender elements is becoming more popular, due to its perceived simplicity. The use of the word “perceived” infers that it might not be as simplistic as first thought and that there might be aspects that users should consider before conducting tests involving bender elements. These aspects are referred to by various authors as concerns, issues, problems, errors, etc. but will be referred to in this report as technical considerations.

An assessment was done of the different technical considerations various researchers put forth and these were consolidated and presented Table 2.6. Some researchers feel stronger about certain aspects depending on their test setup and limitations, and more often these aspects overlap between authors indicating that there are universal aspects that should be considered. Although most of the technical considerations presented in the literature are based on bender element test setups, these aspects applies to extender elements as well since they are in essence the same as bender elements.

Table 2.6: Technical considerations for bender/extender elements

Technical consideration	Description	Issues and Recommendations	Reference
Dimensions	The physical dimension of the element with specific reference to the protrusion into the soil	<ul style="list-style-type: none"> • The protrusion will affect the tip-to-tip distance and reduced travel distance causes reduced accuracy. • The soil type will affect installation depending on the protrusion length (stiffer soil will make installation difficult with long protrusions). 	Clayton (2011)
Design	Series or parallel configuration for transmitter and receiver elements	<ul style="list-style-type: none"> • Discussed in Section 2.5.1 • Certain configuration produce better receiver or transmitter elements • Series connection work better for x-poled transmitter bender- and y-poled receiver extender elements. • Parallel connection work better for y-poled receiver bender- and x-poled transmitter extender elements. 	Clayton (2011)
Travel distance	Tip-to-tip distance affects the travel time resolution with large distances affecting attenuation.	<ul style="list-style-type: none"> • More scatter is observed when elements are closely spaced, but wider spaced elements are noisier. • For small specimens with large protrusions higher input frequencies are required to keep wavelengths down. 	Clayton (2011)
Transmitting wave	The wave type of the transmitting element. Square and Sine waves are common.	<ul style="list-style-type: none"> • Square waves contain a broad spectrum of frequencies and can only be used with certain travel time determination methods. • Sine waves can be applied continuously or as single pulses and can be used with all determination methods. • Square waves have a shorter rise time resulting in higher initial response of the element. 	Clayton (2011)
Transmitting wave frequencies	Frequencies affect wavelengths	<ul style="list-style-type: none"> • Long wavelengths may induce near field effect of the receiver element influencing travel time determination. • It is recommended that 2-3 wavelengths should be between transmitting and receiving signals. • With continuous input waves, higher frequencies will affect receiving signal as a received signal may not have dissipated by the time the next input wave is triggered. 	Clayton (2011)
Noise	The noise includes electrical as well as mechanical noise and greatly affects low amplitude signals.	<ul style="list-style-type: none"> • When the noise is greater than the received signal, the signal-to-noise ratio (SNR) decreases. • Determination of travel time becomes problematic when SNR decreases. 	Clayton (2011)

Technical consideration	Description	Issues and Recommendations	Reference
Travel time determination	The estimation of the travel time to calculate wave velocities.	<ul style="list-style-type: none"> • Discussed in Section 2.5.3. • Method will be based on input wave. • Different travel times have been observed when using different methods. • Visual picking are routinely used. • Some methods may not be usable due to noise. 	Clayton (2011)
Sampling rate	The sampling rate will affect the resolution of the received signal.	<ul style="list-style-type: none"> • Higher sampling rates will produce higher resolution received signal. • Lower sampling rates might render inaccurate estimation of the arrival time. • A sampling time interval of 1/100th of the travel time between transmitter and receiver is recommended. 	Clayton (2011)
Signal analysis and filtering	Manipulating data for better data interpretation.	<ul style="list-style-type: none"> • Methods include signal filtering and stacking. • Band-pass, low-pass or high-pass filters may be applied to filter out unwanted signals and/or noise. • The minimum cut-off frequency for a low-pass filter should be at least 10 times the resonant frequency. • Stacking is the process of adding repeated signal with the assumption that the random noise dissipates and the inherent signal becomes clearer, i.e. increasing the SNR. 	Lee (2003)
Near-field effects	An effect influencing the arrival of a signal at the receiver element. It is believed to be the influence of p-waves arriving at the receiver element before shear waves; hence the effect is more prevalent with bender elements.	<ul style="list-style-type: none"> • Makes reading of the first arrival difficult when using a visual picking method due to the near-field effect masking the arrival of the shear wave. • The problem is amplified when transmitter and receiver elements are spaced too close to each other, in the order of 0.25-4 wavelengths. • One method of avoiding this effect is to adjust the input frequency until the effect is negligible. • Another method is if the first break produces wave velocities resembling p-wave velocities when measuring s-waves then the first break may be a near-field effect. 	Asslan (2008) Yamashita et al. (2009) Fu (2004)
Effective length	The effective free bending or extending length of the elements.	<ul style="list-style-type: none"> • The free bending or extending lengths are the “cantilever” lengths of the elements. • Different lengths will produce different SNR. • The optimum length should be determined for the specific setup. 	Archer & Heymann (2014)

Technical consideration	Description	Issues and Recommendations	Reference
Crosstalk	Also known as electromagnetic coupling and is a phenomena where an output signal manifests as an early received signal which is quasisimultaneous with the input signal.	<ul style="list-style-type: none"> • This early wave can be mistaken for an output signal. • Crosstalk is very important in conductive soils such as wet clays. • Effect can be minimised by grounding or shielding the elements. • When using a parallel-to-parallel (source-to-receiver) connection crosstalk may be eliminated. 	Lee & Santamarina (2005) Lee (2003)
Specimen size	A big enough specimen size is required to avoid early arrival of p-waves.	<ul style="list-style-type: none"> • A formula can be used to determine the minimum radius (R) required to prevent this effect: $R = \frac{1}{2\sqrt{1-2\nu}}H$Where H is the tip-to-tip distance and ν the Poisson's ratio. • For dry soils, i.e. $\nu = 0.1$, $R > 0.56H$ • For saturated soils, i.e. $\nu = 0.5$, $R > 3.7H$ 	Lee (2003)
Installation/Mounting	This refers to the mounting or installation of the elements within the soils.	<ul style="list-style-type: none"> • Some researchers use mounting frames while others use free type elements. • With free type elements minimise the mass of elements and are easy to install. • Mounting frames can influence the dynamic behaviour of the soil and can cause the elements to break more easily. 	Brandenberg et al. (2006) Kim & Kim (2010) Fu (2004) Zhou et al. (2010)
Resonant frequency	The resonant frequency of the element itself.	<ul style="list-style-type: none"> • Resonant frequency affects the near-field effect influence, travel time determination and resolution. • Output signal amplitude will be increased when using sine input waves if the resonant frequency of the elements is known. • When using square waves, the response will be a maximum since a square wave includes all frequencies. • Square waves are recommended when resonant frequency is unknown or expected to change. 	Lee (2003)
Amplifiers	Amplifiers are required to amplify the output or input signals.	<ul style="list-style-type: none"> • For the input signal a voltage amplifier can be used to increase the transmitter voltage which will lead to enhanced signal quality due to higher SNR. • A charge amplifier is important for the receiver signal in order to convert the charge created by the element to a voltage value and to amplify the signal to increase the SNR. 	Experience of the researcher during the project

2.6 SUMMARY

A literature review of the aspects relevant to this research topic was conducted and presented in this chapter. The aspects with regard to foundations included the general concept of foundation design, settlement calculation and bearing capacity of shallow foundations, small-strain stiffness with focus on various aspects relevant to foundation design. Information regarding geotechnical centrifuge testing as well as the piezoceramic elements relevant for the experimental design have been discussed.

Based on the information presented it is clear that much work and research has been done on the topic of shallow foundation settlement, but what is also noticeable is that there are still shortcomings. These shortcomings relate to the stiffness measurement of the soil beneath a foundation and once the stiffness has been measured, the most efficient and accurate way of incorporating it into design equations. Another important aspect is the fact that when it comes to stiffness measurements, especially with granular soils (sands), in-situ test methods are more popular due to quicker measurements, less or no sample disturbance, etc. Of the different soil stiffness moduli that are measured, the initial small-strain shear stiffness (G_0) is important and settlement prediction methods using this value are becoming more common. Most methods presented utilising the small-strain stiffness value also requires the calculation of the ultimate bearing capacity which can only be done accurately with parameters obtained from laboratory test results or plate load tests. Another issue with some methods are that the assumptions, on which the methods are based, are not always applicable or suited to the specific design problem encountered which may lead to inaccuracies.

All this information leads to a question and in essence a hypothesis which forms the basis of the experimental work. The hypothesis is thus:

“Shallow foundation settlement on cohesionless granular soil can be estimated using only the small-strain stiffness”

The hypothesis will be used as the basis for the experimental design. The aim of the research will be to assess the shortcomings obtained from the literature, conducting centrifuge test experiments and combining the results of the latter with the former in order to arrive at a conclusion for rejecting or accepting the hypothesis. In the ensuing chapters the experimental design as well as the finding will be discussed.

3 EXPERIMENTAL WORK

The aim of this chapter is to convey all aspects of the experimental setup and design essential to obtain reliable data for analysis and validation of the hypothesis. The experimental work for this research project comprise of two parts. The first part is to characterise the geomaterial to be used. Fine silica sand was used for the experiments and will be referred to as **Cullinan Sand** for the remainder of this report. Section 3.1 will summarise the testing done on the sand in order to obtain all the properties required to design the rest of the experiment and to characterise the sand properly. Centrifuge testing was chosen as the experimental method and this method involved developing instrumentation and designing an experiment that complies with all the principle modelling requirements and centrifuge testing. Sections 3.2 - 3.3 will discuss the application and calibration of the instrumentation used and developed, the different components involved in the experiment and the data acquisition systems used for the centrifuge model. Section 3.4 will focus on the complete experiment design as well the testing procedure followed.

As mentioned previously, it was decided to focus on different relative densities and for this research project the relative densities chosen were 20%, 50% and 80%, which represents loose, medium dense and dense sand respectively. Tests to classify the soil were conducted at these relative densities to assess the characteristics of the loose, medium dense and dense sand. Accordingly, the experiment was also designed taking into account the different relative densities.

3.1 SAND CLASSIFICATION

3.1.1 DENSITY

As discussed previously, relative density (D_r) is an important factor to be considered for cohesionless soil when it comes to foundation design and its engineering properties. The relative density is related to the maximum (e_{max}) and minimum (e_{min}) void ratios according to the relationship given in Equation 3.1.

$$D_r = \frac{e_{max} - e}{e_{max} - e_{min}} \quad 3.1$$

where: e = current void ratio

Hilf (1991) indicates that to determine the relative density, the dry density of the soil in its loosest and densest state should be determined, where after an intermediate density will give an indication of the relative density. Since the minimum and maximum void ratios are related to the minimum and maximum density of the soil, it is necessary to determine the latter.

For the Cullinan Sand, the following two ASTM standard test methods were used to determine the minimum and maximum densities, and hence the minimum and maximum void ratios:

- D4254 – 00: Minimum Index Density and Unit Weight of Soils and Calculation of Relative Density
- D4253 – 00: Maximum Index Density and Unit Weight of Soils Using a Vibratory Table

A total of four tests were conducted and the average values for the minimum and maximum densities were used. Table 3.1 indicates the average results for the minimum and maximum density tests together with the corresponding void ratios.

Table 3.1. Minimum and maximum density test results.

Parameter	Value
Maximum dry density (kg/m^3)	1669.1
Minimum dry density (kg/m^3)	1392.0
Maximum void ratio (e_{max})	0.92
Minimum void ratio (e_{min})	0.60

For the purpose of this research project it was necessary to use different relative density values, which corresponds to loose, medium dense and dense sand, hence relative density values of 20%, 50% and 80% were used. Using Equation 3.1 and the results from the minimum and maximum density tests, different density values for the Cullinan Sand were calculated based on several relative density values. Table 3.2 depicts the results of the calculations.

Table 3.2. Density values based on relative densities results.

Relative Density (%)	Dry Density (kg/m ³)	Void ratio
0	1392.0	0.92
10	1419.7	0.88
20	1447.4	0.84
30	1475.1	0.81
40	1502.8	0.77
50	1530.6	0.74
60	1558.3	0.71
70	1586.0	0.68
80	1613.7	0.65
90	1641.4	0.62
100	1669.1	0.60

3.1.2 PARTICLE SIZE DISTRIBUTION

The particle size distribution is an indication of the percentage of particles, typically by mass or volume, within certain particle sizes. The particle distribution is a physical description of the soil which in turn provides an idea of the engineering behaviour of the soil. The particle size distribution determines the type of soil and for this research project a sandy material was sought with no clay particles. For centrifuge testing it is preferable to have a uniformly graded sand to minimise the settlement or compaction during spin-up. If the soil is well-graded, smaller size particles will fill the voids as acceleration is increased, resulting in excessive settlement and considerable change in density. A uniformly-graded soil will not compact easily during spin-up since the particle sizes are uniform; no fine particles can fill the voids, resulting in a more constant density during centrifuge spin-up.

To determine the particle size distribution of the sand used for the project, a sieve analysis was firstly conducted according to the British Standard BS1377-2:1990. The smallest sieve size available was 53 μm . Since it is important establish the percentage of fines in the sand, a test had to be conducted to determine this. Normal convention is to conduct a hydrometer test, but due to time constraints, a Malvern Mastersizer 2000 apparatus was used.

The Malvern Mastersizer 2000 is an apparatus that uses the technique of laser diffraction to calculate the percentage of particle sizes. A laser beam is passed through a dispersed particulate sample and the intensity of the scattered light is measured. The particles creating the scattered pattern are then measured to calculate the particle size distribution. The particle size distribution is however not calculated as a percentage by mass, but rather as a percentage by volume. Using the specific gravity (G_s), which will be discussed later, the percentage by

volume can be converted to a percentage by mass and the results can be used together with the sieve analysis results to obtain a complete particle size distribution.

Figure 3.1 shows the results of the sieve analysis as well as the Mastersizer 2000 results, denoted as “Malvern test”. From the results it can be seen that the Malvern test results produced an evenly distributed curve and compares well with the sieve analysis. The difference in the graphs can be attributed to the sieve apparatus used. It was therefore decided to use the Malvern Mastersizer 2000 results as the final graph for the particle size distribution.

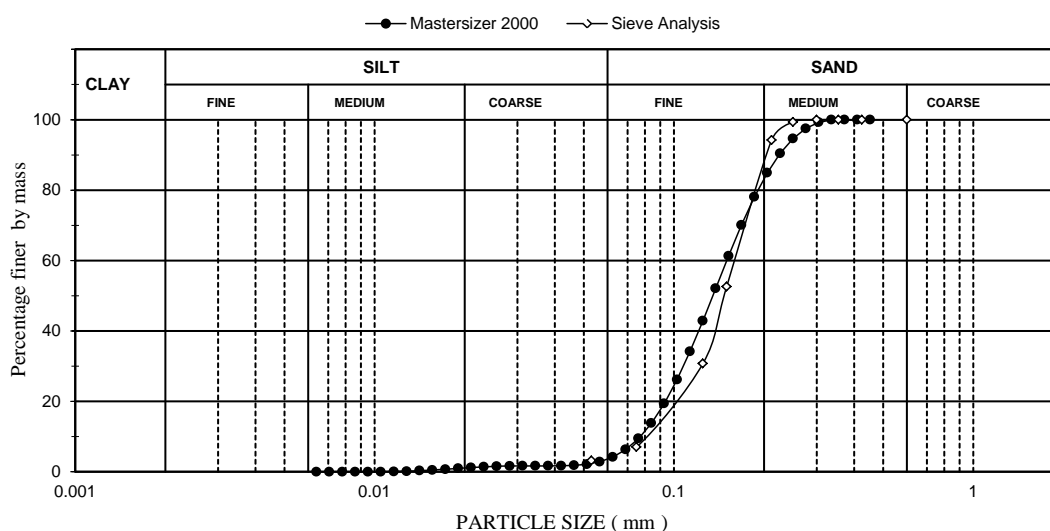


Figure 3.1. Particle size distribution of Cullinan sand.

Based on the results presented in Figure 3.1 the soil can be classified as a **slightly silty sand** and referring to the Unified Soil Classification System – USCS (ASTM Standard D2487, 2011), the soil is characterised as **poorly graded sand (SP)**. In order to assess the grading, a grading parameter referred to as the uniformity coefficient (C_U) can be calculated using Equation 3.2.

$$C_U = \frac{D_{60}}{D_{10}} \tag{3.2}$$

where: D_{10} = the largest size at which 10% of the particles passes

D_{60} = the largest size at which 60% of the particles passes

Smith (2006) indicates that if C_U is smaller than four (4), the soil is uniformly graded and if it is greater than four (4), the soil is either well- or gap graded. From the results of the Malvern

test, the C_U for the soil used in this project was calculated as 1.95 which indicates that the Cullinan sand is uniformly graded. Other conclusions that can be drawn from the particle size distribution graph are that the maximum particle size is 300 μm and the D_{50} (mean/average particle size) is 135 μm .

When considering foundations Kusakabe (1995) suggests that in order to reduce the scale effect of the particle size, a foundation width to grain-size ratio of greater than 50-100 should be used. The grain-size according to Kusakabe (1995) is defined as the mean grain diameter, i.e. the D_{50} value. Since a foundation diameter of 100mm will be used for the centrifuge tests (which will be discussed later), and considering the D_{50} value of 135 μm the foundation width to grain-size ratio of this particular project is ± 740 . This value is significantly more than the suggested 50-100 and it can be safely assumed that the grain-size effect for this project is negligible.

3.1.3 SPECIFIC GRAVITY

For the specific gravity (G_s) determination an AccuPyc II 1340 Pycnometer from Micromeritics was used. The pycnometer works on the principle of gas pycnometry. This is a gas displacement method where an inert gas, in this case helium, is used as a displacement medium and admitted to a soil sample of known weight and in a container of known volume. The volume of the sample is calculated from the measured pressure at which the gas is admitted and with the known weight and volume, the particle density can be determined.

Three cycles were run during the test and the average was taken as the particle density. The results of the pycnometer test produced a particle density value for the Cullinan sand of 2.666g/m³.

3.1.4 TRIAXIAL TEST RESULTS

In order to determine the strength characteristics of the Cullinan sand, triaxial tests were conducted since the triaxial test is the most widely used shear strength test (Craig 2004). For the purpose of centrifuge testing it was decided to conduct consolidation drained (CD) triaxial tests.

The triaxial tests included local strain measurements to assess the small-strain stiffness characteristics of the Cullinan sand. Stage consolidation was also conducted to assess the consolidation characteristics at different effective stresses. As mentioned in the introduction of this chapter, the triaxial tests were conducted at different relative densities (denoted as 20% RD, 50% RD and 80% RD) and since a complete triaxial test consists of three sets at different effective stresses, a total of nine triaxial tests were conducted. The effective stresses

chosen were 50 kPa, 200 kPa and 500 kPa which represent different depths depending on the density of the soil. These effective stresses represent a maximum depth of ± 34 m, calculated using the maximum density presented earlier. For reasons that will be provided later, this depth is more than sufficient for depth range of the centrifuge tests. Triaxial permeability tests were also conducted for the Cullinan sand at 200 kPa effective stress.

Initial conditions

The initial conditions for all three triaxial tests are presented in Table 3.3. The samples were re-compacted to target relative density values corresponding to 20%, 50% and 80% relative density. The initial moisture contents were chosen purely on the basis of workability with the 80% RD test being compacted on the triaxial pedestal, hence the low initial water content.

What should be noted from the initial conditions are the density values. For the 20% RD, 50% RD and 80% RD tests, the relative density values obtained ranged from 11-16%, 42-44% and 80-81% respectively. The relative density values were calculated based on the initial dry density and the minimum and maximum density values discussed previously. Although the RD values for the 20% and 50% tests were lower than the target values, the material still fell into the loose and medium-dense categories respectively. The RD values for the 80% test were very close to the target 80% RD which will result in dense sand behaviour.

Table 3.3: Initial conditions for triaxial tests

Relative density and initial condition		Triaxial 1 ($p_0' = 50\text{kPa}$)	Triaxial 2 ($p_0' = 200\text{kPa}$)	Triaxial 3 ($p_0' = 500\text{kPa}$)
20% RD	Water content (%)	5.9	6.0	6.0
	Dry density (g/cm^3)	1.421	1.436	1.425
	Void ratio ($G_s = 2.667$)	0.88	0.86	0.87
	Degree of saturation (%)	18	18.7	18.3
	Relative density (%)	11	16	12
50% RD	Water content (%)	5.8	5.9	5.9
	Dry density (g/cm^3)	1.508	1.506	1.514
	Void ratio ($G_s = 2.667$)	0.77	0.77	0.76
	Degree of saturation (%)	20.1	20.1	20.6
	Relative density (%)	42	41	44
80% RD	Water content (%)	0.1	0.1	0.1
	Dry density (g/cm^3)	1.618	1.614	1.618
	Void ratio ($G_s = 2.667$)	0.65	0.65	0.65
	Degree of saturation (%)	0.3	0.4	0.3
	Relative density (%)	81	80	81

Consolidation results

The samples were consolidated to the different effective stresses of 50kPa, 200kPa and 500kPa with the 500kPa samples consolidated in six stages with the first stage being at 50kPa and the subsequent stages in increments of 100kPa up to 500kPa. The consolidation data can be used to calculate the coefficient of consolidation (c_v). The stage consolidation data results were used to obtain critical state parameters which will be discussed in a subsequent section. The consolidation results together with the coefficient of consolidation results will be conveyed in this section.

Since the material tested is sand and consolidation was rapid, Taylor's method was used for the coefficient of consolidation calculation. Taylor's method use the root time during consolidation and determines the time to 90% consolidation (t_{90}). The coefficient of consolidation is calculated using Equation 3.3.

$$c_v = \frac{0.848d^2}{t_{90}} \quad 3.3$$

where: d = Length of the drainage path (i.e. the length of the specimen)

t_{90} = time of 90% consolidation

Figure 3.2 shows the consolidation curve for the 20% RD 200eff test indicating the different lines for determining t_{90} . All the consolidation curves rendered the same result for t_{90} , therefore only Figure 3.2 will be shown. The figure shows that by the time the first reading was taken, consolidation was finished; hence t_{90} should be less than 15sec. Using the t_{90} value from the figure, the value for c_v must be higher than 31000m²/year. The c_v values calculated are high, but are not relevant for this project as dry sand was used.

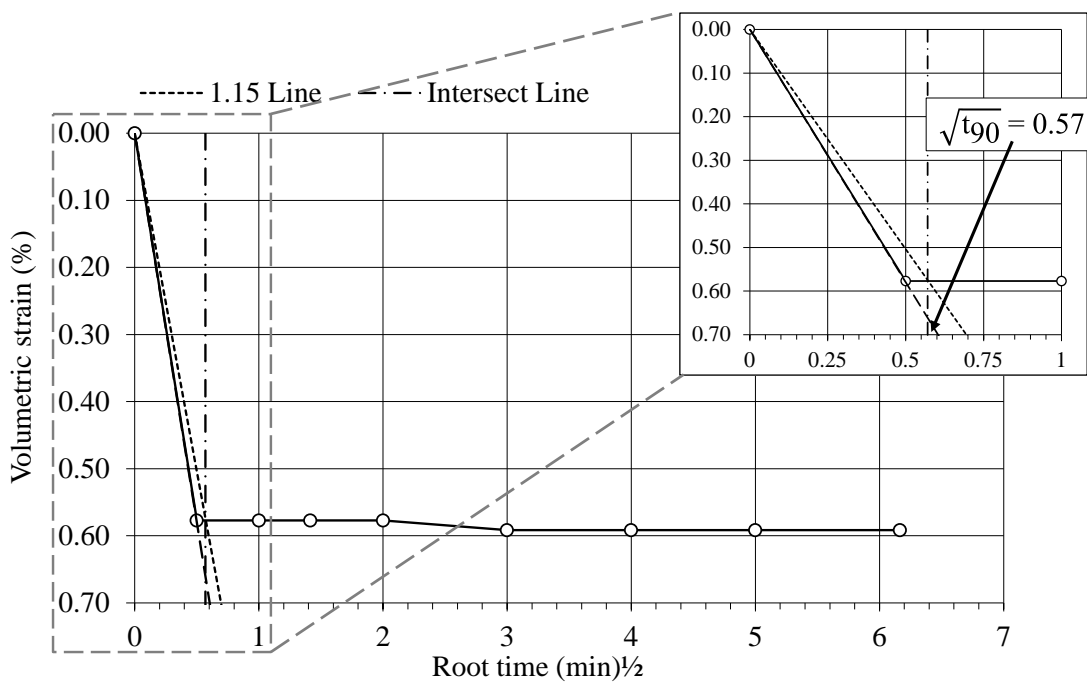


Figure 3.2: Consolidation curve for 20% RD 200eff test showing $c_v t_{90}$ determination

Permeability results

Triaxial permeability test were conducted on the 200 kPa effective stress samples. Table 3.4 summarises the permeability results for the Cullinan sand. The results indicate a coefficient of permeability for the sand of 10^{-5} m/s. Comparing this to Table 2.1 in Craig’s Soil Mechanics (Craig 2004) which have been reproduced in Table 3.5, the permeability coefficient falls into the category of very fine sand which is in agreement with the grading classification discussed previously. It is also noticeable that the RD value does not influence the permeability of the sand significantly. This is to be expected for a material with little fines.

Table 3.4: Triaxial permeability results

Relative density and effective stress		Permeability (m/s)
20% RD	Triaxial 2 - 200 kPa eff. stress	1.1×10^{-5}
50% RD	Triaxial 2 - 200 kPa eff. stress	1.9×10^{-5}
80% RD	Triaxial 2 - 200 kPa eff. stress	1.8×10^{-5}

Table 3.5: Coefficient of permeability (Reproduced from Craig, 2004)

1	10 ⁻¹	10 ⁻²	10 ⁻³	10 ⁻⁴	10 ⁻⁵	10 ⁻⁶	10 ⁻⁷	10 ⁻⁸	10 ⁻⁹	10 ⁻¹⁰
Clean gravels	Clean sands and sand-gravel mixtures			Very fine sands, silts and clay-silt laminate			Unfissured clays and clay-silts (>20% clay)			
	Desiccated and fissured clays									

Shear strength results

The shear strength parameters (i.e. angle of friction (ϕ') and cohesion (c')) for the sand were obtained from the shear stage of the drained triaxial tests. The relative densities prior to the shear stage (after consolidation) are shown in Table 3.6.

Table 3.6: Relative density prior to shear stage

Relative density test and effective stress		Relative density (%)
20% RD	Triaxial 1 - 50 kPa eff. stress	12
	Triaxial 2 - 200 kPa eff. stress	19
	Triaxial 3 - 500 kPa eff. stress	19
50% RD	Triaxial 1 - 50 kPa eff. stress	42
	Triaxial 2 - 200 kPa eff. stress	44
	Triaxial 3 - 500 kPa eff. stress	49
80% RD	Triaxial 1 - 50 kPa eff. stress	83
	Triaxial 2 - 200 kPa eff. stress	83
	Triaxial 3 - 500 kPa eff. stress	87

Stress paths were constructed for the drained tests in t' , s' space which represents the maximum shear and normal effective stress values respectively. Figure 3.3 to Figure 3.5 represents the stress path results for the different triaxial tests. The critical state line or failure line was drawn on the stress path graphs which is a tangent line connecting the top of each stress path. In t' , s' space, the tangent line can be used to calculate the angle of friction together with the cohesion value using Equations 3.4 and 3.5 respectively.

$$\tan \theta = \sin \phi' \quad 3.4$$

where: θ = angle from tangent line in t' , s' space

ϕ' = angle of friction

$$c' = \frac{t_0}{\cos\phi'}$$

3.5

where: t_0 = intercept value of tangent line with y-axis in t', s' space

c' = cohesion

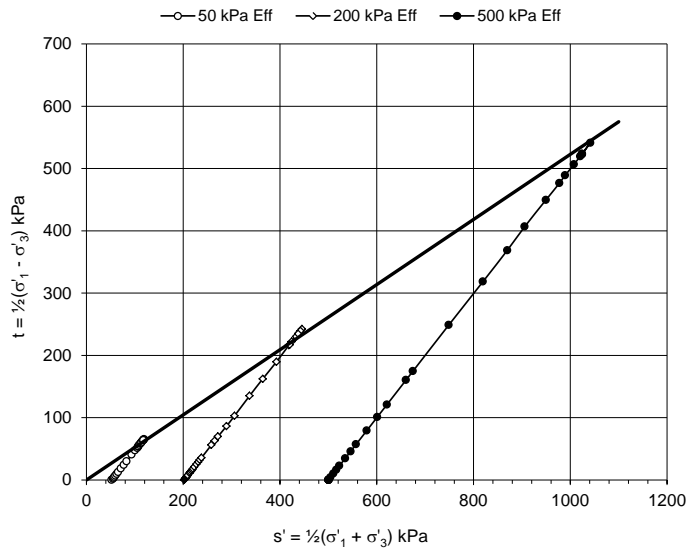


Figure 3.3: Stress path results for 20% RD test

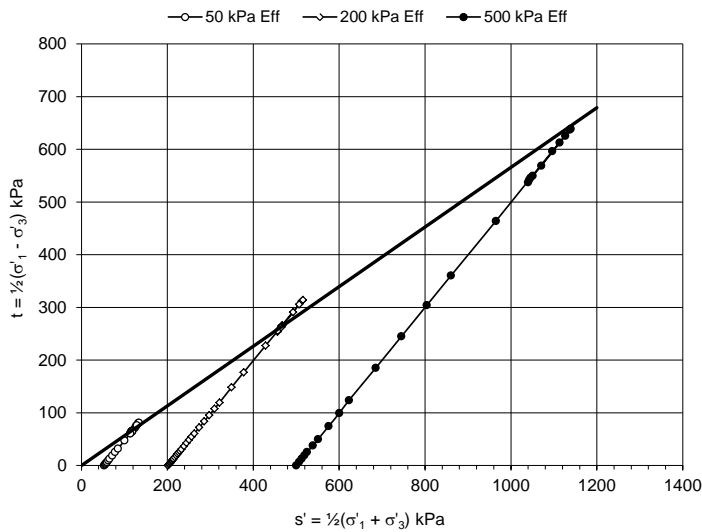


Figure 3.4: Stress path results for 50% RD test

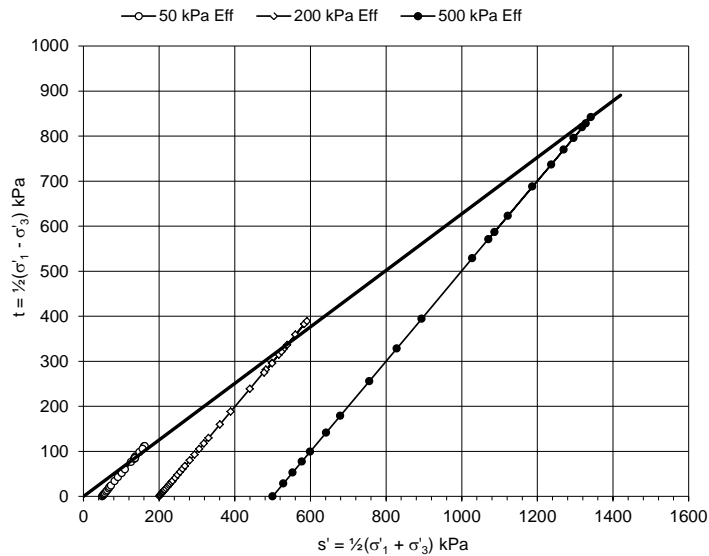


Figure 3.5: Stress path results for 80% RD test

Using Equations 3.4 and 3.5 the angle of friction and cohesion was determined and the results are presented in Table 3.7. As expected the angle of friction increases as the RD values increases due to the degree of particle interlocking being higher at higher RD values. Look (2014) provides typical friction angle values for loose to dense sands which are given in Table 3.8. As stated previously the 20% RD, 50% RD and 80% RD, represents loose, medium dense and dense sand respectively and comparing the results obtained from the drained triaxial results to the typical values in Table 3.8, the obtained values are in good agreement.

Table 3.7: Strength parameters from triaxial tests

Parameter	20% RD Test	50% RD Test	80% RD Test
Angle of friction, ϕ' (°)	32	34	39
Cohesion, c' (kPa)	0	0	0

Table 3.8: Typical friction angle values from Look (2014)

Soil type	State	Friction angle (°)
Cohesionless sands	Very loose/loose	27-32
	Medium dense	32-37
	Dense	37-42
	Very dense	42-47

Local strain measurement results

In order to assess the stiffness response of Cullinan sand at small-strains as well as larger working strain levels, local strain measurements were conducted on the 200 kPa effective stress specimens. Due to bedding and compliance errors external strain measurement devices will give inaccurate stiffness values at small strains (Yimsiri & Soga 2002). Local strain measurements will give more accurate measurements of the stress-strain behaviour at smaller strain levels (Yimsiri & Soga 2002).

Local axial strains were measured with linear variable differential transducers (LVDTs) mounted locally onto the sample. Axial strain values down to 0.002 % were measured together with the corresponding stiffness values. Secant stiffness values were plotted. The secant stiffness is defined as the ratio of the change in stress to the change in strain measured from the same origin. Equation 3.6 was used to calculate the secant Young's modulus.

$$E_{\text{secant}} = \frac{\sigma}{\varepsilon_a} \quad 3.6$$

where: σ = axial stress

ε_a = axial strain

The result of stiffness behaviour for the different density tests are shown in Figure 3.6 to Figure 3.8, where the secant young modulus (E_{sec}) is plotted against the local axial strain. What should be noticed from the figures is that there is some scatter in the data at strain levels below 0.01%. The scatter reduces from strains above 0.01% and it is interesting to note that for all the graphs, there is no significant scatter for stiffness values from 250MPa and lower. For ease of comparison, Figure 3.9 shows the combined plot for the different density tests.

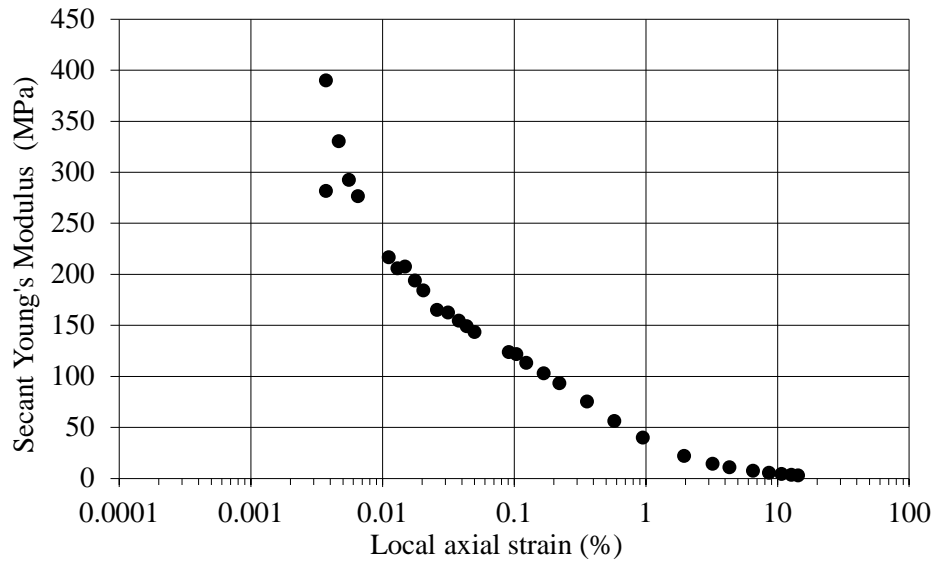


Figure 3.6: Stiffness behaviour of 20% RD Cullinan sand

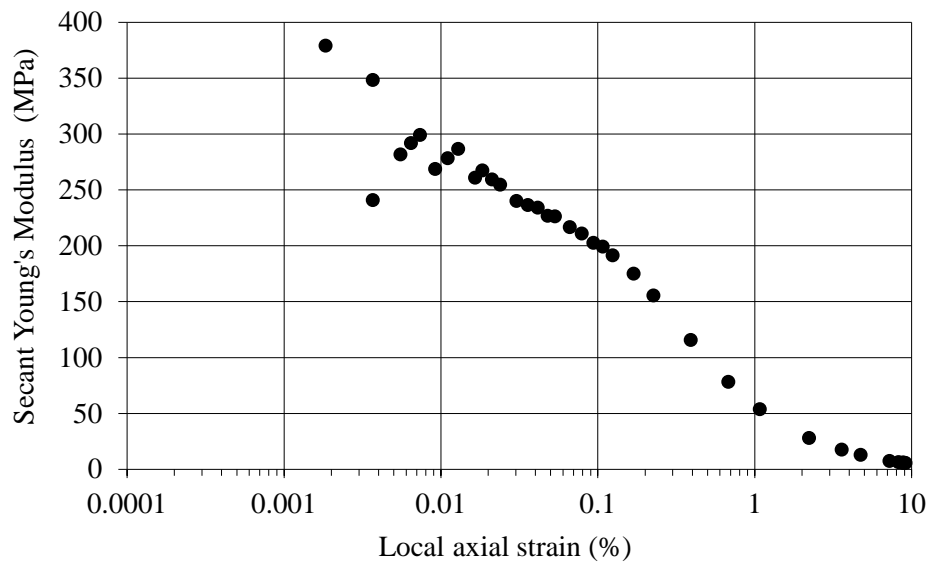


Figure 3.7: Stiffness behaviour of 50% RD Cullinan sand

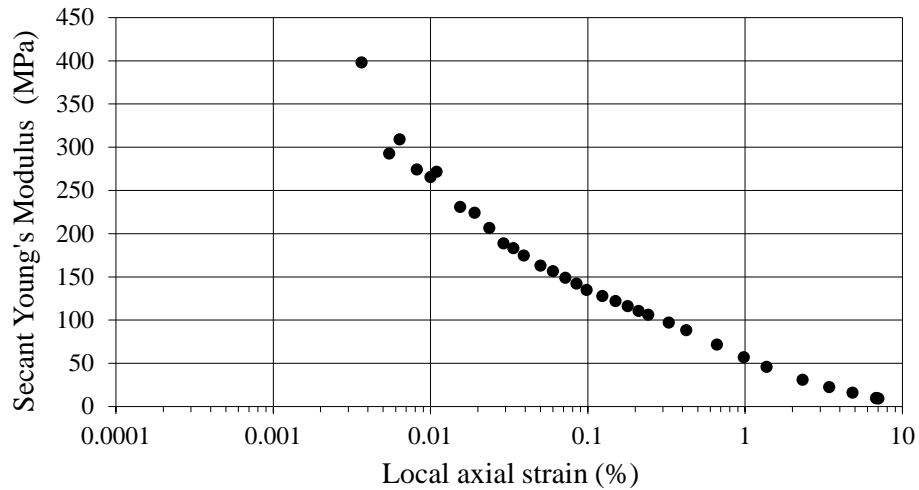


Figure 3.8: Stiffness behaviour of 80% RD Cullinan sand

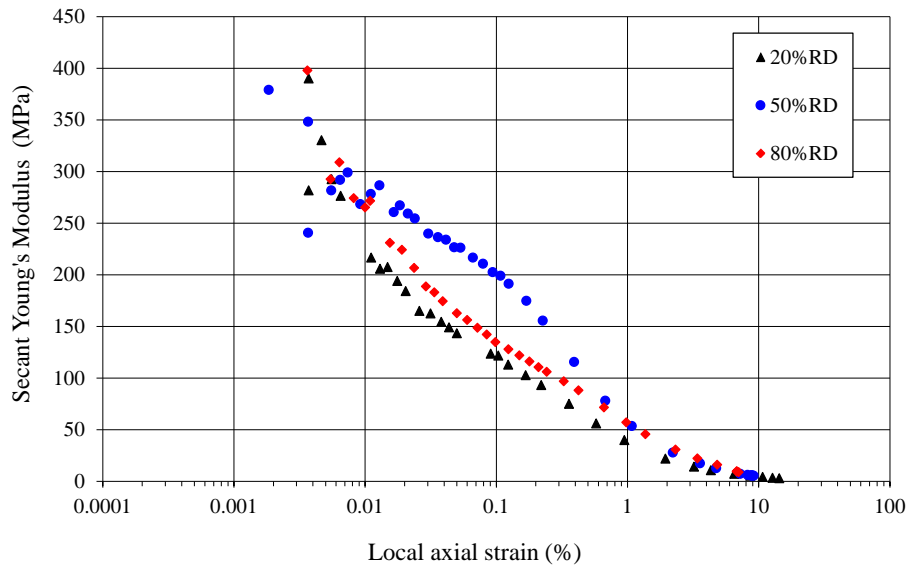


Figure 3.9: Combined stiffness behaviour of Cullinan sand

Critical State Parameters

Atkinson & Bransby (1978) states that the “critical state” of soil is a function of the following parameters:

- The mean stress (p')
- The shear stress or deviator stress (q')
- The specific volume (v)

These parameters can be represented in a three-dimensional space illustrated in Figure 3.10. Equations 3.7 – 3.9 are the formulas with which the mean stress (p'), deviator stress (q') and specific volume (v) can be calculated. It should be noted that the mean and deviator stress equations are with reference to the triaxial tests.

$$p' = \frac{1}{3}(\sigma'_1 + 2\sigma'_3) \quad 3.7$$

$$q' = \sigma'_1 - \sigma'_3 \quad 3.8$$

$$v = 1 + e \quad 3.9$$

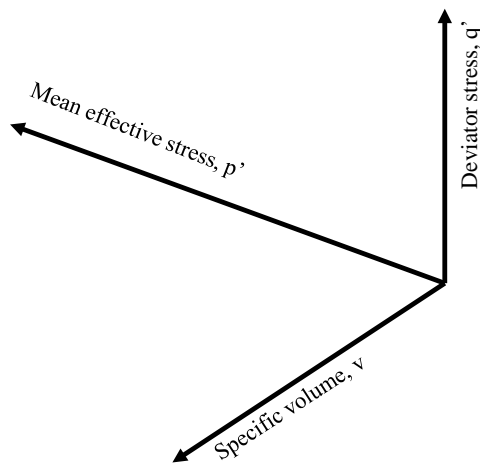


Figure 3.10: Critical state space plot (adapted from (Barnes 2000))

Atkinson (1993) provides a presentation of the critical state lines that can be obtained through triaxial tests. Figure 3.11 depicts an adaptation of the figures presented by Atkinson (1993) for the critical state lines from triaxial tests. Based on the information provided, it can be deduced that the critical state parameters are obtained from the consolidation, as well as the stress path data during shearing.

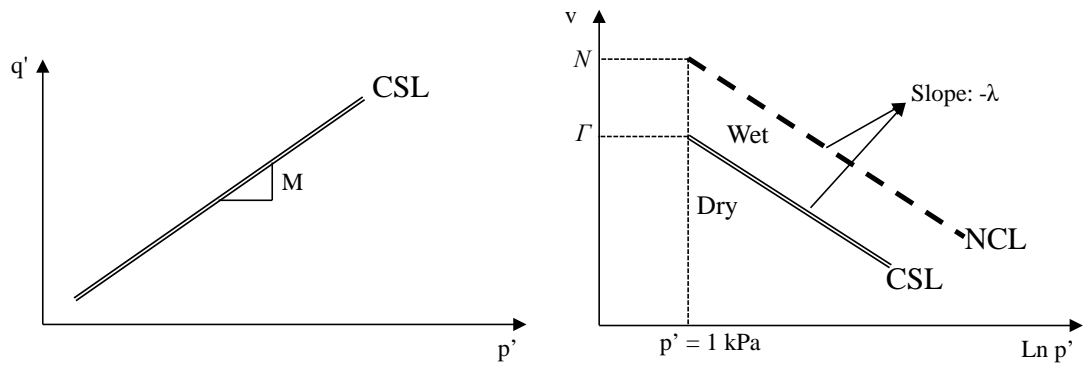


Figure 3.11: Critical state lines from triaxial tests (redrawn from Atkinson (1993))

The stress path results shown previously was plotted in the t' , s' space, but for the critical state behaviour the triaxial results should be plotted in p' , q' space. From Figure 3.11 the critical state parameters to be calculated are M , N , Γ , and λ which are regarded as constants for a particular soil (Atkinson 1993). The critical state line (CSL) is the failure line obtained from the stress paths during shearing and the normal consolidation line (NCL) is obtained from the consolidation data when the sample is consolidated in effective stress increments. It is also important to note that, since isotropic consolidation takes place during triaxial test, the NCL line from triaxial data is also referred to as the isotropic normal consolidation line. This isotropic NCL line should not be confused with the NCL obtained from oedometer tests which will be discussed in Section 3.1.5. It should be noted that “Dry” and “Wet” have been added to the graph which is not shown on the one in Atkinson (1993). These two terms are critical state expressions describing the behaviour of material relative to the critical state. If a soil is said to be on the “wet” side of critical, contractive behaviour will be noticed as the soil approach the CSL. If a soil is on the “dry” side of critical, dilative behaviour is expected as the soil approach the CSL.

The values of N and Γ are the specific volume values when $p' = 1 \text{ kN/m}^2$. The parameter M is the slope of the critical state line in p' , q' space and is also known as the critical state ratio. As depicted, λ is the slope of the CSL as well as the NCL when plotted on a logarithmic plot of p' versus specific volume. It should be noted that the slope of the CSL and NCL is a straight line only when plotted in $\ln p'$, v space and not when plotted in p' , v space. The equations for the CSL in p' , q' space and $\ln p'$, v space, as well as the NCL in $\ln p'$, v space are given in Equations 3.10 – 3.12 respectively.

$$q' = Mp'$$

3.10

$$v = \Gamma - \lambda \ln p' \tag{3.11}$$

$$v = N - \lambda \ln p' \tag{3.12}$$

Since the 500 kPa effective stress sample were conducted in different consolidation stages, the critical state plots from the triaxial results can be constructed using the aforementioned equations. Figure 3.12 to Figure 3.14 show the critical state results calculated from the triaxial data.

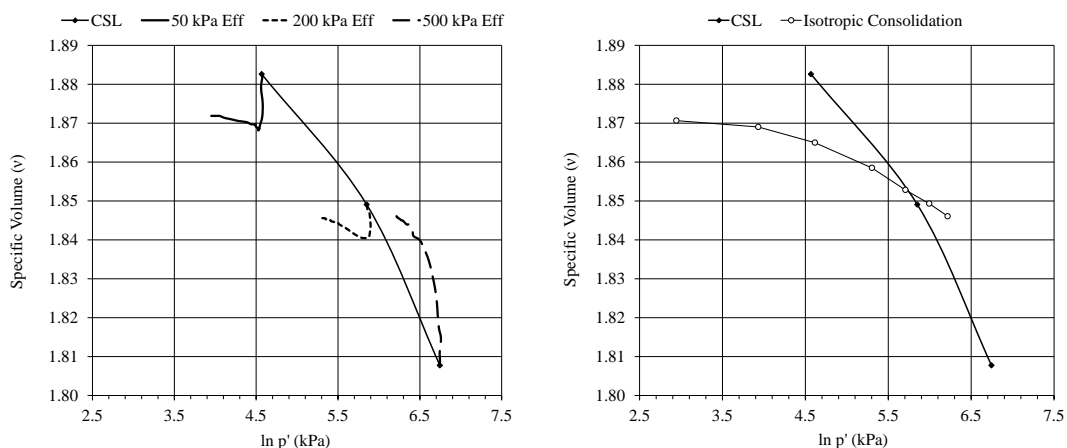


Figure 3.12: Triaxial critical state plot - 20% RD test

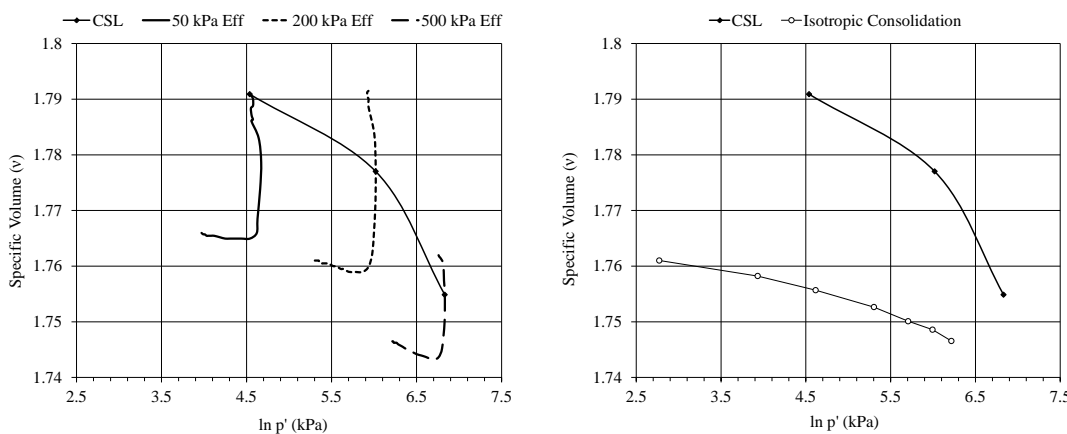


Figure 3.13: Triaxial critical state plot - 50% RD test

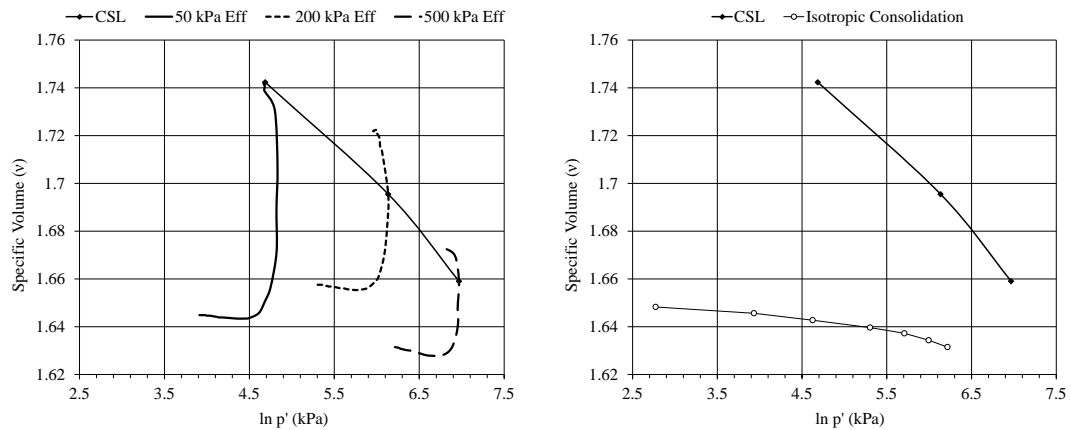


Figure 3.14: Triaxial critical state plot - 80% RD test

From the consolidation results plotted in $\ln p'$, v space, it should be noted that the graphs appear fairly flat. This is due to the behaviour of sand at critical states as discussed in Atkinson & Bransby (1978). It is stated by Atkinson & Bransby (1978) that sand behaves as if it were overconsolidated during modest stresses, regardless of their stress history. And therefore the stress state of the sand has not yet reached the NCL. This is evident from the fact that the state during consolidation is below the CSL, or marginally above the CSL. It is only during large stress (i.e. in excess of 1000 kPa mean effective stress) that sands approach the NCL and behave as if they were normally consolidated. This behaviour is noticed for the Cullinan sand due to the small difference in specific volume during the staged consolidation phase. It should be noticed that the specific volume difference for the 20% RD sample is greater than for the other two tests and that the graph shows a higher curvature. This is also explained in Atkinson & Bransby (1978) where it is stated that if a sample is initially loose and hence has a higher initial specific volume (as with the 20% RD test), the consolidation line will be closer to the NCL for modest stress levels. This is noticeable due to the fact that the 500 kPa sample shows contractive behaviour during the shear phase and is on the “Wet” side of the CSL as discussed previously.

Since none of the tests reached the NCL line due to the low stress levels, the value for λ cannot be calculated from the triaxial data, and neither the values for N and Γ . The only critical state parameter that can be obtained with certainty from the triaxial results is M , the critical state stress ratio. Table 3.9 presents the critical state stress ratio values calculated from the different triaxial tests. Since the friction angle is higher for higher RD, it is expected that the critical state ratio increase as the RD value increase as shown in Table 3.9.

Table 3.9: Critical state ratio, M, values from triaxial tests

Relative density test	Critical state ratio, M
20% RD	1.261
50% RD	1.379
80% RD	1.591

3.1.5 HIGH LOAD OEDOMETER TEST RESULTS

High load oedometer tests were conducted to observe the behaviour of the sand at high stresses. The procedure for the high load oedometer is the same as for the standard oedometer test, except for the loading component. In order to induce high enough stresses (in the MPa range) for the sand to compress sufficiently, a high load is required. This was achieved by modifying a standard oedometer apparatus to fit into a MTS 810 Uniaxial servohydraulic loading frame. For the displacement measurement, three linear variable differential transducers (LVDTs) were fitted onto the apparatus. Figure 3.15 shows the high load oedometer setup in the loading frame, as well the apparatus with the LVDTs during a test.

In order to assess the compression, as well as swelling characteristics of the sand, it was decided to conduct three load-unload cycles. The maximum stress applied to the sample had to be restricted due to limitations of the oedometer apparatus to withstand too high forces. The forces applied for the three load-unload cycles were 5 kN, 46 kN and 113 kN which corresponds to approximately 1 MPa, 10 MPa and 25 MPa respectively. To compensate for creep, once the desired load was reached, the load was kept constant for approximately 20min. As with the previous tests, 20% RD, 50% RD and 80% RD tests were conducted. The vertical displacement during the tests was taken as the average of the measurements from the three LVDTs.

In order to calculate the preconsolidation pressure the void ratio (e) vs. log vertical effective stress (σ'_v) were plotted. An empirical construction procedure proposed by Casagrande was then used to determine the preconsolidation pressure as set out by Craig (2004) as follows:

1. Produce back the lower straight line part of the curve.
2. Determine the point of maximum curvature (P) on the recompression part of the curve.
3. Draw a tangent line through the maximum curvature point and bisect the angle between the tangent line and a horizontal line through P.
4. The vertical line through the intersection between the bisector and the extended straight line gives the approximate value for the σ'_p .

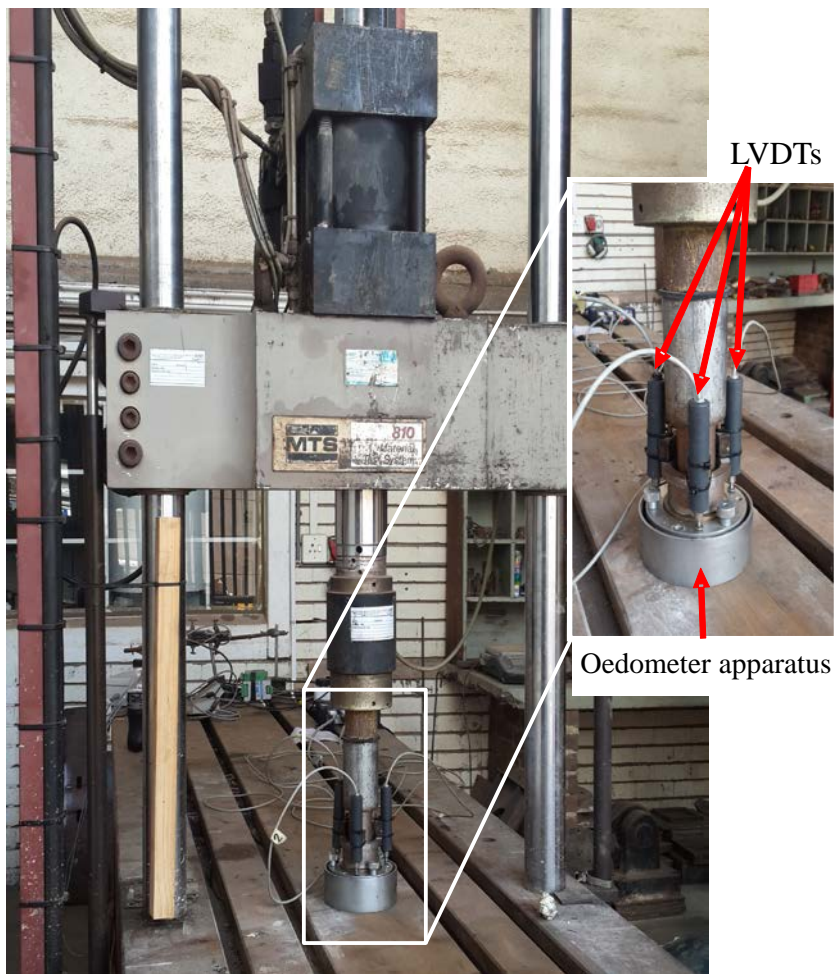


Figure 3.15: High load oedometer test setup

Table 3.10: Initial conditions for high load oedometer tests

Relative density and initial condition		Value
20% RD	Water content (%)	0.1
	Dry density (g/cm^3)	1.450
	Void ratio ($G_s = 2.667$)	0.839
	Relative density (%)	21
50%RD	Water content (%)	0.1
	Dry density (g/cm^3)	1.540
	Void ratio ($G_s = 2.667$)	0.731
	Relative density (%)	53
80% RD	Water content (%)	0.1
	Dry density (g/cm^3)	1.610
	Void ratio ($G_s = 2.667$)	0.656
	Relative density (%)	79

Figure 3.16, Figure 3.17 and Figure 3.18 presents the graphs for the e vs. σ'_v for the 20% RD, 50% RD and 80% RD test respectively. The three load-unload cycles can clearly be seen from the graphs. The near vertical parts of the curves at the end of each loading stage represents the time the load was kept constant to allow for creep. What should be noticed from the graphs is the distinct curve which leads to the straight-line part at high stress, which is a good indication that the sand has compressed sufficiently to calculate the preconsolidation pressure.

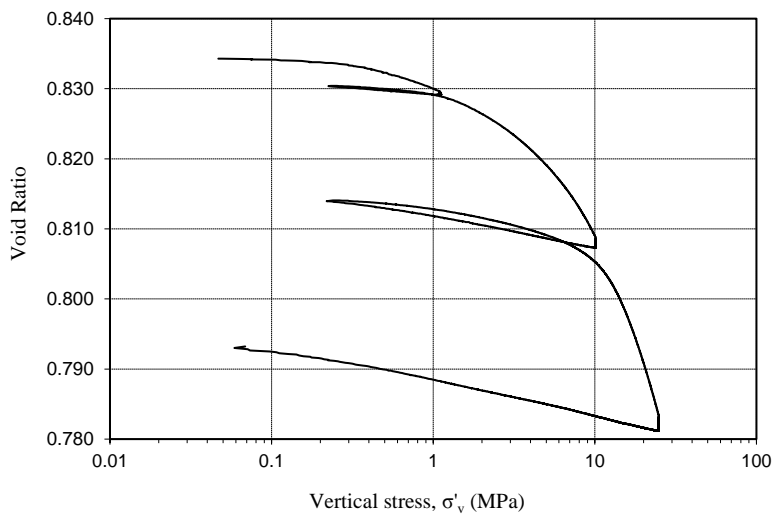


Figure 3.16: e vs. σ'_v curve for 20% RD high load oedometer test

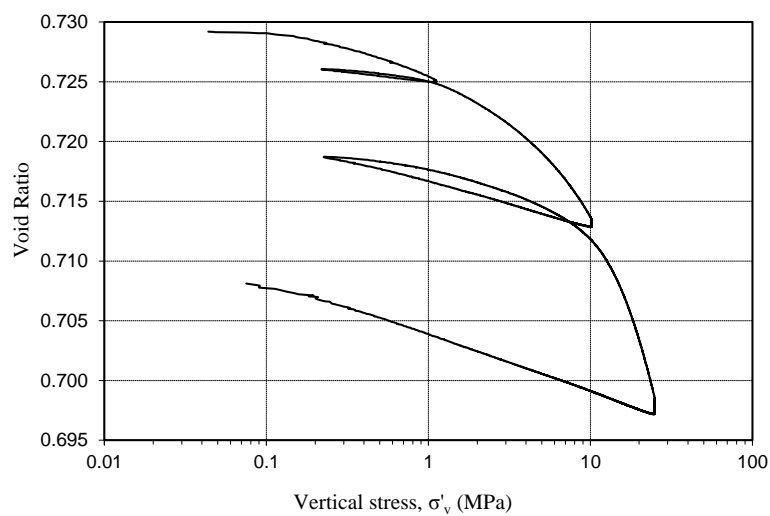


Figure 3.17: e vs. σ'_v curve for 50% RD high load oedometer test

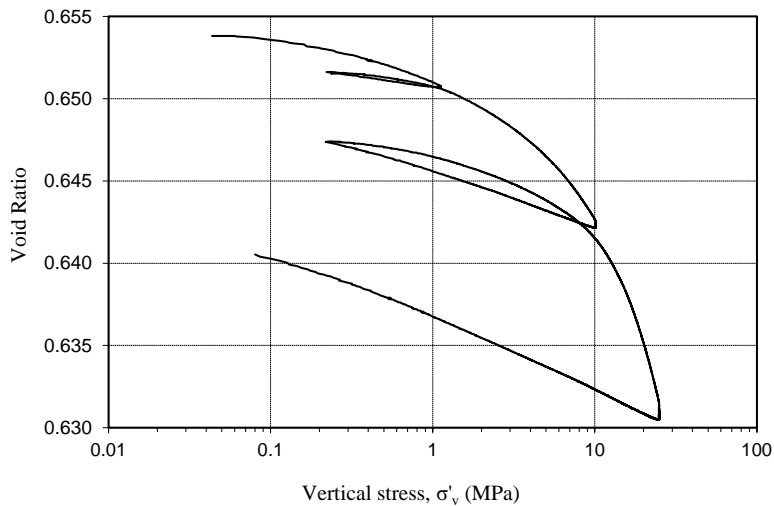


Figure 3.18: e vs. σ'_v curve for 80% RD high load oedometer test

Figure 3.16 to Figure 3.18, together with the procedure described, can be used to calculate the preconsolidation pressure. Figure 3.19 shows the empirical construction to determine the preconsolidation pressure for the 50% RD test. The different lines described in the construction procedure are shown on the graph. The preconsolidation pressures for the 20% RD and 80% RD tests were determined in the same manner as for the 50% RD test. Table 3.11 is the results of the preconsolidation pressures determined for the different densities.

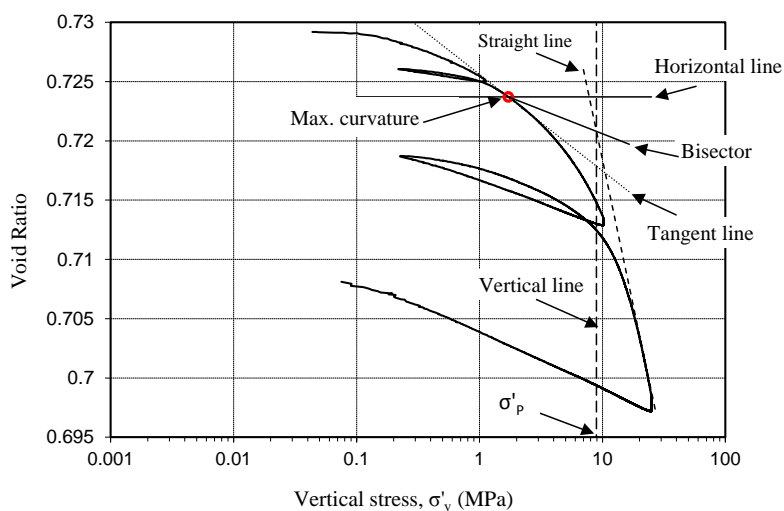


Figure 3.19: Empirical construction to determine σ'_p for 50% RD test

Table 3.11: Preconsolidation pressure values

Relative density test	Preconsolidation pressure, σ'_p (MPa)
20% RD	7.27
50% RD	8.94
80% RD	9.91

The preconsolidation pressure values determined can now be used to determine if the sand will reach the normal consolidation line while accelerated in the centrifuge. As an example, the pressure at 100G for 80% RD sand in a container 0.4m high will be approximately 650kPa. Since the preconsolidation pressure for the 80% RD sand is 9.91MPa, which is one order of magnitude higher than the calculated value, it can be safely assumed that in the centrifuge the sand will not reach the NCL and hence deformation of the sand will be small.

Critical State Parameters

Since the high load oedometer tests were conducted at stresses much higher than the triaxial tests, it is possible to determine the critical state parameters associated with consolidation (i.e. in the v vs. $\ln p'$ space). Equations 2.26 and 2.27 can be used to convert the vertical effective stress to the mean effective stress (p') which is required to determine the critical state parameters.

Figure 3.20 show a typical plot presented by Atkinson & Bransby (1978) which indicates the typical isotropic (triaxial) and one-dimensional (oedometer) plots in v vs. $\ln p'$ space to determine the critical state parameters. From this figure the critical state parameters that can be determined from the oedometer data are λ , N_0 , κ and $v_{\kappa 0}$. The parameters λ and κ are the slopes of the normal consolidation and swell lines respectively, with N_0 and $v_{\kappa 0}$ the specific volume values for the normal consolidation and swell lines respectively at $p' = 1\text{kPa}$. When there are more than one swell line it is usually assumed that the value for κ (the slope of the swell lines) are the same. It should also be noticed that although the one-dimensional line plots lower than the isotropic line, it is a good approximation to assume that the slopes of these line are both equal to λ (Atkinson & Bransby 1978).

Equations 3.13 and 3.14 show the equations for the compression and swell lines in terms of the critical state parameters.

$$v = N_0 - \lambda \ln p' \quad 3.13$$

$$v = v_{\kappa 0} - \kappa \ln p' \quad 3.14$$

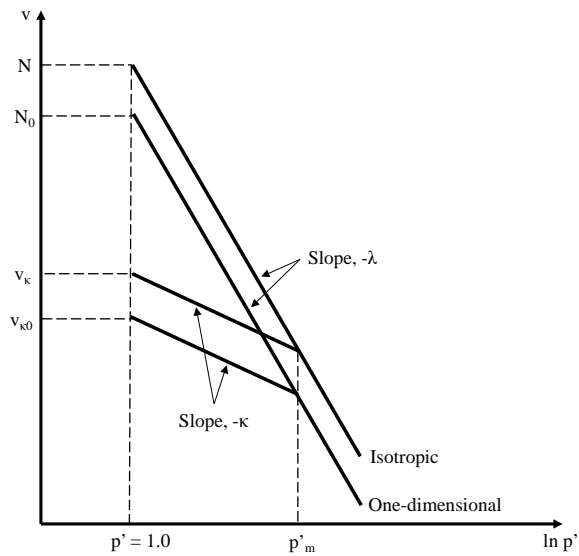


Figure 3.20: Critical state plot from consolidation data

Converting the vertical effective stress to the mean effective stress will give graphs with the same trend as the e vs. $\log \sigma'_v$ graphs, except that the x-axis will be in $\ln p'$ values. Figure 3.21 shows the 50% RD high load oedometer test result in v vs. $\ln p'$ space. Also indicated on the graph is the compression and swell lines used to determine the critical state parameters (i.e. the slopes of the lines). The 20% RD and 80% RD test produced similar graphs together with the compression and swell lines. Table 3.12 shows the results for the critical state parameters calculated from the high load oedometer tests.

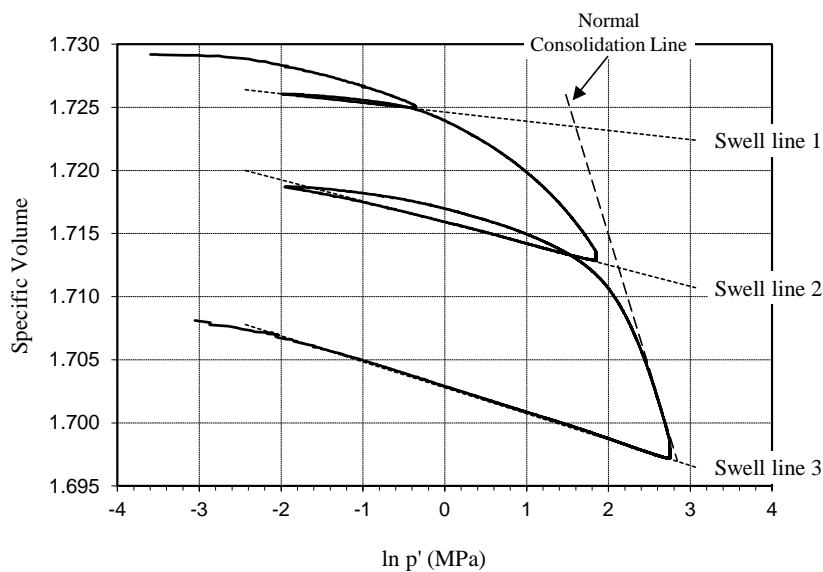
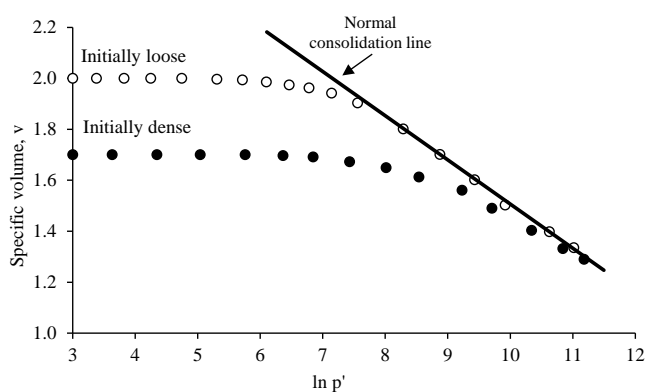


Figure 3.21: v vs. $\ln p'$ for 50% RD high load oedometer test

Table 3.12: Critical state parameters from high load oedometer test results

Critical State Parameter	20% RD	50% RD	80% RD
λ - compression	0.03134	0.02131	0.01681
N_0	1.871	1.758	1.677
κ - swell line 1	0.00078	0.00073	0.00064
κ - swell line 2	0.00204	0.00169	0.00149
κ - swell line 3	0.00224	0.00205	0.00198
$v_{\kappa 0}$ - swell line 1	1.829	1.725	1.650
$v_{\kappa 0}$ - swell line 2	1.811	1.716	1.645
$v_{\kappa 0}$ - swell line 3	1.787	1.703	1.636

A noticeable aspect of Table 3.12 is the low κ values for the swell lines. As Atkinson & Bransby (1978) states, values for κ (with reference to sand) are approximately linear and almost equal to zero which is what the results convey. It was stated previously that the values for κ for all swell lines are the same, but this is not the case from the results. This may be explained by observing the values for λ . It is noticed that the values for λ is different for the different density tests which cannot be true if the samples were compressed to the normal consolidation line (where the values for λ are equal). Consider the results by Atkinson & Bransby (1978) which have been redrawn in Figure 3.22. The graph shows isotropic compression results for Chattahoochee River sand which have been compressed to very high stress (in excess of 40 MPa). Because of the high stresses, it is clear that whether the sand was initially dense or loose it will still reach a common envelope which is the normal consolidation line. It is also stated that similar patterns of behaviour will be noticed for other sands.

**Figure 3.22: Isotropic compression of Chattahoochee River sand (redrawn from Atkinson & Bransby, 1978)**

In order to assess if the tests on the Cullinan sand produced similar results, a graph combining the high load oedometer results was constructed. Figure 3.23 shows the results of the combined plot for the high load oedometer tests. It is clear from the figure that the 20% RD sample compressed more than the 50% RD and 80% RD samples, with the 80% RD the least. Beyond the curvature points, it is clear that the slopes decrease as the density increases, and none of the curves have the same slope and neither do any of the curves converge to a common envelope. It is clear that the stress applied to the sand was still not enough to reach the normal consolidation line. It can thus be assumed that the values for λ calculated is in fact not the slope of the normal consolidation line and that is why the values differ. It is also clear why the values for κ are different for the different tests, which is a combination of the low stresses and the fact that the normal consolidation line was not reached. That is why the values for the 80% RD test is closer to zero since the results are essentially very high up on the swell curve, and vice versa for the lower density tests. From the aforementioned, it is clear that in order to reach the normal consolidation line, much higher stresses would be required.

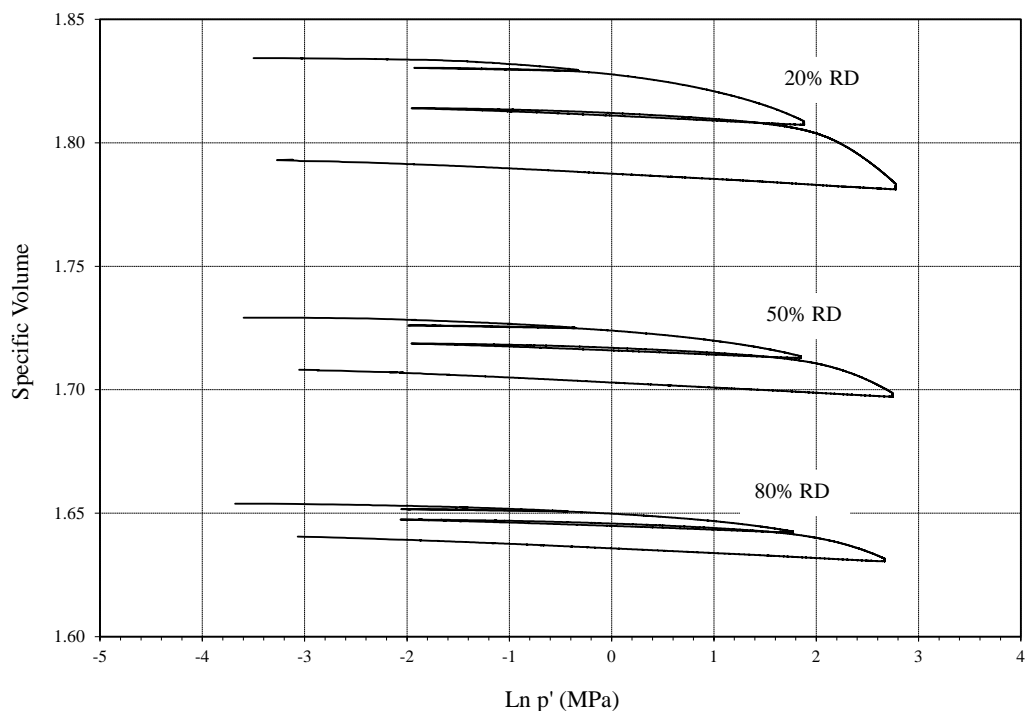


Figure 3.23: Combined high load oedometer results

3.1.6 OEDOMETER WITH BENDER AND EXTENDER ELEMENTS TEST RESULTS

Oedometer tests at 20% RD, 50% RD and 80% RD were conducted. The oedometer apparatus was modified to incorporate bender- and extender elements as discussed previously. The bender and extender elements were used to obtain results for the small-strain shear (G_0) and constrained modulus (M_0) as well as the Poisson's ratio (ν) using Equations 2.20 to 2.22. Since the displacement during the oedometer test is known, the density at each stress increment could be calculated and used to calculate stiffness from the wave velocities.

The oedometer test were conducted in vertical stress increments of 50, 100, 200, 400 and 800 kPa and unloaded in the same stress increments. The shear- (V_s) and compression (V_p) wave velocities from the bender and extender elements respectively were measured at each of the stress increments to obtain the small-strain values at the different stress levels. The first arrival method was used for the calculation of the wave velocities and the piezoelectric transducers used in these tests will be discussed in Section 3.2.4. The hardware components used with the piezoelectric transducers consisted of a Rigol DS1064B four channel digital oscilloscope, a Kistler 5001 charge amplifier and a HP 33120A arbitrary function generator. A single sine pulse was used as the trigger signal with varying input frequencies in order to obtain the best possible signal.

Table 3.13 shows the initial conditions calculated for the different oedometer tests. It should be noted that the initial water content for all the tests are 0 % due to the fact the tests were conducted with dry sand.

Table 3.13: Initial conditions from oedometer tests

Relative density and initial condition		Value
20% RD	Water content (%)	0
	Dry density (g/cm^3)	1.435
	Void ratio ($G_s = 2.667$)	0.858
	Relative density (%)	15
50% RD	Water content (%)	0
	Dry density (g/cm^3)	1.514
	Void ratio ($G_s = 2.667$)	0.760
	Relative density (%)	44
80% RD	Water content (%)	0
	Dry density (g/cm^3)	1.596
	Void ratio ($G_s = 2.667$)	0.670
	Relative density (%)	74

Figure 3.24 to Figure 3.26 presents the results for the oedometer tests indicating the loading and unloading curves in the e vs. $\log \sigma'_v$ space. As with the triaxial consolidation results, the stresses for the oedometer tests may be described as modest regarding sand behaviour and from the previous section it is clear that during the loading phase the NCL was not reached. The coefficient of volume compressibility (m_v) was calculated from the results, which is defined as the volume change per unit volume per unit increase in effective stress. In the case of an oedometer test the volume change is defined by the change in void ratio and for a specific effective stress increment m_v is calculated using Equation 3.15 (Barnes 2000).

$$m_v = \frac{\Delta e}{1 + e_i} \frac{1}{\Delta \sigma} \quad 3.15$$

where: $\Delta \sigma$ = pressure increment

Δe = change in void ratio during pressure increment

e_i = initial void ratio at start of pressure increment

Based on the values from the e vs. $\log \sigma'_v$ plots, Table 3.14 shows the results for the calculated compressibility characteristics.

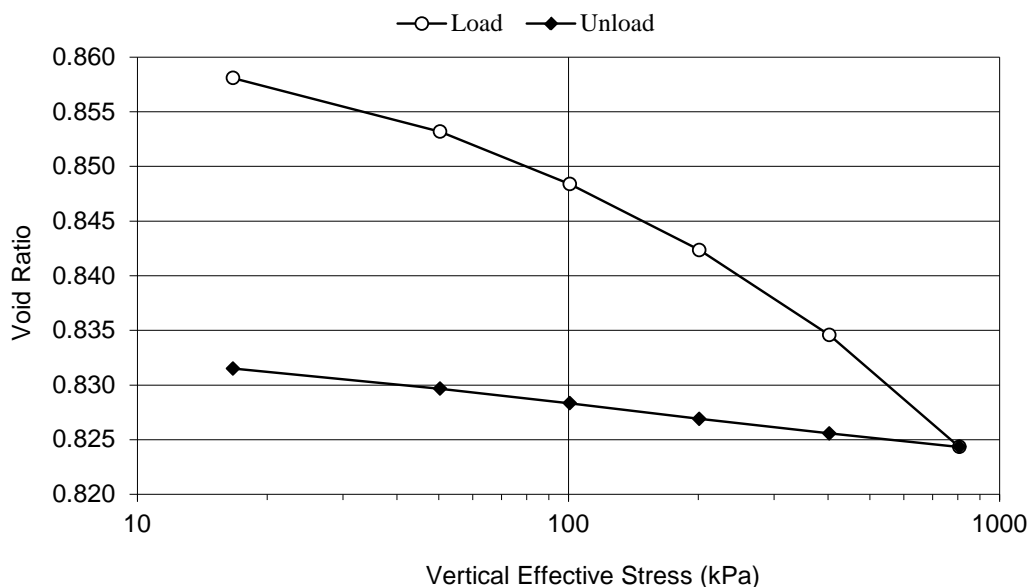


Figure 3.24: e vs. $\log \sigma'_v$ for 20% RD oedometer test

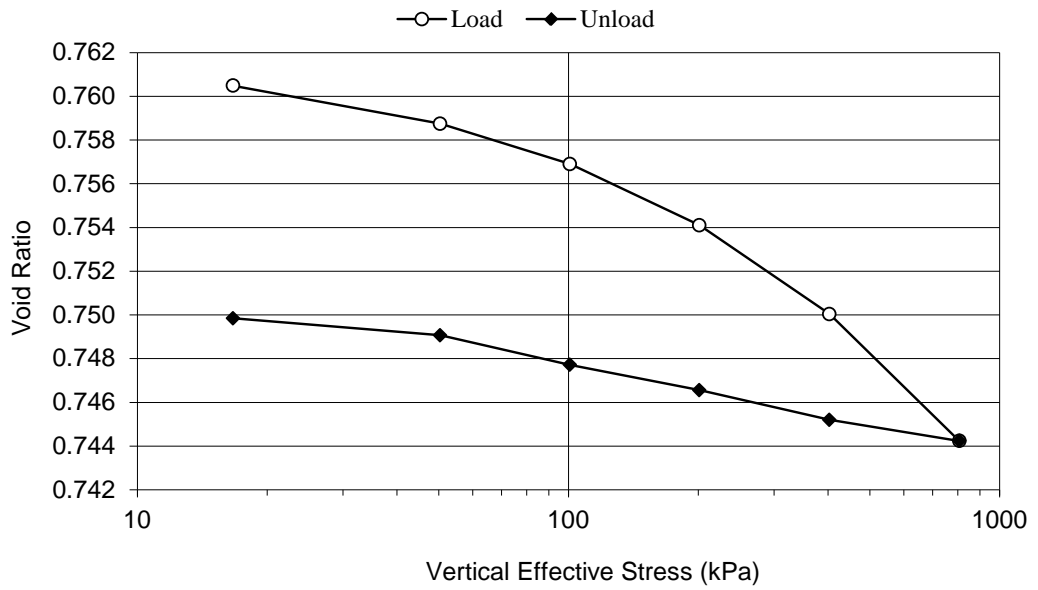


Figure 3.25: e vs. $\log \sigma'_v$ for 50% RD oedometer test

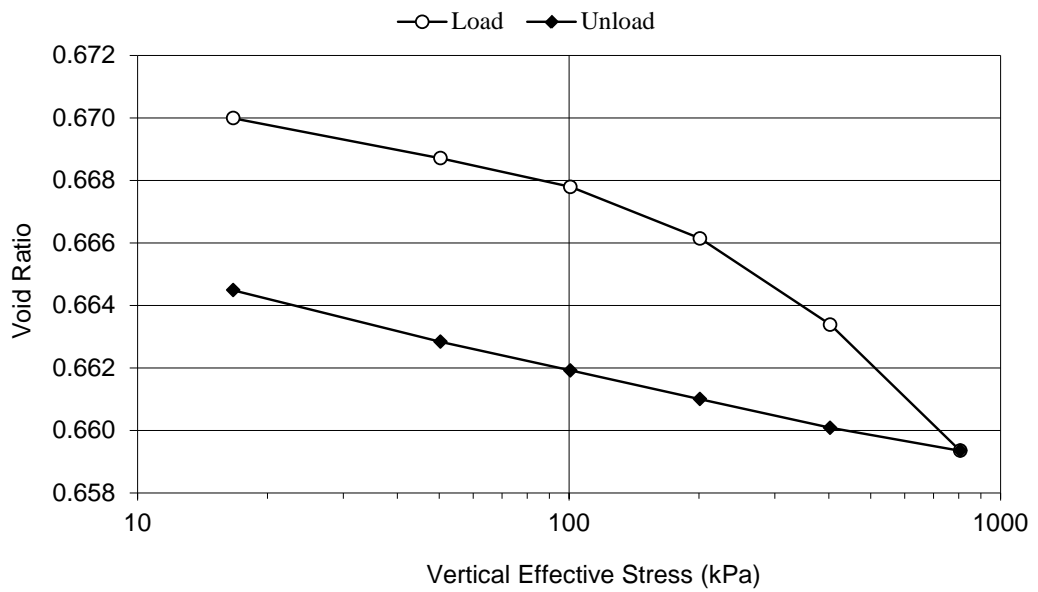


Figure 3.26: e vs. $\log \sigma'_v$ for 80% RD oedometer test

Table 3.14: Compressibility characteristics from oedometer results

Relative density test	Pressure increment (kPa)	$\Delta\sigma$ (kPa)	Δe	Δ Vertical Strain (%)	m_v (m^2/MN)	Constrained Modulus, D' (1/mv)
20% RD	17 - 50	33	0.0049	0.264	0.078	12.8
	50 - 101	51	0.0048	0.259	0.051	19.4
	101 - 201	100	0.0060	0.325	0.032	30.8
	201 - 403	202	0.0078	0.418	0.021	47.8
	403 - 807	404	0.0102	0.550	0.014	72.4
50% RD	17 - 50	33	0.0017	0.099	0.029	34.1
	50 - 101	51	0.0018	0.104	0.021	48.2
	101 - 201	100	0.0028	0.159	0.016	63.0
	201 - 403	202	0.0041	0.231	0.011	87.2
	403 - 807	404	0.0058	0.330	0.008	121.8
80% RD	17 - 50	33	0.0013	0.077	0.023	43.9
	50 - 101	51	0.0009	0.055	0.011	91.7
	101 - 201	100	0.0017	0.099	0.010	101.6
	201 - 403	202	0.0028	0.165	0.008	122.2
	403 - 807	404	0.0040	0.242	0.006	166.4

Using the first arrival method to calculate the time for either a shear- or compression wave to travel, the known distance apart and the density during each load increment, the small-strain shear- (G_0) and constrained (M_0) moduli can be determined. Figure 3.27 and Figure 3.28 are examples of results from the oscilloscope for the bender and extender element tests for the 400 kPa stress increment during the loading cycle for 20% RD test. Indicated on the figures are the first arrivals as well the time difference. The time differences for the other pressure increments were obtained in the same manner. Table 3.15 is a summary of the results from the bender- and extender elements tests during the different pressure increments indicating the various small-strain moduli values.

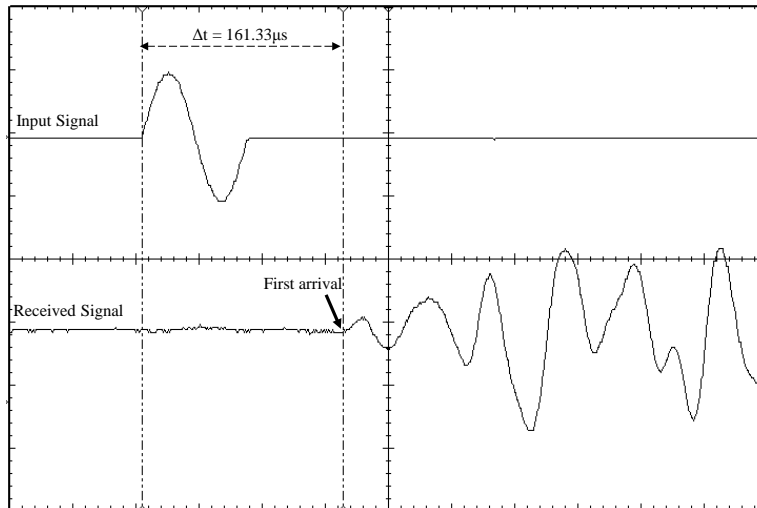


Figure 3.27: Example of bender element results from oedometer test

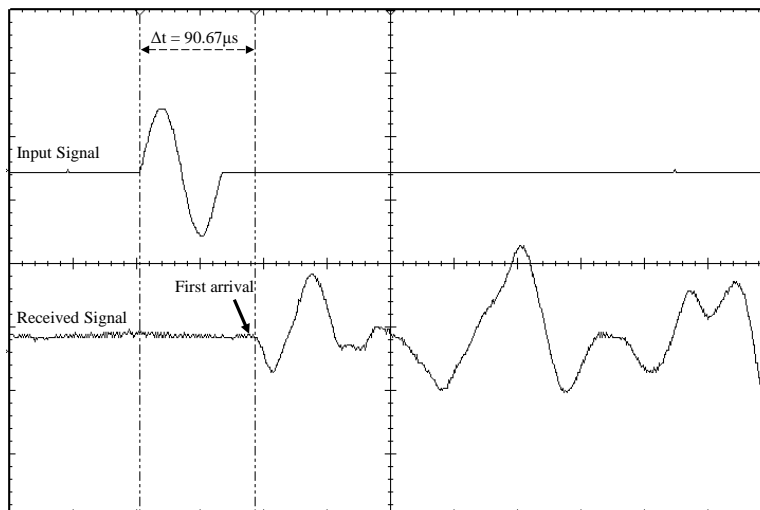


Figure 3.28: Example of extender element results from oedometer test

Various graphs can be constructed from the results given in Table 3.15 for a more visual interpretation. Asslan (2008) indicates that small-strain stiffness values of clean sands are mainly affected by three parameters namely: the strain, confining pressure and void ratio. Figure 3.29 and Figure 3.30 presents the shear- and constrained modulus values versus the vertical strain plotted on a logarithmic scale for the different density tests. Since the oedometer test is a one-dimensional test, it is expected that the stiffness will increase with increasing strain levels due to the increase in vertical effective stress. When the samples are unloaded the moduli values decrease, but not along the same line as the loading curves, but approximately linear. The difference in stiffness values are a good indication of the effect

that the void ratio have on the small-strain values as indicated by Asslan (2008) as well as concluded by Bødker (1996).

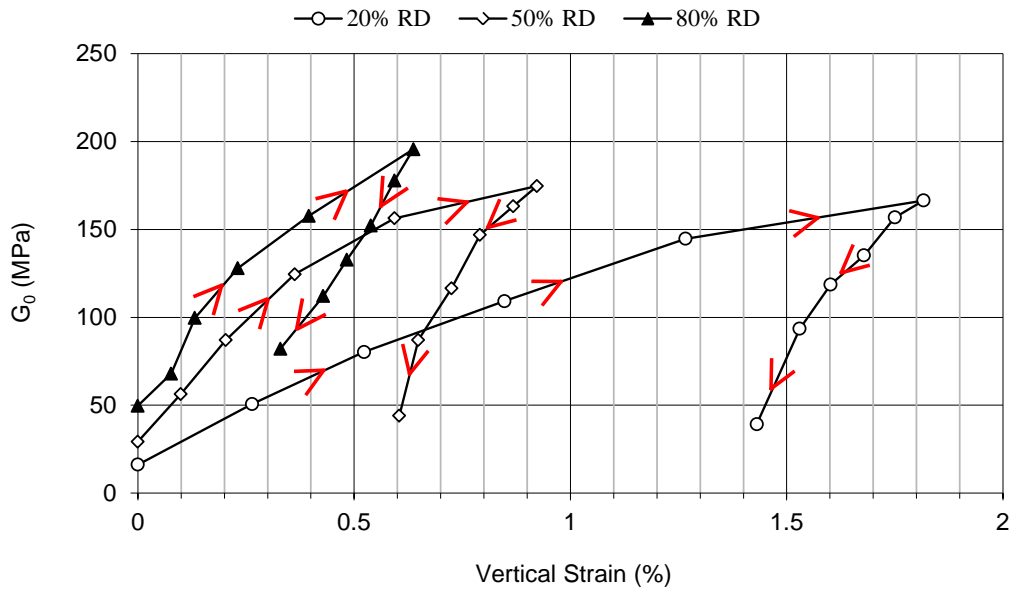


Figure 3.29: G_0 vs. Vertical strain from standard oedometer results

Table 3.15: Small-strain results for standard oedometer tests

Relative density test	Vertical Stress (kPa)	Vertical Strain (%)	Void Ratio	Bender time diff. (μ s)	Extender time diff. (μ s)	Density (kg/m^3)	V_s (m/s)	V_p (m/s)	G_0 (MPa)	M_0 (MPa)	Poisson's ratio	E_{secant} (MPa)
20% RD	17	0.00	0.858	490.00	218.67	1434.9	106.2	234.4	16.2	78.8	0.37	-
	50	0.26	0.853	276.00	138.67	1438.7	187.7	367.9	50.7	194.7	0.32	12.8
	101	0.52	0.848	218.67	117.33	1442.4	235.9	432.8	80.2	270.1	0.29	16.1
	201	0.85	0.842	186.67	102.67	1447.1	274.7	491.7	109.2	349.8	0.27	21.8
	403	1.27	0.835	161.33	90.67	1453.3	315.5	552.6	144.7	443.7	0.26	30.5
	807	1.82	0.824	149.33	76.67	1461.4	337.5	646.9	166.5	611.6	0.31	43.5
	403	1.75	0.826	154.00	80.00	1460.4	327.7	620.8	156.8	562.7	0.31	22.1
	201	1.68	0.827	166.00	86.67	1459.4	304.4	573.7	135.2	480.4	0.30	11.0
	101	1.60	0.828	177.33	100.00	1458.2	285.3	498.0	118.7	361.6	0.26	5.3
	50	1.53	0.830	200.00	116.00	1457.2	253.3	429.8	93.5	269.2	0.23	2.2
17	1.43	0.832	309.33	202.67	1455.7	164.1	246.5	39.2	88.4	0.10	-	
50% RD	17	0.00	0.760	376.00	188.00	1514.4	138.9	273.5	29.2	113.3	0.33	-
	50	0.10	0.759	270.67	130.67	1515.9	192.6	392.9	56.2	234.0	0.34	34.1
	101	0.20	0.757	217.33	112.00	1517.5	239.5	457.5	87.0	317.6	0.31	41.4
	201	0.36	0.754	181.33	96.00	1519.9	286.2	532.2	124.5	430.6	0.30	51.0
	403	0.59	0.750	161.33	86.67	1523.5	320.4	587.1	156.4	525.1	0.29	65.2
	807	0.92	0.744	152.00	77.33	1528.5	338.1	654.1	174.7	654.1	0.32	85.6
	403	0.87	0.745	157.33	84.67	1527.7	326.9	598.0	163.3	546.4	0.29	44.5
	201	0.79	0.747	166.00	92.00	1526.5	310.3	551.1	147.0	463.7	0.27	23.4
	101	0.73	0.748	186.67	104.00	1525.5	276.2	488.1	116.4	363.5	0.26	11.6
	50	0.65	0.749	216.00	120.00	1524.3	239.1	423.6	87.1	273.5	0.27	5.2
17	0.60	0.750	304.00	178.67	1523.6	170.0	284.7	44.0	123.5	0.22	-	
80% RD	17	0.00	0.670	296.00	157.33	1596.5	176.4	326.9	49.7	170.6	0.29	-
	50	0.08	0.669	233.33	116.67	1597.7	223.5	440.2	79.8	309.6	0.33	43.9
	101	0.13	0.668	208.67	107.33	1598.6	249.7	478.0	99.7	365.3	0.31	63.8
	201	0.23	0.666	184.00	100.00	1600.2	282.7	512.2	127.9	419.7	0.28	80.1
	403	0.40	0.663	165.33	89.33	1602.8	313.7	571.6	157.7	523.8	0.28	97.7
	807	0.64	0.659	148.00	76.00	1606.7	349.0	669.0	195.6	719.1	0.31	124.0
	403	0.59	0.660	155.33	80.00	1606.0	332.7	636.1	177.8	649.7	0.31	65.2
	201	0.54	0.661	168.00	84.00	1605.1	307.9	606.4	152.2	590.2	0.33	34.3
	101	0.48	0.662	180.00	92.00	1604.2	287.7	554.2	132.8	492.7	0.32	17.4
	50	0.43	0.663	196.00	100.00	1603.3	264.5	510.4	112.1	417.6	0.32	7.9
17	0.33	0.664	229.33	146.67	1601.8	226.4	348.6	82.1	194.6	0.14	-	

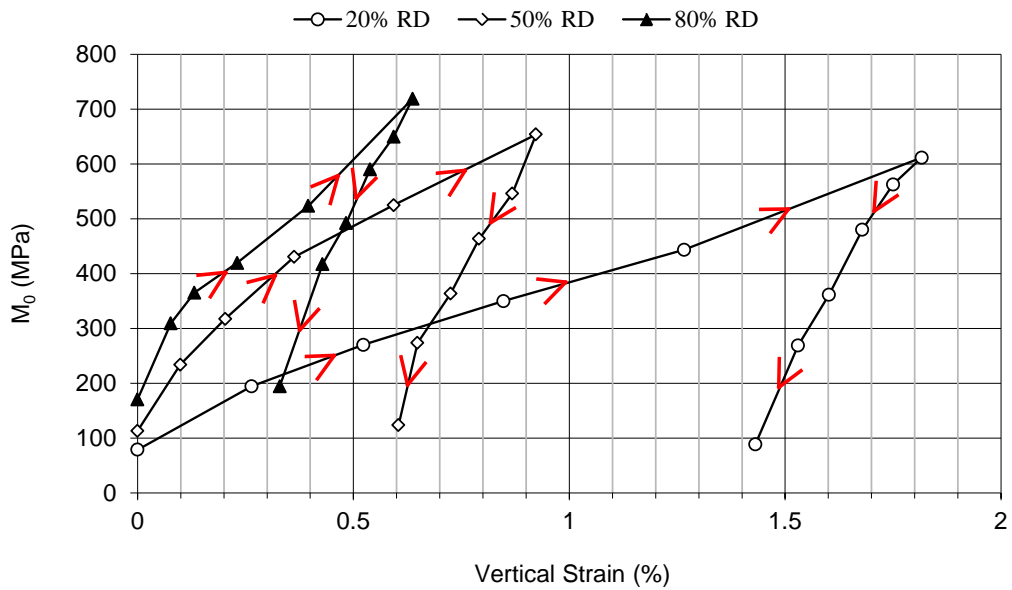


Figure 3.30: M_0 vs. Vertical strain from standard oedometer results

Figure 3.31 and Figure 3.32 show the graphs of the small-strain shear- and constrained modulus values against the vertical effective stress. It should be observed that an almost linear relationship exist for stress levels higher than 200 kPa with the small-strain stiffness values increasing as the vertical effective stress increases. It is also interesting to observe that at higher stress levels the small-strain stiffness values tend to converge..

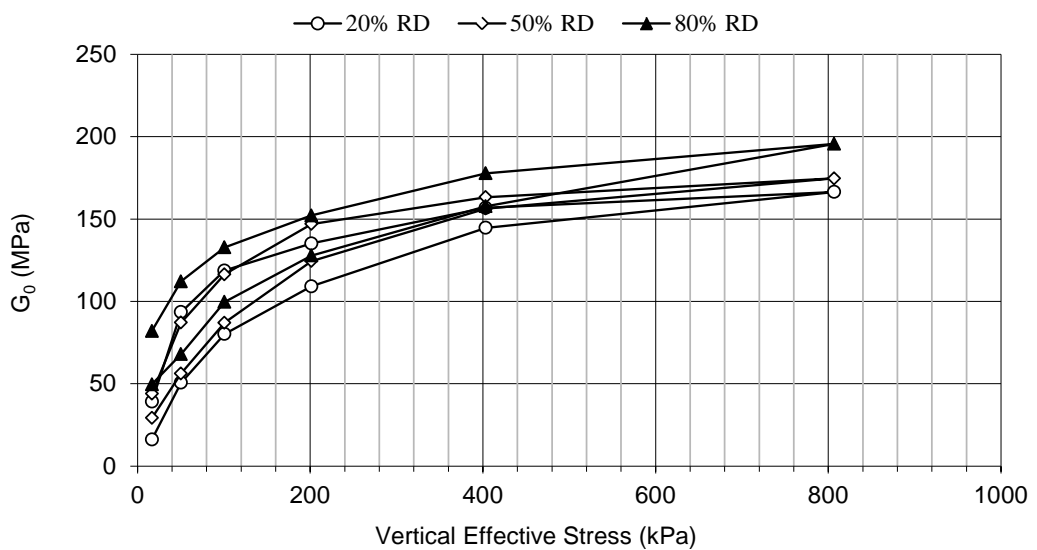


Figure 3.31: G_0 vs. Vertical effective stress from standard oedometer results

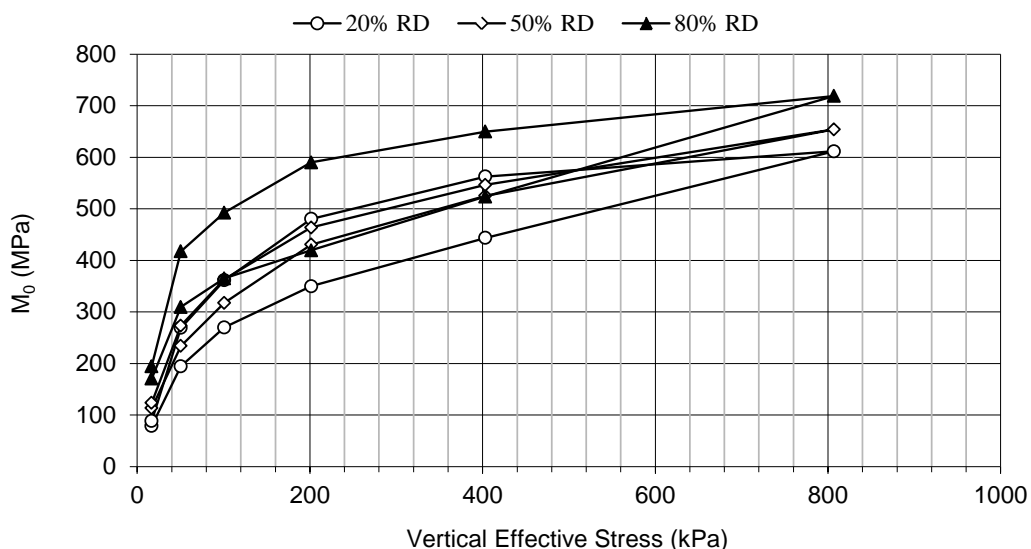


Figure 3.32: M_0 vs. Vertical effective stress from standard oedometer results

In order to account for the parameters influencing the small-strain values as well as to compare the small-strain behaviour of the Cullinan sand to other sands, it will be useful to obtain an empirical equation to estimate G_0 . This will also be useful in cases where G_0 cannot be measured. A number of empirical equations have been introduced for sands and based upon Salgado et al. (2000) and a survey by Yongqing (2011) the most commonly adopted equation for estimating the small-strain shear modulus is presented by Equation 3.16.

$$G_0 = C_g F(e) P_a^{1-n_g} p'^{n_g} \quad 3.16$$

where: G_0 = small-strain shear modulus

C_g, n_g = intrinsic material constants

$F(e)$ = void ratio function

p' = mean affective stress

P_a = reference stress (in the same units as p')

Numerous void ratio functions exist as given by Yongqing (2011), but the void ratio function adopted in this project is presented in an equation for sands similar to Equation 3.16 by Clayton (2011) where $F(e) = (1+e)^{-3}$. This equation is also used by Vardanega & Bolton (2013) where the authors state that this void ratio function is based on a physical parameter

which is equivalent to the dry density (i.e. the specific volume). The reference pressure typically used is atmospheric pressure equal to 101.3 kPa and will also be used in this report. Using Equations 2.26 and 2.27 the value for p' can be calculated with the vertical effective stress values from the oedometer tests.

The intrinsic material parameters C_g and n_g are dependent on the soil and can be obtained by means of a regression analysis. With the data obtained from the oedometer test as well as the triaxial data, the values for C_g and n_g can be calculated for the different density sands. This is achieved by rewriting Equation 3.11 to produce a power function where C_g and n_g are a constant and exponent respectively. It should be noted that the regression analysis was only conducted for the loading cycle.

Figure 3.33 shows the graphs for the regression analysis to obtain C_g and n_g . In the figure the axis titles indicates the “x” and “y” variables after Equation 3.16 was rewritten as a power function. After a regression analysis was conducted the values for C_g and n_g were obtained for the different density tests. The results for the regression analysis are given in Table 3.16. The coefficient of determination (R^2) indicates a good fit with the data.

By replacing G_0 with M_0 in Equation 3.16, the empirical relationship for the small-strain constrained modulus can be obtained as shown in Equation 3.17. Using the same procedure described to determine the regression parameters for G_0 , the regression parameters for the M_0 empirical equation can be determined.

$$M_0 = C_g F(e) P_a^{1-n_g} p^{n_g} \quad 3.17$$

Figure 3.34 depicts the graph for the regression analysis and Table 3.17 shows the results from the regression analysis. As with the G_0 parameter regression analysis, the coefficient of determination (R^2) indicates a good fit with the data with the high value.

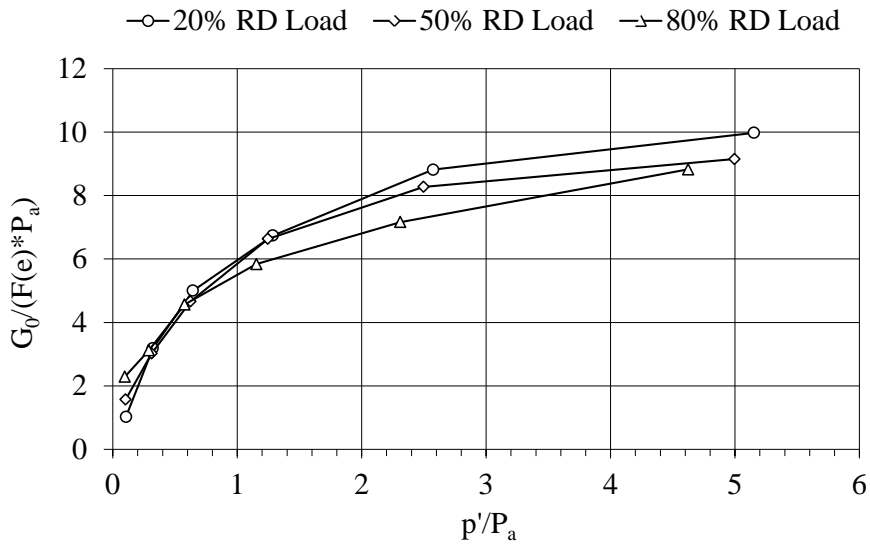


Figure 3.33: Regression data plot for G_0 empirical equation

Table 3.16: Regression parameters C_g and n_g for G_0 calculation

Test	C_g	n_g	R^2
20% RD	5.070	0.574	0.92
50% RD	5.173	0.468	0.96
80% RD	5.277	0.360	0.99

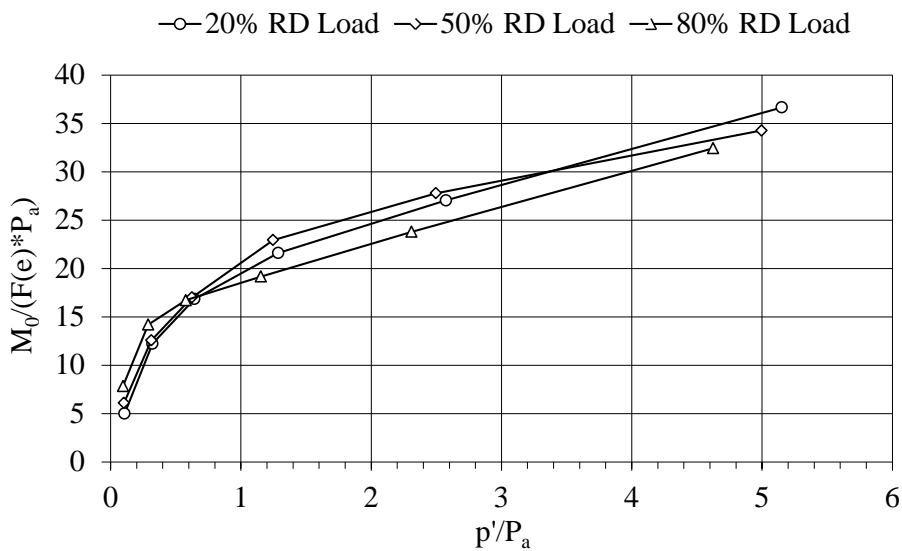
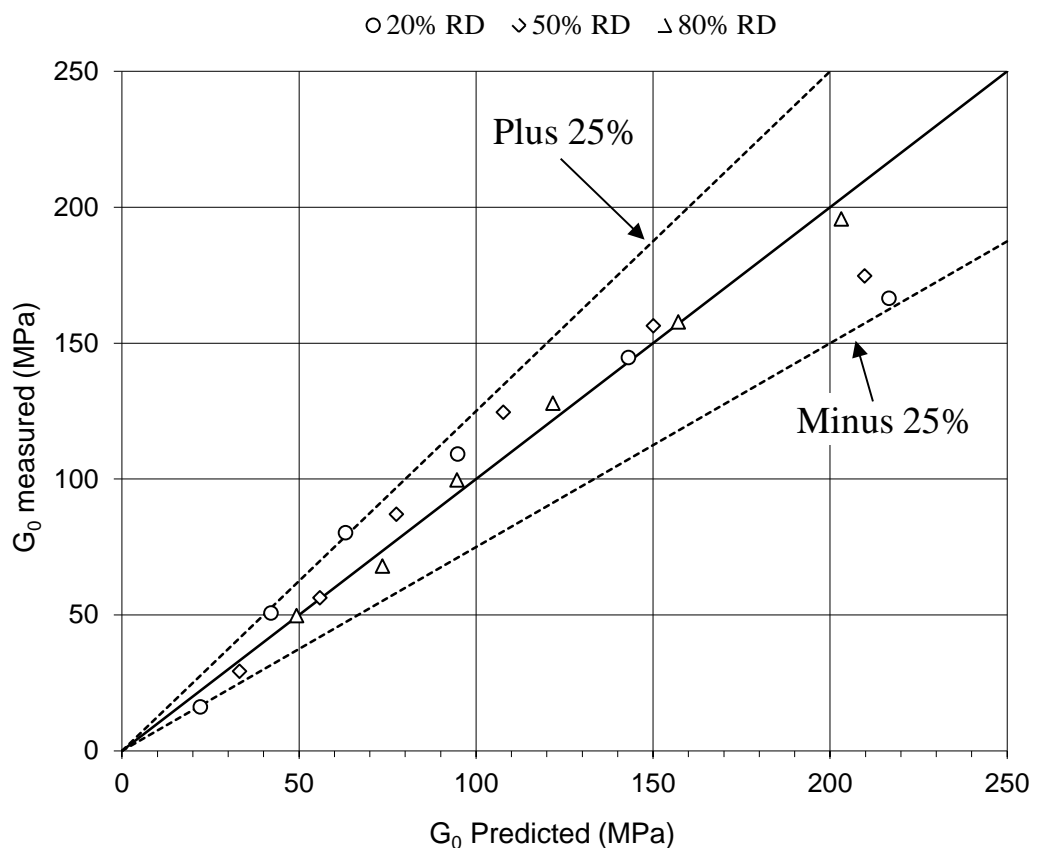


Figure 3.34: Regression data plot for M_0 empirical equation

Table 3.17: Regression parameters C_g and n_g for M_0 calculation

Test	C_g	n_g	R^2
20% RD	18.126	0.487	0.96
50% RD	19.015	0.436	0.97
80% RD	19.046	0.338	0.97

The coefficient of determination may not always be sufficient to indicate a good data correlation. Using the regression parameters, Figure 3.35 and Figure 3.36 shows the predicted G_0 and M_0 values compared with the measured G_0 and M_0 values respectively. Indicated on the graphs are lines showing how the data falls within a certain margin of error. The G_0 values falls within a $\pm 25\%$ margin and M_0 within a $\pm 15\%$ margin. It should be noticed that at higher G_0 and M_0 values are less accurate than at lower predicted values, but the data appears to fit reasonably well.

**Figure 3.35: Measure vs. Predicted G_0**

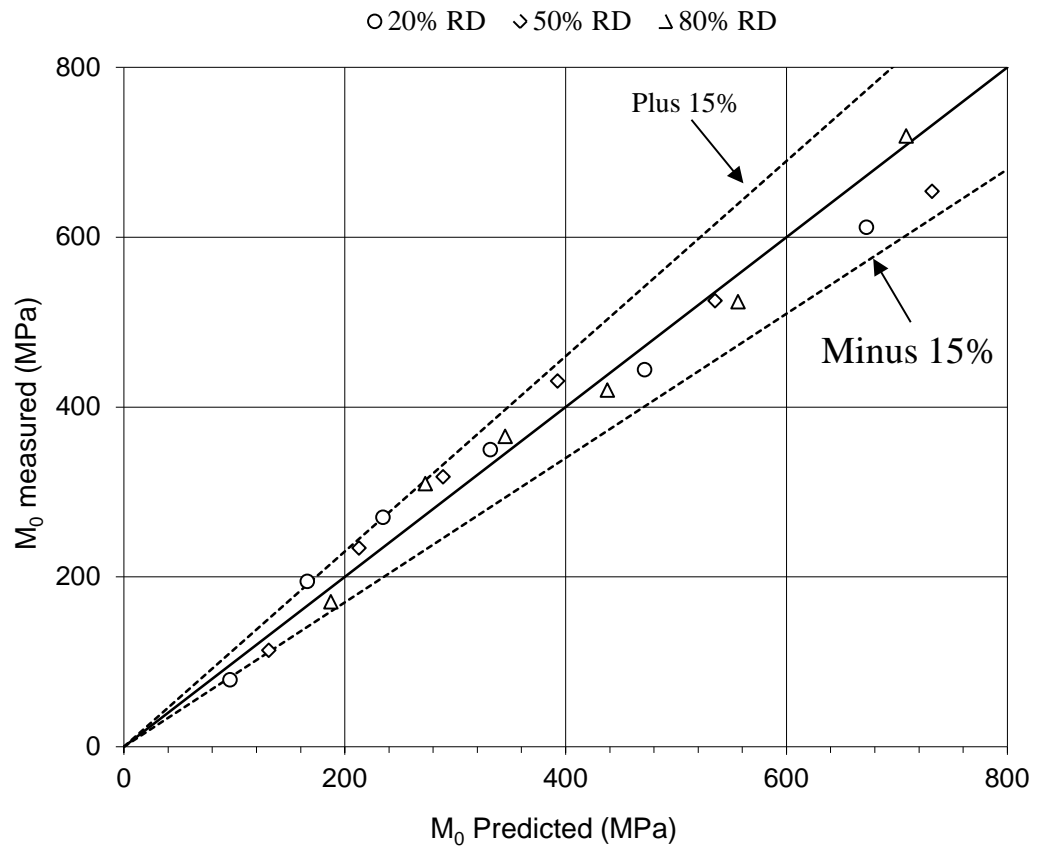


Figure 3.36: Measure vs. Predicted M_0

3.1.7 SCANNING ELECTRON MICROSCOPE PHOTOS

Scanning electron microscope (SEM) images were taken of the Cullinan sand to examine its characteristics. Figure 3.37 shows the image of the SEM photo taken of the sand particles. The shape of the particles can be characterised as **angular to sub-rounded**. Figure 3.38 shows a close up of one the sand particles from which the roughness can be assessed. It is clear that the particle surface is very rough and uneven based on the image.

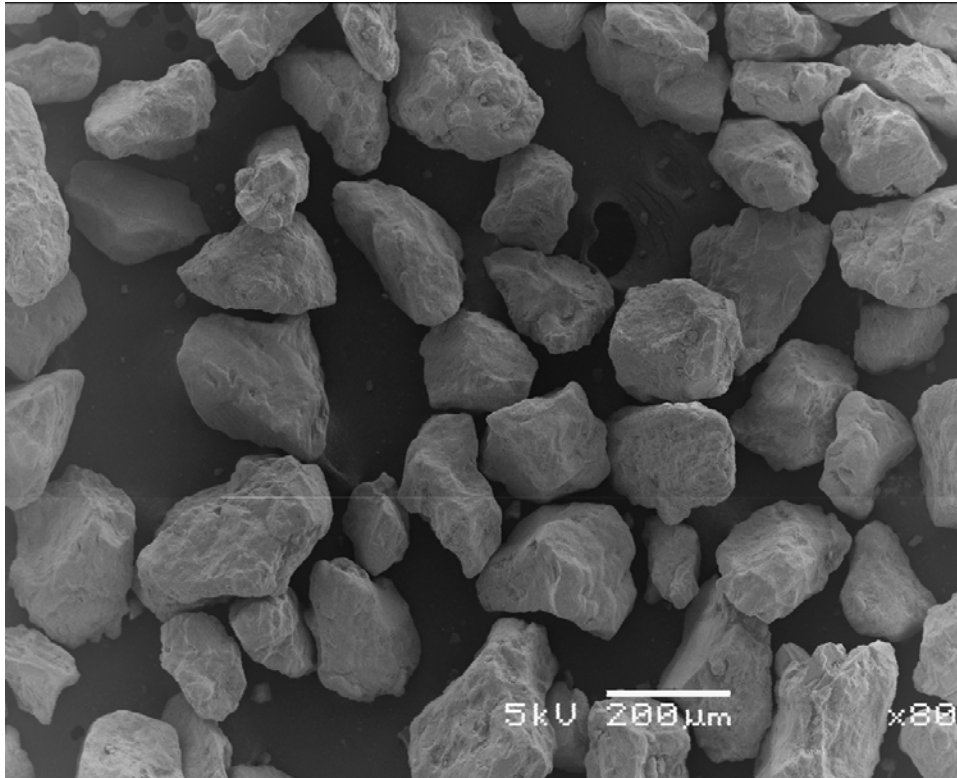


Figure 3.37: SEM image of Cullinan sand

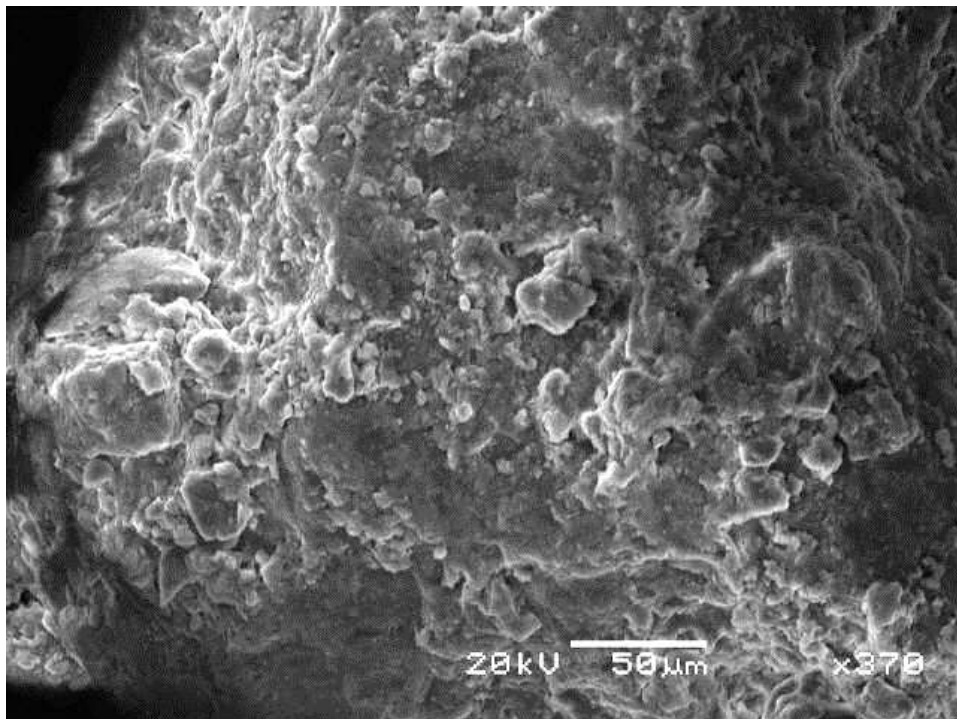


Figure 3.38: SEM image of surface of sand particle

3.1.8 SUMMARY

The sand, named **Cullinan sand**, used for the centrifuge tests have been characterised through various test methods. Relative densities 20% RD, 50% RD and 80% RD were tested corresponding to loose, medium dense and dense sand respectively. These characteristics and values were used for the experimental design as well as to understand the soil behaviour during centrifuge testing. Table 3.18 provides a summary of the properties for the Cullinan sand. The properties presented are the properties required for most design problems and provide a good description of the sand.

Table 3.18: Summary of Cullinan sand properties

Parameter	20% RD	50% RD	80% RD
D10 (mm)	0.077		
D30 (mm)	0.108		
D50 (mm)	0.135		
D60 (mm)	0.150		
Uniformity coefficient, C_U	1.95		
Max. Dry Density (kg/m^3)	1669		
Min. Dry Density (kg/m^3)	1392		
e_{\max}	0.92		
e_{\min}	0.60		
Specific gravity, G_s	2.67		
Particle shape ^a	Angular to sub-rounded		
USCS ^b Classification	SP		
Angle of friction, ϕ' ($^\circ$)	32	34	39
Cohesion, c' (kPa)	0	0	0
Dry density (kg/m^3)	1447	1531	1614
e_{RD}^c	0.84	0.74	0.65
Permeability (m/s)	1.1×10^{-5}	1.9×10^{-5}	1.8×10^{-5}
Preconsolidation pressure, σ'_p (MPa)	7.27	8.94	9.91

^aBased on visual interpretation of the SEM photos

^bUnified Soil Classification System

^cVoid ratio at the relative density value

3.2 CENTRIFUGE MODEL DESIGN

Taking into consideration the information discussed in Sections 2 and 3.1 the experimental design could be done in order to test the hypothesis. Centrifuge testing was chosen as the

experimental method. The geomaterial used for the experiment was Cullinan Sand and was discussed in the previous section. In this section the design and setup of the different elements that made up the experiment are conveyed. Firstly the different elements will be discussed where after the complete design will be summarised.

3.2.1 CENTRIFUGE

The centrifuge used for this study was the 150g-ton geotechnical centrifuge of the University of Pretoria. Details of various aspects of the centrifuge facility were given by Jacobsz et al. (2014) with a photo of the centrifuge presented in Figure 3.39. A summary of the general specifications with regard to this project is given in Table 3.19. It should be mentioned that the centrifuge is automatically balanced by an adjustable counterweight; hence there is no need to calculate a counterweight mass beforehand. The only input parameters required are the model mass, the radius where the maximum g-level should be and the centre of gravity of the model measured from platform level.

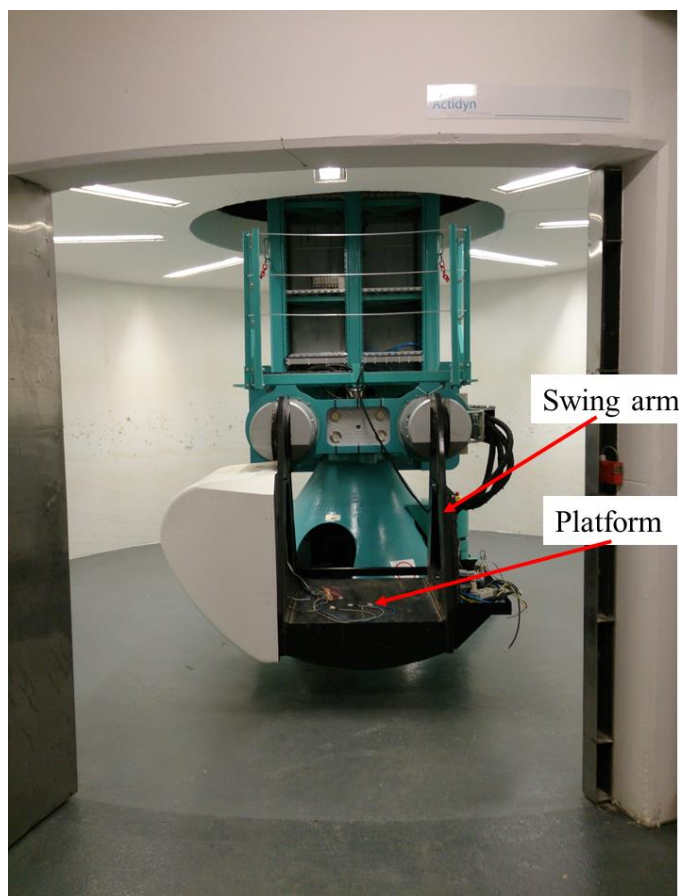


Figure 3.39: University of Pretoria geotechnical centrifuge

Table 3.19: University of Pretoria geotechnical centrifuge specifications (Jacobsz et al. 2014)

Specification	Value
Centrifuge Make & Model	Actidyn C67-4
Capacity	150g-ton
Radius	3m
Model platform dimensions	0.8m X 1.0m X 1.3m
Rated payload	1500kg to 100g

3.2.2 MODEL CONTAINER

The model container used was a standard container of the centrifuge facility. The container was manufactured from 50mm thick aluminium. The inside dimensions of the container were 600mm X 400mm X 400mm (Length X Width X Height). Figure 3.40 shows a picture of the model container indicating the dimensions. The dimensions of the container governed the experiment design in the sense that the size of the foundation were chosen to take into account boundary effects. This will be discussed in a subsequent section.



Figure 3.40: Centrifuge model container

3.2.3 MODEL FOUNDATION

For the model foundation design, the first aspect to consider was the prototype foundation size. Since the focus of this research project is to assess the settlement of a foundation, the foundation size should be chosen to ensure that settlement will be the dominant mechanism. Another consideration was whether the foundation should be circular or square. A circular foundation was chosen for two reasons; 1 - most of the settlement methods discussed assumes circular foundations, 2 – if it is decided in future to do a finite element calculation based on the experiment, a circular foundation will be beneficial for an axis-symmetric model.

Considering Figure 2.11, it was decided to use a prototype footing size of 5m to ensure that settlement is the controlling mechanism. A ratio of foundation embedment depth to diameter of 0.2 was assumed in order to have a constant ratio for scaling purposes.

The vertical stress distribution below a circular foundation given in Figure 2.4 was used as the boundary conditions to limit the model foundation size. Based on this, together with the assumption by most methods that the major stress influence from a foundation is twice the diameter ($2D$), it was decided that use a boundary value of $3D$ below the model foundation. This ensured that the loads distributed to the base of the model container during testing did not influence the results significantly. Also from Figure 2.4, the vertical stress influence outside the footing perimeter at approximately $2D$ is approximately $1.1D$. Thus, a boundary value of $1.5D$ from the sides of the model container was chosen. A minimum sand height in the model contained of **350mm** was calculated.

For the model foundation material **aluminium** was chosen as this material has roughly the same density as concrete, i.e. 2.7g/cm^3 , and it is an easy material to machine.

From the aforementioned information, a circular **aluminium** model foundation of **100mm diameter** and **20mm thick** was calculated as the most suitable. It was decided that the foundation will be embedded in the soil to a depth equalling the thickness (i.e. 20mm in the model case and 1m in the prototype case). The g-level at which the model foundation was found to be most suitable was **50g** which was the g-level (i.e. scale factor) where the tests were conducted and with which other scaling calculations will be done. Appendix A shows the results of the scaling calculations, as well as the foundation position relative to the inside edges of the strongbox.

From the information discussed in Section 2.4.2, it was stated that it is common practice to ensure a rough foundation base. For this research project, fine P100 grit sandpaper was glued to the bottom of the foundation to replicate a rough base. Since aluminium is a relatively soft metal, a hardened steel insert was also added to the foundation at the position of load application. The insert minimised any indentation made in the foundation which could lead to

settlement measurement errors or the transfer of moments. Figure 3.41 shows pictures of the model foundation used indicating the different aspects discussed.

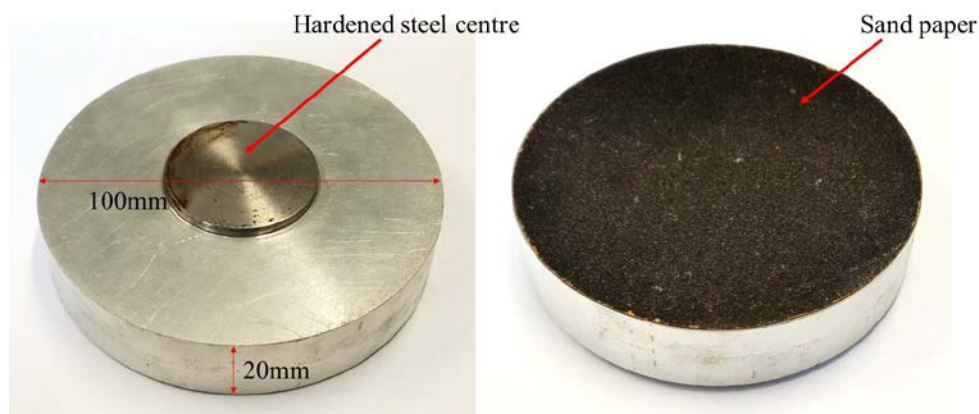


Figure 3.41: Model foundation

To ensure that the foundation chosen behaved as a rigid foundation, Equation 2.9 was used. The elastic modulus of aluminium, as well as the Poisson's ratio (i.e. foundation material) was taken from Illston & Domone (2001) as 69GPa and 0.33, respectively. Using the foundation dimensions and material values, K_F could be calculated. Using the local strain measurement results and Figure 2.13 that shows that for a foundation an average strain level of 0.1% can be assumed, the stiffness values for the sand ranged between 120MPa and 200MPa. These values can be seen as conservative values since the actual values observed during centrifuge testing were lower. The foundation rigidity was calculated for a soil elastic modulus values ranging between 100MPa and 200MPa, together with an assumed soil Poisson's ratio of 0.15 (for dry sand). The results of the rigidity calculations are presented in Table 3.20. It is clear from the table that for the ranges chosen the foundation was perfectly rigid.

Table 3.20: Model foundation rigidity

E_s (MPa)	K_F	Rigidity
100	39.4	$K_F > 10$, Perfectly Rigid
120	32.8	$K_F > 10$, Perfectly Rigid
140	28.1	$K_F > 10$, Perfectly Rigid
160	24.6	$K_F > 10$, Perfectly Rigid
180	21.9	$K_F > 10$, Perfectly Rigid
200	19.7	$K_F > 10$, Perfectly Rigid

3.2.4 BENDER AND EXTENDER ELEMENTS

This section takes into account the information provided on bender- and extender elements in Section 2.5.

Bender and extender elements

Since the centrifuge facility at the University of Pretoria was fairly new at the time this research was done, it was decided to opt for standard bender- and extender elements that were already wired and cut to a specific size. Standard quick mount bender- and extender elements from Piezo Systems, Inc. (Woburn, Mass.) were thus used for this project. The following elements were chosen as the transmitter and receiver bender- and extender elements:

- Transmitter bender - Q220-A4-203YB
- Receiver bender - Q220-A4-203XB
- Transmitter bender - Q220-A4-203XE
- Receiver bender - Q220-A4-203YE

Both the bender- and extender elements had the dimensions which are shown in Figure 3.42 together with a photo of the one of the bender elements. Performance guidelines were given by Piezo Systems, Inc. (2011) for both the bender- and extender elements and these values are presented in Table 3.21. Figure 3.43 shows a picture of a typical bender element used indicating the different parts.

Table 3.21: Performance guidelines for bender- and extender elements (Piezo Systems, Inc., 2011)

Element Type	Weight (g)	Stiffness (N/m)	Capacitance (nF)	Maximum Voltage (V)	Resonant Frequency (Hz)
Bender	1.4	380	26	±90	275
Extender	1.4	4×10^6	26	±90	26200

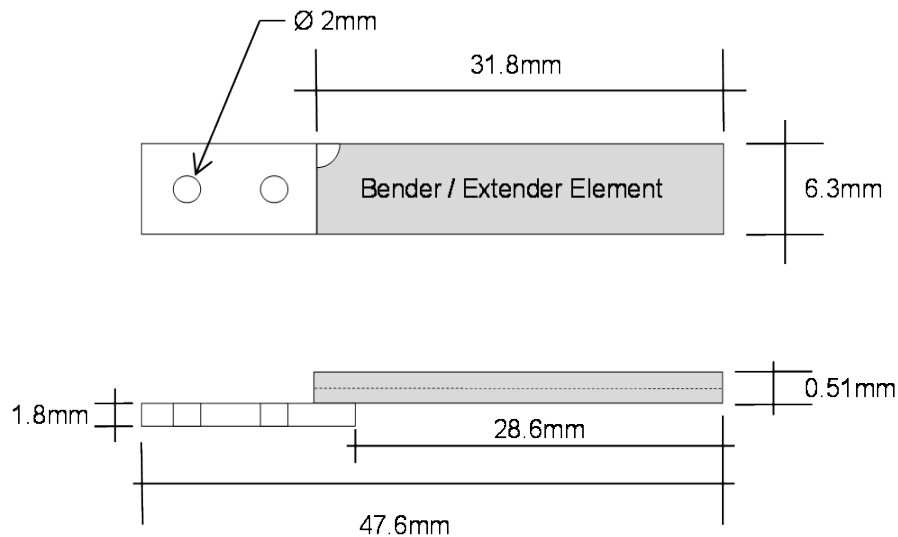


Figure 3.42: Dimensions of bender and extender elements

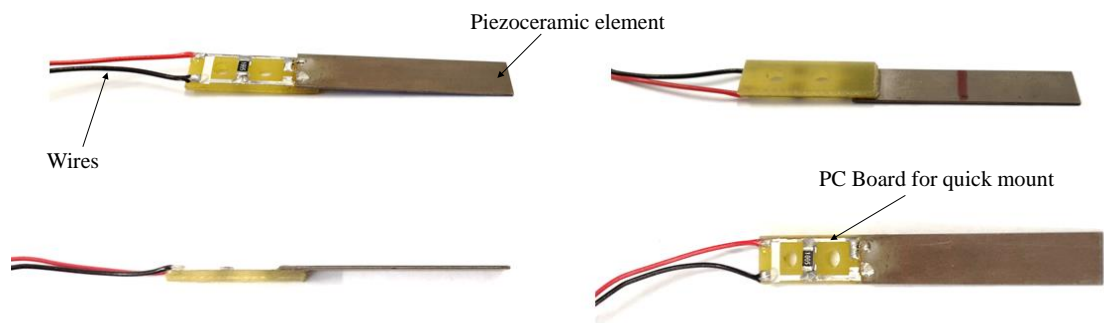


Figure 3.43: Picture of a typical bender element used

Bender and extender element housing

With regard to the mounting/installation of the elements it was decided to opt for free type elements for the reasons discussed previously. To protect the elements a housing block was developed within which the elements could fit and be protected. The housing was developed in such a way that the element could slide back and forth and be clamped to fix the free length. The free length of the bender- or extender elements could therefore be adjusted by shifting the element backwards or forwards in the housing before clamping it with fastening screws. It was found that different free bending/extending lengths produced different signal qualities. Archer & Heymann (2014) concluded that in order to produce the best quality signal, the free bending length of receiver bender elements should be as short as possible and for receiver extender elements, longer elements were better. Since the free length could be

adjusted, it was decided that for the receiver elements, a free length of 4mm and 15mm was chosen for the bender and extender elements, respectively.

A RepRap three dimensional printer was used to produce the housing blocks from an Acrylonitrile butadiene styrene (ABS) polymer. The three dimensional printer could create components within a tolerance of 0.1mm.

Figure 3.44 shows the design drawing for the housing with Figure 3.45 showing the completed housing with a bender element inside. It should be noticed that the housing was small enough to fit into the centrifuge model fairly easily.

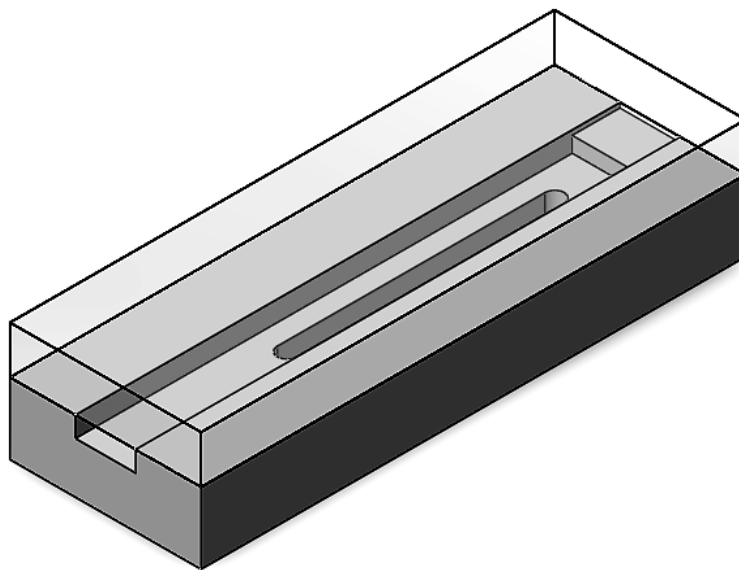


Figure 3.44: Design drawing of bender- and extender element housing

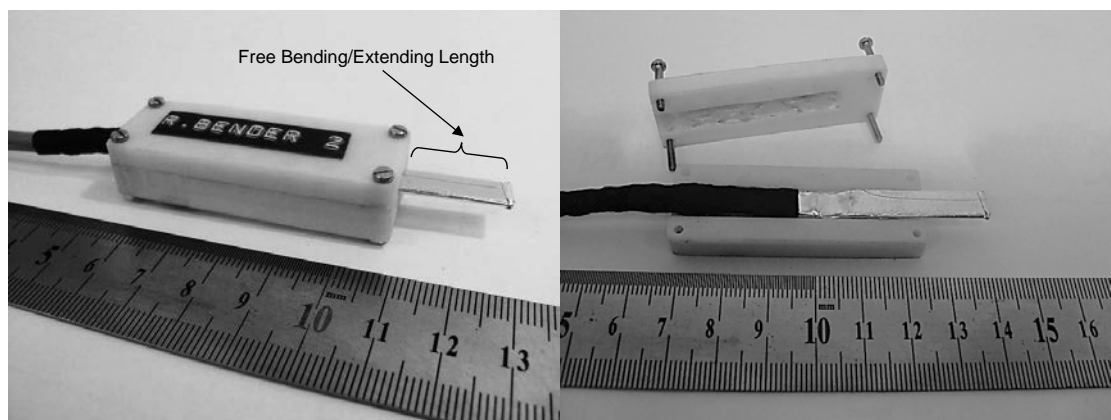


Figure 3.45: Completed housing with element inside

Bender and extender element wires

Since the elements were already wired to the piezoceramic material by means of a small pc-board to produce the different element types, the only extra wire required was for the connection of the element with the data acquisition system. For this purpose a shielded cable was used in order to reduce ambient noise as much as possible. Another aspect of the wire was its flexibility which affected the workability of the wire.

The wire chosen for this project was 22 AWG 7/30 braided shield cable from Alpha Wire. The wire consisted of two core wires and a separate ground wire; all shielded by an outer tinned copper braiding. The wire had a rated voltage of 300V and was 4.8mm thick. The two core wires were connected to the wires already connected to the element and at the other end the wires were connected to BNC connectors to connect to the data acquisition system. Figure 3.46 show a stripped section of the wire used indicating the different wire parts.

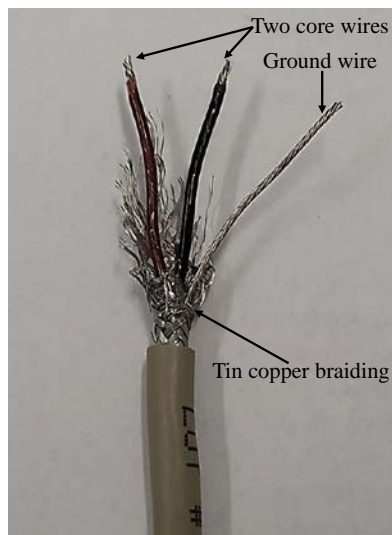


Figure 3.46: Stripped wire used for bender- and extender elements

Bender and extender element isolation

To reduce the ambient noise even further, the elements were isolated in order to create a “Faraday cage” which shielded the elements. The Faraday cage was created by “grounding” the material used to isolate the element, which in this case was aluminium tape. To separate the aluminium tape from the element, to avoid an electrical short circuit, the elements was covered with heat shrink tubing. Heat shrink tubing was chosen as this provided sufficient separation from the aluminium tape, but also a “snug” fit onto the element to ensure that its behaviour was not compromised. At the end of the element, the heat shrink tubing was

melted together, which ensured that the end of the element was also separated from the aluminium tape. A schematic showing the isolation of an element is given in Figure 3.47.

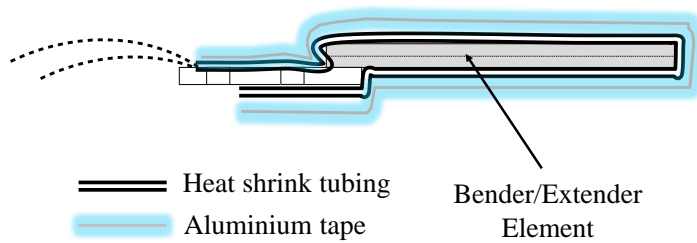


Figure 3.47: Schematic of the bender- and extender element isolation

Charge amplifier

A problem when using bender- or extender elements in a centrifuge is the external noise affecting the output signal by reducing the signal-to-noise ratio. The noise component that has the biggest influence is the mechanical noise created by the centrifuge. Figure 3.48 depicts a schematic of the mechanical noise problem. The output signal from the bender- or extender element is superimposed on the low frequency noise wave. The SNR is reduced, since the low frequency voltage is higher than the output voltage from the signal as shown in the figure. The mechanical noise had to be addressed to increase signal quality. Figure 3.48 shows that the mechanical noise was of a low frequency whereas the output signal had a high frequency content.

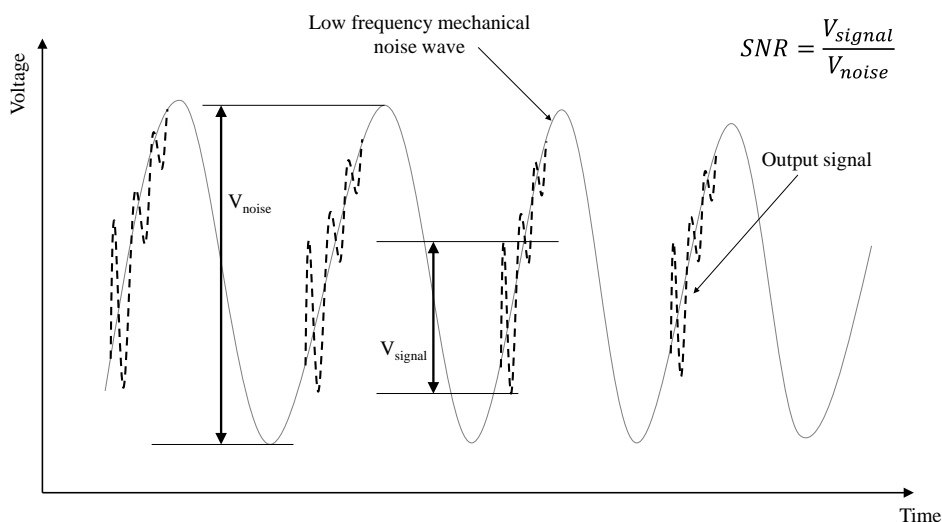


Figure 3.48: Mechanical noise problem schematic

Two ways of addressing the noise is by (1) increasing the output signal and/or (2) reducing the mechanical noise by filtering. With both methods the aim is to increase the signal-to-noise ratio (SNR). An amplifier is required to increase the signal output and a filter is required to reduce the mechanical noise and usually a combination of these two strategies is used. The author developed the bender- and extender elements system used in the centrifuge. For clarity, the design will be briefly discussed.

The amplifier required for the piezoceramic elements is a charge amplifier which is in essence an integrator circuit combined with Resistor-Capacitor (RC) filter circuit which behaves as a low pass filter for the sine wave input from the elements (Tapashetti et al. 2012).

An integrator circuit is designed using an operational amplifier with a feedback circuit consisting of a capacitor and a resistor which, in the case of a charge amplifier, is a RC-filter. The feedback RC-filter circuit is a low pass filter due to the parallel connection of the capacitor and the resistor (with the signal first passing through the capacitor). The output signal can be passed through a RC-filter with the resistor being the first component to create a high pass filter. The cut-off frequency for either the high pass or low pass filter is referred to as the corner frequency, f_c (or cut-off frequency). Equation 3.18 can be used to calculate the corner frequency for both filter types by using the capacitor and resistor values.

$$f_c = \frac{1}{2 \cdot \pi \cdot C \cdot R} \quad 3.18$$

where: C = capacitance of capacitor (Farad)

R = resistance of resistor (Ω)

The charge amplifier solves one problem by filtering the mechanical noise while converting the charge created by the piezoceramic element to a voltage value. The other problem is to increase the output signal and this can be achieved with the use of a non-inverting voltage amplifier which increases the voltage value while keeping the signal in its original form. A voltage follower is also a simple integrator circuit combined with feedback resistors which causes the signal gain. The gain can be calculated using Equation 3.19 with the values of the resistors.

$$\text{Gain} = \frac{V_{\text{out}}}{V_{\text{in}}} = 1 + \frac{R_1}{R_2} \quad 3.19$$

where: V_{out} = output voltage value

V_{in} = input voltage value

R_1 = feedback resistor (connected between negative input and output of the op-amp)

R_2 = resistor connected to ground (0V)

In view of the information discussed, Figure 3.49 shows the charge amplifier circuit designed by the researcher for use in the centrifuge. The figure indicates the different facets discussed with the different components and their respective values. What should be noticed from the design circuit is that for the feedback circuit (high pass filter) of the charge amplifier, a trimmer (variable) resistor and capacitor was used in order for the filter to be adjusted, as the mechanical noise changed. Hence, the calculation for the high pass filter is subject to the values set on the components, but for the low pass filter, the component values used with Equation 3.18 gave a corner frequency of $\pm 15.9\text{kHz}$ which was found to be sufficient to cut-off the high frequency electrical noise encountered. The design circuits were different for the bender- and extender elements. This is due to the fact that it was found, during preliminary testing, that the extender elements produce lower output voltage values compared to the bender elements. This implies that the extender elements should have a higher gain. Using Equation 3.19 together with the resistor values from the voltage amplifier circuit, a gain factor of 48 and 101 were calculated for the bender- and extender elements, respectively. The input signal of the elements passes through the negative input of the first op-amp, causing the output signal to be the inverse of the original signal. This in no way affected the interpretation of the signal as the signal is not altered; only the sign is the opposite.

Figure 3.50 shows a picture of the completed charge amplifier.

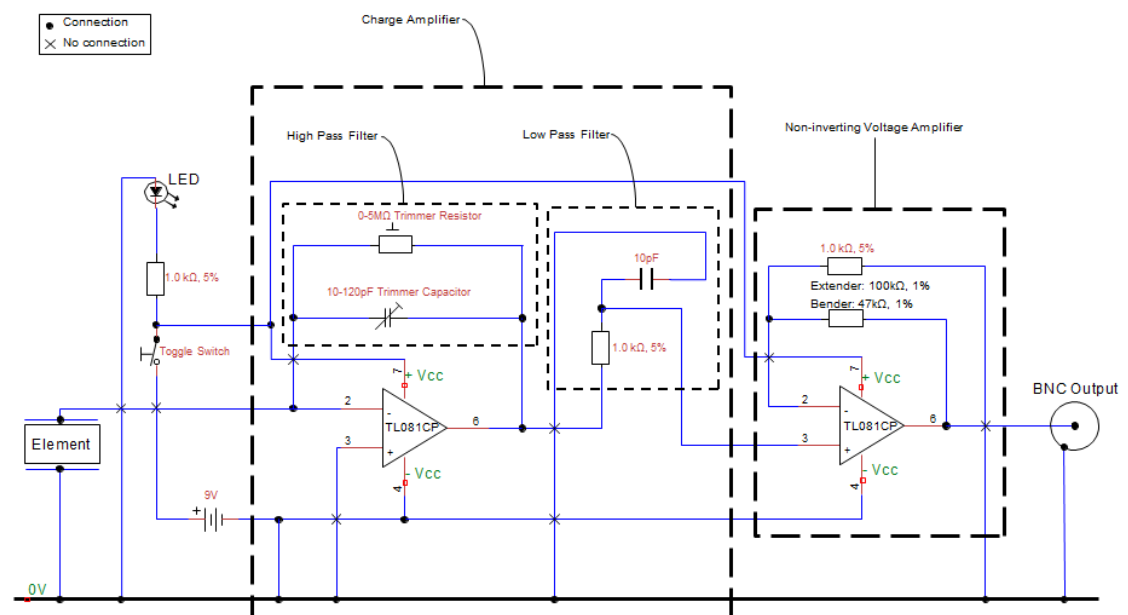


Figure 3.49: Charge amplifier circuit design



Figure 3.50: Picture of the completed charge amplifier box

3.2.5 LOAD-DISPLACEMENT MEASUREMENT SYSTEM

In this section the load-displacement instrumentation is discussed. The load capacity of the system was 50kN and this was adequate to achieve between 0.2D and 0.3D settlement for all relative densities tested.

Mechanical screw jack

The load instrument chosen was a Pfaff-silberblau SHE3.1 Mechanical Ball Screw Jack. Specifications for the jack are given in Table 3.22. One of the main reasons a ball screw jack was chosen was the efficiency rating of 90% (Pfaff-silberblau 2010). Figure 3.51 shows schematics of the jack as provided by the manufacturer. The jack does not come standard with a motor and a wiper motor was used to drive the jack. The wiper motor was adapted to fit the jack and drive it by means of a chain and sprocket system. As mentioned previously, it is desired to have a slow load application rate, and the slowest rate that could be obtained with the best fit sprockets was 5mm/min, which was deemed adequate. The final setup of the jack system will be shown later.

Table 3.22: Specifications for SHE3.1 mechanical ball screw jack

Specification	Value
Max. lifting capacity (static)	49.9kN
Screw (Ball screw)	25 x 5 (Diameter x Pitch)
Stroke	150mm
Design Type	Type B
Gear ratio	24:1
Lift per revolution of ratio	0.25mm/per rev.

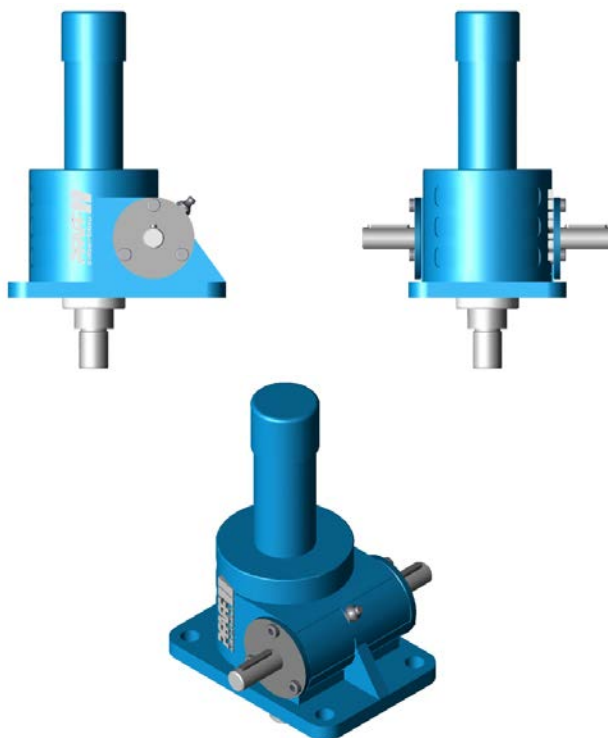


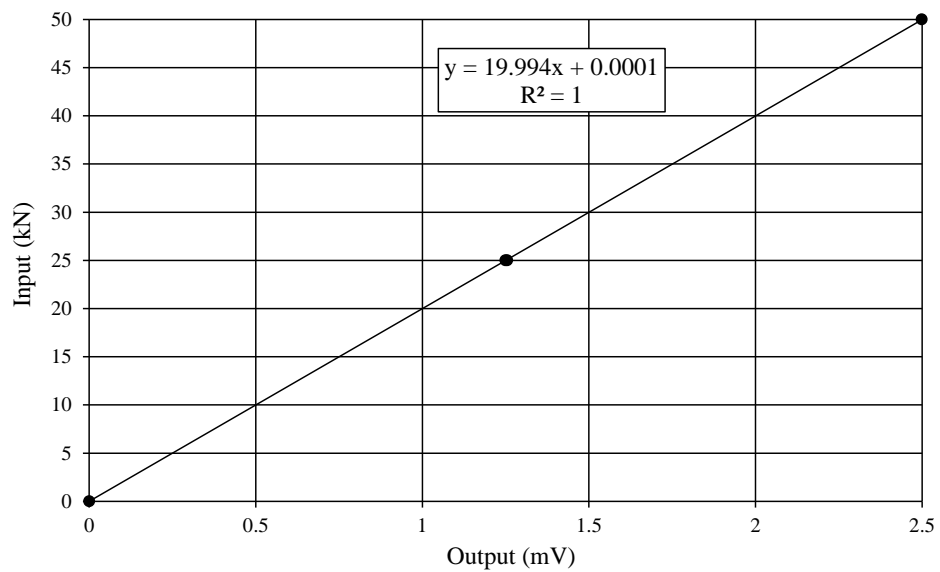
Figure 3.51: Schematic of SHE3.1 mechanical ball screw jack (Pfaff-silberblau, 2010)

Load cell

From the specifications of the jack, the maximum capacity was 49.9kN. The load cell was chosen accordingly as the U93 50kN Force Transducer from HBM. Table 3.23 shows the general specifications of the load cell. The load cell was purchased from the manufacturer for the purpose of the project which provided a calibration certificate. The calibration data provided by the manufacturer is given in Figure 3.52. The sensitivity of the load cell was given from the certificate as 0.9996mV/V at full scale and from the data the calibration factor is 19.994kN/mV. The calibration of the load cell was confirmed with a Budenberg press by comparing a load applied to the measured load. Figure 3.53 show the measured load compared to the applied load for the calibration confirmation. There is a linear agreement between the measured and applied load indicating that the calibration was done correctly and can be will correctly predict the load applied to the foundation. Figure 3.54 shows a close-up photo of the load cell used attached to the jack system. What should be noticed from the picture is the half sphere attached to the load cell pressing on the foundation as shown. The system therefore did not constrain the footing against rotation.

Table 3.23: U93 load cell specifications

Specification	Value
Nominal rated force	50kN
Diameter	54mm
Mass	600g
Operating temperature	-30°C to +85°C
Excitation voltage	2.5V
Rated Sensitivity	1mV/V
Maximum operating force	180% of full scale
Breaking force	>300% of full scale

**Figure 3.52: Calibration curve for the U93 load cell**

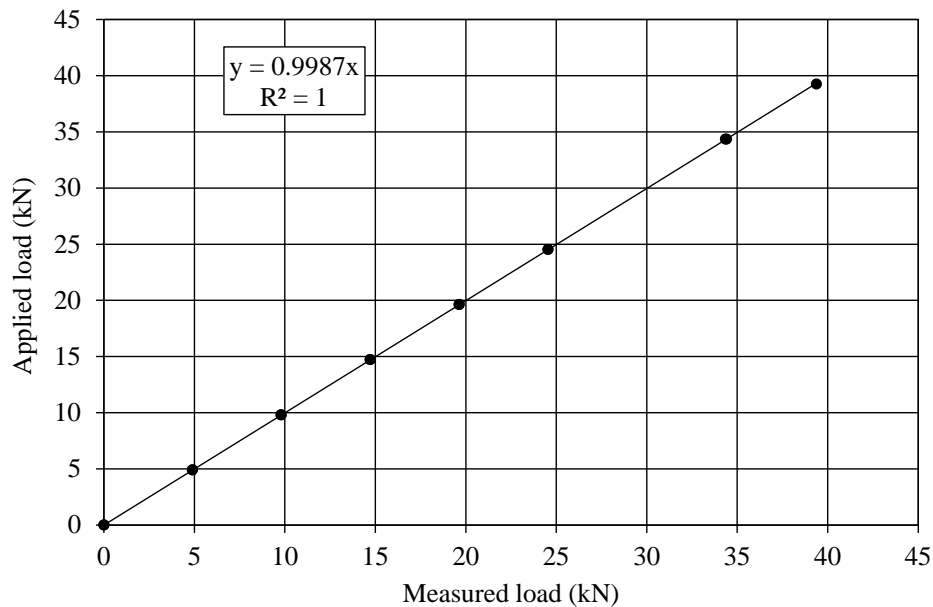


Figure 3.53: Load cell calibration confirmation

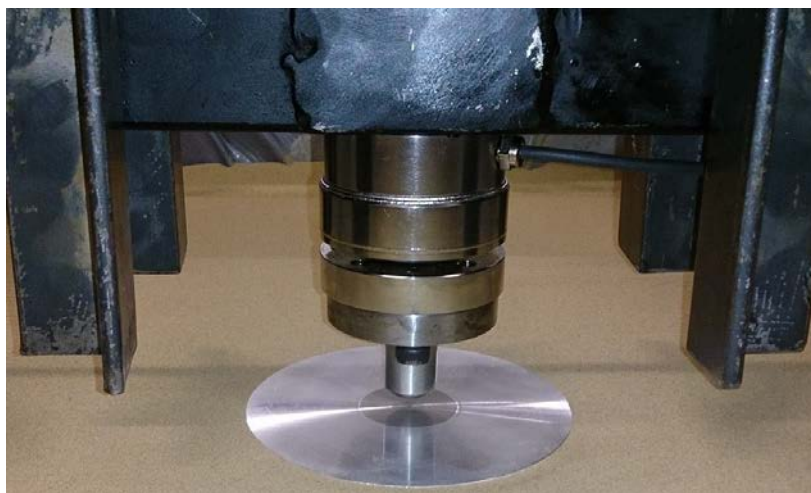


Figure 3.54: Close up of load cell

Linear Variable Differential Transformer (LVDT)

For the displacement measurement it was decided to fix a LVDT to the jack and measure the jack displacement. It was therefore assumed that the jack displacement corresponded to the foundation displacement. A HBM WA50 50mm displacement transducer was chosen as the displacement measurement instrument. Table 3.24 provides the general specifications for the LVDT. As with the load cell, the LVDT was calibrated by the manufacturer. The data from the calibration certificate is presented in Figure 3.55. The sensitivity of the LVDT was given

from the certificate as 0.80mV/V at full scale and from the data the calibration factor is 0.2499mm/mV. The calibration of the LVDT was confirmed with a digital dial gauge by comparing an applied displacement to the measured displacement. Figure 3.56 show the measured displacement compared to the applied displacement for the calibration confirmation. There is a good linear agreement indicating that the calibration was done correctly and can be will correctly predict the displacement of the foundation. Figure 3.57 shows a close up image of the HBM WA50 displacement transducer as it is attached to the jack.

Table 3.24: General specifications for the HBM WA50 displacement transducer

Specification	Value
Nominal displacement	50mm
Rated Sensitivity	0.80mV/V
Mass	77g
Operating temperature	-25°C to +80°C
Excitation voltage	2.5V
Type	Plunger
Core type	Loose core

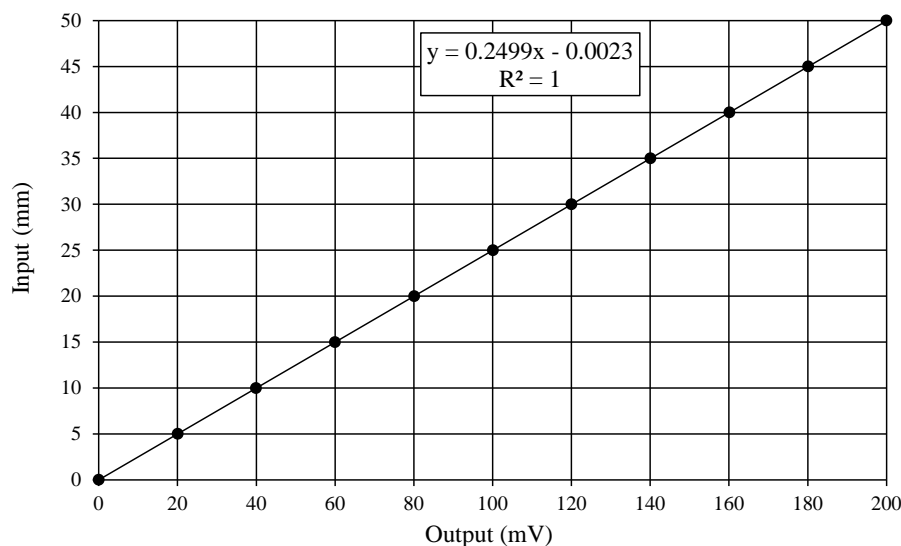


Figure 3.55: Calibration curve for the displacement LVDT

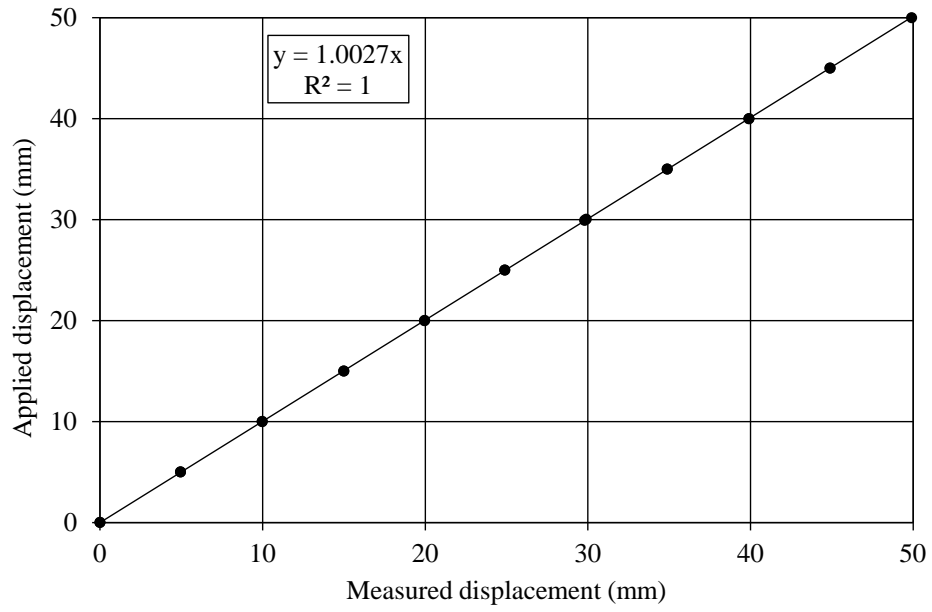


Figure 3.56: Calibration confirmation of the displacement LVDT



Figure 3.57: Close up of displacement transducer attached to jack

Load-displacement system assessment

The jack, together with the LVDT and motor, were mounted onto a purpose-built frame consisting of two channel-beams. It was therefore necessary, considering the amount of force exerted by the jack system, to assess the displacement of the jack system when a force is applied. This was necessary to account for any system compliance, including bending of the beams during loading. The displacement assessment involved pressing on a stiff steel column assumed to be incompressible (very stiff relative to the loading system) and measuring the displacement of the LVDT. It was therefore assumed that the only displacement that occurred was due to the beams bending. A displacement adjustment factor was then calculated and used with the test data by subtracting the factor from the displacement measured at a specific force. Figure 3.58 shows the setup for the assessment. Although it was assumed that the steel column is incompressible, LVDTs were used to measure compression of the steel column and this value (if any) was subtracted from the adjustment data. Figure 3.59 shows the data measured during the assessment of the load-displacement system and from the figure the adjustment factor was calculated as 0.0489mm/kN.

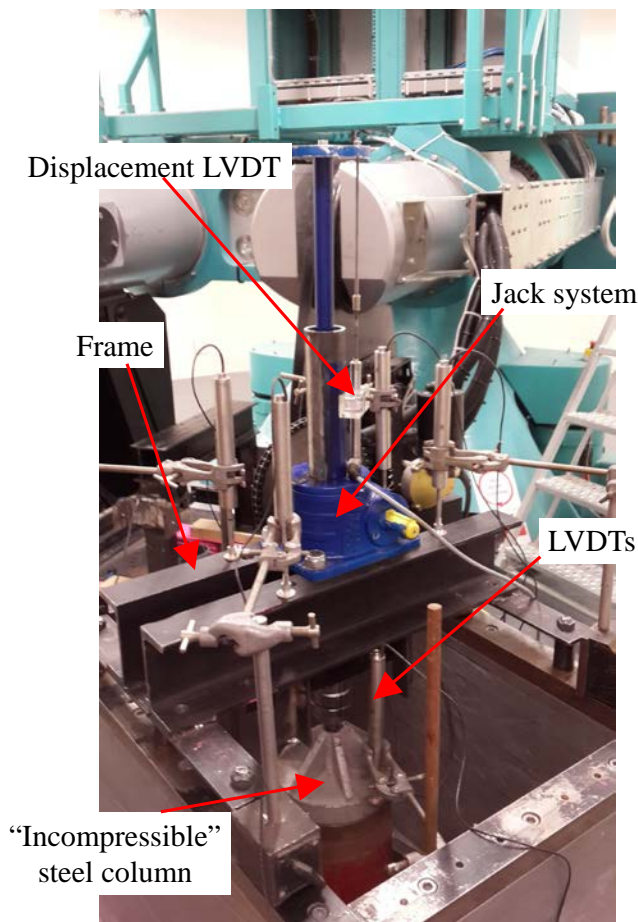


Figure 3.58: Load-displacement system assessment setup

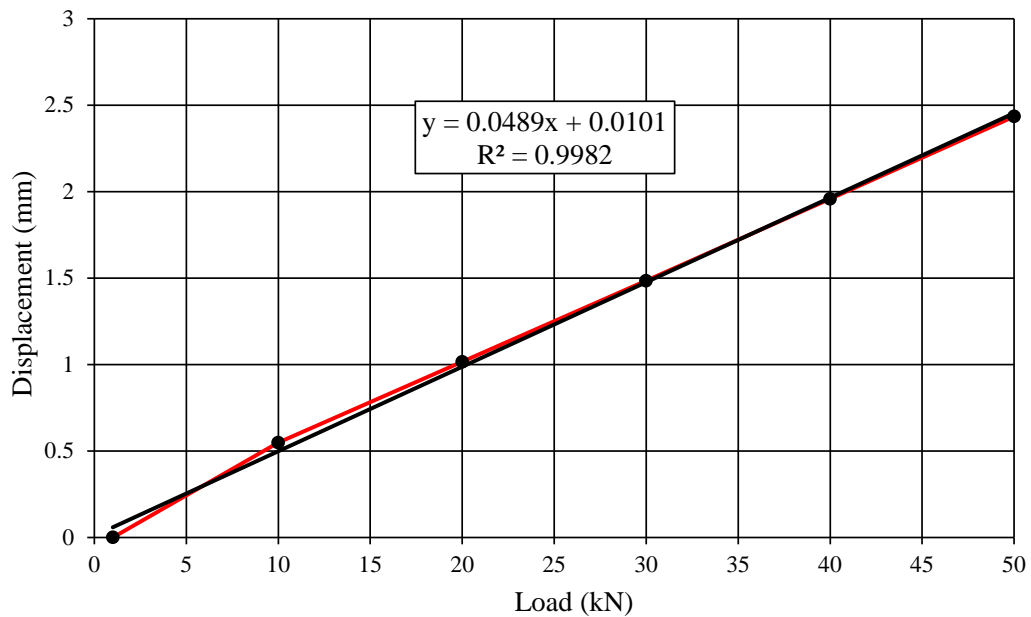


Figure 3.59: Load-displacement system assessment curve

3.2.6 SAND SETTLEMENT LVDT'S

The small-strain stiffness is dependent on the density of the soil. Some settlement of the sand was expected to occur during centrifuge acceleration. It was therefore necessary to measure this settlement in order to calculate the sand density at the different g-levels. For this purpose four LVDTs were placed on top of the sand to measure the settlement. The LVDTs used for this purpose were AS/15 S series 30mm displacement sensors from Solartron Metrology. Figure 3.60 shows a close-up picture of one of the LVDTs with Table 3.25 presenting the general specification of the LVDTs. These LVDTs did not come with calibration certificates and had to be calibrated. For the purpose of this report the LVDTs will be referred to as LVDT 1 to LVDT 4. The calibration curve for LVDT 1 is shown in Figure 3.61. All the LVDTs follow the same calibration pattern as LVDT 1 and therefore only the results of the calibration factors for the LVDTs are given in Table 3.26. It can be seen that the calibration factors were fairly similar.



Figure 3.60: Close-up of AS/15 S series LVDT

Table 3.25: General specifications for the AS/15 S series LVDT

Specification	Value
Measurement range	±15mm (total of 30mm)
Sensitivity at 5kHz ±10%	60 mV/V/mm
Mass	98.4g
Operating temperature	-40°C to +120°C
Excitation voltage	1-10V
Type	Guided core
Body diameter	19mm

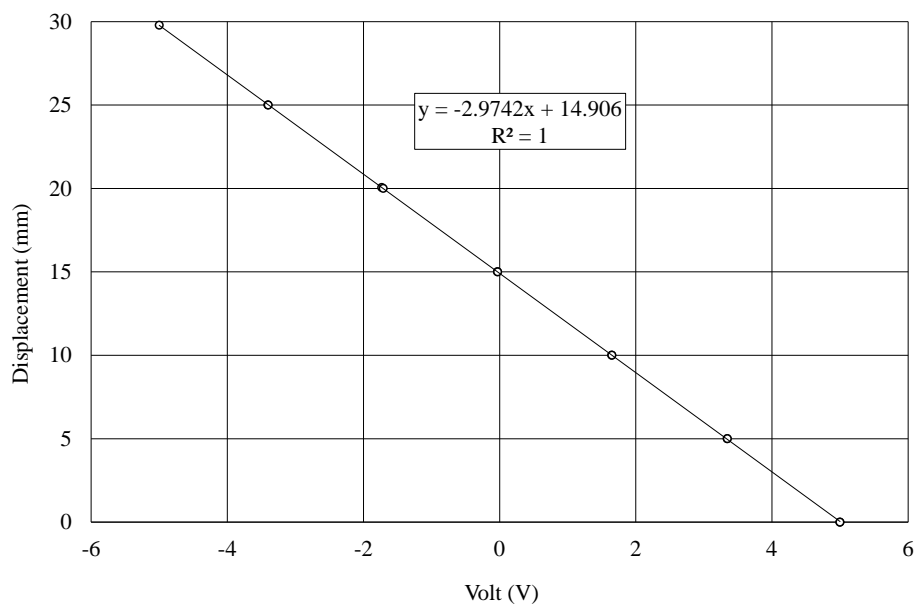


Figure 3.61: Calibration curve for LVDT 1

Table 3.26: Calibration factors for LVDT 1-4

LVDT	Calibration factor (mm/V)
LVDT 1	2.974
LVDT 2	2.975
LVDT 3	2.977
LVDT 4	2.971

3.3 DATA ACQUISITION SYSTEM

The data acquisition system on the centrifuge consisted of three Digidaq modules developed by the University of Western Australia as well as HBM's Quantum X System (Jacobsz et al. 2014). Detail description of the Digidaq modules are given by Gaudin et al. (2010). The HBM system consisted of a MX840 module as well as four MX410 modules.

One of the Digidaq modules was used to record the sand settlement data from LVDTs 1-4. The data was recorded at a sampling rate of 1Hz, which was more than sufficient to capture the required values.

For the load-settlement data the MX840 HBM module was used and the sampling rate for this purpose was set to 50Hz. For the bender- and extender elements three of the MX410 modules were used. As stated previously, the sampling rate is an important aspect to consider and the MX410 modules were specifically chosen due to their relatively high sampling rate. A sampling rate of 192kHz was used, which was high enough to capture the seismic signal from the bender- and extender elements. Both transmitter and receiver elements were measured with the 192kHz sampling rate. For the measurement of the bender- and extender elements, the receiver signals were first passed through the charge amplifier before connected to the HMB system.

The data acquisition software used was the Catman AP Measurement Software from HBM. The software was specifically designed to work with the HBM Quantum Modules. For the Digidaq hardware, the software written, also known as Digidaq, was used to record data from instrument plugged into the Digidaq system.

3.4 COMPLETE EXPERIMENTAL SETUP

In view of the all the different components, the complete model setup could be done. The following aspects with regard to the complete experimental design are necessary to convey:

- The sand for the model was placed by hand (as shown in Figure 3.62) in the container and a vibrating table was used to vibrate the sand to achieve the 50% and 80% RD values.
- The sand was placed in 5 layers of equal thickness with the bottom layers placed at an initially lesser density since it was expected to become denser as the top layers were placed and compacted.
- The model foundation was placed in the middle of the model container by means of the purpose built frame keeping the foundation in place during vibration. Care was taken to ensure that the load was applied to the centre of the foundation.
- A half sphere fitting was fixed to the end of the jack to press on the model foundation. This was done to ensure that the foundation was free to rotate.
- Three sets of bender- and extender elements were placed at three depths below the foundation. Each set consisted of bender- and extender element transmitter and receiver pairs (i.e. one bender- and extender transmitter and receiver per depth). The placement depths were 50mm, 100mm and 150mm which corresponds to depths of 0.5D, 1.0D and 1.5D.
- Care was taken to place the elements firmly in the sand to avoid unwanted movement during vibration and placement which might change the position. The assumption was made that the elements will remain the same distance apart during the test as it was initially placed during the setup of the model.
- It was decided to place the bender- and extender elements a distance of approximately 150mm apart. This value was chosen as it was close enough to still obtain a good quality signal but far enough not to influence the load-settlement behaviour or be damaged during loading. Since the foundation was placed in the centre of the container, the elements were also placed in the middle below the foundation (i.e. 75mm from either side of the centre line).
- Since the elements were placed at different depth, it was decided to take small-strain measurements at difference g-levels. At different g-levels the depths correspond to different prototype depths, a better small-strain stiffness with depth profile could be obtained. Therefore small-strain measurements were taken at 10g, 20g, 30g, 40g and 50g which gave prototype depths ranging between 0.5m to 7.5m.
- Once 50g was reached, the final small-strain measurements were taken, where after the foundation was loaded with the jack. Load-settlement measurements were taken until either the maximum capacity of the load cell was reached or to maximum displacement of 30mm (i.e. 0.3D).

For the experimental testing a total of six tests were conducted, i.e. two tests at each relative density value. Reasons for conducting two tests at each relative density value were to assess the repeatability of the results and to obtain enough data for analysis.

Figure 3.62 to Figure 3.66 depicts a brief sequence of the model preparation. Figure 3.62 shows the initial placements of the sand in the model container for the 20% RD test. Figure 3.63 depicts the placement of a bender- and extender elements pair with a ruler in order to measure the distance apart. Figure 3.64 shows the model container after the elements were placed in the soil as well as the foundation (i.e. before the load-settlement system was placed on the container). Figure 3.65 is a schematic of a section through the model, indicating the elements in the soil, as well as the foundation. Figure 3.66 shows the complete model setup after the load-displacement system was added, indicating the LVDTs measuring sand settlement. The model setup as shown in Figure 3.66 was loaded onto the centrifuge platform where all the necessary electrical connections were made and the test conducted.



Figure 3.62: Initial placement of the sand in the model container

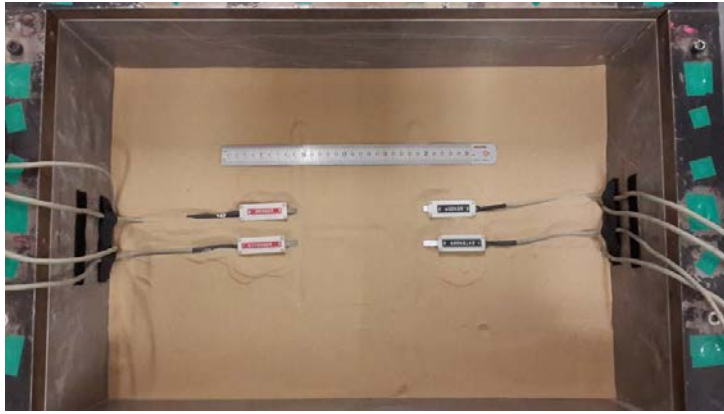


Figure 3.63: A bender- and extender element pair placed in the soil

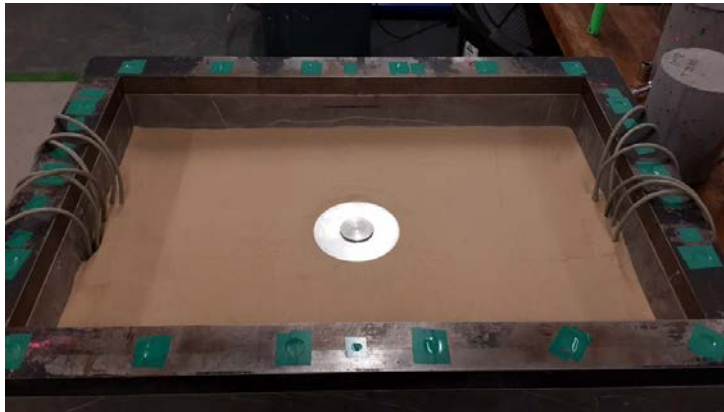
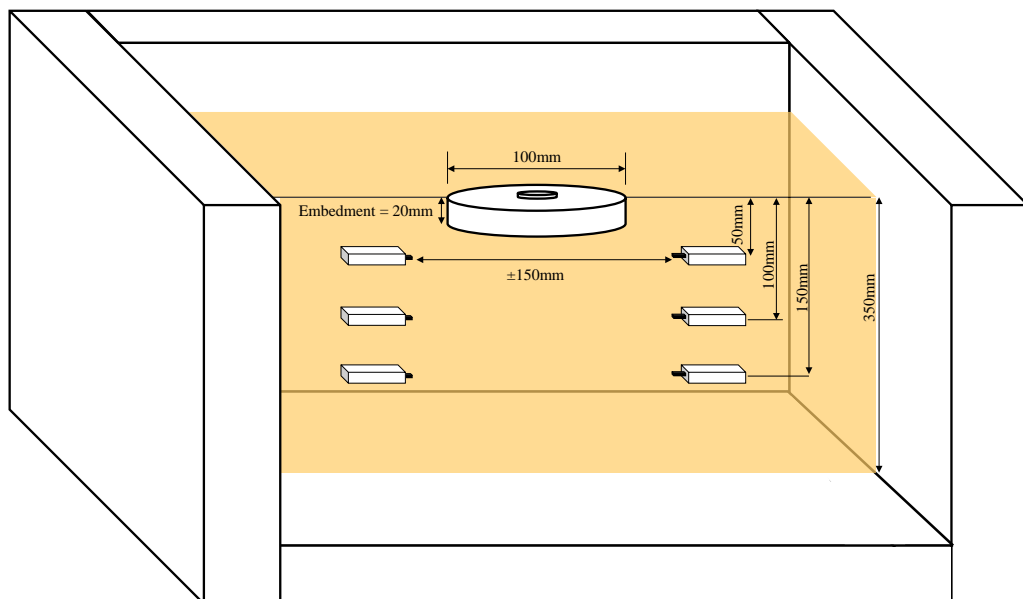


Figure 3.64: Model after foundation and elements have been placed in the soil



PS. Not to scale

Figure 3.65: Schematic of model setup showing the inside of the model

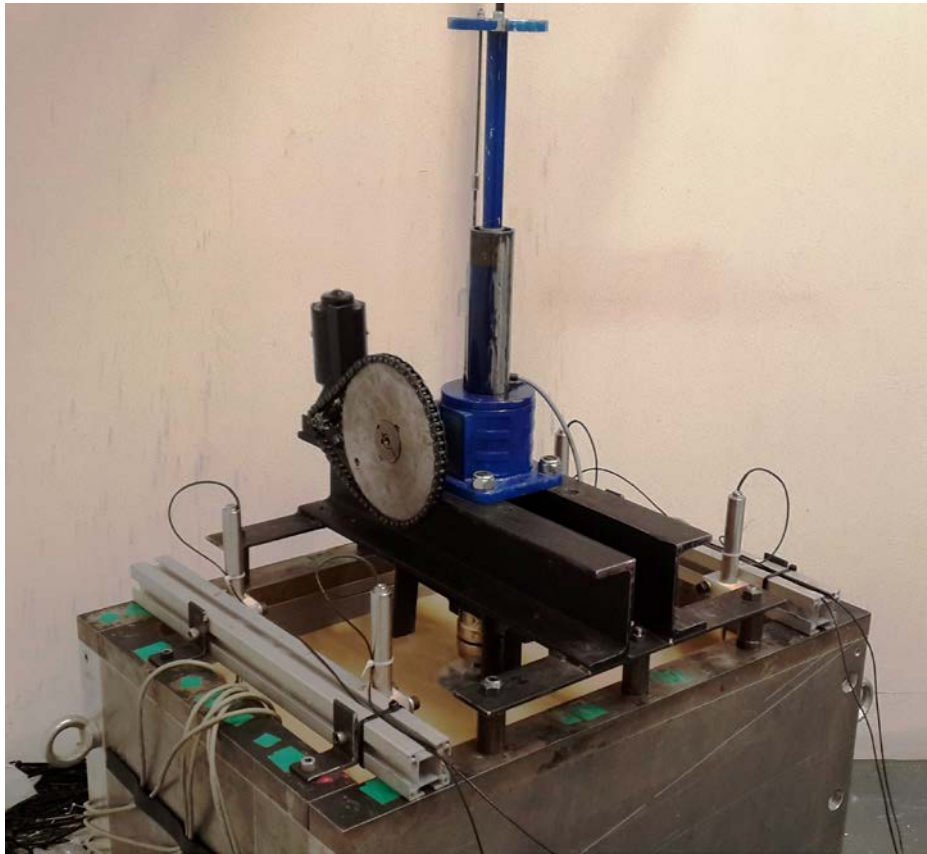


Figure 3.66: Complete experimental model setup

4 DISCUSSION

This chapter discusses the results obtained from the centrifuge tests as presented in Section 3.2. As mentioned, in total six centrifuge tests were conducted, two tests for each relative density. The tests will be referred to as 20%RD Test 1, 20%RD Test 2, 50%RD Test 1, 50%RD Test 2, 80%RD Test 1 and 80%RD Test 2.

First, the small-strain stiffness results will be conveyed, where after the results of the load-displacement measurements of the foundation will be discussed. The proposed settlement prediction method will then be discussed that was derived from the experimental data with the final section of this chapter evaluating the proposed method.

4.1 SOIL DENSITY

In order to use the S-wave and P-wave results to calculate the small-strain stiffness values, the density of the soil is required. Since the sand settles during acceleration in the centrifuge, the initial density cannot be used for calculation purposes. Therefore, LVDTs were used to determine the settlement of the sand at the different g-levels during acceleration. The LVDTs used were discussed previously and the average of the four LVDTs was taken as the settlement. The sand settlement result for the 20%RD Test 1 is shown in Figure 4.1. The different settlements at the different g-levels can be seen from the figure. These values were used to adjust the initial sand height to determine the density during each test. Table 4.1 shows the values of the sand settlement results for the different tests. The initial and in-flight density and relative density values obtained are presented in

Table 4.2. The initial values obtained are within 2% of the desired relative densities.

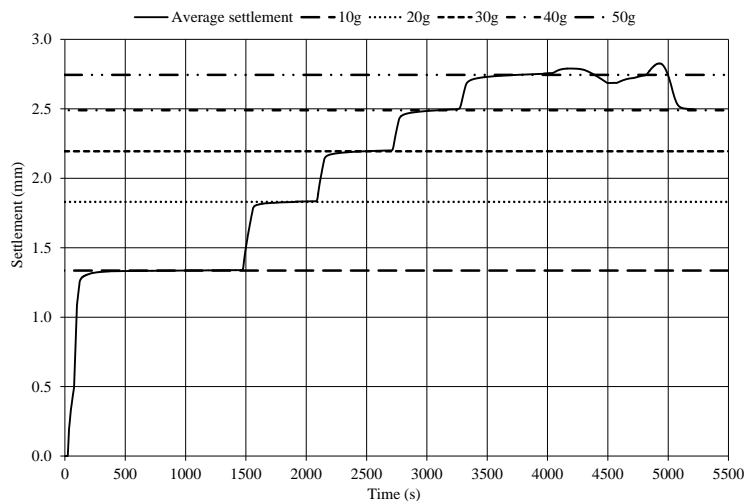


Figure 4.1: 20%RD Test 1 sand settlement result**Table 4.1: Sand settlement LVDT results**

G-level	Sand settlement (mm)					
	20%RD Test 1	20%RD Test 2	50%RD Test 1	50%RD Test 2	80%RD Test 1	80%RD Test 2
10	1.34	1.17	0.14	0.11	0.02	0.03
20	1.83	1.59	0.28	0.24	0.08	0.11
30	2.19	1.89	0.42	0.38	0.17	0.18
40	2.49	2.15	0.55	0.51	0.27	0.26
50	2.74	2.36	0.68	0.63	0.35	0.32

Table 4.2: Densities obtained during model tests

G-level	Density results											
	20%RD Test 1		20%RD Test 2		50%RD Test 1		50%RD Test 2		80%RD Test 1		80%RD Test 2	
	OD ¹	RD ²										
1 - Initial	1448.4	20.4	1450.6	21.1	1526.2	48.4	1528.9	49.4	1608.8	78.2	1608.5	78.1
10	1453.9	22.4	1455.4	22.9	1526.8	48.6	1529.3	49.6	1608.9	78.3	1608.6	78.2
20	1456.0	23.1	1457.2	23.5	1527.4	48.9	1529.9	49.8	1609.2	78.4	1609.0	78.3
30	1457.5	23.6	1458.5	24.0	1528.0	49.1	1530.5	50.0	1609.6	78.5	1609.3	78.4
40	1458.8	24.1	1459.5	24.4	1528.6	49.3	1531.1	50.2	1610.1	78.7	1609.7	78.5
50	1459.8	24.5	1460.4	24.7	1529.1	49.5	1531.6	50.4	1610.4	78.8	1610.0	78.7

¹Obtained density in kg/m³, ²Relative density in %

4.2 SMALL-STRAIN STIFFNESS DATA

In order to reduce the amount of data to be presented in certain graphs, it was decided to present the small-strain stiffness data with respect to the different density tests. This grouping can also be considered as grouping the results in terms of different density sands, i.e. loose, medium dense and dense as discussed previously.

It should be mentioned that due to the large amount of data obtained during this project, only selected results will be shown in certain circumstances. However, where important all the data will be shown.

4.2.1 BENDER- AND EXTENDER DATA ANALYSIS

Due to limitations of the signal function generator, the input signal that could be used for the bender- and extender elements in the centrifuge was a $\pm 10\text{V}$ continuous square wave. After various preliminary tests and based on results during the testing of the elements, the frequency of the input signal was chosen as 25Hz. The input frequency allowed the received signal to dissipate completely before the next signal was triggered; hence no interference occurred between two consecutive signals. Since a square wave input signal was used, the best suited method to determine the first arrival was visual picking of the first arrival/break for reasons discussed in Sections 2.5.3 and 2.5.4.

As explained previously, one of the major difficulties encountered with the bender- and extender elements was the mechanical noise induced by the centrifuge itself. One of the methods used to mitigate this effect was the filters designed with the charge amplifier. Although the filters made it possible to receive in-flight signals (i.e. reducing the mechanical noise to such an extender that the data acquisition system did not overload), the SNR was still too low to obtain clear signals. As mentioned in Section 2.5.4 signal stacking was used as a signal processing tool, to increase the SNR by summing successive signals, increasing the inherent received signal and reducing the random noise. The random noise in this case was the mechanical noise induced by the centrifuge. Stacking is a common signal processing tool which has been used with much success and without impeding the judgement of the output signals (Brandenberg et al., 2006; Brandenberg et al., 2008). A stacking algorithm was written as a macro in Microsoft Excel for this purpose and the exported results from the Catman AP software were imported and the stacking algorithm was run. A total of 60 stacks were used for each data set as this amount was found to be sufficient to reduce the random noise and obtain a clear signal. Figure 4.2 shows a section of typical bender element result before any data processing was applied, indicating that although the signal can be seen, it is not clear where the first arrival is due to a low SNR. Figure 4.3 shows the result before and after stacking of the output signal shown in Figure 4.2. Only one received signal is shown since the stacking produce the results as a single signal. It is clear that the stacked signal has a significant higher SNR and the first arrival is much clearer in relation to the noise. Figure 4.3 also shows that the signal dissipates completely, indicating that the input frequency is not too high.

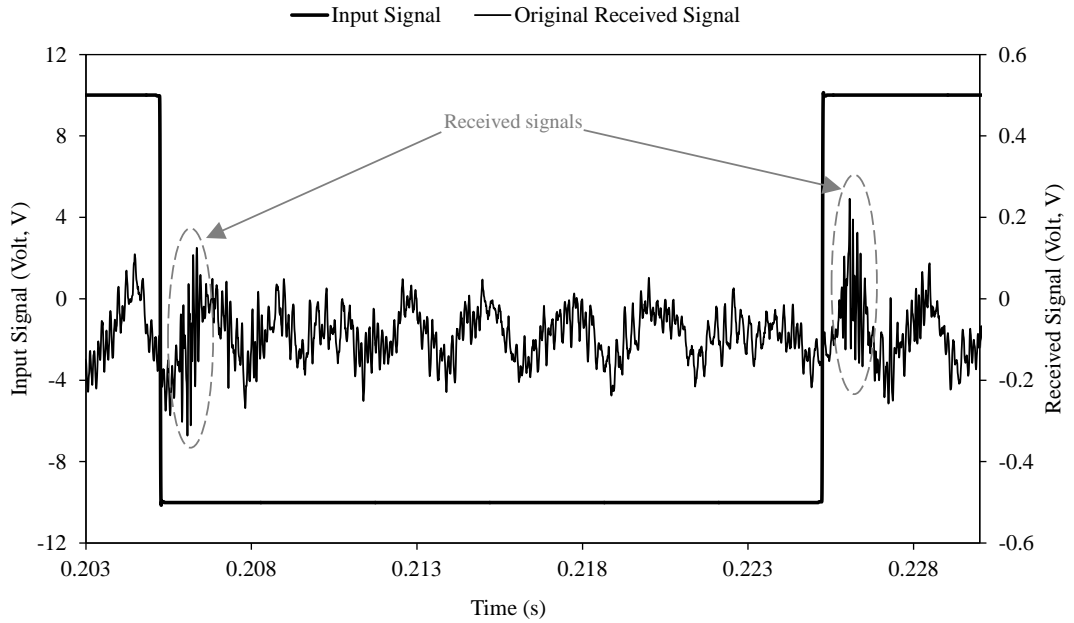


Figure 4.2: Typical bender element result before stacking

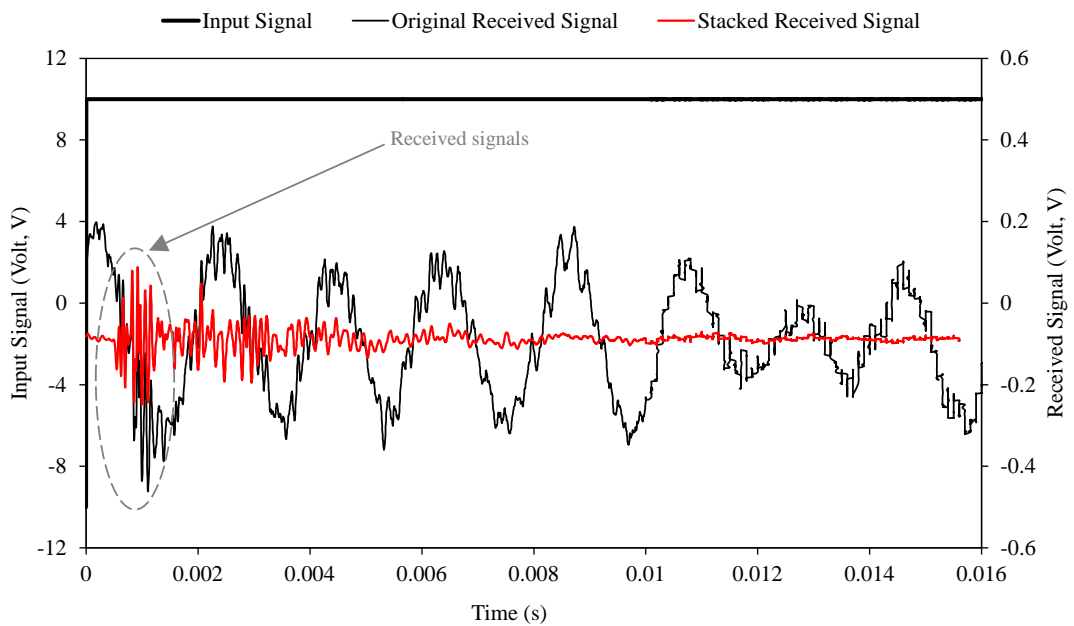


Figure 4.3: Typical results of bender element before and after stacking

The stacking procedure was conducted for all the signals obtained, which amounted to a total of 180 signals, 90 bender element and 90 extender element signals. After the stacking algorithm was run on a signal, the first arrival was chosen. P-waves arriving before S-waves were prominent in the stacked signal, since P-waves are faster travelling waves. It was

therefore decided, to ensure correct assessment of the first arrival, to first assess the extender element results which only produced P-waves. The first arrival time of the P-waves was then used to establish a benchmark for the first arrival of the S-waves. P-wave results were rarely affected by near-field effects making it easier to identify the first arrival. Figure 4.4 shows the extender element result (after stacking) for the middle extender at 40g for 80%RD Test 2. From the figure the first break is clearly defined from which the first arrival can be visually determined. Figure 4.5 shows the bender element result for the same g-level, test and depth (middle bender at 40g for 80%RD Test 2) as the extender element result in Figure 4.4. The extender element first arrival time is 0.000479s (determined from Figure 4.4) and using this value as a benchmark for the P-wave arrival time, the S-wave first arrival can be determined. The bender element result shows two distinct sets of waves, with the first break arrival time (of the first wave set) approximately the same as the P-wave first arrival time. From Figure 4.5 it is clear that there is a portion of the graph before the second wave set that is a distinct change before the second wave set arrives. The second wave set is the arrival of the S-wave and the first break of this set is taken as the first arrival of the S-wave signal.

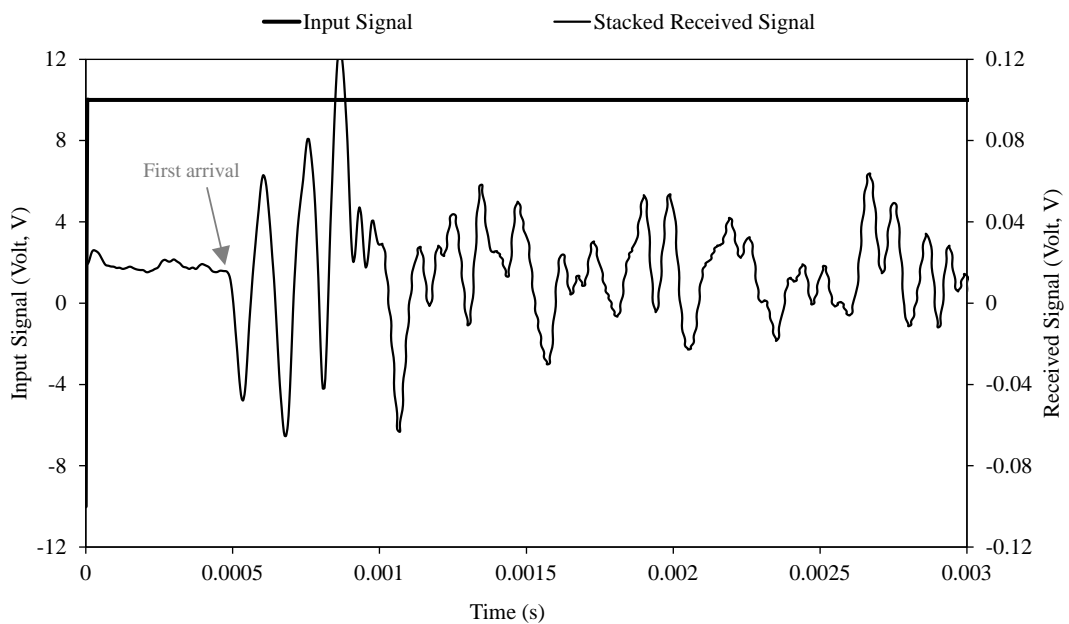


Figure 4.4: Received stacked signal for middle extender 40g 80%RD Test 2

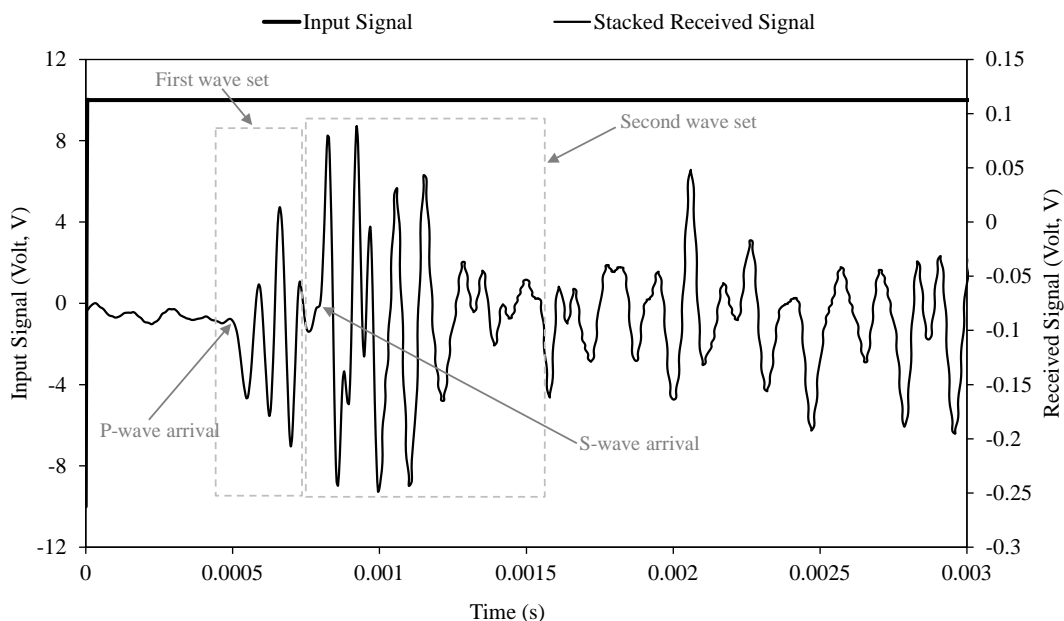


Figure 4.5: Received stacked signal for middle bender 40g 80%RD Test 2

4.2.2 20%RD SMALL-STRAIN STIFFNESS RESULTS

After all the first arrival times were determined, the tip-to-tip distance (L_{tt}) between the bender- and extender elements were divided by these values to obtain the shear and compression wave velocities. The values for L_{tt} were measured when each model was built, and since the distances during the test cannot be measured, the initial distance was assumed to stay constant. Once the shear and compression wave velocities were determined, they were squared and multiplied with the corresponding density values to obtain the shear- and constrained small-strain moduli values (G_0 and M_0).

The values for G_0 and M_0 were plotted against depth. To calculate the depths, the depths at which the bender- and extender element were placed were converted to the prototype depth using the length scaling law (Table 2.5).

Using Equation 2.22 the Poisson's ratio was calculated from the shear- and compression wave velocities. The overburden stress was also calculated using the depth and the density value at each depth. As explained in Section 4.2.1 the extender element results were used to assist in the estimation of the shear wave first arrival.

Table 4.3 and Table 4.4 show the results for the 20%RD Test 1 and Test 2 respectively. The results are best depicted in graph format for comparison purposes. Figure 4.6 and Figure 4.7 show the results for the wave velocities and the small-strain values for the 20%RD tests respectively. The results between the two tests compared relatively well. The difference between tests can be attributed to slight density differences between tests. Another reason,

which could also cause the scatter in the data, can be that there might be some denser sections in the sand as the sand settled due to initial placement. The vibrations caused by the centrifuge could also be a source of distortion of the data. It is therefore more suitable to use trend lines for the data which produces the average values for the data. Power functions proved to be best suited and these lines are also shown on the relevant figures. Table 4.5 shows the values obtained from the power regression lines. The coefficient of correlation (R^2) for the regression lines indicates a good fit with the data for all the data sets with values close to one (1). The power functions for the small-strain shear stiffness values will be used for the proposed method to predict foundation settlement.

Table 4.3: Small-strain stiffness results for 20%RD Test 1

G-level	Position	First Arrival (s)		Velocity (m/s)		V_s/V_p	Model B&E Depth (mm)	Prototype B&E Depth (m)	Depth % of Diameter	Density (kg/m ³)	Overburden Stress (kPa)	G_0 (MPa)	M_0 (MPa)	Poisson's Ratio
		Bender	Extender	Bender	Extender									
10	Top	0.00122	0.000828	119.7	178.7	0.67	50	0.5	0.1D	1453.9	7.3	20.8	46.5	0.09
10	Middle	0.0012	0.000755	129.2	206.6	0.63	100	1	0.2D	1453.9	14.5	24.3	62.1	0.18
10	Bottom	0.00102	0.000708	153.9	227.4	0.68	150	1.5	0.3D	1453.9	21.8	34.4	75.2	0.08
20	Top	0.00111	0.000688	131.5	215.1	0.61	50	1	0.2D	1456.0	14.6	25.2	67.4	0.20
20	Middle	0.000911	0.000625	170.1	249.6	0.68	100	2	0.4D	1456.0	29.1	42.1	90.7	0.07
20	Bottom	0.000828	0.000568	189.6	283.5	0.67	150	3	0.6D	1456.0	43.7	52.3	117.0	0.10
30	Top	0.000995	0.00062	146.7	238.7	0.61	50	1.5	0.3D	1457.5	21.9	31.4	83.1	0.20
30	Middle	0.000865	0.000563	179.2	277.1	0.65	100	3	0.6D	1457.5	43.7	46.8	111.9	0.14
30	Bottom	0.000813	0.000536	193.1	300.4	0.64	150	4.5	0.9D	1457.5	65.6	54.4	131.5	0.15
40	Top	0.000901	0.000615	162.0	240.7	0.67	50	2	0.4D	1458.8	29.2	38.3	84.5	0.09
40	Middle	0.000813	0.000526	190.7	296.6	0.64	100	4	0.8D	1458.8	58.4	53.0	128.3	0.15
40	Bottom	0.000755	0.0005	207.9	322.0	0.65	150	6	1.2D	1458.8	87.5	63.1	151.3	0.14
50	Top	0.00087	0.000604	167.8	245.0	0.68	50	2.5	0.5D	1459.8	36.5	41.1	87.7	0.06
50	Middle	0.000786	0.000536	197.2	291.0	0.68	100	5	1D	1459.8	73.0	56.8	123.7	0.08
50	Bottom	0.000714	0.000469	219.9	343.3	0.64	150	7.5	1.5D	1459.8	109.5	70.6	172.0	0.15

Table 4.4: Small-strain stiffness results for 20%RD Test 2

G-level	Position	First Arrival (s)		Velocity (m/s)		V_s/V_p	Model B&E Depth (mm)	Prototype B&E Depth (m)	Depth % of Diameter	Density (kg/m ³)	Overburden Stress (kPa)	G_0 (MPa)	M_0 (MPa)	Poisson's Ratio
		Bender	Extender	Bender	Extender									
10	Top	0.001286	0.000828	116.6	182.4	0.64	50	0.5	0.1D	1455.4	7.3	19.8	48.4	0.15
10	Middle	0.00117	0.000771	130.8	203.6	0.64	100	1	0.2D	1455.4	14.6	24.9	60.4	0.15
10	Bottom	0.00107	0.000682	143.0	225.8	0.63	150	1.5	0.3D	1455.4	21.8	29.8	74.2	0.17
20	Top	0.00106	0.000677	141.5	223.0	0.63	50	1	0.2D	1457.2	14.6	29.2	72.5	0.16
20	Middle	0.000917	0.000604	166.8	259.9	0.64	100	2	0.4D	1457.2	29.1	40.6	98.5	0.15
20	Bottom	0.000875	0.000563	174.9	273.5	0.64	150	3	0.6D	1457.2	43.7	44.6	109.0	0.15
30	Top	0.000948	0.000615	158.2	245.5	0.64	50	1.5	0.3D	1458.5	21.9	36.5	87.9	0.14
30	Middle	0.000896	0.000542	170.8	289.7	0.59	100	3	0.6D	1458.5	43.8	42.5	122.4	0.23
30	Bottom	0.000802	0.0005	190.8	308.0	0.62	150	4.5	0.9D	1458.5	65.6	53.1	138.4	0.19
40	Top	0.000865	0.000568	173.4	265.8	0.65	50	2	0.4D	1459.5	29.2	43.9	103.2	0.13
40	Middle	0.000823	0.0005	185.9	314.0	0.59	100	4	0.8D	1459.5	58.4	50.4	143.9	0.23
40	Bottom	0.000734	0.000469	208.4	328.4	0.63	150	6	1.2D	1459.5	87.6	63.4	157.4	0.16
50	Top	0.000859	0.000526	174.6	287.1	0.61	50	2.5	0.5D	1460.4	36.5	44.5	120.4	0.21
50	Middle	0.000781	0.000474	195.9	331.2	0.59	100	5	1D	1460.4	73.0	56.0	160.2	0.23
50	Bottom	0.000703	0.000438	217.6	351.6	0.62	150	7.5	1.5D	1460.4	109.5	69.2	180.5	0.19

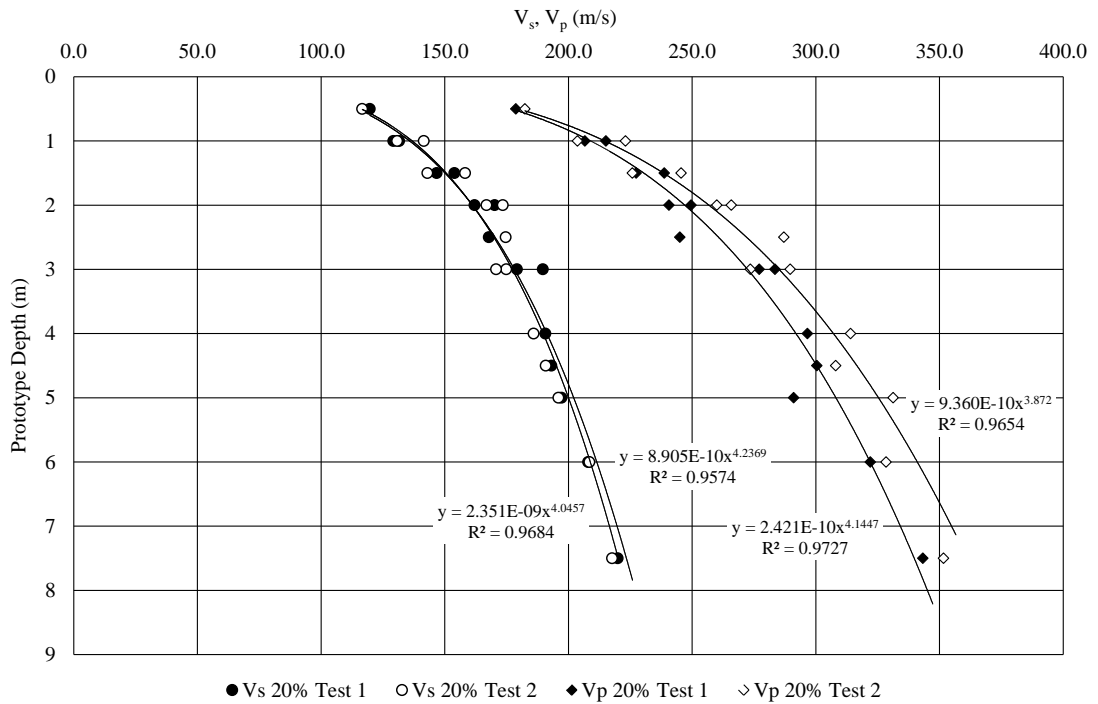


Figure 4.6: V_s and V_p for the 20%RD Tests

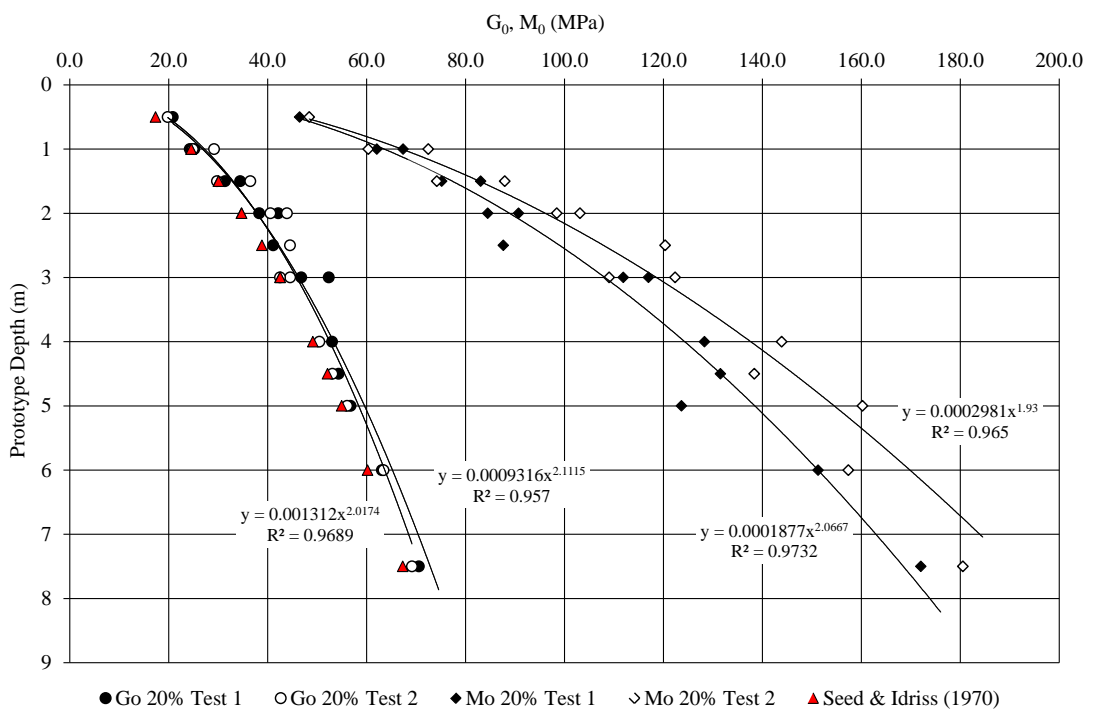


Figure 4.7: G_0 and M_0 for the 20%RD Tests

The results for the shear- and compression wave velocities range from 116m/s to 220m/s and 178m/s to 343m/s with depth respectively. The shear- and constrained small-strain values

range from 19MPa to 71MPa and 47MPa to 181MPa with depth respectively. Also shown on the small-strain shear stiffness data is the values proposed by Seed & Idriss (1970) (Equation 2.23) for loose sand. The values for Seed & Idriss (1970) fall in close proximity to the values obtained which confirms that the results compare well with typical small-strain shear stiffness results. For the 20%RD Tests, the average Poisson's ratio calculated was 0.12 and 0.18 for Test 1 and Test 2 respectively.

Table 4.5: 20%RD Tests regression line values

Coefficients for power function: $y = ax^b$	20%RD Test 1				20%RD Test 2			
	V_s	V_p	G_0	M_0	V_s	V_p	G_0	M_0
a	2.351x10 ⁻⁰⁹	2.421x10 ⁻¹⁰	1.312x10 ⁻⁰³	1.877x10 ⁻⁰⁴	8.905x10 ⁻¹⁰	9.360x10 ⁻¹⁰	9.316x10 ⁻⁰⁴	2.981x10 ⁻⁰⁴
b	4.0457	4.1447	2.0174	2.0667	4.2369	3.872	2.1115	1.93
R ²	0.9684	0.9727	0.9689	0.9732	0.9574	0.9654	0.957	0.965

4.2.3 50%RD SMALL-STRAIN STIFFNESS RESULTS

The results for the 50%RD Tests follow the same discussion as the 20%RD Tests with reference to the determining of the values. Table 4.6 and Table 4.7 show the results for the 50%RD Test 1 and Test 2 respectively. The results are shown in graph format for comparison purposes. Figure 4.8 and Figure 4.9 show the results for the wave velocities and the small-strain values for the 20%RD tests respectively. The figures show that the results between the two tests correlate fairly well indicating a good repeatability between the results.

Power functions were also used to obtain the best fit data through the stiffness and wave velocity data. Table 4.8 shows the values obtained from the power regression lines. The coefficient of correlation (R²) for the regression lines indicates a good fit with the data for all the data sets with values close to one (1). The power functions for the small-strain shear stiffness values will be used for the proposed method to predict foundation settlement.

Table 4.6: Small-strain stiffness results for 50%RD Test 1

G-level	Position	First Arrival (s)		Velocity (m/s)		V_s/V_p	Model B&E Depth (mm)	Prototype B&E Depth (m)	Depth % of Diameter	Density (kg/m ³)	Overburden Stress (kPa)	G_0 (MPa)	M_0 (MPa)	Poisson's Ratio
		Bender	Extender	Bender	Extender									
10	Top	0.00111	0.000646	138.7	238.4	0.58	50	0.5	0.1D	1526.8	7.6	29.4	86.8	0.24
10	Middle	0.00104	0.000599	146.2	250.4	0.58	100	1	0.2D	1526.8	15.3	32.6	95.7	0.24
10	Bottom	0.000885	0.000547	172.9	279.7	0.62	150	1.5	0.3D	1526.8	22.9	45.6	119.5	0.19
20	Top	0.000964	0.000599	159.8	257.1	0.62	50	1	0.2D	1527.4	15.3	39.0	101.0	0.19
20	Middle	0.000906	0.000531	167.8	282.5	0.59	100	2	0.4D	1527.4	30.5	43.0	121.9	0.23
20	Bottom	0.000755	0.000474	202.6	322.8	0.63	150	3	0.6D	1527.4	45.8	62.7	159.1	0.17
30	Top	0.00087	0.000552	177.0	279.0	0.63	50	1.5	0.3D	1528.0	22.9	47.9	118.9	0.16
30	Middle	0.000755	0.000484	201.3	309.9	0.65	100	3	0.6D	1528.0	45.8	61.9	146.8	0.13
30	Bottom	0.000719	0.000438	212.8	349.3	0.61	150	4.5	0.9D	1528.0	68.8	69.2	186.5	0.20
40	Top	0.000865	0.000526	178.0	292.8	0.61	50	2	0.4D	1528.6	30.6	48.5	131.0	0.21
40	Middle	0.000781	0.000458	194.6	327.5	0.59	100	4	0.8D	1528.6	61.1	57.9	164.0	0.23
40	Bottom	0.000708	0.000417	216.1	366.9	0.59	150	6	1.2D	1528.6	91.7	71.4	205.8	0.23
50	Top	0.000823	0.0005	187.1	308.0	0.61	50	2.5	0.5D	1529.1	38.2	53.5	145.1	0.21
50	Middle	0.00075	0.000432	202.7	347.2	0.58	100	5	1D	1529.1	76.5	62.8	184.4	0.24
50	Bottom	*	0.000396	*	386.4	*	150	7.5	1.5D	1529.1	114.7	*	228.3	*

*No bender element result was measured

Table 4.7: Small-strain stiffness results for 50%RD Test 2

G-level	Position	First Arrival (s)		Velocity (m/s)		V_s/V_p	Model B&E Depth (mm)	Prototype B&E Depth (m)	Depth % of Diameter	Density (kg/m ³)	Overburden Stress (kPa)	G_0 (MPa)	M_0 (MPa)	Poisson's Ratio
		Bender	Extender	Bender	Extender									
10	Top	0.00114	0.000625	132.5	243.2	0.54	50	0.5	0.1D	1529.3	7.6	26.8	90.5	0.29
10	Middle	0.00102	0.000578	148.0	259.5	0.57	100	1	0.2D	1529.3	15.3	33.5	103.0	0.26
10	Bottom	0.000922	0.000557	165.9	276.5	0.60	150	1.5	0.3D	1529.3	22.9	42.1	116.9	0.22
20	Top	0.000953	0.000563	158.4	270.0	0.59	50	1	0.2D	1529.9	15.3	38.4	111.5	0.24
20	Middle	0.00087	0.0005	173.6	300.0	0.58	100	2	0.4D	1529.9	30.6	46.1	137.7	0.25
20	Bottom	0.000792	0.000474	193.2	324.9	0.59	150	3	0.6D	1529.9	45.9	57.1	161.5	0.23
30	Top	0.000865	0.00051	174.6	298.0	0.59	50	1.5	0.3D	1530.5	23.0	46.6	136.0	0.24
30	Middle	0.000813	0.000458	185.7	327.5	0.57	100	3	0.6D	1530.5	45.9	52.8	164.2	0.26
30	Bottom	0.000729	0.000453	209.9	340.0	0.62	150	4.5	0.9D	1530.5	68.9	67.4	176.9	0.19
40	Top	0.000797	0.000479	189.5	317.3	0.60	50	2	0.4D	1531.1	30.6	55.0	154.2	0.22
40	Middle	0.000724	0.000432	208.6	347.2	0.60	100	4	0.8D	1531.1	61.2	66.6	184.6	0.22
40	Bottom	0.000667	0.000427	229.4	360.7	0.64	150	6	1.2D	1531.1	91.9	80.6	199.2	0.16
50	Top	0.00076	0.000448	198.7	339.3	0.59	50	2.5	0.5D	1531.6	38.3	60.5	176.3	0.24
50	Middle	0.000698	0.000417	216.3	359.7	0.60	100	5	1D	1531.6	76.6	71.7	198.2	0.22
50	Bottom	0.000646	0.000411	236.8	374.7	0.63	150	7.5	1.5D	1531.6	114.9	85.9	215.0	0.17

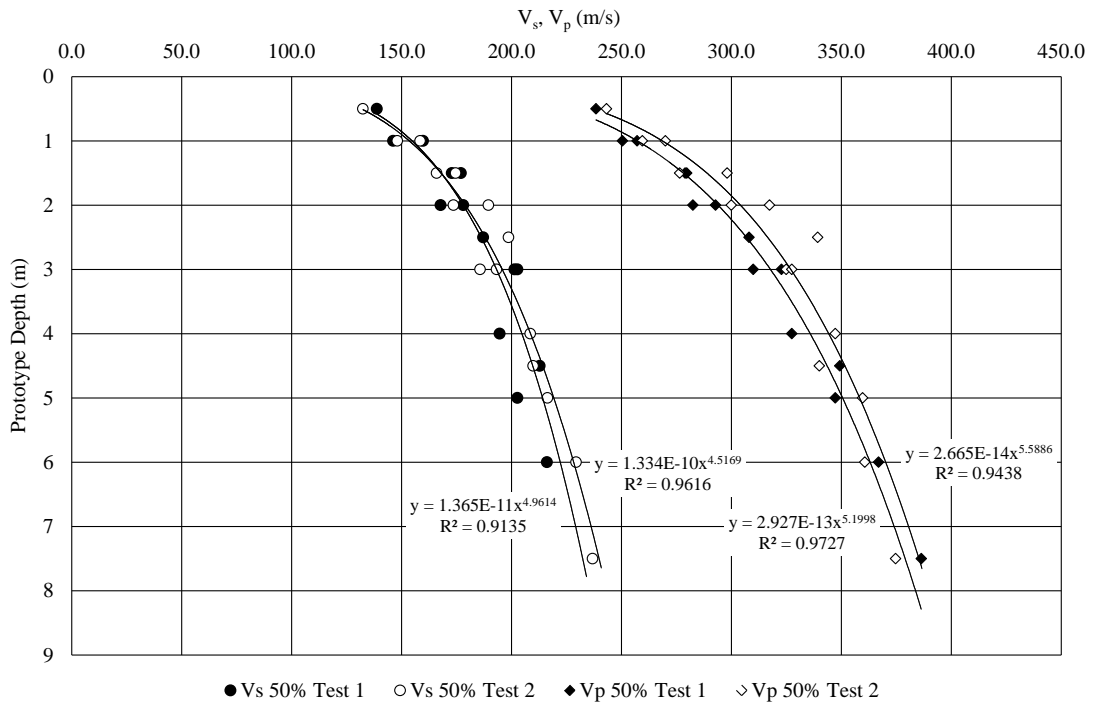


Figure 4.8: V_s and V_p for the 50%RD Tests

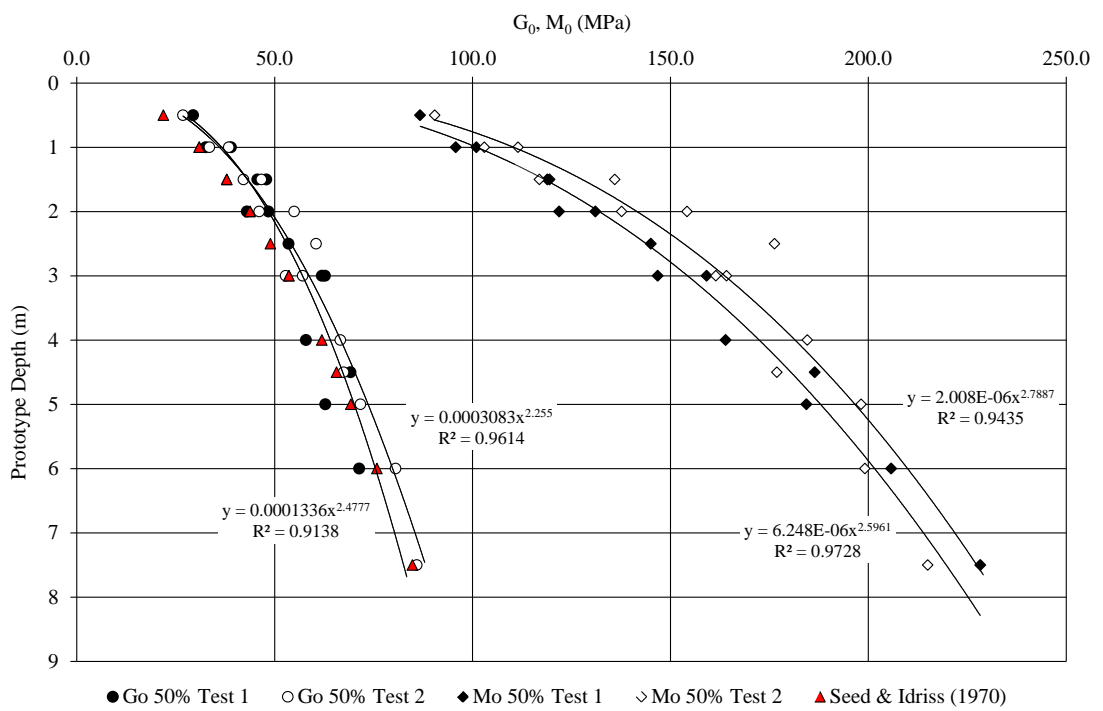


Figure 4.9: G_0 and M_0 for the 50%RD Tests

The results for the shear- and compression wave velocities range from 132m/s to 237m/s and 238m/s to 386m/s with depth respectively. The shear- and constrained small-strain values range from 27MPa to 86MPa and 87MPa to 228MPa with depth respectively. Also depicted on the small-strain shear stiffness data is the values proposed by Seed & Idriss (1970) (Equation 2.24) for medium dense sand. Again the values for Seed & Idriss (1970) fall in close proximity to the values obtained. For the 50%RD Tests, the average Poisson's ratio calculated is 0.22.

Table 4.8: 50%RD Tests regression line values

Coefficients for power function: $y = ax^b$	50%RD Test 1				50%RD Test 2			
	V_s	V_p	G_0	M_0	V_s	V_p	G_0	M_0
a	1.365×10^{-11}	2.927×10^{-13}	1.336×10^{-04}	6.248×10^{-06}	1.334×10^{-10}	2.665×10^{-14}	3.083×10^{-04}	2.008×10^{-06}
b	4.9614	5.1998	2.4777	2.5961	4.5169	5.5886	2.255	2.7887
R^2	0.9135	0.9727	0.9138	0.9728	0.9616	0.9438	0.9614	0.9435

4.2.4 80%RD SMALL-STRAIN STIFFNESS RESULTS

The results for the 80%RD Tests follow the same discussion as the 20%RD Tests with reference to the determining of the values. Table 4.9 and Table 4.10 show the results for the 80%RD Test 1 and Test 2 respectively. Figure 4.10 and Figure 4.11 show the results for the wave velocities and the small-strain values for the 80%RD tests respectively. The figures indicate shows that the results between the two tests correlate fairly well indicating a good repeatability between the results.

Power functions were also use to obtain the best fit data through the stiffness and wave velocity data. Table 4.11 shows the values obtained from the power regression lines. The coefficient of correlation (R^2) for the regression lines indicates a good fit with the data for all the data sets with values close to one (1).

Table 4.9: Small-strain stiffness results for 80%RD Test 1

G-level	Position	First Arrival (s)		Velocity (m/s)		V_s/V_p	Model B&E Depth (mm)	Prototype B&E Depth (m)	Depth % of Diameter	Density (kg/m ³)	Overburden Stress (kPa)	G_0 (MPa)	M_0 (MPa)	Poisson's Ratio
		Bender	Extender	Bender	Extender									
10	Top	0.00114	0.000708	131.6	211.9	0.62	50	0.5	0.1D	1608.9	8.0	27.9	72.2	0.19
10	Middle	0.00102	0.00062	156.9	246.8	0.64	100	1	0.2D	1608.9	16.1	39.6	98.0	0.16
10	Bottom	0.000984	0.000583	171.7	274.4	0.63	150	1.5	0.3D	1608.9	24.1	47.5	121.2	0.18
20	Top	0.000938	0.000615	159.9	243.9	0.66	50	1	0.2D	1609.2	16.1	41.2	95.7	0.12
20	Middle	0.000927	0.000521	172.6	293.7	0.59	100	2	0.4D	1609.2	32.2	47.9	138.8	0.24
20	Bottom	0.000844	0.000505	200.2	316.8	0.63	150	3	0.6D	1609.2	48.3	64.5	161.5	0.17
30	Top	0.000859	0.000557	174.6	269.3	0.65	50	1.5	0.3D	1609.6	24.1	49.1	116.7	0.14
30	Middle	0.000823	0.000469	194.4	326.2	0.60	100	3	0.6D	1609.6	48.3	60.8	171.3	0.22
30	Bottom	0.000766	0.000464	220.6	344.8	0.64	150	4.5	0.9D	1609.6	72.4	78.4	191.4	0.15
40	Top	0.000797	0.000479	188.2	313.2	0.60	50	2	0.4D	1610.1	32.2	57.0	157.9	0.22
40	Middle	0.000734	0.000443	218.0	345.4	0.63	100	4	0.8D	1610.1	64.4	76.5	192.1	0.17
40	Bottom	0.000703	0.000438	240.4	365.3	0.66	150	6	1.2D	1610.1	96.6	93.0	214.9	0.12
50	Top	0.00076	0.000453	197.4	331.1	0.60	50	2.5	0.5D	1610.4	40.3	62.7	176.6	0.22
50	Middle	0.000708	0.000411	226.0	372.3	0.61	100	5	1D	1610.4	80.5	82.2	223.2	0.21
50	Bottom	0.000677	0.000406	249.6	394.1	0.63	150	7.5	1.5D	1610.4	120.8	100.4	250.1	0.16

Table 4.10: Small-strain stiffness results for 80%RD Test 2

G-level	Position	First Arrival (s)		Velocity (m/s)		V_s/V_p	Model B&E Depth (mm)	Prototype B&E Depth (m)	Depth % of Diameter	Density (kg/m ³)	Overburden Stress (kPa)	G_0 (MPa)	M_0 (MPa)	Poisson's Ratio
		Bender	Extender	Bender	Extender									
10	Top	0.00116	0.000682	129.3	219.9	0.59	50	0.5	0.1D	1608.6	8.0	26.9	77.8	0.24
10	Middle	0.00109	0.000661	146.8	233.0	0.63	100	1	0.2D	1608.6	16.1	34.7	87.3	0.17
10	Bottom	0.00105	0.00062	160.0	254.8	0.63	150	1.5	0.3D	1608.6	24.1	41.2	104.5	0.17
20	Top	0.000948	0.00062	158.2	241.9	0.65	50	1	0.2D	1609.0	16.1	40.3	94.2	0.13
20	Middle	0.000885	0.000568	180.8	271.1	0.67	100	2	0.4D	1609.0	32.2	52.6	118.3	0.10
20	Bottom	0.000844	0.000526	199.1	300.4	0.66	150	3	0.6D	1609.0	48.3	63.7	145.2	0.11
30	Top	0.000865	0.000563	173.4	266.4	0.65	50	1.5	0.3D	1609.3	24.1	48.4	114.2	0.13
30	Middle	0.000833	0.00051	192.1	302.0	0.64	100	3	0.6D	1609.3	48.3	59.4	146.7	0.16
30	Bottom	0.000776	0.000474	216.5	333.3	0.65	150	4.5	0.9D	1609.3	72.4	75.4	178.8	0.14
40	Top	0.000797	0.000479	188.2	313.2	0.60	50	2	0.4D	1609.7	32.2	57.0	157.9	0.22
40	Middle	0.000797	0.000479	200.8	321.5	0.62	100	4	0.8D	1609.7	64.4	64.9	166.4	0.18
40	Bottom	0.000755	0.000453	222.5	348.8	0.64	150	6	1.2D	1609.7	96.6	79.7	195.8	0.16
50	Top	0.000755	0.000453	198.7	331.1	0.60	50	2.5	0.5D	1610.0	40.2	63.5	176.5	0.22
50	Middle	0.00076	0.000453	210.5	340.0	0.62	100	5	1D	1610.0	80.5	71.4	186.1	0.19
50	Bottom	0.000656	0.000417	256.1	378.9	0.68	150	7.5	1.5D	1610.0	120.7	105.6	231.1	0.08

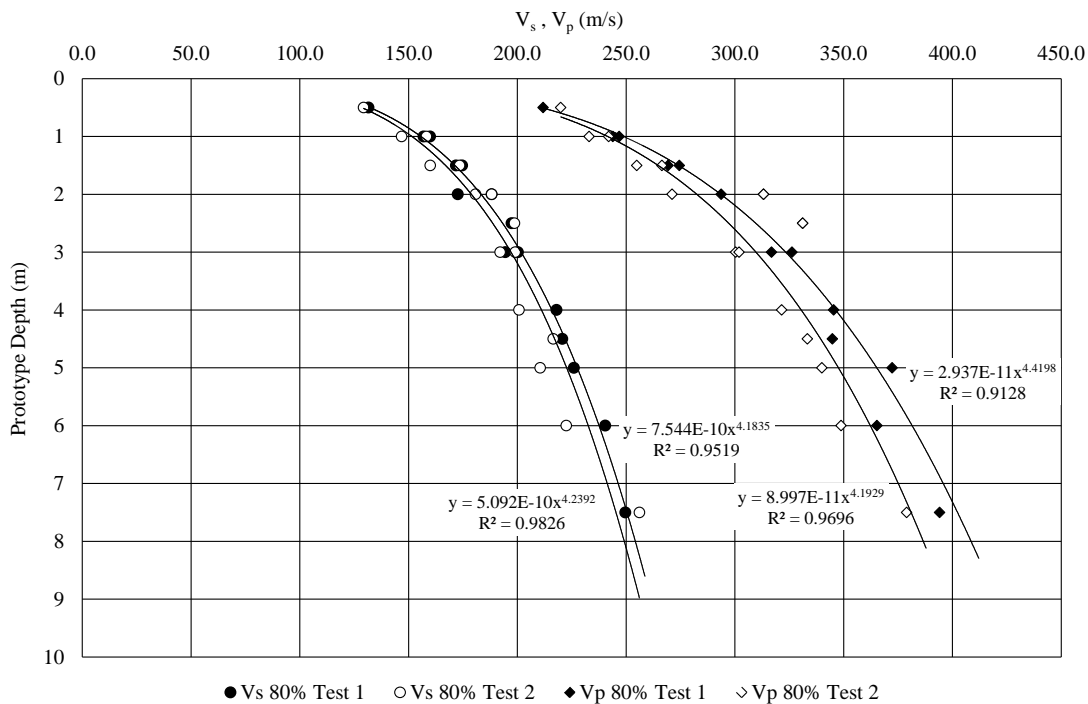


Figure 4.10: V_s and V_p for the 80%RD Tests

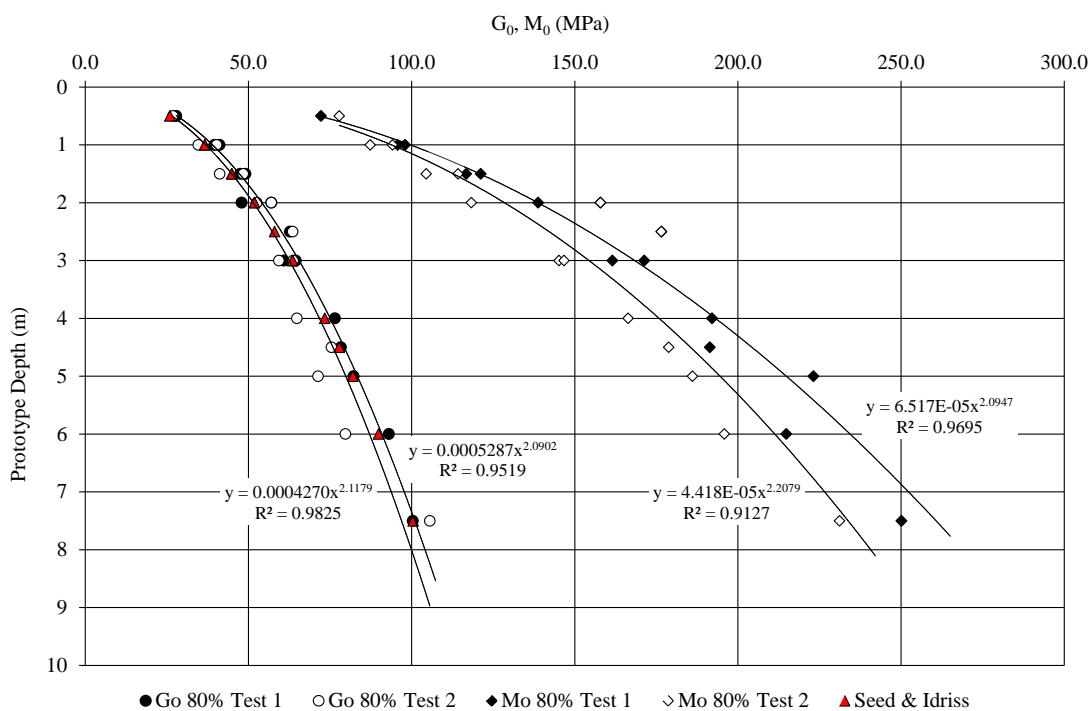


Figure 4.11: G_0 and M_0 for the 80%RD Tests

The results for the shear- and compression wave velocities range from 130m/s to 256m/s and 212m/s to 394m/s with depth respectively. The shear- and constrained small-strain values range from 27MPa to 106MPa and 72MPa to 250MPa with depth respectively. The small-strain shear stiffness values proposed by Seed & Idriss (1970) (Equation 2.25) for dense sand, compare well to the measured values. For the 80%RD Tests, the average Poisson's ratio calculated is 0.17.

Table 4.11: 80%RD Tests regression line values

Coefficients for power function: $y = ax^b$	80%RD Test 1				80%RD Test 2			
	V_s	V_p	G_0	M_0	V_s	V_p	G_0	M_0
a	5.092×10^{-10}	8.997×10^{-11}	4.270×10^{-04}	6.517×10^{-05}	7.544×10^{-10}	2.937×10^{-11}	5.287×10^{-04}	4.418×10^{-05}
b	4.2392	4.1929	2.1179	2.0947	4.1835	4.4198	2.0902	2.2079
R^2	0.9826	0.9696	0.9825	0.9695	0.9519	0.9128	0.9519	0.9127

4.2.5 EFFECT OF INCREASING DENSITY AND STRESS

From Section 4.1 it is clear that the density increases as the centrifuge g-level increases. As with the density, the overburden stress increases as the g-level increase and both these increases affect the wave velocities. Figure 4.12 show the shear- and compression wave velocities versus different density values. The results for all the tests indicate the same trend, therefore only the results for the 20%RD Test 1 are shown. The increase in density is due to the increase in g-level as indicated on the graph. The overall trend, as expected, is that the wave velocities increase as the density increase. What should be noticed is that at each density value three wave velocity values are shown. These data points indicate the different depths at which the bender- and extender elements were placed, and are also an indication of different overburden stresses at each density (increasing as shown on the figure). What can also be inferred from the data is that the wave velocities increase with decreasing void ratio (due to the increase in density). The effect of increasing overburden pressure is the same for increasing density i.e. that the wave velocities increasing with increasing overburden stress as shown in Figure 4.13.

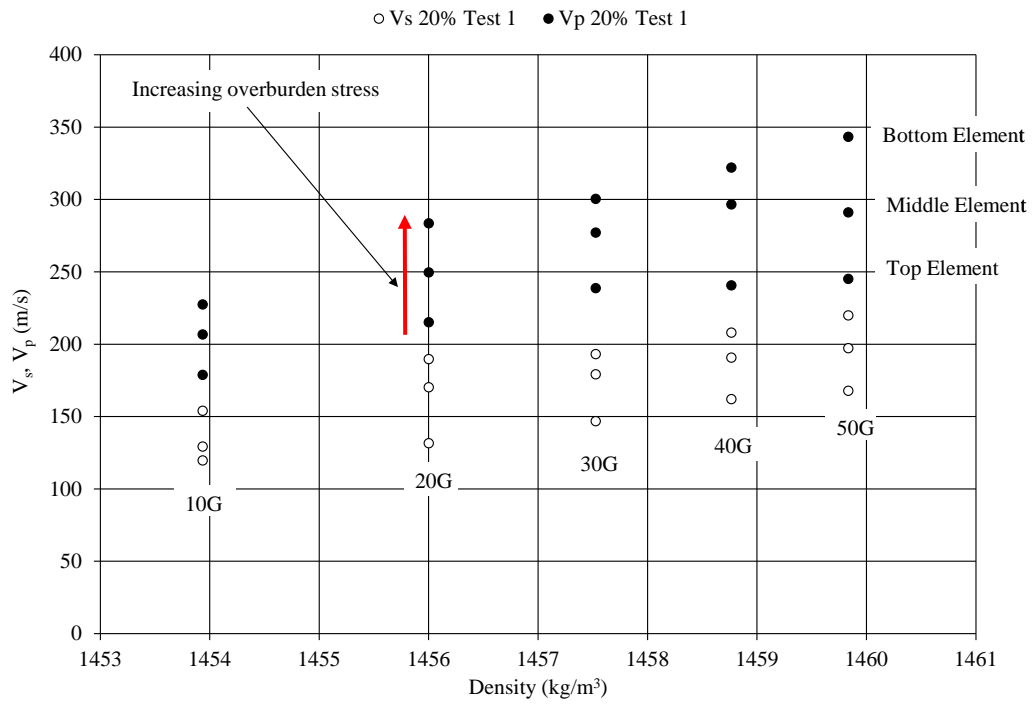


Figure 4.12: Wave velocities vs. density 20%RD Test 1

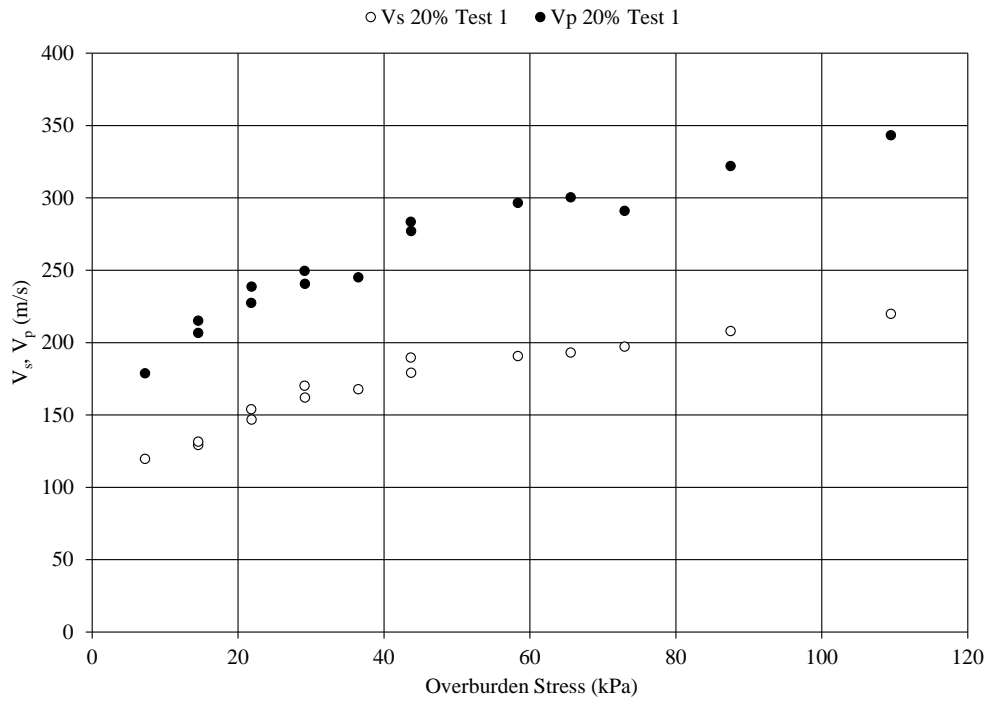


Figure 4.13: Overburden stress vs. wave velocities 20%RD Test 1

4.3 LOAD-SETTLEMENT RESULTS

For the load-settlement data, the calibration factors were imported into the data acquisition software before the tests were conducted. This allowed real time results to be in the correct units in order to assess the tests progress and stop it when the limiting criteria were reached as discussed in Section 3.4. Results were obtained for all the tests discussed previously, i.e. six data sets, two sets for each density.

As the results obtained were for the model setup, the data had to be converted to the prototype scale. Using the scaling laws for force and length in Table 2.5, the centrifuge values were converted to the prototype values, i.e. for a 5m foundation.

With reference to the settlement data, it was decided to represent the relative settlement (or pseudo-strain) rather than the actual settlement values. In effect, the relative settlement is a method of normalising the settlement for comparison between data sets. The relative settlement is calculated by dividing the settlement (s) value with the foundation diameter (D), i.e. s/D which is presented as a percentage. Most of the methods presented in Table 2.2 are in the form of the relative settlement (or can be easily written in the relative settlement format). Figure 4.14 shows the force - relative settlement result for the prototype foundation for the three different relative density tests. As expected, the force at a particular settlement increased as the relative density increased as depicted in Figure 4.14. The results were also repeatable as they compared reasonably well. Since most settlement methods use stress as an input value, it was also plotted as stress versus relative settlement, the results of which is shown in Figure 4.15. The graph shows the same trend as in Figure 4.14, the only difference being the vertical axis values depicting the stress. The values shown are far higher than typical observed practical values, but for the purpose of this project the foundation was loaded to failure. Considering the typical tolerable settlement value of 25mm, it was decided to plot the graph of stress versus relative settlement for values up to the tolerable settlement values which is a relative settlement of 0.50%. The graph depicting this is presented in Figure 4.16. What should be noticed from Figure 4.16 is that the stress values (between 200kPa and 300kPa) at the tolerable settlement (0.50%) are comparable to practical bearing values.

The undulations in the data presented in Figure 4.16 were caused by the vibrations of the centrifuge during testing. This, however, did not influence the objectives of this project since the stress-relative settlement data was used to acquire a trend rather than specific data points.

The data obtained was used to establish and evaluate the proposed method to predict foundation settlement for this project.

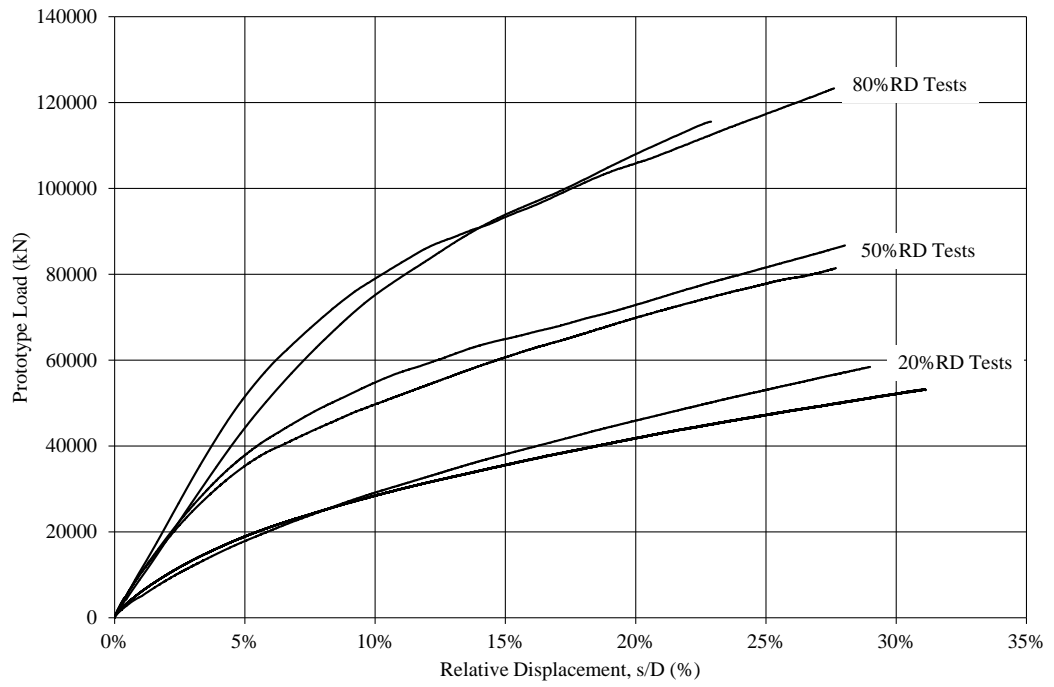


Figure 4.14: Force vs. relative settlement for prototype foundation

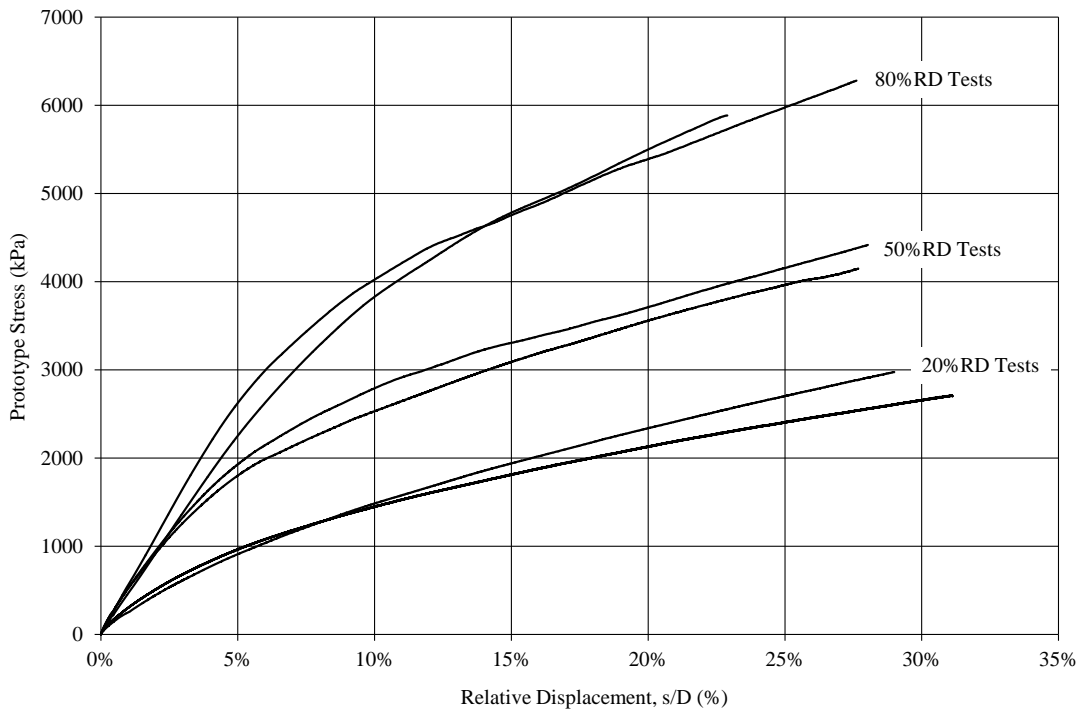


Figure 4.15: Stress vs. relative settlement for prototype foundation

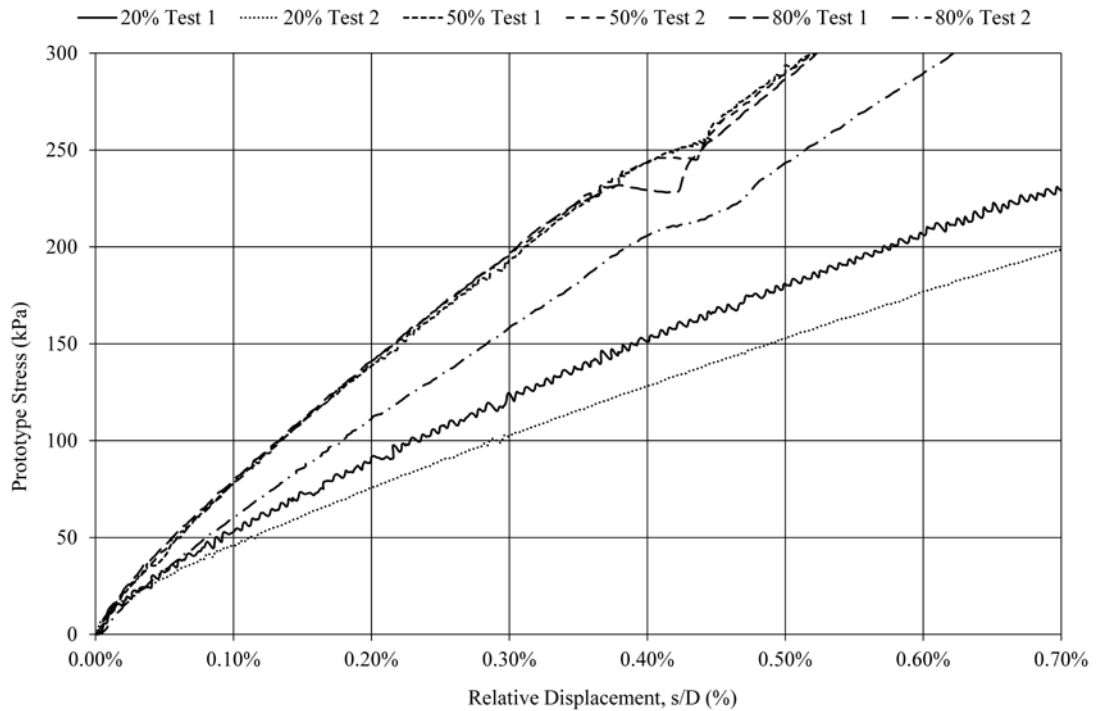


Figure 4.16: Stress vs. relative settlement for tolerable settlement of 25mm

4.4 FOUNDATION SETTLEMENT PREDICTION

The objective of this research project was to assess whether the load-settlement curve for a shallow foundation in sand can be predicted using only small-strain shear stiffness data. Various methods for settlement determination based on elastic theory were presented in Section 2. There are two main complications with the elastic theory methods presented; (1) some form of laboratory or in-situ testing is required to obtain some additional parameters (i.e. ultimate bearing capacity), and (2) the difficulty of knowing what the stiffness value for the soil is (whether it is small-strain stiffness or the stiffness at some higher strain value). The problem with point 1 is that it is sometimes not possible to obtain high quality samples for laboratory tests (especially in sands and gravels) and sensitive in-situ testing such as SPT or CPT are not possible or practical either. The second point is concerned with the fact that most methods require a single stiffness value. Since the stiffness increases with depth and the fact that stiffness is strain dependent, makes it difficult for the design engineer to know which value to use and in most cases the authors of different methods don't indicate which stiffness value should be used.

Considering the above, it was decided to use the non-linear stepwise approach presented in Section 2.3.3. The advantage of this approach is that it incorporates the stiffness with depth,

making it easier for a design engineer to use. It also requires no laboratory tests to be conducted, only in-situ seismic tests to determine the small-strain shear stiffness profile with depth.

The non-linear stepwise method to calculate the settlement, using small-strain shear stiffness data for a circular footing assuming axis-symmetrical conditions is as follows:

1. Obtain the small-strain shear stiffness profile with depth from in-situ test methods.
2. Subdivide the material below the foundation into layers down to at least a depth equalling twice the foundation width or diameter.
3. Assign E_0 as initial Young's modulus for each layer calculated from G_0 together with the Poisson's ratio. Equation 2.11 should be used.
4. Decide on the maximum applied stress as well as the number of load steps to be used.
5. Using Boussinesq's theory, calculate the vertical stress increment at the centre of each layer from Equation 2.7 and the radial stress σ_r from Equation 2.8.
6. Calculate the vertical strain (ϵ_v) for the first load step for each layer. Equation 4.1 should be used for the vertical strain calculation which incorporates the vertical (σ_z), as well as the circumferential (σ_θ) and radial stresses (σ_r).

$$\epsilon_v = \frac{[\sigma_z - 2\nu\sigma_r]}{E} \quad 4.1$$

where: ν = Poisson's ratio

E = Young's modulus

The vertical strain calculated for the first load step is done with the use of the small-strain Young's modulus values.

Since the strain calculated is the axial strain, the values should be transformed to shear strain (ϵ_s) values for use with the stiffness degradation curves. Equation 4.2 is used for this purpose.

$$\epsilon_s = \epsilon_v \frac{2}{3} (1 + \nu) \quad 4.2$$

7. Using a stiffness degradation curve together with the strain in each layer after application of the first load step, a new Young's modulus value is calculated for use in the next load step.
8. For each load step, the strain is calculated which together with a stiffness reduction curve is used to calculate a new Young's modulus (E_i) at each strain value (ϵ_i).

9. The process is repeated until the maximum applied stress is reached.
10. The total settlement is the combined settlement for all sub-layers (sub-layer thickness multiplied by the vertical strain calculated) for all the load steps:

$$\text{Total settlement} = \sum_j \sum_i (H_i \varepsilon_i) \quad 4.3$$

where: i = number of sub-layers

j = number of load steps

11. The predicted load-settlement curve is then constructed.

The methodology described was used together with the small-strain shear stiffness and load-settlement results from the centrifuge tests to assess the prediction ability of the method. It should be noted that no specific stiffness degradation curve is inherently associated with the method. Therefore it is up to the design engineer to choose an appropriate stiffness degradation curve. Considering the discussion of the different stiffness degradation curves in Section 2.3.1, it was decided to assess the curves presented by Oztoprak & Bolton (2013), Bolton & Whittle (1999) and Massarsch (2004). The equations used for the different methods are Equation 2.15 for Oztoprak & Bolton (2013), Equation 2.17 for Bolton & Whittle (1999) and Equation 2.18 for Massarsch (2004). The reason for using these curves is that they only require two variables to define the curve, making them attractive for this project as well as for engineers in practice.

4.4.1 FULL-RANGE RESULTS

For each of the density tests conducted, the proposed method was used to predict the stress-settlement curves. It was decided for the purpose of assessing the method to use 100 load increments with the maximum stress values as the maximum measured values. The variables of the three stiffness degradation curves were varied using an Excel optimisation algorithm (solver function) to obtain the best fit solution. Figure 4.17 to Figure 4.19 presents the full range stress-settlement results for the 20%RD, 50%RD and 80%RD tests, respectively. The results indicate the measured centrifuge curves as well as the proposed method results based on the different stiffness degradation curves used. The results presented are for the full range case, i.e. the full stress-settlement curve obtained from the centrifuge tests.

The proposed method together with the curves from Oztoprak & Bolton (2013) and Bolton & Whittle (1999) produced accurate results for the 20%RD test and coincided closely with each other. For the results based on the curve by Massarsch (2004), the predicted curve did not

conform well to the measured curve. The curve by Massarsch (2004) does not degrade the initial stiffness values sufficiently quickly to render accurate results.

For the 50%RD tests, similar results were obtained as for the 20%RD tests. Again the methods based on Oztoprak & Bolton (2013) and Bolton & Whittle (1999) stiffness degradation curves produced more accurate results than for the Massarsch (2004) case. Compared to the 20%RD test results, the methods based on Oztoprak & Bolton (2013) and Bolton & Whittle (1999) does not conform as well, but the predicted results are still in good agreement with the measured values.

The 80%RD test results indicate good agreement at large settlement and stress values, while there is a poor match between in the predicted and measured results at smaller stress and settlement values. An interesting characteristic is that for the 80%RD results, the proposed method for the three different stiffness degradation curve match relatively well with each other. However, there is still a slightly better agreement between the Oztoprak & Bolton (2013) and Bolton & Whittle (1999) results.

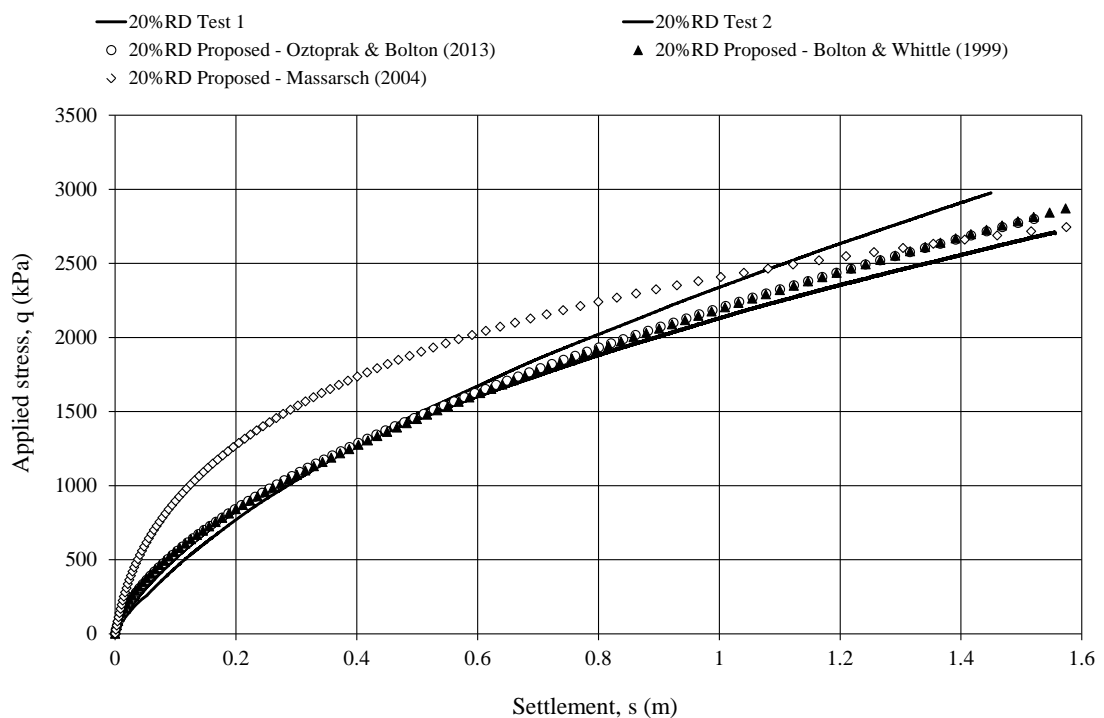


Figure 4.17: Predicted vs. measured results - 20%RD Tests – Full range

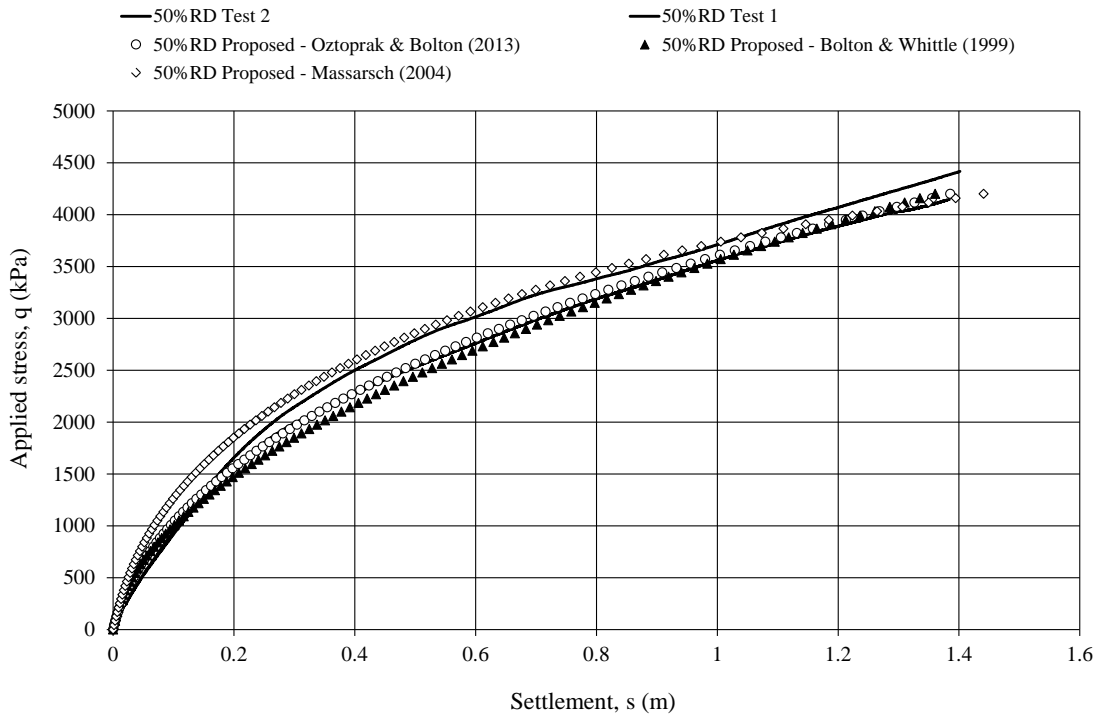


Figure 4.18: Predicted vs. measured results - 50%RD Tests – Full range

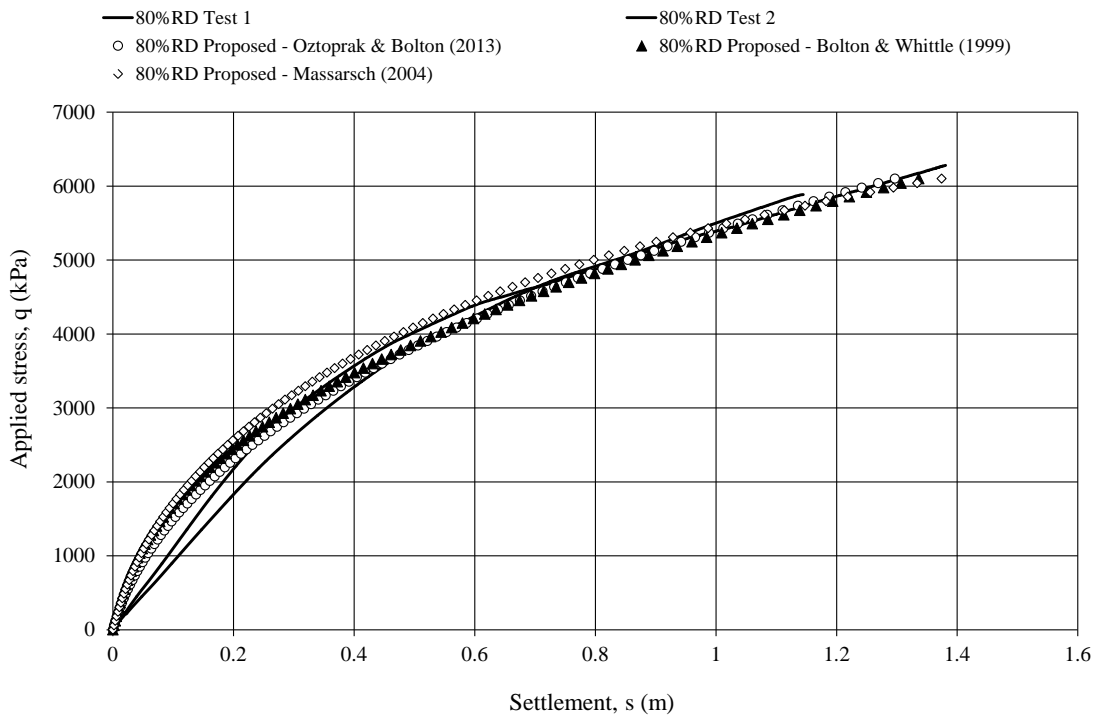


Figure 4.19: Predicted vs. measured results - 80%RD Tests – Full range

The values obtained for the variables of different stiffness degradation curves are presented in Table 4.12. It should be noticed that for the Oztoprak & Bolton (2013) variables, the elastic threshold strain value used was fixed at 0.001% strain. This value is the same as the value given in Section **Error! Reference source not found.** in which the small-strain stiffness is constant. Keeping this variable fixed renders a two-variable Oztoprak & Bolton (2013) stiffness degradation curve, which give the same number of variables as the other two methods. Figure 4.20 depicts the different stiffness degradation curves graphically based on the variables obtained for the best fit. As mentioned previously, the tests were setup with the different densities representing loose-, medium dense- and dense sand. Therefore, for practical purposes the variables can be grouped into the same categories are indicated in Table 4.12 and Figure 4.20.

Table 4.12: Proposed method stiffness degradation curve variables - Full range results

Curve	Variables					
	Loose sand (LS)		Medium Dense Sand (MDS)		Dense Sand (DS)	
Oztoprak & Bolton (2013)	y_e	0.001	y_e	0.001	y_e	0.001
	y_r	0.03	y_r	0.21	y_r	0.4
	a	0.47	a	0.65	a	0.68
Bolton & Whittle (1999)	α	0.16	α	0.23	α	0.35
	β	0.6	β	0.53	β	0.42
Massarsch (2004)	α	1.65	α	1.23	α	0.85
	β	0.15	β	0.13	β	0.11

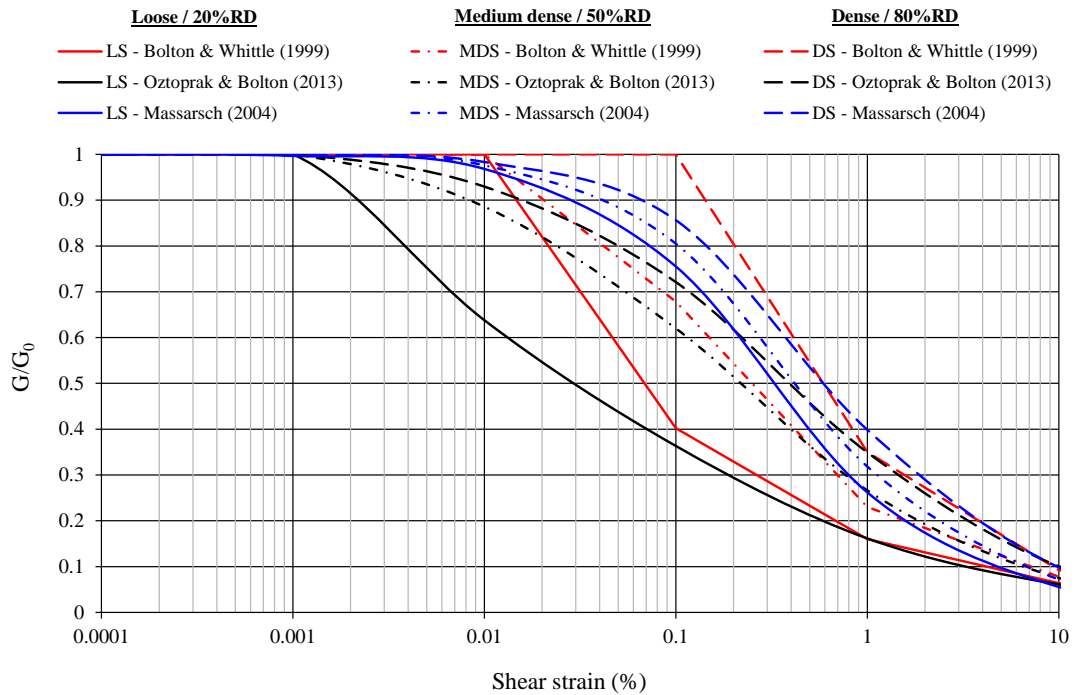


Figure 4.20: Proposed method stiffness degradation curves - Full range results

From the full range test results the main conclusion that can be made is that for lower density sands, the proposed method predicts the stress-settlement curve accurately. For high density sands (80%RD) the accuracy is poor for small settlements, with an improved fit at higher settlement values. For the medium dense case the results are more accurate than the high density case, but not as accurate as the low density case.

The reason for the differences might be due to the different failure mechanisms associated with the different densities. Considering Figure 2.9, higher density sands are associated with a general failure type. The failure mechanism for this type is elastic-plastic, indicating that yielding of the soil will not occur immediately, but rather after some amount of settlement has occurred. In contrast, low density sands conform to punching failure, which renders a mechanism that almost immediately behaves plastically. This indicates that yielding starts soon after application of the load. With the proposed method the small-strain stiffness value is used initially and subsequently degraded. This indicates that the proposed method takes into account immediate yielding from the small-strain stiffness value which is associated with the low density sand. For the high density sands, the fact that initial settlements occur during an elastic state, shows that the proposed method will not conform well to the actual behaviour. This is expected until yield of the soil occurs. Medium dense sands yield quicker than the dense case, but not as quickly as the low density sands. Therefore, results from the

proposed method will not be as accurate as the low density case, but more accurate than the high density case.

With reference to the different stiffness degradation curves, it can be said that the two best stiffness degradation curves to use are the curves from Oztoprak & Bolton (2013) and Bolton & Whittle (1999). Although the curve from Massarsch (2004) produces results that are more accurate at higher densities, it is not as accurate as the other two curves. It can also be said that, in order for the proposed method to produce more accurate results at higher densities, the stiffness degradation curves require more degrees of freedom in the form of more variables. This will however reduce the simplicity of the method and make it less attractive for practicing engineers to use.

4.4.2 PRACTICAL-RANGE RESULTS

In practice, settlements larger than 10% of the diameter (D) are usually not tolerated. It was therefore decided to follow the same procedure as for the full-range results, but to limit the prediction of the stress-settlement curve to a settlement of $0.1D$ of the centrifuge results, to assess how the proposed method performs for practical range levels. Thus, the centrifuge results up to 0.5m for the different density tests were compared with the best fit results of the proposed method. Figure 4.21 to Figure 4.23 presents the practical range stress-settlement results for the 20%RD, 50%RD and 80%RD tests, respectively.

As for the full-range, the practical-range results show that there is better agreement between the measured and predicted values at low densities than higher densities. The variables for the different stiffness degradation curves were adjusted to obtain a best fit for the proposed method. For the practical-scale cases none of the results using the Massarsch (2004) stiffness degradation curve proved to be satisfactory. For the Oztoprak & Bolton (2013) and Bolton & Whittle (1999) curves both results rendered similar stress-settlement curves and were in reasonably good agreement with the measured results.

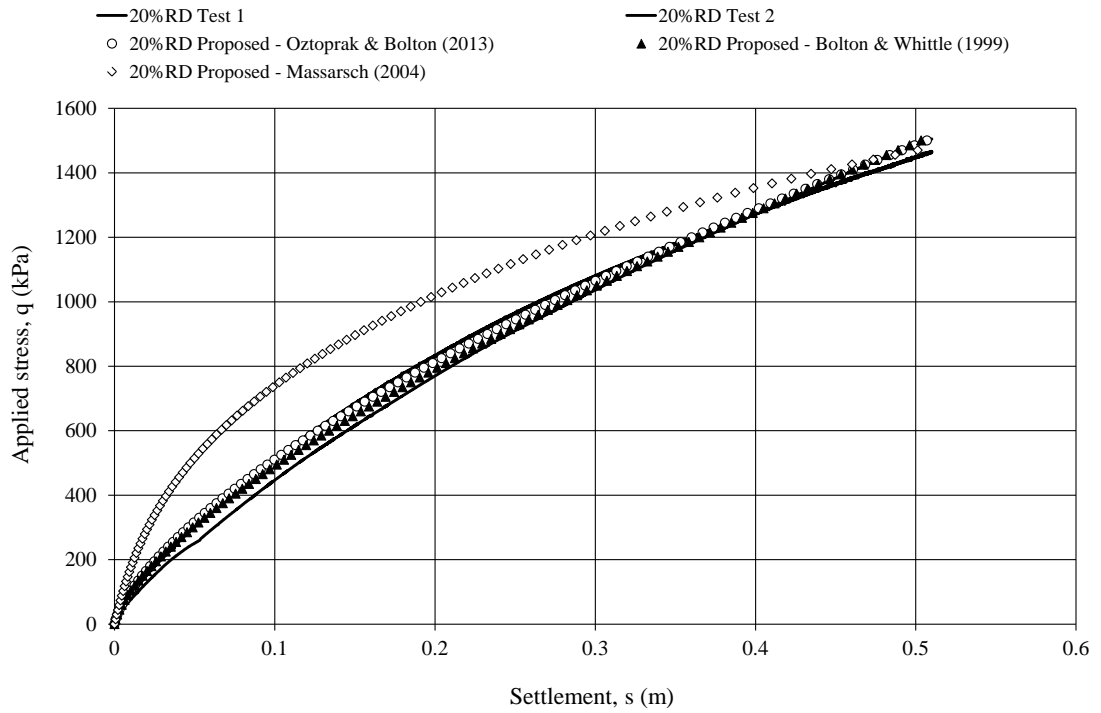


Figure 4.21: Predicted vs. measured results - 20%RD Tests – Practical range

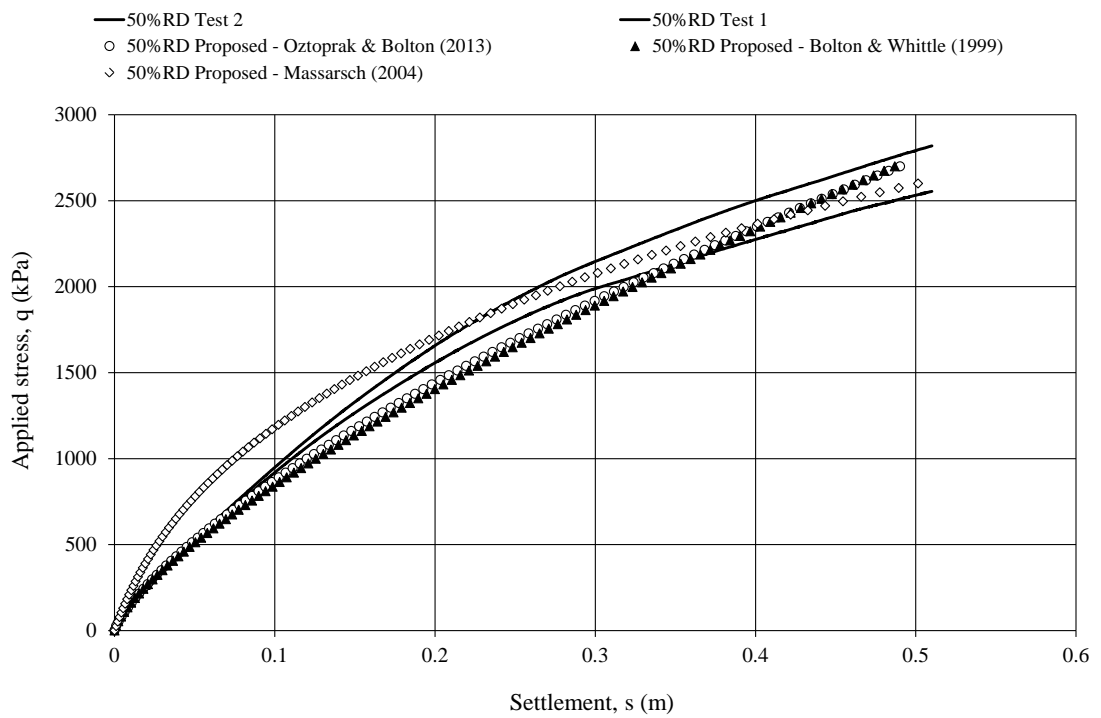


Figure 4.22: Predicted vs. measured results - 50%RD Tests – Practical range

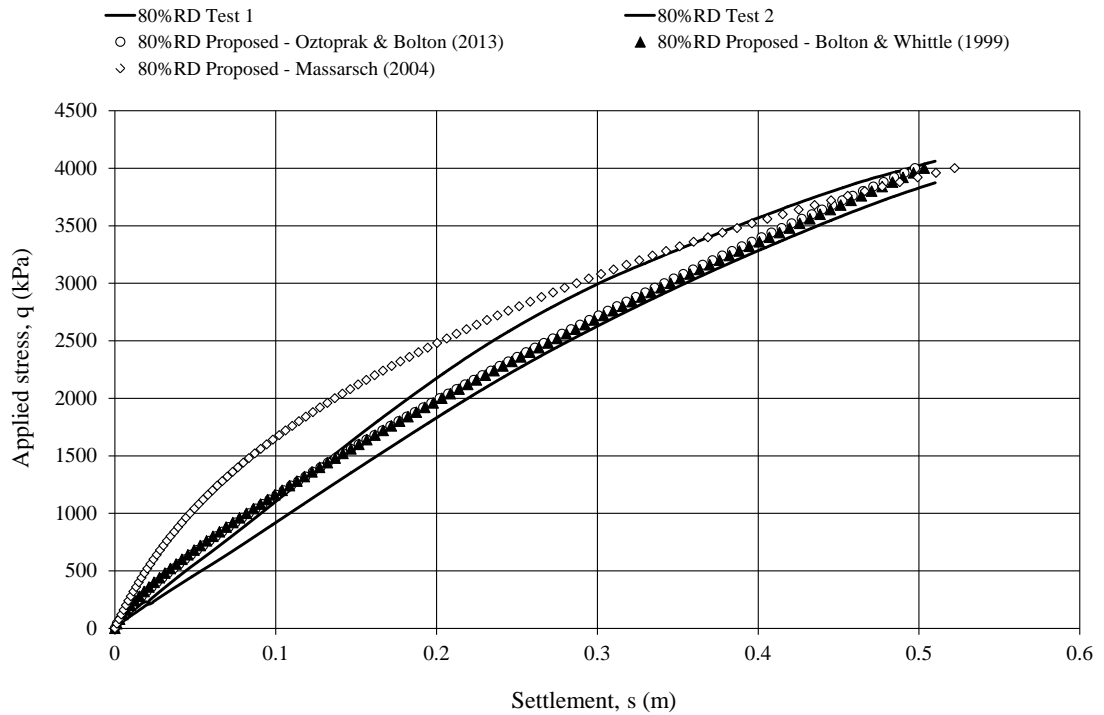


Figure 4.23: Predicted vs. measured results - 80%RD Tests – Practical range

The values for the variables for the practical-range results are given in Table 4.13 and it should be noticed that these value are slightly different from the full-scale variable values. The elastic threshold strain for the Oztoprak & Bolton (2013) curve was taken as the same for the full-range case, i.e. 0.001%. Figure 4.24 is the graphical representation of the different stiffness degradation curves for the practical range. From the figure it can be seen that the Oztoprak & Bolton (2013) and Bolton & Whittle (1999) graphs are in good agreement from approximately 0.1% strain. The Massarsch (2004) curve, however, does not agree well with any of the other curves, with the main difference being the fact the stiffness degradation starts at higher strain levels. What is also interesting to note is that for 0.1% strain (typical strain level for foundations), for dense and medium dense sands $\frac{G}{G_0} \approx 0.5$ and for loose sand $\frac{G}{G_0} \approx 0.3$.

Table 4.13: Proposed method stiffness degradation curve variables - Practical range results

Curve	Variables					
	Loose sand (LS)		Medium Dense Sand (MDS)		Dense Sand (DS)	
Oztoprak & Bolton (2013)	y_e	0.001	y_e	0.001	y_e	0.001
	y_r	0.012	y_r	0.065	y_r	0.0095
	a	0.38	a	0.39	a	0.32
Bolton & Whittle (1999)	α	0.16	α	0.24	α	0.29
	β	0.7	β	0.74	β	0.77
Massarsch (2004)	α	2.3	α	1.4	α	0.9
	β	0.15	β	0.13	β	0.11

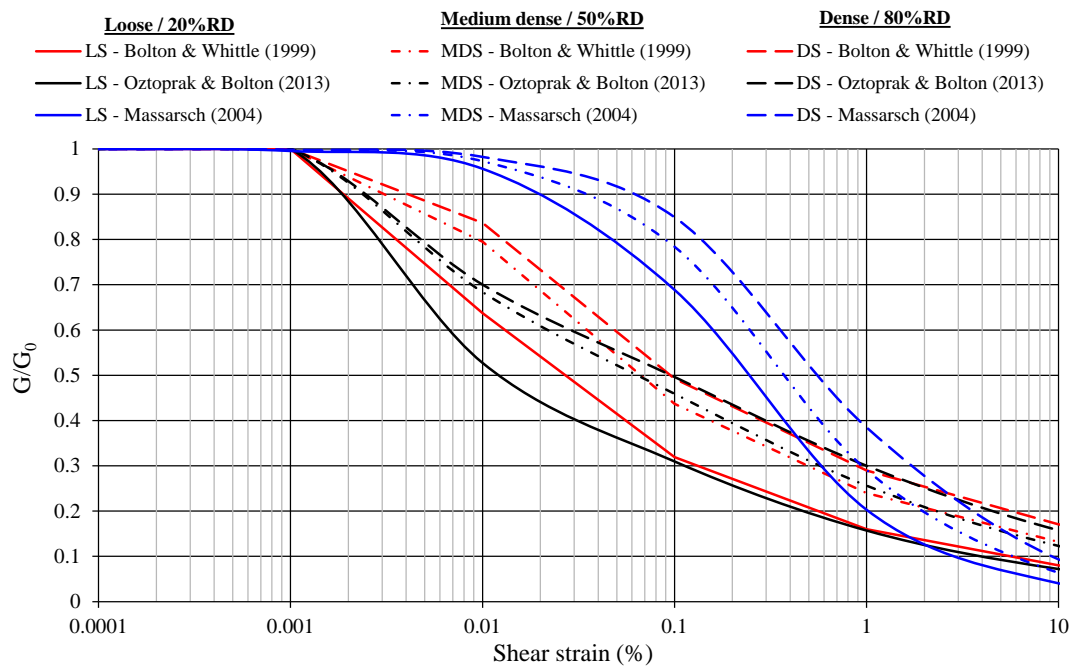


Figure 4.24: Proposed method stiffness degradation curves - Practical range results

As with the full-range results, the same conclusion can be drawn which is: for lower densities more accurate results are predicted by the proposed method. The reason for the less accurate results at higher densities is the same as discussed for the full-range results.

The best suited stiffness degradation curves together with the best fit variable values are the ones proposed by Oztoprak & Bolton (2013) and Bolton & Whittle (1999). The Massarsch (2004) curve did not render satisfactory results and can be disregarded for practical purposes.

What can be deduced is that for accurate settlement prediction a stiffness degradation curve is required that degrades from approximately 0.001% strain with a sharp initial degradation. Notwithstanding that there are some differences between the predicted and measured values at higher densities, for practicing engineers, the results should be satisfactory.

5 CONCLUSIONS AND RECOMMENDATIONS

In this section the main conclusions reached based on the results obtained will be conveyed. The conclusions will focus on the objectives of the report as outlined in Section 1.1. Subsequently, recommendations will be given to assist future research relating to the project topic.

5.1 CONCLUSIONS

The first conclusions are drawn from the experimental work conducted and are as follows:

- A thorough characterisation of the sand used in the centrifuge model was done. The tests done include:
 - Minimum and maximum density tests;
 - Particle size distribution;
 - Specific gravity;
 - Consolidated-drained triaxial tests;
 - Standard oedometer tests with bender- and extender elements;
 - A high load oedometer test up to 25MPa;
 - Scanning electron microscope photos

A summary of all the sand properties are given in Table 3.18. The sand was named **Cullinan Sand** and will be the standard testing sand to be used at the geotechnical centrifuge facility of the University of Pretoria.

- An instrumentation system was developed which enabled use of bender- and extender elements in the centrifuge. Standard quick-mount bender- and extender elements from Piezo Systems Inc. were used. A housing was developed in which the elements fit which allowed them to be used as free elements in the centrifuge model. The main aspect of the system, which the researcher developed, is the charge amplifier which increases the signal-noise ratio. The charge amplifier is an essential part of the system because without it, no bender- or extender elements signal could be measured during centrifuge testing. The system proved to be adequate and satisfactory small-strain results were obtained.

The main conclusion drawn from this dissertation is:

- A non-linear stepwise method was proposed to predict the stress-settlement behaviour of a shallow foundation. The method only requires the small-strain shear stiffness profile below the foundation.

- The method utilises a stiffness degradation curve, but is not bound by a specific stiffness degradation curve. Three stiffness degradation curves were investigated, due to their simplicity and that only two variables are required as input parameters. The stiffness degradation curves used is curves given by Oztoprak & Bolton (2013), Bolton & Whittle (1999) and Massarsch (2004).
- A non-linear stepwise method was used to predict the measured stress-settlement behaviour of a 5m circular shallow foundation on a young uncemented sand of different densities. The densities were loose, medium dense and dense sand. The three different stiffness degradation curve variables were varied until a best fit with the measured data was obtained. The variables were grouped to correspond to the three different density sands. The final conclusions based on the predictions are grouped as follows:

Full-range

The full-scale case refers to the entire measured stress-settlement curve. The proposed method renders accurate results for the loose sand utilising the degradation curves of Oztoprak & Bolton (2013) and Bolton & Whittle (1999). The Massarsch (2004) curve did not predict satisfactory results for the loose sand. For the medium dense sand, the method with Oztoprak & Bolton (2013) and Bolton & Whittle (1999) again rendered fairly accurate results but not the Massarsch (2004) case. The predicted stress-settlement curves for the dense sand produced similar results with the three different degradation curves. However, the comparison with the measured data showed good agreement at higher settlement values but not so well at smaller settlement values. The reason for this was attributed to the different failure modes associated with different density sands. Therefore it was finally concluded that utilising the degradation curves by Oztoprak & Bolton (2013) and Bolton & Whittle (1999) rendered similar results, with better agreement for low density sand with less accurate agreement for higher density sand.

Practical-range

For the practicing engineer, the full-scale results might not be relevant and it was decided to assess the proposed method for settlements up to 0.1D, which is more suitable for general design in practice. The method utilising the Massarsch (2004) curve rendered no satisfactory results and can be omitted. The methods utilising the degradation curves by Oztoprak & Bolton (2013) and Bolton & Whittle (1999) rendered similar results for the three soil densities. For the loose sand case, the proposed method produced accurate stress-settlement curves compared to the

measured curve. The accuracy decreases for the medium dense and dense sands, but for the practicing engineer the results should be satisfactory.

- It should be noted that the fitting parameters chosen for this project relates to loose, medium dense and dense sand and were specifically calibrated against the measured load - settlement data. For any new project, the designer should choose a stiffness degradation curve suitable for the soil conditions on site, with fitting parameters calibrated for the soil conditions. However, if the site conditions coincide with the data presented in this report, these fitting parameters together with the given stiffness degradation curves can be used.

Thus, considering the hypothesis, it can be concluded that the settlement of a foundation can be predicted using only the small-strain shear stiffness data. Therefore the hypothesis is accepted.

5.2 RECOMMENDATIONS

The following aspects are recommended for future research to calibrate the proposed method further or for other research based on the topic at hand:

- Other soil types should be tested which can include clays, cemented sands, etc.
- Assessing the method for other shallow foundation types and shapes.
- Evaluating if the proposed method is applicable for deep foundations.
- Since only two variables are required for the stiffness degradation curves, it may be researched if curves with more degrees of freedom are required to produce more accurate results for higher densities.
- The proposed method should be compared against actual in-situ stress-settlement data.
- Mini-cone penetrometer tests can be conducted in future experiments in order to assess the uniformity of the sand. It can also be used to obtain soil data at higher strain levels.

6 REFERENCES

- Amat, A. 2007. *Elastic Stiffness Moduli of Hostun Sand*. Master's Thesis. University of Bristol.
- Archer, A. & Heymann, G. 2014. Optimal free length of bender and extender elements used for seismic testing in geotechnical centrifuges. In Gaudin, C. & White, D., eds. *Proceedings of the 8th International Conference on Physical Modelling in Geotechnics*. Perth, 2014. CRC Press.
- Asslan, M. 2008. *Factors Influencing Small-Strain Stiffness of soils and its Determination*. Term Paper. Bauhaus-Universität Weimar.
- ASTM Standard D2487. 2011. *Standard Practice for Classification of Soils for Engineering Purposes (Unified Soil Classification System)*. DOI: 10.1520/D2487-11. West Conshohocken, PA: www.astm.org ASTM International.
- Atkinson, J. 1993. *An introduction to the mechanics of soils and foundations: Through critical state soil mechanics*. McGraw-Hill Book Co Ltd.
- Atkinson, J. & Bransby, P. 1978. *The Mechanics of Soils: An Introduction to Critical State Soil Mechanics*. McGraw-Hill Book Co Ltd.
- Barnes, G. 2000. *Soil Mechanics: Principles and Practice*. 2nd ed. Macmillan press ltd.
- Benz, T. 2007. *Small-Strain Stiffness of Soils and its Numerical Consequences*. PhD Thesis. Universität Stuttgart.
- Benz, T., Schwab, R. & Vermeer, P. 2009. Small-strain stiffness in geotechnical analyses. *Bautechnik*, 86(1), p.16–27.
- Berardi, R. & Lancellotta, R. 1991. Stiffness of granular soils from field performance. *Géotechnique*, 41(1), pp.149-57.
- Bødker, L. 1996. Gmax for Sand by Bender Elements at Anisotropic Stress States. In Erlingsson, S. & Sigursteinsson, H., eds. *Proceedings of the XII Nordic Geotechnical Conference : NGM-96*. Reykjavik, 1996. Icelandic Geotechnical Society.
- Bolton, M. & Whittle, R. 1999. A non-linear elastic/perfectly plastic analysis for plane strain undrained expansion tests. *Géotechnique*, 49(1), pp.133-41.
- Bovolenta, R. 2011. Settlement of shallow foundations on sand. *Geotechnical Engineering*, 164(GE5), pp.317-26.

- Bowles, J. 1987. Elastic Foundation Settlement on Sand Deposits. *Journal of Geotechnical Engineering*, 113(8), pp.846-60.
- Brandenberg, S.J. et al. 2006. A bender element system for measuring shear wave velocities in centrifuge models. In Ng, C., Wang, Y. & Zang, L., eds. *6th International Conference on Physical Modelling in Geotechnics*. Hong Kong, 2006. Taylor & Francis.
- Brandenberg, S., Kutter, B. & Wilson, D. 2008. Fast Stacking and Phase Corrections of Shear Wave Signals in a Noisy Environment. *Journal of Geotechnical and Geoenvironmental Engineering*, 134(8), pp.1154-65.
- Brown, P.T. 1969. Numerical analyses of uniformly loaded circular rafts on deep elastic foundations. *Geotechnique*, 19(3), pp.399-404.
- Campanella, R. 1994. Fields Methods for Dynamic Geotechnical Testing: An overview of Capabilities and Needs. In Ebelhar, R., Drnevich, V. & Kutter, B., eds. *Dynamic Geotechnical Testing II, ASTM STP 1213.*, 1994. American Society for Testing and Materials.
- Canadian Geotechnical Society 1992. *Canadian Foundation Engineering Manual*. 3rd ed. Vancouver: Bitech Publishers Ltd.
- Canadian Geotechnical Society 2006. *Canadian Foundation Engineering Manual*. 4th ed. Canadian Geotechnical Society.
- Cernica, J. 1995. *Geotechnical Engineering: Foundation Design*. New York: John Wiley & Sons.
- Chai, J. 2000. Shallow Foundations. In W. Chen & L. Duan, eds. *Bridge engineering handbook*. CRC Press. Ch. 31.
- Chan, C.-M. 2010. Bender Element Test in Soil Specimens: Identifying the Shear Wave Arrival Time. *The Electronic Journal of Geotechnical Engineering*, 15(Bundle M), pp.1263-76.
- Chen, W. & McCarron, W. 1991. Bearing Capacity of Shallow Foundations. In H. Fang, ed. *Foundation Engineering Handbook*. 2nd ed. New York: Van Nostrand Reinhold. Ch. 4. pp.144-61.
- Chen, L. et al. 2001. Consolidation and Stability Behaviour of a High Rockfill Dam Built on Soft Clay Foundation. In C. Lee et al., eds. *Soft Soil Engineering*. Hong Kong: A.A. Balkema. pp.175-80.
- Clayton, C. 2011. Stiffness at small strain: research and practice. *Géotechnique*, 61(1), pp.5-37.
- Craig, R.F. 2004. *Craig's Soil Mechanics*. 7th ed. New York: Spon Press.

- Das, B. 2008. *Advanced Soil Mechanics*. Taylor & Francis.
- Das, B. 2009. *Shallow foundations: bearing capacity and settlement*. 2nd ed. CRC Press.
- Das, B. 2011. *Principles of Foundation Engineering*. 7th ed. Stamford: Cengage Learning.
- Das, B. & Sivakugan, N. 2007. Settlements of shallow foundations on granular soil — an overview. *International Journal of Geotechnical Engineering*, 1(1), pp.19-29.
- Deniz, R. 2008. *Bender elements and bending disks for measurement of shear and compressional wave velocities in large sand specimens*. Master's Thesis. Northeastern University: <http://hdl.handle.net/2047/d10018645>.
- Düzceer, R. 2009. Observed and predicted settlement of shallow foundation. In Atalar, C. et al., eds. *2nd International Conference on New Developments in Soil Mechanics and Geotechnical Engineering*, 2009. Near East University Press.
- Elhakim, A. 2005. *Evaluation of shallow foundation displacements using soil small-strain stiffness*. PhD Thesis. Georgia Institute of Technology.
- Elhakim, A. & Mayne, P. 2003. Derived stress-strain-strength of clays from seismic cone tests. In Di Benedetto, H., Doanh, T., Geoffroy, H. & Sauzéat, C., eds. *Deformation Characteristics of Geomaterials*. Lyon, 2003. Swets & Zeitlinger.
- Enkhtur, O., Nguyen, T., Kim, J. & Kim, S. 2013. Evaluation of the Settlement Influence Factors of Shallow Foundation by Numerical Analyses. *KSCE Journal of Civil Engineering*, 17(1), pp.85-95.
- Fahey, M. & Carter, J. 1993. A finite element study of the pressuremeter test in sand using a nonlinear elastic plastic model. *Canadian Geotechnical Journal*, 30(2), pp.348-62.
- Fellenius, B. 2009. *Basics of foundation design*. Electronic ed. www.Fellenius.net.
- Fu, L. 2004. *Application of piezoelectric sensors in soil property determination*. PhD Thesis: Case Western Reserve University.
- Fu, L., Zeng, X. & Figueroa, J. 2004. Shear Wave Velocity Measurement in Centrifuge Using Bender Elements. *International Journal of Physical Modelling in Geotechnics*, 4(2), pp.1-11.
- Garnier, J. et al. 2007. Catalogue of scaling laws and similitude questions in geotechnical centrifuge modelling. *International Journal of Physical Modelling in Geotechnics*, 3, pp.1-23.
- Gaudin, C. et al. 2010. A miniature high speed data acquisition system for geotechnical centrifuges. In *Proceedings of the 7th International Conference on Physical Modelling in Geotechnics*. Zurich, Switzerland, 2010. Taylor & Francis Group.

- Gunn, M. 1993. The prediction of surface settlement profiles due to tunneling. In Houslyby, G. & Schofield, A., eds. *Predictive Soil Mechanics: Proceedings of the Wroth Memorial Symposium*. St. Catherine's College, Oxford, 27-29 July 1992, 1993. Thomas Telford.
- Hadad, A. & Ahidashti, R. 2013. Prediction of immediate settlement of shallow foundation over granular soils using small-strain stiffness. *Journal of American Science*, 9(6), pp.480-89.
- Hardin, B. & Drnevich, V. 1972. Shear modulus and damping in soils: design equations and curves. *Journal of the Soil Mechanics and Foundations Division, ASCE*, 98(SM 7), pp.667-92.
- Heymann, G. 1998. *The stiffness of soils and weak rocks at very small strains*. PhD Thesis. UK: University of Surrey.
- Heymann, G. 2007. Ground stiffness measurement by the continuous surface wave test. *Journal of the South African Institution of Civil Engineering*, 49(1), p.25–31.
- Hilf, J. 1991. Compacted Fill. In H. Fang, ed. *Foundation Engineering Handbook*. 2nd ed. New York: Van Nostrand Reinhold. pp.249-316.
- Holtz, R. 1991. Stress Distribution and Settlement of Shallow Foundations. In H. Fang, ed. *Foundation Engineering Handbook*. 2nd ed. New York: Van Nostrand Reinhold. Ch. 5. pp.166-216.
- Holtz, B. & Kovacs, W. 1981. *An Introduction to Geotechnical Engineering*. New Jersey: Prentice-Hal.
- Illston, J. & Domone, P. 2001. *Construction Materials: Their Nature and Behaviour*. 3rd ed. Spon Press.
- Jacobsz, S., Kearsley, E. & Kock, J. 2014. The geotechnical centrifuge facility at the University of Pretoria. In Gaudin, C. & White, D., eds. *Proceedings of the 8th International Conference on Physical Modelling in Geotechnics*. Perth, 2014. CRC Press.
- Jastrzębska, M. & Łupieżowiec, M. 2011. The influence of the choice of strain modulus value on foundation settlement. *Studia Geotechnica et Mechanica*, XXXIII(2), pp.31-39.
- Kim, N. & Kim, D. 2010. Development of VS tomography testing system for geotechnical centrifuge experiments. Zurich, 2010. CRC Press.
- Kusakabe, O. 1995. Foundations. In R. Taylor, ed. *Geotechnical Centrifuge Technology*. Blackie Academic and Professional. pp.120-72.
- Kusakabe, O. 1995. Foundations. In R. Taylor, ed. *Geotechnical centrifuge technology*. Blackie Academic & Professional. pp.120-72.

- Lee, J.-S. 2003. *High resolution geophysical techniques for small-scale soil model testing*. PhD Thesis. Georgia Institute of Technology.
- Lee, J.-S. & Santamarina, J. 2005. Bender Elements: Performance and Signal Interpretation. *Journal of geotechnical and geoenvironmental engineering*, 131(9), pp.1063-70.
- Lee, J.-S. & Santamarina, J. 2006. Discussion “Measuring shear wave velocity using bender elements” by Leong E. C., Yea, S. H. and Rahardjo, H. *Geotechnical Testing Journal*, 29(5), pp.439-41.
- Leong, E., Cahyadi, J. & Rahardjo, H. 2005. Measuring shear wave velocity using bender elements. *Geotechnical Testing Journal*, 28(5).
- Leong, E., Cahyadi, J. & Rahardjo, H. 2009. Measuring shear and compression wave velocities of soil using bender–extender elements. *Canadian Geotechnical Journal*, 46(7), pp.792-812.
- Look, B. 2014. *Handbook of Geotechnical Investigation and Design Tables*. 2nd ed. London: CRC Press/Balkema.
- Lutenegger, A. & DeGroot, D. 1995. *Settlement of shallow foundations on granular soils*. Research Report. Massachusetts Highway Department.
- Mair, R. 1993. Developments in geotechnical engineering research: applications to tunnels and deep excavations. *Unwin Memorial Lecture 1992. Proceedings of the Institution of Civil Engineers, Civil Engineering*, 97(1), pp.27-41.
- Massarsch, K. 2004. Deformation properties of fine-grained soils from seismic tests. In Viana da Fonseca, A. & Mayne, P., eds. *Proceedings ISC-2 on Geotechnical and Geophysical Site Characterization*. Rotterdam, 2004. Millpress.
- Mayne, P. 1995. Evaluating Foundation Response by G/Gmax Modulus Degradation Relationships in Soils. In Council/ROC, N.S.F.a.N.S., ed. *Proceedings, NSF Workshop on U.S.-Taiwan Geotechnical Collaboration*. Taipei, 1995.
- Mayne, P. & Poulos, H. 1999. Approximate displacement influence factors for elastic shallow foundations. *Journal of Geotechnical and Geoenvironmental Engineering*, 125(6), pp.453-60.
- Mayne, P. & Poulos, H. 2001. Approximate Displacement Influence Factors for Elastic Shallow Foundations - Closure. *Journal of Geotechnical and Geoenvironmental Engineering*, 127(1), pp.99-102.
- Menzies, B. 2000. Near-surface site characterisation by ground stiffness profiling using surface wave geophysics. In Saxena, K. & Sharma, V., eds. *Instrumentation in Geotechnical*

Engineering. H.C.Verma Commemorative Volume. New Delhi, 2000. Oxford & IBH Publishing Co. Pvt. Ltd.

Micromeritics 2014. *AccuPyc II 1340 Pycnometer*. [Online] Micromeritics Available at: <http://www.micromeritics.com/Product-Showcase/AccuPyc-II-1340.aspx> [Accessed 30 January 2014].

Moxhay, A., Tinsley, R., Redgers, J. & Gravell, D. 2008. The prediction of ground settlement from continuous surface wave data. *Ground Engineering*, July. pp.34-38.

Ng, C. et al. 2001. The Hong Kong Geotechnical centrifuge and its unique capabilities. *Sino-Geotechnics*, 83, pp.5-12.

Oweiss, I. 1979. Equivalent Linear Model for Predicting Settlements of Sand Bases. *Journal of Geotechnical Engineering*, 105(No. GT12), pp.1525-44.

Oztoprak, S. & Bolton, M. 2013. Stiffness of sands through a laboratory test database. *Géotechnique*, 63(1), pp.54-70.

Papadopoulos, B. 1992. Settlement of Shallow Foundations on Cohesionless Soils. *Journal of Geotechnical Engineering*, 118(3), pp.377-93.

Peck, R.B., Hanson, W.E. & Thornburn, T.H. 1953. *Foundation engineering*. New York: John Wiley & Sons Inc.

Perloff, W. 1975. Pressure distribution and Settlement. In H. Winterkom & H.-Y. Fang, eds. *Foundation Engineering Handbook*. 1st ed. Van Nostrand Reinhold Company. pp.148-96.

Pfaff-silberblau 2010. *Compendium Screw Jacks*. 3rd ed. Pfaff-silberblau.

Phillips, R. 1995. Centrifuge modelling: practical considerations. In R. Taylor, ed. *Geotechnical centrifuge technology*. Blackie Academic & Professional. pp.35-61.

Piezo Systems, Inc. 2011. *CATALOG #8*. [Online] Woburn: Piezo Systems, Inc. Available at: <http://www.piezo.com/catalog.html>.

Poulos, H. 2006. Foundation Design – The Research-Practice Gap. In *2nd Jennings Memorial Lecture*. Australia, 2006. Coffey Geosciences, Australia & University of Sydney.

Powrie, W. 1997. *Soil Mechanics: Concepts and Applications*. 1st ed. E & FN Spon.

Prevost, J. & Keane, C. 1990. Shear stress-strain curve generation from simple material parameters. *Journal of Geotechnical and Geoenvironmental Engineering*, 116(8), pp.1250-54.

Puzrin, A. & Burland, J. 1996. A logarithmic stress-strain function for rocks and soils. *Geotechnique*, 46(1), pp.157-64.

- Puzrin, A. & Burland, J. 1998. Non-linear model of small-strain behavior of soils. *Geotechnique*, 48(2), pp.217-33.
- Ramberg, W. & Osgood, W. 1943. *Description of stress-strain curves by three parameters*. Technical Note No. 902. Washington: National Advisory committee for Aeronautics.
- Rio, J. 2006. *Advances in Laboratory Geophysics Using Bender Elements*. PhD Thesis. London: University College London.
- Salgado, R., Bandini, P. & Karim, A. 2000. Shear Strength and Stiffness of Silty Sand. *Journal of Geotechnical and Geoenvironmental Engineering*, 126(5), p.451–462.
- Samtani, N. & Nowatzki, E. 2006. *Soils and Foundations Reference Manual - Volume II*. Technical Report. Federal Highway Administration, U.S. Department of Transport. Report No. FHWA-NHI-06-089.
- Seed, H. & Idriss, I. 1970. *Soil Moduli and Damping Factors for Dynamic Response Analyses*. Research Report EERC70-10. Berkeley: University of California.
- Shibuya, S., Mitachi, T., Fukuda, F. & Hosomi, A. 1997. Modeling of strain-rate dependent deformation of clay at small strains. In *Proceedings of the 14th International Conference on Soil Mechanics and Geotechnical Engineering*. Hamburg, 1997. Vol. 1.
- Smith, I. 2006. *Smith's Elements of Soil Mechanics*. Blackwell Publishing.
- Szczepański, T. 2008. Soil small strain parameters derived from wave velocity measurements. *Geologija*, 50(Supplement P), p.S85–S89.
- Tapashetti, P., Gupta, A., Mithlesh, C. & Umesh, A. 2012. Design and Simulation of Op Amp Integrator and Its Applications. *International Journal of Engineering and Advanced Technology*, 1(3), pp.12-19.
- Taylor, R. 1995. Centrifuges in modelling: principles and scale effects. In R. Taylor, ed. *Geotechnical centrifuge technology*. Blackie Academic & Professional. pp.20-34.
- Terzaghi, K., Peck, R. & Mesri, G. 1996. *Soil Mechanics in Engineering Practice*. 3rd ed. John Wiley & Sons, Inc.
- Tschebotarioff, G. 1953. *Foundations, Retaining and Earth Structures*. New York: McGraw-Hill Book Co.
- Tschebotarioff, G. 1971. *Foundations, Retaining and Earth Structures*. New York: McGraw-Hill Co.
- University of Bolton 2010. *Bearing Capacity - Shallow and Deep Foundations*. [Online] (1.0) [Accessed 8 January 2013].

- Vardanega, P. & Bolton, M. 2013. Stiffness of Clays and Silts: Normalizing Shear Modulus and Shear Strain. *Journal of Geotechnical and Geoenvironmental Engineering*, 139(9), p.1575–1589.
- Venkatramaiah, C. 2006. *Geotechnical Engineering*. 3rd ed. New Delhi: New Age International.
- Vesic, A. 1975. Bearing Capacity of Shallow Foundations. In H. Winterkorn & H. Fang, eds. *Foundation Engineering Handbook*. 1st ed. Van Nostrand Reinhold. Ch. 3. pp.121-47.
- Viggiani, G. & Atkinson, J. 1995. Interpretation of bender element tests. *Géotechnique*, 45(1), p.149 –154.
- Wahls, H. & Gupta, M. 1994. Settlement of Shallow Foudations on Sand. *Vertical and Horizontal Deformations of Foundations and Embankments*, 1, pp.190-206.
- Wood, D. 2004. *Geotechnical Modelling*. Spon Press.
- Woods, R. 1978. Measurement of Dynamic Soil Properties. In ASCE, ed. *Earthquake engineering and soil dynamics: proceedings of the ASCE Geotechnical Engineering Division specialty conference*. Pasadena, CA, 1978. ASCE.
- Yamashita, S. et al. 2009. International Parallel Test on the Measurement of Gmax Using Bender Elements. *Soils and Foundations*, 49(4), pp.631-50.
- Yang, J. & GU, X. 2013. Shear stiffness of granular material at small strains: does it depend on grain size? *Géotechnique*, 63(2), pp.165-79.
- Yimsiri, S. & Soga, K. 2002. Technical Note: A Review of local strain measurement systems for triaxial testing of soils. *Journal of the Southeast Asian Geotechnical Society*, (4), pp.41-52.
- Yongqing, H. 2011. *Settlement of Shallow foundation on cohesionless soil considering modulus degredation of soil*. PhD Thesis. Nanyang Technological University.
- Zhou, Y. 2006. *Soils and Foundations: Reference Manual – Volume II*. Technical Report. National Highway Institute.
- Zhou, Y. et al. 2010. Free type bender elements for characterizing soil in centrifuge model tests. In Seward, L., ed. *Conference on Physical Modelling in Geotechnics (ICPMG 2010)*. Zurich, 2010. CRC Press.

APPENDIX A – MODEL FOUNDATION SCALING CALCULATION

Centrifuge Foundation Setup

Scale Factor (N) = 50 $\phi' = 39.0$ deg
 Foundation diameter, D (mm) = 100 $c' = 0.0$ kPa
 Foundation area (mm²) = 7854
 Embedded Depth in Centrifuge (mm) = 20

 Distance from side - length = 3D
 Distance from side - width = 2D
 Distance from bottom = 3.3D

 Depth from foundation to bottom (mm) = 330

 Ultimate bearing capacity (kPa) = 3053

 Force adjustment factor for centrifuge (kN) = $4E-04$ (1/N²)

 Force on foundation in centrifuge (kN) = 24.0 - Ultimate bearing capacity

